Exploitation of the Mesosphere (MesosphEO)

ESA MesosphEO

Algorithm Theoretical Basis Document (ATBD)

ITT ESA/AO/1-7759/14/SB-NC
Date: 13-12-2017
Version: ATBD 2.2

WP Manager:
Alexei Rozanov
WP Manager Organization:
Intitute of Enironmental Physics, University of Bremen (UB)

Document Change Record

Issue	Revision	Date	Modified Items
1	0	16.11.2015	First draft of the document
2	0	29.05.2016	Descriptions of the algorithms which were improved or newly developed are added
2	1	09.12.2016	Contributions from GOMOS(BISA), MIPAS (IMK/IAA) and SCIAMACHY (UB) are updated, author list introduced
2	2	13.12.2017	Update of MIPAS O_3 and CO_2 ATBDs

List of authors

Section 2.1: Patrick Sheese (psheese@atmosp.physics.utoronto.ca) and Chris Boone
Section 2.2: Erkki Kyrölä (Erkki.Kyrola@fmi.fi), Viktoria Sofieva, Alain Hauchecorne
Section 2.3: Manuel López-Puertas (puertas@iaa.es), Maya García-Comas, Angela Gardini, Bernd Funke
Section 2.4: Patrick Sheese (psheese@atmosp.physics.utoronto.ca)
Section 2.5: Alexei Rozanov (alex@iup.physik.uni-bremen.de)
Section 2.6: Kristell Perot (kristell.perot@chalmers.se)
Section 3.1: Patrick Sheese (psheese@atmosp.physics.utoronto.ca)
Section 3.2: Bernd Funke (bernd@iaa.es), Maya García-Comas, Angela Gardini, Manuel López-Puertas
Section 3.3: (Kristell Perot) kristell.perot@chalmers.se
Section 4.1: Patrick Sheese (psheese@atmosp.physics.utoronto.ca)
Section 4.2: Bernd Funke (bernd@iaa.es), Maya García-Comas, Angela Gardini, Manuel López-Puertas
Section 4.3: Patrick Sheese (psheese@atmosp.physics.utoronto.ca)
Section 4.4: Stefan Bender (stefan.bender@kit.edu), Miriam Sinnhuber
Section 4.5: (Kristell Perot) kristell.perot@chalmers.se
Section 5: Bernd Funke (bernd@iaa.es), Maya García-Comas, Angela Gardini, Manuel López-Puertas
Section 6.1: Patrick Sheese (psheese@atmosp.physics.utoronto.ca)
Section 6.2: Maya García-Comas (maya@iaa.es), Angela Gardini, Bernd Funke, Manuel López-Puertas
Section 7.1: Erkki Kyrölä (Erkki.Kyrola@fmi.fi), Viktoria Sofieva, Alain Hauchecorne
Section 7.2: Bernd Funke (bernd@iaa.es), Maya García-Comas, Angela Gardini, Manuel López-Puertas
Section 8: Alain Hauchecorne (alain.hauchecorne@latmos.ipsl.fr)
Section 9.1: Patrick Sheese (psheese@atmosp.physics.utoronto.ca)
Section 9.2: Maya García-Comas (maya@iaa.es), Angela Gardini, Bernd Funke, Manuel López-Puertas
Section 9.3: (Kristell Perot) kristell.perot@chalmers.se
Section 10.1: Patrick Sheese (psheese@atmosp.physics.utoronto.ca)
Section 10.2: Maya García-Comas (maya@iaa.es), Angela Gardini, Bernd Funke, Manuel López-Puertas
Section 11.1: Patrick Sheese (psheese@atmosp.physics.utoronto.ca)
Section 11.2: Manuel López-Puertas (puertas@iaa.es), Maya García-Comas, Angela Gardini, Bernd Funke
Section 12.1: Didier Fussen (Didier.Fussen@oma.be)
Section 12.2: Alexei Rozanov (alex@iup.physik.uni-bremen.de) and Martin Langowski
Section 12.3: Alexei Rozanov (alex@iup.physik.uni-bremen.de)
Section 12.4: Christian von Savigny (csavigny@physik.uni-greifswald.de)
Section 13.1: Alain Hauchecorne (alain.hauchecorne@latmos.ipsl.fr)
Section 13.2: Manuel López-Puertas (puertas@iaa.es), Maya García-Comas, Angela Gardini, Bernd Funke
Section 13.3: Christian von Savigny (csavigny@physik.uni-greifswald.de) and Tobias Bachmann
Section 14.1: Patrick Sheese (psheese@atmosp.physics.utoronto.ca)
Section 14.2: Didier Fussen (Didier.Fussen@oma.be)
Section 14.3: Alain Hauchecorne (alain.hauchecorne@latmos.ipsl.fr)
Section 14.4: Maya García-Comas (maya@iaa.es), Angela Gardini, Bernd Funke, Manuel López-Puertas
Section 14.5: Bernd Funke (bernd@iaa.es), Maya García-Comas, Angela Gardini, Manuel López-Puertas
Section 14.6: Patrick Sheese (psheese@atmosp.physics.utoronto.ca)
Section 14.7: (Kristell Perot) kristell.perot@chalmers.se
Section 15.1: Alexei Rozanov (alex@iup.physik.uni-bremen.de) and Martin Langowski
Section 15.2: Alexei Rozanov (alex@iup.physik.uni-bremen.de)

Other contributors

John.P. Burrows, Doug Degenstein, Kaley Walker

Contents

1. Introduction

This document was prepared as deliverable D4 of the ESA Exploration of the Mesosphere project (MesosphEO). The document describes retrieval algorithms selected for usage within the MesosphEO project. For some of the algorithms a need for improvements has been identified at an early stage of the project. A detailed description of these improvements is also included in the document below. Each section of the document describes a method to obtain vertical distributions of a mesospheric species from measurements of a particular satellite instrument, detailed specifications of the used data sets and auxiliary parameters needed to initialise the retrievals.

2. Ozone

2.1 ACE-FTS (UoT)

The ACE-FTS v3.5 temperature and VMR retrievals are described in detail by Boone et al. (2005, 2013). The following description is taken from those papers. For ACE-FTS processing, CO_2 is analyzed to determine pressure. A crucial aspect of the pressure and temperature retrieval process is pointing knowledge. No information from sensors onboard the satellite (other than a clock) is used in the computation of tangent altitudes. The current approach treats tangent altitudes as unknown parameters in the pressure/temperature retrievals. Rather than fitting the entire spectrum, we analyze microwindows that contain spectral features from a molecule of interest with minimal spectral interference from other molecules. For some molecules it is not possible to find a comprehensive set of microwindows free from significant interferences. Thus the VMR retrieval software allows for retrieval of multiple molecules simultaneously. All retrievals employ a modified global fit approach (Carlotti, 1988), in which all parameters are determined simultaneously with the Levenberg–Marquardt (Press et al., 1992) nonlinear least-squares method. The wavenumber calibration for the ACE-FTS is not reliable, and cross-correlation is used to align the measured and calculated spectra. Without a strong spectral feature to guide the cross-correlation process, spectral features near the noise limit can end up being aligned with a strong noise feature. Where no strong interfering line was available for microwindows containing weak spectral features of the target molecule, the wavenumber shifts at the highest altitudes within the microwindow were constrained to match the wavenumber shifts determined at lower altitudes within that same microwindow, where the signal from the target molecule was stronger, thereby allowing an accurate determination of wavenumber shift via cross correlation.

Calculating spectra (for least-squares fitting) must invoke a parameterized model of the Earth's atmosphere. For the effective sea level as a function of latitude we adopt the ellipsoid model from the World Geodetic System 1984 (WGS 84, 1998). The acceleration due to gravity at sea level as a function of latitude is derived from the WGS 84 model. In order to keep calculations analytical (including derivatives for the least-squares process), the variation in acceleration due to gravity with altitude is approximated as a linear function, accurate to within a tenth of a percent in the altitude range of interest. By virtue of its long atmospheric lifetime, CO_2 is well-mixed and has a nearly constant VMR over much of the middle atmosphere. At high altitudes, photodissociation and diffusion reduce the VMR. The altitude above which the CO_2 VMR drops off varies with season and location: typically 80–90 km but extending below 60 km during the polar winter at extreme latitudes. To account for the increase in CO_2 VMR as a function of time, we adopt the equation used by the Halogen Occultation Experiment (HALOE):

$$\text{CO}_2\ \text{VMR}\ (\text{ppm}) = 326.909 + 1.50155(t - t_0),\ t_0 = 1\ \text{Jan}\ 1977 \quad (1)$$

in which $t - t_0$ is time in years. No provisions are made for variations with location or season.

At high altitudes the CO_2 VMR cannot be readily determined from a priori information. However, there are no features (such as significant refraction or optically thick clouds) that affect instrument pointing in this altitude region, and so tangent heights can be reliably calculated from geometry, from knowledge of the relative

positions of the Sun, Earth, and satellite. This requires an accurate characterization of the satellite's orbit and an accurate measure of time. Note that there is a known systematic problem with ACE-FTS measurement times. The absolute values for time stamps are not considered reliable, but differences between time stamps are presumed accurate. As a consequence only the spacing between calculated tangent heights is reliable. Absolute tangent heights in this altitude region are determined through the registration procedure described below.

A crossover measurement is taken as the third measurement greater than 43 km and is typically around 50 km. An analysis extends from the crossover to as high as 120 km. For each measurement there are four potential variables (P, T, VMR, and tangent height z) that must be either fixed or fitted. The data support at most two unknowns per measurement for least-squares fitting (two because there is information from both the absolute and relative intensities of the lines). In the high-altitude region the set of fitting parameters includes $1/T$ for each measurement. However, the region requires only one parameter for pressure: P_c, the pressure at the crossover measurement. From this single parameter (and values for tangent height and temperature at each measurement) the pressures for all other measurements in this region are calculated by integrating upward from the crossover measurement, using,

$$P(z') = P_3 \exp\left[-\frac{g_0}{k}\int_{z_3}^{z'} m_a(z)\left(1-\frac{2z}{R_e}\right)\left(\frac{(z-z_2)(z-z_3)}{(z_1-z_2)(z_1-z_3)}\frac{1}{T_1}+\frac{(z-z_1)(z-z_3)}{(z_2-z_1)(z_2-z_3)}\frac{1}{T_2}+\frac{(z-z_1)(z-z_2)}{(z_3-z_1)(z_3-z_2)}\frac{1}{T_3}\right)dz\right] \quad (2)$$

where g_0 is acceleration due to gravity at sea level, k is Boltzmann's constant, $m_a(z)$ is the atomic mass of air, and R_e is the effective radius of the Earth at a given latitude (determined from the WGS 84 model). In the altitude range between the crossover and ~70 km the CO_2 VMR is fixed. Above this the CO_2 VMR is fitted. CO_2 VMR for the highest analyzed measurement is determined by using a least-squares fitting with P and T fixed to NRL-MSISE-00 (Picone et al., 2002a) values. With the expectation that CO_2 VMR at high altitudes does not exhibit sharp structure, an empirical function is used to reduce the number of fitting parameters:

$$\text{CO}_2\ \text{VMR (ppm)} = \frac{\text{VMR}_{\text{strat}} + a(z-z_0) + b(z-z_0)^2 + c(z-z_0)^3}{1 + d(z-z_0) + e(z-z_0)^2} \quad (3)$$

where $\text{VMR}_{\text{strat}}$ is the assumed stratospheric value for CO_2 and z_0 is taken as the highest tangent height for which CO_2 VMR is assumed constant. The CO_2 VMR is assumed constant as high as 75 km for latitudes less than 60° and 65 km for latitudes greater than 60°. A Padé approximant form (the ratio of two polynomials) is used in Eq. 3 because it requires fewer parameters than a straight polynomial, and the extrapolation beyond the fitting region is better. CO_2 VMR at the first measurement below the crossover is also included as a fitting point in the least-squares analysis, in order to ensure the slope near the crossover is at least roughly correct, generating a smooth transition between the fixed portion and the retrieved portion of the CO_2 VMR profile. The portion of the CO_2 VMR profile above the highest analyzed measurement (i.e., between ~125 and 150 km) is fixed to a constant, to the value calculated from the empirical function in the tangent layer of the highest analyzed measurement.

The calculation grid adopted for the ACE-FTS analysis is divided into 150 layers of 1 km thickness. Each layer is assumed to have a constant temperature, pressure, and VMR for a given molecule with no consideration of horizontal gradients within a layer. Diurnal corrections are not currently applied, although diurnal effects are likely to be significant for photosensitive molecules such as NO_2. The raw wavenumber spacing for the ACE-FTS spectra is 0.02 cm^{-1}. To achieve accurate results for the narrow lines found at high tangent altitudes, forward model calculations are performed on a much finer grid, with a wavenumber spacing reduced by a factor of 16. The forward model for ACE-FTS is the same radiative-transfer model used for ATMOS with some notable exceptions: (1) ACE-FTS forward model calculations employ the HITRAN 2004 line list and cross

sections (with updates noted in (Boone et al., 2013)). (2) Partition functions for the ACE-FTS forward model are calculated from the total internal partition sums (TIPS) approach (Fischer et al., 2003). (3) The Voigt line-shape function is calculated from the Humlicek algorithm (Kuntz, 1997; Ruyten, 2004) rather than from a lookup table. (4) No apodization is used for the ACE-FTS instrumental line shape (ILS). (5) The ILS for the ACE-FTS requires an empirical adjustment to account for self-apodization effects beyond the normal field of view contribution.

The finite scan time of an FTS imposes a lower limit on the width of spectral features measured by the instrument. The instrument line shape (ILS) of an FTS is primarily governed by this finite scan time but will also include the effects of any deviations from an ideal instrument, such as off-axis rays from a finite field of view or changes in the modulation efficiency of the FTS mirrors as a function of optical path difference (Davis et al., 2001). The ILS is defined as the Fourier transform of the modulation function (MF), which can be written as follows:

$$MF(\nu, x) = F_{clip}(x)\,\eta(\nu, x)\,\frac{\sin\left(\frac{1}{2}\pi r^2 \nu x\right)}{\frac{1}{2}\pi r^2 \nu x}\,, \tag{4}$$

where x is optical path difference in cm^{-1}, ν is wavenumbers in cm^{-1}, and r is the radius in radians of the instrument's circular field of view. The term F_{clip} is a rectangular function associated with the finite scan time of the instrument. It is 1 for x between $\pm$25 cm (the maximum optical path difference for the ACE-FTS) and 0 otherwise. The third term in Eq. 4, with the form sin x/x, represents the effect of a finite field of view, accounting for the broadening of spectral lines that arise from off-axis rays in the instrument. The middle term in Eq. 4, η, represents any apodization applied to the measurements (other than the sin x/x term associated with off-axis rays). The finite scan time imparts a "ringing" effect to spectral features measured by the FTS, generating side-lobes when the width of a spectral feature is less than the width of the ILS. Apodization is a process that reduces the abruptness of the transition near $\pm$25 cm in F_{clip} which decreases the amplitude of the side lobes at the expense of a broader ILS. There are also inherent instrumental effects that can cause the modulation function to vary with optical path difference. This is known as self-apodization.

The ACE-FTS suffers from major self-apodization of unknown origin. It is necessary to include an empirical function in ν in the equation above in order to properly reproduce the ACE-FTS ILS. Otherwise, it is impossible to derive accurate information on the atmosphere from the ACE-FTS measurements. For this data version, a study of the ACE-FTS ILS determined that a particular shape of the empirical function for self-apodization provided a significant improvement in fitting residuals: a gradual decrease in the modulation function with increasing $\mid x \mid$ (i.e., increase in the absolute value of optical path difference), combined with a sharp decrease of the modulation function for optical path difference near maximum path difference (± 25 cm). An expression was selected that reproduced this behaviour with a minimum number of parameters:

$$\exp(1) \times \exp\left[-\exp\left(\frac{ax^{10}}{1+bx^{10}}\right)\right]\left(1 - c\frac{x}{25}\right)\,. \tag{5}$$

There is nothing intrinsic about the form of Eq. 5; it is simply the form that gave the best residuals in the analysis of ACE-FTS spectra.

The ACE-FTS instrument has two detectors, a mercury cadmium telluride (MCT) detector that measures from 750–1810 cm^{-1}, and an Indium Antimonide (InSb) detector that measures from 1810–4400 cm^{-1}. These two detector regions were treated separately. Variation of the self-apodization effects with wavenumber was treated by using an effective field-of-view rather than true, physical internal field-of-view for the instrument (6.25 mrad diameter). The values of the empirical parameters were determined by performing a non-linear least-squares fitting using a set of microwindows that spanned as much of the wavenumber range as possible and were restricted to high altitude (above about 40 km), where the spectral features were narrow enough that the shapes of the measured lines were close to the ILS. The fitting was performed for more than 400 occultations, and average values were then calculated. For the MCT detector, the parameters were $a = 4.403 \times 10^{-16}$, $b = -9.9165 \times 10^{-15}$, $c = 0.03853$, and an effective field of view of 7.591 mrad diameter.

For the InSb detector, the parameters were $a = 2.762 \times 10^{-16}$, $b = -1.009 \times 10^{-14}$, $c = 0.0956$, and an effective field of view of 7.865 mrad diameter.

Ozone profiles are retrieved between altitudes of 5 and 95 km using 33 microwindows between 1027 and 1169 cm^{-1}, with no interfering species in the mesosphere and above. Additional microwindows at 829, 923, 1105, 2149 and 2566 to 2673 cm^{-1} have been included to improve results for several interfering species and isotopologues below 25 km.

2.2 GOMOS (FMI)

The GOMOS retrieval of O_3, NO_2, NO_3, and aerosol extinction vertical profiles is based on horisontal transmission spectra in the UV-VIS region (245–690 nm). Transmissions are calculated from star spectra measured above and through the atmosphere. Data from two fast photometers are used to correct transmissions for scintillation effects. Geolocation data and the apriori atmospheric data (from ECMWF up to 1 hPa and MSIS90 above 1 hPa) are used to calculate LOS ray paths and determine refractive dilution. For mesospheric altitudes refractive effects (scintillation and dilution) have negligible effects.

Ignoring refraction and possible atmospheric emissions transmissions can be modelled by the so-called Beer-Lambert law:

$$T_{\text{ext}} = e^{-\tau} = \exp\left(-\sum_j \int_\ell \sigma_j(\lambda, T(\bar{r}(s)))\rho_j(\bar{r}(s))ds\right) \tag{6}$$

Temperature dependent cross sections in Eq. (6) couple the spectral and spatial dimensions of the problem. In the GOMOS operational retrieval algorithm spectral and spatial parts are decoupled by writing the extinction τ as

$$\tau(\lambda, \ell) = \sum_j \sigma_j^{\text{eff}}(\lambda, \ell) N_j, \tag{7}$$

where N_j are the horizontal column densities of the species j

$$N_j = \int_\ell \rho_j(z(s))\, ds \tag{8}$$

and σ^{eff} are the effective cross-sections of species j defined by

$$\sigma_j^{\text{eff}}(\lambda, \ell) = \frac{\int_\ell \sigma_j(\lambda, \mathsf{T}(z(s)))\rho_j(z(s))\, ds}{N_j}. \tag{9}$$

In the retrieval, an iterative loop over spectral and vertical retrieval is needed to handle the unknowns included in Eq. (9)

Simulations performed before and after the GOMOS launch showed that in the UV-VIS spectral region O_3, NO_2, NO_3, aerosols and neutral density are retrievable from GOMOS measurements. The kernels of the spectral inversion problem Eq. (7) are the cross sections. Except for the neutral density and aerosols, the cross sections are obtained from laboratory measurements. GOMOS O_3 cross sections are from Bogumil et al., 2001 (mentioned references and data can be found in (Keller-Rudek et al., 2013) and additional GOMOS specific details in GOMOS ATBD). The Rayleigh cross section needed for the extinction by neutral air scattering follows the familiar λ^{-4} law. Aerosol content in the atmosphere varies all the time and therefore there is no single correct aerosol cross section valid at all times and all places. The present GOMOS software version IPF 6.01 solves this problem by assuming that a polynomial expansion of wavelength covers the possible aerosol cross sections:

$$\tau(\lambda)_{\text{aer}} = c_0 + c_1\Delta\lambda + c_2(\Delta\lambda)^2 \tag{10}$$

Here $\Delta\lambda = \lambda - \lambda_{\text{ref}}$ (λ_{ref}=500 nm) and the coefficients c_i are unknowns to be determined from data.

In the GOMOS spectral UV-VIS region there are no clean spectral windows that would allow a retrieval of any of constituents mentioned above separately from each other. Instead we retrieve these constituents simultaneously from the whole spectral range. At low tangent altitudes the effective UV-VIS spectral window narrows to a limited region in the visible region where Rayleigh, ozone and aerosol cross sections become increasingly similar and the accuracy of retrievals suffers. In order to improve especially the aerosol retrieval, the present GOMOS operational processing does not retrieve neutral density at all, but uses a priori information (ECMWF+MSIS90) to remove the Rayleigh extinction.

The unknown horisontal column densities N_j in Eq. (7) are determined by minimising the quadratic distance between observed (refraction corrected) transmission and the transmission model Eqs. (6)–(7) using the Levenberg-Marquardt algorithm. The distances are weighted by the sum of estimated error covariance and modelling covariance (see (Sofieva et al., 2010)). The algorithm also produces an estimate for the covariance matrix of column densities.

The GOMOS vertical inversion determines a profile $\rho_j(z)$ by solving Eq. (8) by a method derived from the simple onion peeling method. The problem is discretised by dividing the atmosphere into layers. The vertical inversion method used in the GOMOS data processing creates continuous constituent profiles instead of the layered structure of the traditional onion peeling technique. We approximate a local densitiy to be a linear function of altitude between two successive GOMOS measurements.

The inversion presented above produces vertical profiles with unphysical oscillations originating from incomplete scintillation removal. In order to diminish these (partly already attenuated by the modelling error covariance in the spectral retrieval), we had to introduce a smoothness constraint for the vertical inversion. Traditionally the amount of smoothing is decided by optimising the trade-off between the smoothness and the vertical resolution. In the GOMOS retrieval a different approach has been taken. As the need for smoothing varies strongly depending on the stellar properties (signal-to-noise) and the measurement geometry (short and long occultations), the traditional approach would result in different resolution for each occultation. Therefore, it was decided to choose an approach that keeps the vertical resolution for each occultation constant (at given altitude) despite of the varying measurement conditions. This was done by applying so-called target resolution form of the Tikhonov regularisation (Sofieva et al., 2004).

The target resolution Tikhonov solution of Eq. (8) is given by

$$\hat{\rho} = (K^T K + \alpha(z) H^T H)^{-1} K^T N. \tag{11}$$

where the regularisation matrix H is

$$H = \text{diag}\left[\frac{1}{h_i^2}\right] \begin{bmatrix} 0 & 0 & 0 & \dots & 0 \\ 1 & -2 & 1 & \dots & 0 \\ \dots & .. & \dots & \dots & \dots \\ 0 & \dots & 1 & -2 & 1 \\ 0 & 0 & \dots & 0 & 0 \end{bmatrix} \tag{12}$$

Here $\left[\frac{1}{h_i^2}\right]$ is shorthand to dividing all matrix elements by the square of the local altitude difference. K is the geometry matrix of the occultation.

The regularisation parameter α in Eq. (11) is selected in such a way that the retrieved profiles have the desired resolution. For ozone the target resolution was selected to be 2 km below 30 km and 3 km above 40 km (with smooth transition between 30 and 40 km).

The retrieval presented is applied to all GOMOS measurements. For day occultations the quality of ozone profiles in the stratosphere is not acceptable, but in the mesosphere several stars show promising results. For night retrievals, good results are obtained in the stratosphere. In the mesosphere reliable results are obtained for stars not too cold and weak. For more information about GOMOS retrieval and measurements, see (Kyrölä et al., 2010; Tamminen et al., 2010) and GOMOS ATBD.

2.3 MIPAS (KIT/IAA)

MIPAS V5r_O3_m22 ozone retrieval is based on constrained inverse modeling of non-LTE limb radiances. That is performed using the IMK/IAA Scientific Processor (von Clarmann et al., 2003, 2009) extended with the non-LTE GRANADA algorithm (Funke et al., 2012), which is able to cope with non-LTE emissions. Funke et al. (2001) describe the particularities of the retrievals under consideration of non-LTE. The basic retrieval equations, the methods for characterization of results through error estimates and vertical and horizontal averaging kernels, the iteration and convergence criteria and the regularization method are described in the Ozone Climate Change Initiative Algorithm Theoretical Basis Document (Ref.: Ozone_cci_ATBD_Phase2_V1_00_01, pp. 60-64, 2014). Ozone is reliably retrieved from 20 km from MIPAS measurements in the MA mode and 40 km in the UA and NLC mode up to $\sim$105 km in nighttime and $\sim$95 km during daytime. A description of the specifics of the ozone retrieval V5r_O3_m22 follows.

2.3.1 Strategy

Ozone is retrieved in the log(vmr) domain from spectral lines covering ro-vibrational emissions of the O_3 main isotope. These have been selected from a broad spectral region, covered by the MIPAS band A (685–970 cm^{-1}), and band AB (1020–1170 cm^{-1}) (see more details below in Sec. 2.3.3). The V5r_O3_m22 retrieval strategy is an extension of the retrieval of ozone from the MIPAS NOM measurements (6-68 km) (von Clarmann et al., 2009) with the consideration of non-LTE emission (Gil-López et al., 2005) and the extension of the microwindow set. Retrievals are performed from MIPAS limb emission measured in the MA (20-102 km), NLC (40-102 km) and UA (40-170 km) modes. Calibrated spectra are as supplied by ESA in version 5.02/5.06 (Raspollini et al. (2010) and references therein). The retrieval is performed after a spectral shift retrieval and the non-LTE retrievals of temperature. The IMK/IAA processor simultaneously retrieves microwindow- and altitude-dependent continuum radiation and zero level calibration corrections (the latter, assumed constant with altitude).

2.3.2 Discretization and setup

The retrievals are performed from the surface to 120 km over a discrete altitude grid of 1 km up to 50 km, 2 km at 50-72 km, 1 km at 72-75 km, 2 km at 75-77 km, 1 km at 77-88 km, 2 km at 88-102 km, and 5 km from 105 up to 120 km. The selected grid provides balanced accuracy and efficiency. The forward calculations are performed using that same grid. The over-sampled retrieval grid, finer than MIPAS vertical sampling (approximately 3 km), makes the use of a regularization mandatory in order to obtain stable solutions.

The numerical integration of the signal over the 3 km field of view is done using five pencil beams. The selected width of the integration window (apodized instrument line shape function) avoids channel border effects.

2.3.3 Microwindows

The retrievals are performed from selected spectral regions (micro-windows) which vary with tangent altitudes in order to optimize computation time and minimize systematic errors (von Clarmann and Echle, 1998). The micro-windows used in the ozone retrieval are listed in Table 1. These height dependent combinations of micro-windows were selected with a trade-off between computation time and total retrieval error. They are an extension of the initial set of micro-windows used for the MIPAS ozone NOM retrieval ($z<70$ km) (von Clarmann et al., 2009). Below 50 km, we use for the MA, UA and NLC measurements modes the same MWs as in the NOM retrieval, located all in band A. Above 50 km, the micro-windows used are mainly located in band AB and are strongly affected by non-LTE.

Table 1: Microwindows and altitude ranges used in the retrieval of MIPAS ozone V5r_O3_m22.

No.	Wavenumber (cm^{-1})		Altitudes (km)																			
	Minimum	Maximum	18	21	24	27	30	33	36	39	42	45	48	51	54	57	60	63	66	69	72	75	78-102
1	687.6875	688.6875						■		■	■	■	■	■	■	■	■	■	■	■	■	■	
2	689.3125	691.8750			■	■	■			■	■	■	■	■	■	■	■	■	■	■	■	■	
3	692.2500	695.1875							■	■	■	■	■	■	■	■	■	■	■	■	■	■	
4	707.1250	710.0625				■	■	■	■	■	■	■	■	■	■	■	■	■	■	■	■	■	
5	712.3125	713.4375								■	■	■	■		■								
6	713.5000	716.4375			■	■	■	■	■	■	■	■	■	■		■	■	■	■	■	■	■	
7	716.5000	719.4375			■	■		■	■	■	■	■	■	■	■	■	■	■	■	■	■	■	
8	720.7500	723.6875				■	■	■	■	■	■	■	■	■	■	■	■	■	■	■	■	■	
9	728.5000	729.3750						■	■	■	■	■	■	■	■	■	■	■	■	■	■	■	
10	730.0625	730.5000						■	■	■	■	■	■	■	■	■	■	■	■	■	■	■	
11	731.9375	732.8750			■	■	■			■				■	■	■	■	■	■		■	■	
12	734.0000	734.7500						■	■		■	■	■	■	■					■	■	■	
13	736.4375	739.3750	■	■		■		■	■	■	■	■	■	■	■	■	■	■	■	■	■	■	
14	739.4375	741.9375					■	■	■	■	■	■	■	■	■	■	■	■	■	■	■	■	
15	745.2500	745.6875	■					■	■	■	■	■	■	■	■	■	■	■	■	■	■	■	
16	746.6875	747.1250		■	■	■	■	■	■	■	■	■	■	■	■	■	■	■	■	■	■	■	
17	747.6250	748.3750				■	■	■	■		■	■	■	■	■				■	■	■	■	
18	749.5625	752.5000		■	■	■	■	■	■	■	■	■	■	■	■	■	■	■	■	■	■	■	
19	752.9375	755.8750	■	■	■			■	■	■	■	■	■	■	■	■	■	■	■	■	■	■	
20	758.3750	759.4375	■	■	■	■	■	■	■	■	■	■	■	■	■	■	■	■	■	■	■	■	
21	759.5000	761.8750			■			■	■	■	■	■	■	■	■	■	■	■	■	■	■	■	
22	765.0000	765.6250							■	■	■	■	■	■	■	■	■	■	■	■	■	■	
23	767.5000	768.0000	■	■	■	■	■	■	■	■	■	■	■	■	■	■	■	■	■	■	■	■	
24	771.8750	772.1250	■	■	■	■	■	■	■	■	■	■			■	■	■	■	■	■	■	■	
25	774.2500	774.5625		■	■	■			■	■	■	■			■				■	■			
26	776.5000	776.7500									■	■		■		■	■	■	■	■			
27	780.2500	781.9375	■					■	■	■	■	■	■	■	■	■	■	■	■	■	■	■	
28	788.9375	789.6875	■					■	■	■	■	■	■	■	■	■	■	■	■	■	■	■	
29	790.7500	791.0000	■										■										
30	791.1875	791.5625	■	■					■	■	■	■	■	■	■	■	■	■	■	■	■	■	
31	1034.1250	1034.3750																	■	■	■	■	■
32	1034.4375	1035.0000												■	■	■	■	■	■	■	■	■	■
33	1038.1875	1039.0000												■	■	■	■	■	■	■	■	■	■
34	1040.0000	1040.8125												■	■	■	■	■	■	■	■	■	■
35	1048.8125	1049.5000																■	■	■	■	■	■
36	1050.6250	1051.8125																■	■	■	■	■	■
37	1053.3125	1053.8125																■	■	■	■	■	■
38	1054.6875	1055.5000																■	■	■	■	■	■

2.3.4 A priori and atmospheric inputs

MIPAS V5r_O3_m22 ozone retrieval setup uses the following inputs:

- O_3 a priori is taken from a MIPAS dedicated climatology (as the one used and described in Funke et al. (2012)).
- Pressure, line of sight information, temperature, and temperature horizontal gradients are taken from MIPAS retrieval version V5r_T_m21.
- Spectroscopic data from HITRAN 2008 (Rothman et al., 2009).

GRANADA calculates the non-LTE populations of the vibrational levels of O_3. Several inputs are needed and Funke et al. (2012) provide information on their effect on the O_3 level populations. The non-LTE model inputs used in V5r_O3_m22 retrievals are:

- The O_3 vibrational level set, non-LTE collisional scheme and rate constants are based on the model described by Funke et al. (2012), with the following changes/updates:
  - The exponent a in the rate $k_1 = 6.0 \times 10^{-34} (T/300)^a$ of reaction $O + O_2 + M \rightarrow O_3(v^*) + M$ has been updated from a=2.3 to a=2.4. This has a small effect, though.
  - Chemical quenching of O_3(*) by O: $O_3^*(v_1, v_3) + O \rightarrow O_3 + O$ has been removed. This implies larger O_3 vibrational temperatures and hence smaller O_3 abundances. Note, however, that the

total quenching by O, including also relaxation by O, i.e., $O_3^*(v_1, v_3) + O \rightarrow O_3(v_2)$, is still within measurements errors (West et al., 1976, 1978).

- The atomic oxygen used in the NLTE model has been updated. Below 97 km (it was 95 km before) during daytime, we use the atomic oxygen derived from photochemical equilibrium with the retrieved O_3. Note that this requires iteration of the non-LTE model with thin retrieval process. At nighttime, O depends not only on O_3 but also on hydrogen, H. We use O_3 from the retrieval and H from the NRLMSIS-00 model (Picone et al., 2002b). Above 97 km we use the atomic oxygen from WACCM in its specified dynamics (SD) configuration (Garcia et al., 2007).

- Solar incoming fluxes at the top of the atmosphere are calculated with GRANADA taking into account attenuation by Fraunhofer lines (Hase et al., 2006) and a solar background radiance as suggested by Platnick and Fontenla (2008) (see Sect. 2.3.4 for details). Solar fluxes required in the non-LTE model are calculated considering the temporal variations of the Sun-Earth distance. Attenuation by solar Fraunhofer lines is taken into account (Hase et al., 2006). The solar background radiance is expressed as a blackbody with effective temperature T_e (in K) depending on wavenumber $\tilde{\nu}$ (in cm^{-1}) through T_e=5450+0.25($\tilde{\nu}$–2000). This parameterization is similar to that developed by Platnick and Fontenla (2008) for 3.7 μm, and they agree within 0.5–1% at that wavelength. Modulations due to temporal variations of the Sun-Earth distance are also included.

- During the inversion process we also include in the calculation of the spectra the contribution (as a potential overlap with O_3 lines) of the CO_2 lines. As for O_3, we also include the emissions by CO_2 bands in non-LTE. A detailed description of the CO_2 non-LTE model used and all the required input parameters can be found in Jurado-Navarro et al. (2016).

Forward model calculations along the line of sight are done considering non-LTE horizontal gradient corrections. These account for changes in the populations of the emitting levels along the line of sight.

2.3.5 Error budget

The error budget described here considers the propagation of the measurement noise and of the uncertainties of model parameters onto the retrieved ozone abundances. Noise-induced retrieval errors and vertical resolutions are estimated routinely for each individual profile by the retrieval algorithm.

The ozone noise error is calculated assuming a wavelength-dependent noise-equivalent-spectral-radiance which has approximated average values of 17 and 10 nW/($cm^2 cm^{-1}$sr) for channels A and AB, respectively. Typical values for daytime are smaller than 2% below 50 km, 2-10% between 50 and 70 km, 10-20% at 70-90 km and about 30% above 95 km. For nighttime, the noise errors are very similar below around 70 km but significantly smaller above, being 10-20% at 75-95 km, 20-30% at 95-100 km and larger than 30% above 100 km.

Errors related to the mapping of uncertain model parameters on the retrieved ozone vmr are estimated for representative profiles for daytime and nighttime conditions. We name these ”systematic” errors to distinguish them from the noise error, although they are not purely systematic but in some cases they also have a random component. Table 2 summarises the estimated errors in MIPAS retrieved ozone vmr.

The uncertainties assumed for the estimation of the systematic errors are 1% for gain calibration and 3% for the instrument line shape (ILS). For the elevation pointing (LOS) we have assumed an error of 150 m below 60 km, where we have information on the relative pointing from the temperature-LOS retrieval (von Clarmann et al., 2009; García-Comas et al., 2012). Above that height, where we obtain the LOS information from the engineering tangent altitudes of MIPAS (adjusted with the LOS retrieved below), we assumed an error of 300 m. For temperature, the errors have been considered as 0.5 K below 50 km, 1 K at 50-70 km, 2 K at 70-80 km, 5 K at 80-100 km and 10 K above (García-Comas et al., 2014).

The spectroscopic errors have been estimated by J.-M. Flaud (personal communication, 2008). The errors assumed for the line intensities of the fundamental v_1, v_2 and v_3 bands (those mainly used here) are 2%

Table 2: Summary of main errors of ozone vmr in %. Errors refer to nighttime conditions with daytime values, when different, in parenthesis. 'NLTE' includes errors due to uncertainties in the collisional rates of the non-LTE model and in the atomic oxygen (see text). 'Total (Syst.)' is the root sum square of all systematic errors (noise is not included). LOS stands for Line Of Sight, 'Tem' for temperature, ILS for Instrument Line of Shape, and 'Spec.' for spectroscopy.

Height (km)	Noise	LOS	Gain	Tem	ILS	Spec.	NLTE	Total (Syst.)
20	2.2	3.1	2.6	2.0	2.2	7.6	0	9
30	1.1	1.6	2.4	1.8	2.6	12	0	13
40	1.5	2.7	2.2	1.7	3.1	9.4 (11)	0	11 (12)
50	2.7	2.1 (3.8)	1.1 (1.5)	1.2	1.9	3.6 (4)	0	4.8 (6)
60	4.2 (5.5)	3.5 (4.1)	1.0 (1.4)	2.8 (2.4)	0.7 (0.9)	2.0	2.0	5.5 (5.7)
70	8.2 (12)	2.5 (4)	2.6 (0.9)	0.4 (0.7)	1.7 (0.7)	1.9	5	6.4 (6.8)
80	14 (15-20)	0.8 (1.3)	0.34 (1.6)	0.8 (2.5)	1.5 (0.9)	1.6 (0.6)	6 (10)	6 (11)
90	12 (26)	1.0 (2.5)	0.32 (3.7)	3.3 (9.5)	1.5 (2.6)	1.8	16	16 (19)
95	17 (36)	1.4 (3.5)	2.1 (5.6)	9 (15)	1.8 (3.3)	1.4 (3.3)	18	21 (25)
100	27 (38)	1.2 (3.8)	5.5 (6.2)	12 (17)	4.0	2.5 (3.7)	19	24 (27)

for the strongest lines, 5% for the moderate lines, and 10% for the weaker lines. For the lines of the hot bands having as lower state (010), (020), (100) or (001), the error is in the range of 4-25%, increasing as the line intensity decreases. The errors considered for the more excited hot bands are larger, up to 30%, but their contributions to the selected MWs is small. The error assumed for the O_3 air-broadened half-widths is 12%. The larger O_3 spectroscopic errors below 50 km are mainly due to the error in the half-widths. The contribution of the error in the line intensities is of only 2–3%.

The modelling of the non-LTE populations of the O_3 vibrational levels emitting near 9.6 μm is an important source of the MIPAS ozone systematic error above the mid-mesosphere. Non-LTE errors are dominated by the uncertainties in the collisional rates used in the non-LTE model. The three major sources are: 1) The error in the three-body reaction rate of O_3 formation; 2) the thermal relaxation of the $O_3(v_1, v_3)$ levels with N_2 and O_2; and 3) the collisional relaxation and/or chemical reaction of $O_3(v_1, v_3)$ levels with atomic oxygen. According to the current literature, we have considered uncertainties of 10% for the first, 20% for the second, and 50% for the third. For the later, West et al. (1976) derived experimentally the deactivation rate of $O_3(v_1, v_3)$ by O, and provided rates for both the thermal relaxation, $O_3(v_1, v_3)$ + O $\rightarrow$ O_3 + O, and the chemical reaction, $O_3(v_1, v_3)$ + O $\rightarrow$ 2 O_2, assuming each one alone was responsible for the total deactivation. These authors could not estimate the relative contribution of each process and the error associated to these two rates is about 50%. West et al. (1978) further reported that the deactivation is most likely to occur through the thermal relaxation. Hence, we have considered that the deactivation takes place through the thermal relaxation and assumed the measured error of West et al. (1976) of 50%.

We have not considered additional errors due to the uncertainty in the atomic oxygen (daytime) or atomic hydrogen (nighttime) below 95 km. During daytime, this is reasonable because atomic oxygen is derived from the photochemical equilibrium with the retrieved O_3. At night, however, when the retrieval depends on the atomic hydrogen concentration, if the error in H is significantly smaller than the 50% assumed for the deactivation of $O_3(v_1, v_3)$, its contribution will not be significant. If comparable, however, we might be underestimating the non-LTE errors. Above 97 km, we have assumed an uncertainty in the WACCM atomic oxygen of 50%, leading to an error of about 10% in the retrieved O_3 in that region. This error has been added, quadratically, to the other components of the non-LTE uncertainties discussed above.

The uncertainty of the first of those three processes on O_3 is only important above $\sim$85 km, reaching a maximum of 5% in the retrieved O_3. The second one is significant only from $\sim$60 km up to $\sim$80 km, introducing an error of 2–5% in ozone for nighttime, and of 2–10% for daytime, including polar summer, where it

might be slightly larger near 80 km. The third one, including the error in the atomic oxygen, is only significant above ∼85 km but it is the largest, with an estimated error in O_3 of 15–20% at 85-100 km. Overall, the non-LTE errors are typically negligible below 60 km, 2-10% at 60-80 km, and 15–20% above 85 km.

The overall estimated O_3 abundance error is dominated by the spectroscopic data uncertainty below 50 km and by the non-LTE and temperature errors above about 70 km. Between 50 and 70 km, the pointing (LOS) and the spectroscopic errors are the dominant uncertainties. The validation performed by López-Puertas et al. (2017b) suggests, however, that the spectroscopic errors below 50 km are overestimated.

The vertical resolution of MIPAS retrieved daytime ozone abundance is the full width at half maximum of the averaging kernels rows. Average vertical resolution is 3-4 km below 70 km, 6-8 km at 70–80 km, 8-10 km at 80–90 km, and 6–8 km at 90–100 km. For nighttime conditions the vertical resolution is better in the upper mesosphere and lower thermosphere. It is 4-6 km at 70–100 km except a narrow region near 80 km where it takes values of 8-10 km, and 6–8 km at 100–102 km.

Two additional criteria are further used to filter out the retrieved IMK/IAA data in order to guarantee the quality of the profile. The following results are discarded: 1) those where the diagonal value (for individual profiles) or the mean diagonal value (for averages) of the averaging kernel is less (in absolute value) than 0.03 are considered non-trustful, and 2) those corresponding to altitudes not sounded by MIPAS (below the lowermost tangent altitude).

2.3.6 Improvements with respect to previous versions

V5r_O3_m22 ozone baseline is an improvement of the previous V4O_O3_m02 version. The changes from the previous version are:

- Updated L1b database to V5.
- Updated version HITRAN database from the 2004 to the 2008 version.
- Updated versions of temperature (V5r_T_m21).
- Improved width of the integration window of the apodized instrument line shape function.
- Extension of top altitude of the continuum retrieval from 30 to 50 km.
- Revised regularization scheme, in line with regularization used in the retrieval of the NOM mode.
- Revised set of micro-windows. Use of micro-windows in band A only below 50 km like in NOM retrievals.
- Use of CO_2 abundance from WACCM-SD.
- Inclusion of atomic oxygen derived from the ozone retrieval itself (photochemical equilibrium) below 97 km during daytime. At nighttime we need, additionally, the H concentration, which has been taken from the NRLMSIS-00 model (Picone et al., 2002b) (see Sec. 2.3.4 above). Above 97 km we use the atomic oxygen from WACCM in its specified dynamics (SD) configuration (Garcia et al., 2007).
- Re-calculation of the O_3 vibrational temperatures during the iterations in the inversion process, following the update of the atomic oxygen.
- Several improvements in the O_3 non-LTE model, as described above in Sec. 2.3.4.

The average impact on ozone retrieval after those changes (see Figs.1 and 2) is an increase of 2-3% (0.2-0.5 ppmv) below around 40 km (except in the polar winter where there is a decrease). The clear increase around 40 km is due to the inclusion of the retrieval of the continuum for this altitude.

There is a clear decrease of ∼5-10% (∼0.4-0.5 ppmv) between 40 and 50 km principally induced by the use of micro-windows in band A only (MWs in band AB for these altitudes were removed).

In the lower and middle mesosphere, 50-80 km, there is an increase of about 2-5% (0.1-0.2 ppmv). In the upper mesosphere, there is a general decrease of ∼0.5-1 ppmv at nighttime conditions, principally caused by neglecting the removal of the excited $O_3(v_3)$ by chemical reaction with atomic oxygen. This produces a larger population of $O_3(v_3)$ and hence less O_3. At daytime the effect is much smaller and has a small impact on the retrieved ozone.

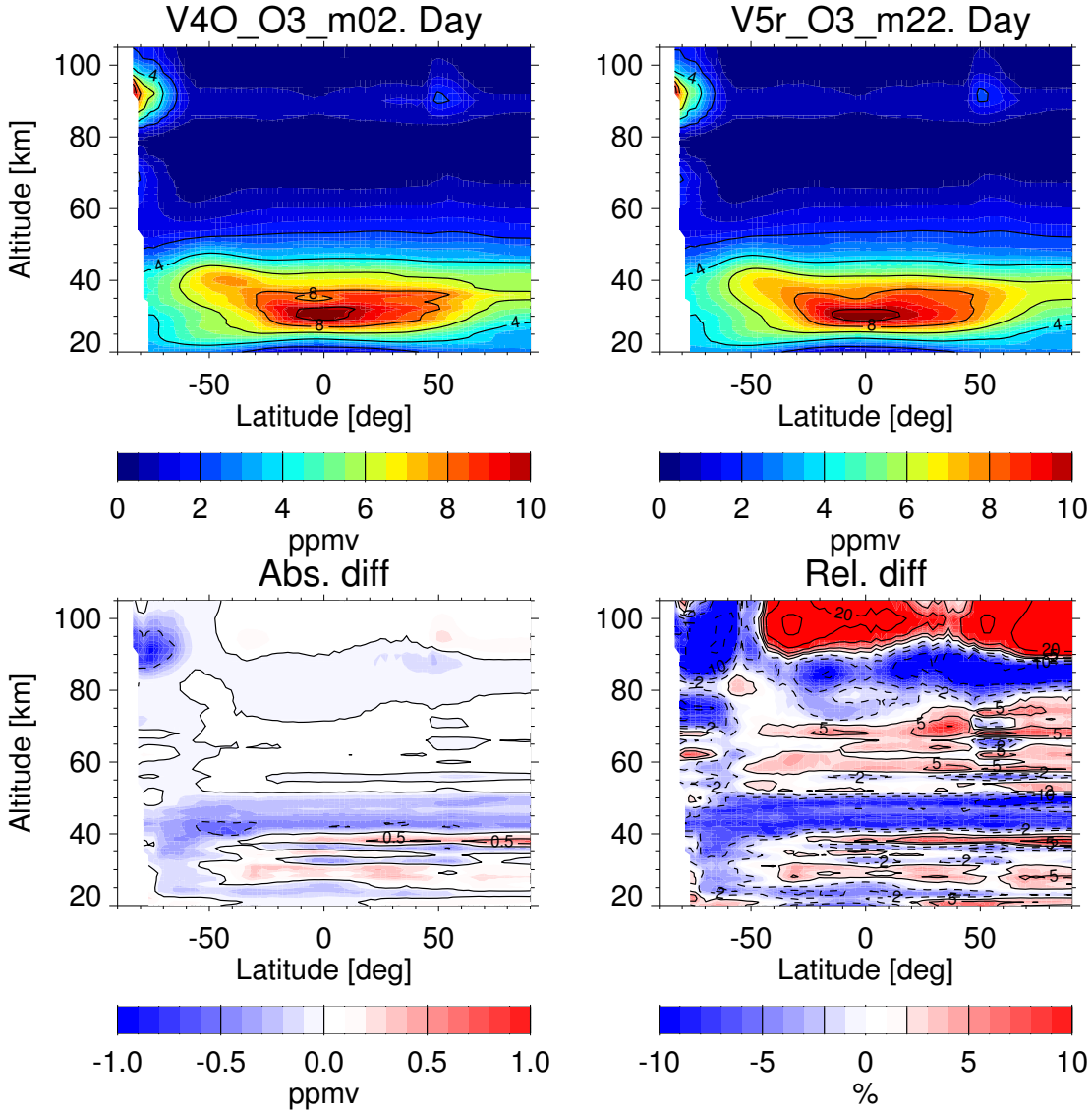

Figure 1: Comparison of O_3 abundance for daytime conditions (10 am) retrieved in the current V5r_O3_m22 and the previous V4O_O3_m02 versions for 5 June 2009. Lower panels show the V5r_O3_m22-V4O_O3_m02 differences.

2.4 OSIRIS (USask)

The molecular oxygen Atmospheric Bands result from the transition between the O_2 ground state, $O_2(X^3\Sigma)$, and the second excited state $O_2(b^1\Sigma)$. The electronic-vibrational-rotational transition between $O_2(X^3\Sigma, \nu = 0)$ and $O_2(b^1\Sigma, \nu = 0)$ is commonly referred to as the A-band and is the dominant transition within the

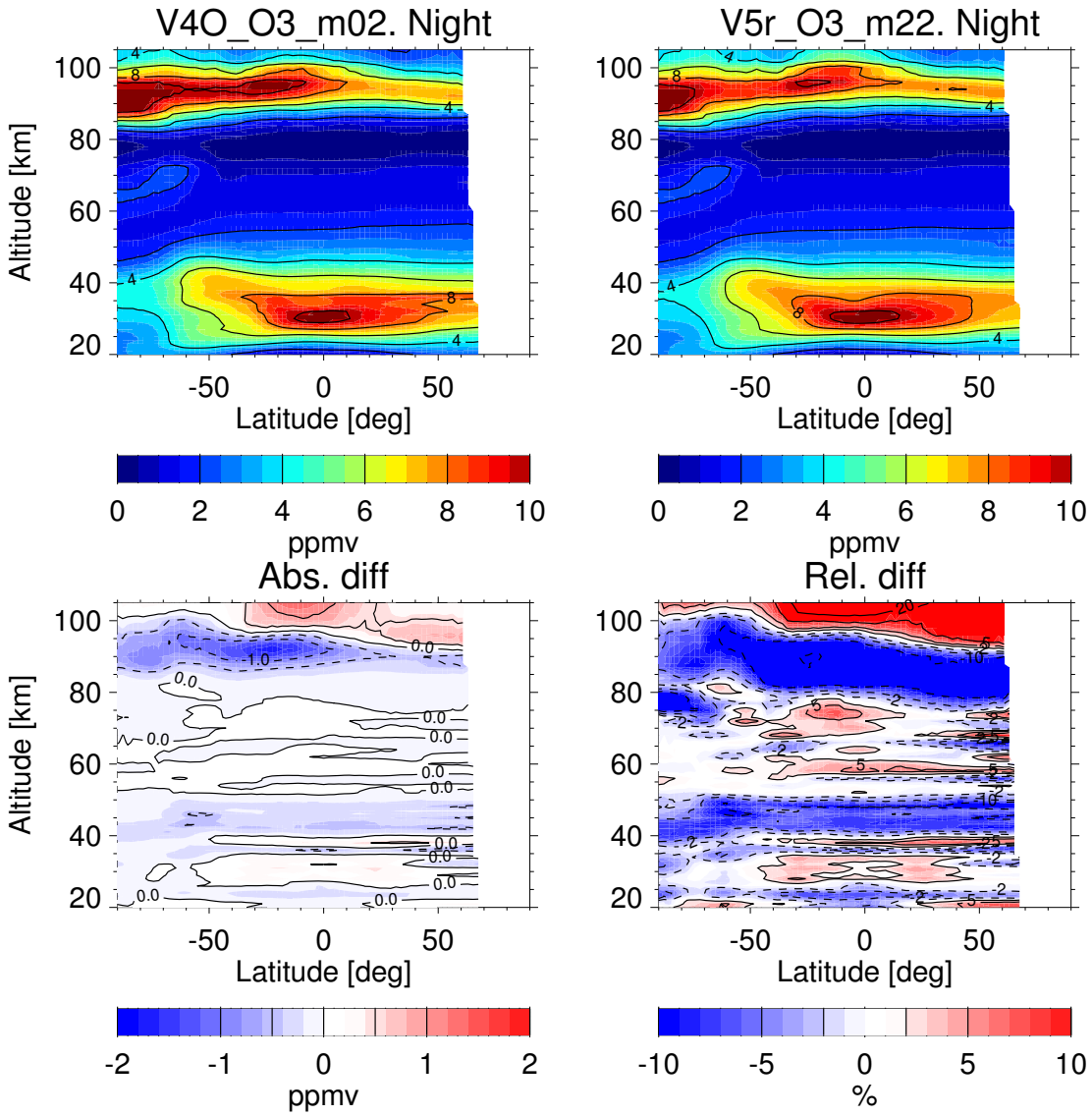

Figure 2: As Figure 1 but for nighttime conditions (10 pm).

Atmospheric Band system.

As detailed by Bucholtz et al. (1986), there are three main production mechanisms of $O_2(b^1\Sigma)$ in the mesosphere. Figure 3 shows a schematic of the significant production mechanisms of $O_2(b^1\Sigma)$. The first source is photon absorption in the Atmospheric Bands. As can be seen in Fig. 3, the γ-band is not considered significant in this study, as Bucholtz et al. (1986) showed that absorption in the γ-band is insignificant in comparison to that of the A- and B-band. However, $O_2(b^1\Sigma)$ in the $\nu = 1$ state is rapidly collisionally deactivated into the $\nu = 0$ state, subsequently leading to A-band emission, and must be considered when modelling A-band dayglow. The second source of $O_2(b^1\Sigma)$ is a two-step Barth-type process,

$$O + O + M \rightarrow O_2{}^* + M, \tag{13}$$

where M is an O_2 or N_2 molecule. Then,

$$O_2{}^* + O_2 \rightarrow O_2(b^1\Sigma) + O_2. \tag{14}$$

The third source is collisional excitation of O_2 by $O(^1D)$,

$$O(^1D) + O_2(X^3\Sigma) \rightarrow O(^3P) + O_2(b^1\Sigma). \tag{15}$$

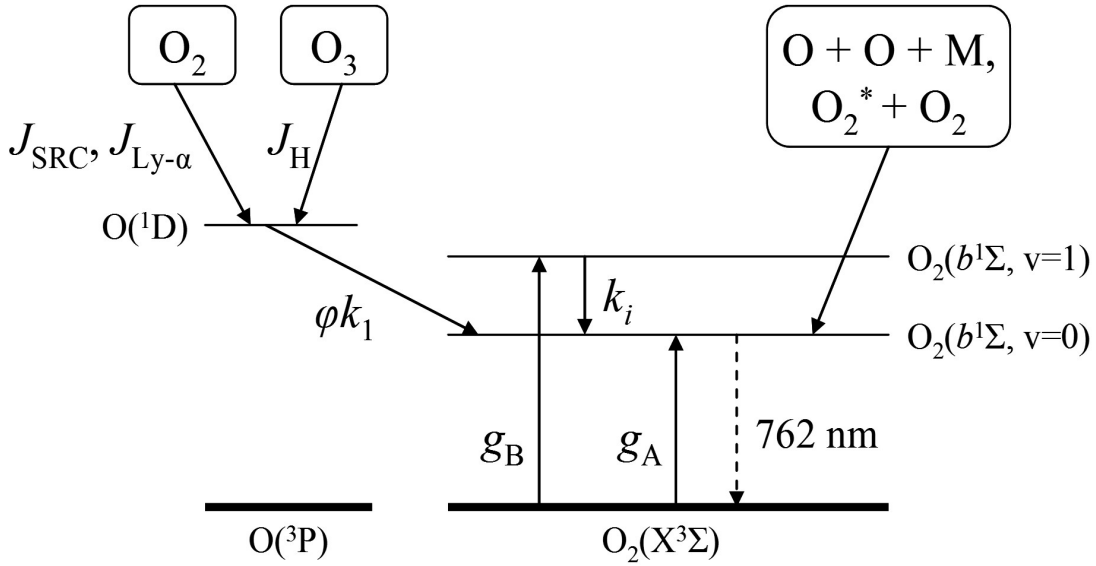

Figure 3: Schematic of significant production mechanisms of A-band dayglow emission. J and g terms are photochemical reaction coefficients, and k terms are collisional quenching rates.

There are only two significant sources of O(^{1}D) in the mesosphere, photolysis of O_2 in the Schumann-Runge Continuum and photolysis of O_3 in the Hartley band,

$$O_2 + h\nu(\lambda \leq 175\text{nm}) = O(^1D) + O(^3P), \quad (16)$$

$$O_3 + h\nu(\lambda \leq 310\text{nm}) = O(^1D) + O(a^1\Delta). \quad (17)$$

Thus the intensity of the A-band dayglow emission is dependent on the local ozone concentration.

A kinetic-photochemical model has been developed in order to predict A-band volume emission rates at a given geographic location. The model assumes an MSIS-E-00 (Hedin, 1991) modelled background atmosphere (O_2, N_2, and T) and assumes a priori ozone and atomic oxygen profiles. Photolysis rates are calculated using input solar flux data from the SORCE (Solar Radiation and Climate Experiment) satellite. The kinetic-photochemical model is discussed in greater detail by Sheese (2009). The results of the kinetic-photochemical model are then forward modelled in order to predict OSIRIS observations in the O_2 A-band region. The forward modelled OSIRIS observations along with actual OSIRIS observations are the input of an iterative Newtonian-Optimal Estimation technique (Rodgers, 2000) in order to retrieve ozone densities. A schematic of the full retrieval process is shown in Fig. 4.

2.5 SCIAMACHY (UB)

This study uses newly developed version 3.5 of SCIAMACHY limb ozone. The retrieval is performed using the nominal limb measurements at tangent heights between about 9 - 61 km (wavelength dependent). The data set is generated using Level 1 V8.02 data with calibration flags 1,2,4,5,7, i.e., including the calibrations for the leakage current, pixel-to-pixel gain, straylight, wavelength and the radiometric calibration while the memory effect and polarization correction are skipped.

The spectral information from Hartley, Huggins and Chappuis absorption bands of ozone is exploited. In the Harley band the limb radiances are normalized by a limb measurement at an upper tangent height (TH) while normalization by the solar irradiance is used in the Huggins and Chappuis bands. In most of the spectral windows polynomials are subtracted to reduce an influence of broadband spectral features. A summary of

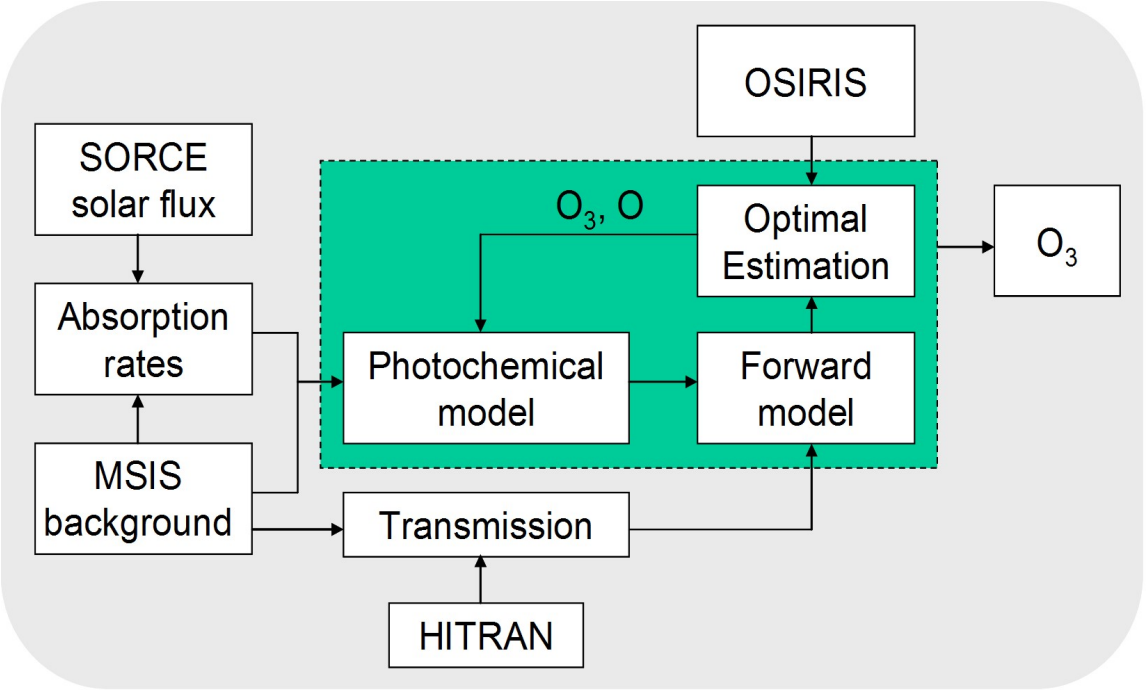

Figure 4: Schematic of the overall ozone retrieval process. The dashed box indicates an iterative process.

the used spectral intervals, tangent height ranges, normalization types and polynomial orders is presented in Table 3.

Table 3: Spectral windows and associated parameters as used in the SCIAMACHY limb ozone retrieval V3.5

Wavelength range	Normalization method	Highest tangent height	Lowest tangent height	Polynomial order	Signal to noise ratio
264.0 - 274.9 nm	Upper TH No.23(∼68 km)	No.21(∼61 km)	No.20(∼58 km)	not used	constant 20
276.5 - 287.0 nm	Upper TH No.22(∼64 km)	No.19(∼55 km)	No.18(∼51 km)	zeroth order	constant 40
289.0 - 309.5 nm	Upper TH No.20(∼58 km)	No.19(∼55 km)	No.14(∼38 km)	zeroth order	estimated from data
325.5 - 331.0 nm	measured solar irradiance	No.14(∼38 km)	No.12(∼32 km)	first order	estimated from data
495.0 - 576.0 nm	measured solar irradiance	No.12(∼32 km)	No.5(∼9 km)	second order	estimated from data

In addition to ozone, NO_2, O_4 and surface albedo are included into the retrieval process. The water vapor absorption and the Raman scattering contributions are considered as corrections in 495 – 580 nm and 288 – 580 nm spectral ranges, respectively. In Huggins and Chappuis bands possible spectral misalignment is accounted for by using shift/squeeze correction algorithm. The surface albedo is retrieved in Huggins and Chappuis bands independently requiring the same ozone amount to results from measurements in different spectral channels. Measurements in the Huggins band are considered to be independent of the surface albedo.

The main equation to be solved by the retrieval algorithm is given by

$$\mathbf{y} = \mathbf{F}(\mathbf{x}), \tag{18}$$

where **y** is the measurements vector containing combinations of measured limb radiances as described below, **F** is the forward model operator, and **x** is the state vector. The measurement vector contains logarithms of the normalized limb radiance in the selected spectral windows and tangent height ranges with a polynomial in spectral domain subtracted (see Table 3 for selected ranges and polynomial order). The state vector contains amounts of O_3 and NO_2 at an altitude grid, total column of O_4 and values of the surface albedo in two spectral ranges. As an altitude grid the tangent heights of the measurements are used.

The inverse problem given by Eq. (18) is linearized to obtain

$$\mathbf{y} = \mathbf{F}(\mathbf{x_a}) + \mathbf{K}(\mathbf{x} - \mathbf{x_a}) \tag{19}$$

and solved with respect to absolute variations of O_3 volume mixing ratio, of NO_2 number density and of surface albedo as well as relative variation of O_4 total column. Here, $\mathbf{F}(\mathbf{x_a})$ denotes the radiance simulated by the radiative transfer model for an a priori ozone profile, $\mathbf{x_a}$ and

$$\mathbf{K} \equiv \left.\frac{\delta \mathbf{F}(\mathbf{x})}{\delta \mathbf{x}}\right|_{\mathbf{x_a}} \tag{20}$$

represents the weighting function matrix. The latter is calculated in the single scattering approximation. The non-linearity of the problem is accounted for using an iterative approach.

The solution of the linearized problem is obtained by minimizing the following quadratic form:

$$\left\| \mathrm{F}\left(\mathbf{x_a}\right) + \mathbf{K}\ \left(\mathbf{x} - \mathbf{x_a}\right) - \mathbf{y} \right\|^2_{\mathbf{S}_\varepsilon^{-1}} \ + \ \left\| \left(\mathbf{x} - \mathbf{x_a}\right) \right\|^2_{\mathbf{S}_a} \tag{21}$$

using the maximum a posteriori information method described by Rodgers (2000). Here, $\mathbf{S}_\varepsilon$ is the noise covariance matrix and $\mathbf{S}_a$ is the regularization matrix containing a priori covariances.

At the $(i+1)$-th iterative step the solution of the minimization problem given by Eq. (21) is obtained as

$$\mathbf{x}_{i+1} = \mathbf{x_a} + \left(\mathbf{K}_i^T\ \mathbf{S}_\varepsilon^{-1}\ \mathbf{K}_i + \mathbf{S}_a\right)^{-1} \mathbf{K}_i^T\ \mathbf{S}_\varepsilon^{-1}\ \left(\mathbf{y} - \mathbf{F}\left(\mathbf{x}_i\right)\ +\ \mathbf{K}_i\ \left(\mathbf{x}_i - \mathbf{x_a}\right)\right). \tag{22}$$

All radiances and weighting functions needed to solve the inverse problem are calculated with the SCIATRAN radiative transfer model (Rozanov et al., 2014) using the ozone cross sections described in (Gorshelev et al., 2014; Serdyuchenko et al., 2014) and NO_2 cross sections from (Bogumil et al., 2003). The noise is assumed to be spectrally and vertically uncorrelated and the diagonal elements of the noise covariance matrix are set in accordance to the signal to noise ratios (SNR) of the measured spectra. For two short wavelength channels the signal to noise ratios are set to constant values of 20 and 40, respectively, rather than estimated from the spectra (see Table 3). The a priori covariance is set to either 1 ppm or the volume mixing ratio corresponding to the number density of 10^{12} molec/cm^3 whichever is smaller. No vertical correlation is assumed. The retrieval is done for variations from zero a priori profile for ozone, from climatological a priori profiles for other species and for a variation from a value of 0.3 for the surface albedo.

Figure 5 shows a typical ozone volume mixing ratio profile retrieved in a tropical region (upper left panel), corresponding averaging kernels (upper right panel), theoretical precision of the retrieval and measurement response (lower left panel) as well as vertical resolution of the retrieval. The averaging kernels are typically close to unity peaking at nominal altitudes for the whole retrieval range. The resulting measurement response shown by the blue line in the lower left panel is always around unity with exception of the lowermost layer where it slightly decreases to about 0.9. This indicates that the retrieval results are almost independent on the a priori information. The resulting precision is about 2-5% above 20 km and rapidly decreases below,

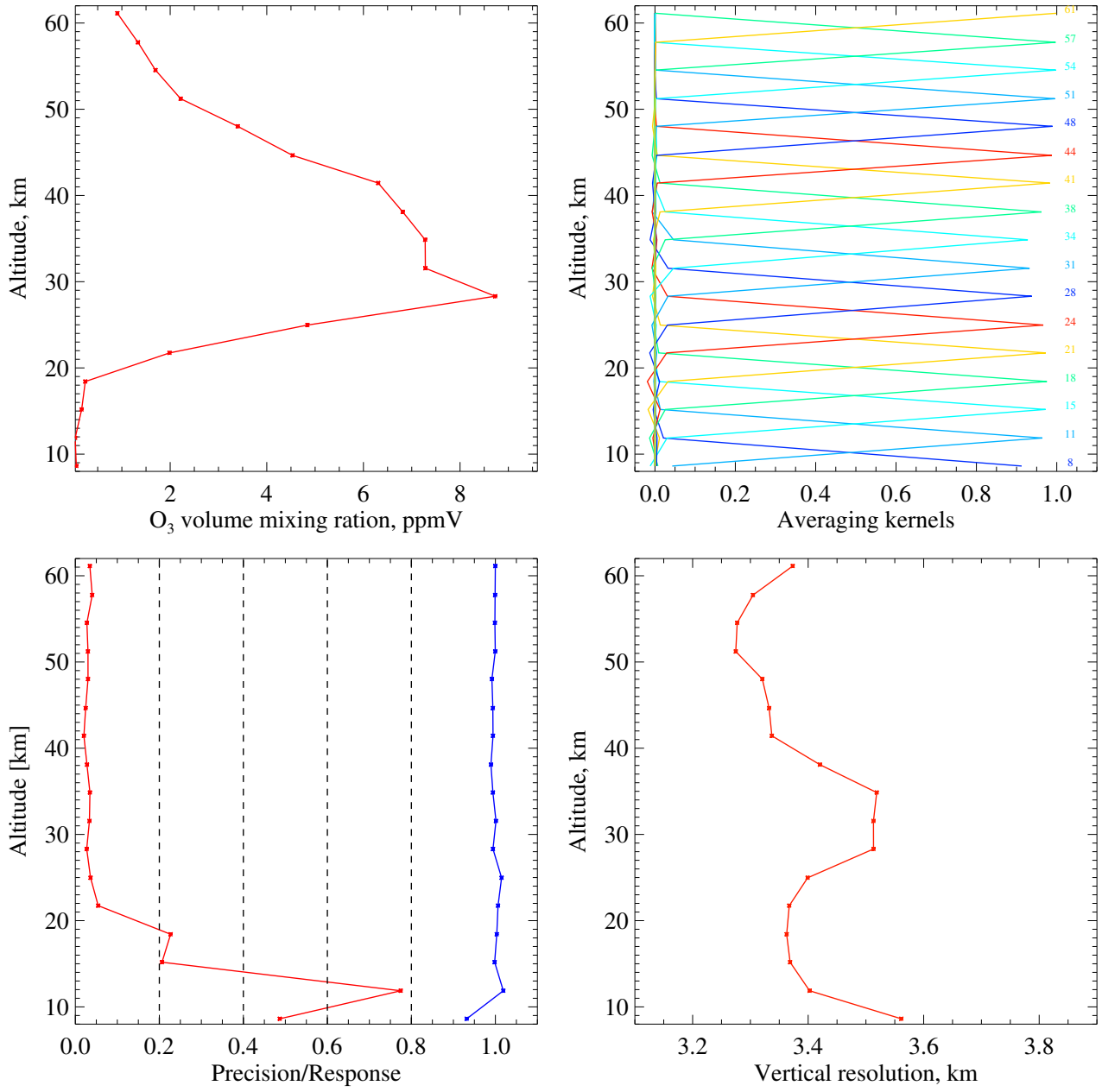

Figure 5: Upper panels: Typical tropical ozone volume mixing ratio profile (left) and corresponding averaging kernels (right). Colored numbers on the right hand side of the plot indicate nominal altitudes of the averaging kernels. Lower panels: theoretical precision of the retrieval (red) and measurement response (blue) in the left panel and vertical resolution of the retrieval in the right panel.

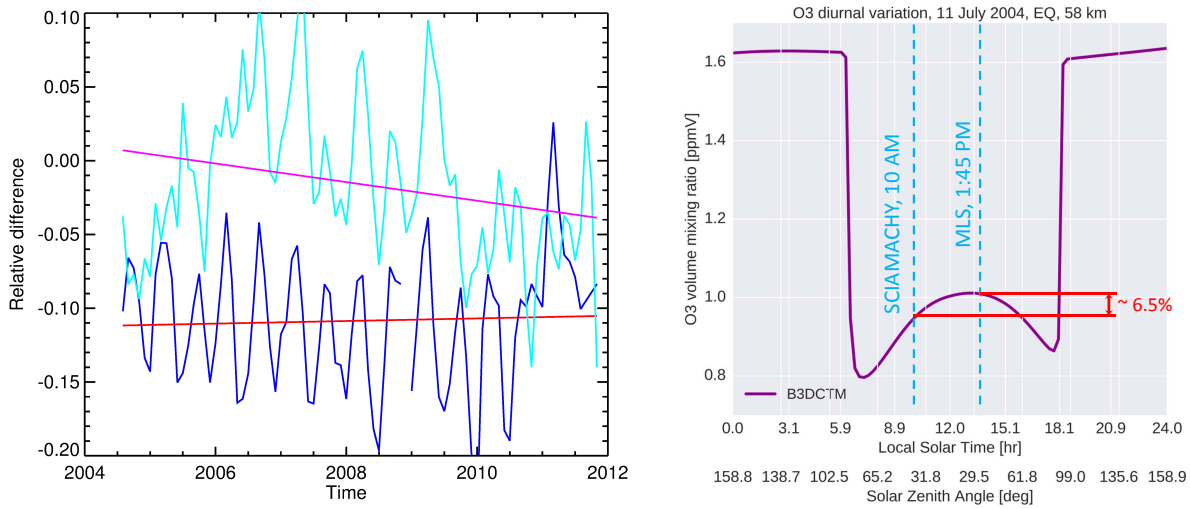

Figure 6: Left panel: Comparison to MLS v3.3 results for the tropics (20°S – 20°N) at 60 km altitude. Blue line shows V3.5 results while cyan line depicts the results from the previous retrieval version, V2.9. Red and magenta lines show linear fits to the relative difference time series for the new (V3.5) and old (V2.9) retrieval versions, respectively. Right panel: ozone diurnal variation at 58 km calculated with a chemical transport model.

where volume mixing ratios of ozone become extremely low. The vertical resolution is between 3.3 and 3.6 km throughout the whole retrieval range.

To estimate a quality of the new retrieval version (V3.5) and illustrate the improvements achieved since the the previous version (V2.9) the ozone time series obtained from SCIAMACHY are compared to those from MLS (Froidevaux et al., 2008). As this project is focused on the mesosphere the comparisons are presented for the uppermost altitude available from SCIAMACHY (around 60 km). Relative deviation between the SCIAMACHY results (both V3.5 and V2.9 depicted by blue and cyan lines, respectively) and MLS retrievals V3.3 are shown in the left panel of Fig. 6. The red and magenta lines show linear fits to the time series of the relative differences. A negative bias of about 11% and a seasonal variation of the relative difference are clearly identified from the plot for V3.5. A long term change in the differences seen in V2.9 is not present any more. The remaining linear change in the relative differences of V3.5 is estimated at about 1% per decade while it was -6% for V2.9. The right panel of the figure shows the diurnal variation of ozone calculated with a chemical transport model at 58 km altitude (uppermost altitude available in the model). One sees what a negative bias of about 7% is expected from the difference in the local time between the SCIAMACHY and MLS measurements.

Similar plots for northern and southern high latitudes are shown in the left and right panels of Fig. 7, respectively. One sees that in both cases the drift in the relative differences has been significantly reduced (from 16% to 7% in the northern and from 24% to 2% in the southern high latitudes).

2.6 SMR (Chalmers)

The Odin satellite was launched on 20 February 2001, into a sun-synchronous 18:00 hour ascending node orbit, carrying two co-aligned limb sounding instruments: OSIRIS (Optical Spectrograph and Infrared Imaging System) and SMR (Sub-Millimetre Radiometer). Originally, Odin was used for both atmospheric and astronomical observations, while since 2007 only its aeronomy mission (Murtagh et al., 2002) is active. Odin is a Swedish-led project, in cooperation with Canada, France and Finland. Both of Odin's instruments are still functional, and the present operation of the satellite is partly performed as a ESA third party mission.

The SMR package is highly tunable and flexible. In short, the four main receiver chains can be tuned to cover frequencies between 486 GHz – 504 GHz and 541 GHz – 581 GHz, but the maximum total instantaneous

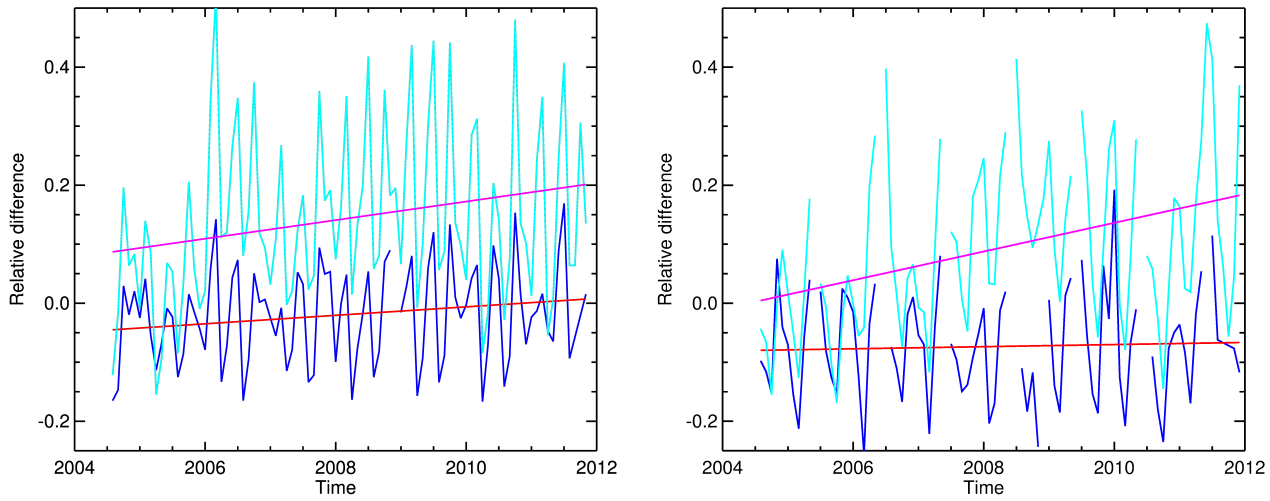

Figure 7: Same as in the left panel of Fig. 6 but for northern high latitudes (60°S – 70°N) in the left panel and for southern high latitudes (60°S – 70°N) in the right panel.

bandwidth is only 1.6 GHz. This bandwidth is determined by the two autocorrelation (AC) spectrometers used for atmospheric observations. The two ACs can be coupled to any of the four front-ends, but only two or three front-ends are used simultaneously. The ACs cover 400 or 800 MHz per front-end, depending on configuration, and are used with a frequency resolution of 2 MHz. To cover all molecular transitions of interest, a number of "frequency modes" have been defined.

Single sideband operation is obtained by tunable Martin-Pupplet interferometers. The main reflector of SMR has a diameter of 1.1 m, giving a vertical resolution at the tangent point of about 2 km. The vertical scanning of the two instruments' line-of-sigh is achieved by a rotation of the satellite platform, with a rate matching a vertical speed of the tangent altitude of 750 m/s. Measurements are performed during both upward and downward scanning. The lower end of the scan is typically at about 7 km, the upper end varies between 70 km and 110 km, depending on observation mode. At tangent altitudes above ≈ 55 km, the integration time is either 1.87 or 3.87 s, giving spectra tangent altitude separation of 3 or 6 km. Measurements are in general performed along the orbit plane, providing a latitude coverage between 82.5°S and 82.5°N. For further basic technical information about SMR, see Eriksson et al. (2002), Merino et al. (2002) and Murtagh et al. (2002).

The standard "optimal estimation method" (OEM) is applied. That is, the retrieved state can be expressed as

$$\hat{\mathbf{x}} = \min_{\mathbf{x}}(C(\mathbf{x})). \tag{23}$$

where

$$C(\mathbf{x}) = (\mathbf{y} - \mathcal{F}(\mathbf{x}, \hat{\mathbf{b}}))^T \mathbf{S}_o^{-1} (\mathbf{y} - \mathcal{F}(\mathbf{x}, \hat{\mathbf{b}})) + (\mathbf{x} - \mathbf{x}_a)^T \mathbf{S}_a^{-1} (\mathbf{x} - \mathbf{x}_a). \tag{24}$$

In the case of Odin/SMR the inversion problem at hand is moderately non-linear and the solution is found by an iterative Levenberg–Marquardt scheme (Rodgers, 2000, Eq. 5.36):

$$\hat{\mathbf{x}}_{i+1} = \hat{\mathbf{x}}_i + \left[(1+\gamma)\mathbf{S}_a^{-1} + \mathbf{K}_i^T \mathbf{S}_o^{-1} \mathbf{K}_i\right]^{-1} \left[\mathbf{K}_i^T \mathbf{S}_o^{-1} (\mathbf{y} - \mathcal{F}(\hat{\mathbf{x}}_i, \hat{\mathbf{b}})) - \mathbf{S}_a^{-1} (\hat{\mathbf{x}}_i - \mathbf{x}_a)\right]. \tag{25}$$

The OEM method and the overall data manipulation are implemented in Matlab, while the ARTS forward model (Eriksson et al., 2011) is used as background computational engine to provide simulated SMR data ($\mathcal{F}$) and the Jacobian matrix ($\mathbf{K}$). Each up- and downward scan is inverted separately, assuming an atmosphere of

1D character. That is, the measurement vector **y** includes only spectra from a single scan, and retrieved atmospheric profiles have only a vertical variation. Pressure is used as the main vertical coordinate, i.e. retrieved species and temperatures are provided on pressure grids.

The covariance matrix of observation uncertainties ($\mathbf{S}_o$) contains a description of the thermal noise. The weak correlation of the noise between different tangent altitudes is neglected, but the correlation between adjacent channels is included.

Among the long list of (assumed) forward model parameters ($\hat{\mathbf{b}}$), spectroscopic data and sensor characteristics are the most influential ones for these retrievals. The bulk of spectroscopic data are taken from HITRAN 2012. Centre frequency, intensity and pressure broadening parameters of some main transitions have been replaced by values taken from JPL or from journal articles. Relative dense monochromatic and pencil beams grids are used and the associated forward model errors should cause marginal errors. Antenna pattern and frequency response of backend channels are known with high accuracy, and the main sensor uncertainty is the sideband suppression, that does not reach its nominal value (19 dB) for all frequency modes. Aspects and requirements of the forward modelling are treated in Eriksson et al. (2002). Regarding mesospheric retrievals, it is notewhorty that LTE can be assumed throughout in inversions of SMR data.

The state vector contains a mix of quantities: one or several gas species profiles, the temperature profile, a baseline off-set for each spectrum included, a pointing off-set and a frequency off-set. Both the pointing and frequency off-sets are scalar values, common for the complete scan. No correlation between baseline off-sets are assumed, and also they can be seen as a set of scalar quantities. Further, the a priori correlation between species and temperature is assumed to be zero, and, hence, the complete covariance matrix $\mathbf{S}_a$ has a block-diagonal structure.

Vertical correlations of gas species and temperature variations are modelled by a parametric expression, using a correlation length l_c. The correlation is modelled to follow an exponential function and covariances are set as

$$\mathbf{S}_{ij} = \sigma_i \, \sigma_j \, exp\left(-\left|z_i - z_j\right| / l_c\right), \tag{26}$$

where z_i and σ_i is the altitude and standard deviation at pressure level i. The inverses of both $\mathbf{S}_a$ and $\mathbf{S}_o$ are calculated by inverting each matrix along the diagonal separately. In addition, for $\mathbf{S}_a$ each inversion is made in an analytic manner (Rodgers, 2000, Eq. B71).

For a more detailed description of the SMR retrievals, see Eriksson (2016). The presentation above is of general validity for the standard SMR inversions. The main adoptions made for retrievals targeting the mesosphere are to select more narrow frequency bands and only consider spectra above 45 km. Some adjustments of a priori uncertainties and settings for the Levenberg–Marquardt scheme are also made.

Several frequency modes cover ozone transitions providing useful mesospheric retrievals. Table 4 gives a summary. As seen in the table, information on mesospheric ozone is provided by several of SMR's frequency modes. The best temporal coverage is obtained by frequency mode 2.

Table 4 indicates also the parameterisation of a priori uncertainty, both for ozone itself and for the background temperature retrieval. Correlation lengths have no altitude variation, while standard deviations are allowed to vary. For species this altitude variation is defined by setting both a relative and an absolute value, where, at each altitude, the least constraining value is selected. For example, if the a priori uncertainty is set to 50%/1ppm and the a priori value at some altitude is 3 ppm, 1.5 ppm will be applied as a priori uncertainty for that altitude.

N.B.: *The reprocessing of the data set is in progress as part of an ESA project dedicated to it. Specific retrieval settings (in the table), figures showing typical averaging kernels and errors, as well as discussion about the improvements with respect to the previous L2 version (v2.3) will be added when the new products will be available.*

3. Carbon monoxide

3.1 ACE-FTS (UoT)

Carbon monoxide profiles are retrieved using the same approach as described in Sect. 2.1 for ozone. The retrievals are performed between altitudes of 5 and 110 km using 34 microwindows between 2046 and 2187 cm^{-1} and between 4209 and 4285 cm^{-1}. In the lower mesosphere, retrievals account for CO_2 as an interfering species. Six additional microwindows at 1950, 1986, 2033, 2083, 2141, and 2150 cm^{-1} have been included to improve the results for interfering species below 22 km.

3.2 MIPAS (KIT/IAA)

MIPAS V5r_CO_m21 carbon monoxide retrieval is based on constrained inverse modeling of non-LTE limb radiances. That is performed using the IMK/IAA Scientific Processor (von Clarmann et al., 2003, 2009) extended with the non-LTE GRANADA algorithm (Funke et al., 2012), which is able to cope with non-LTE emissions. The basic retrieval equations, the methods for characterization of results through error estimates and vertical and horizontal averaging kernels, the iteration and convergence criteria and the regularization method are described in the Ozone Climate Change Initiative Algorithm Theoretical Basis Document (Ref.: Ozone_cci_ATBD_Phase2_V1 _00_01, pp. 60-64, 2014). MIPAS carbon monoxide is reliably retrieved from from 20 km from MIPAS measurements in the MA mode and 40 km in the UA and NLC mode up to ∼105 km (MA and NLC mode) and 170 km(UA mode). A description of the specifics of the carbon monoxide retrieval V5r_CO_m21 follows.

3.2.1 Strategy

Carbon monoxide is retrieved in the log(vmr) domain from spectral lines covering ro-vibrational emissions of the CO_2 main isotope. These have been selected from a broad spectral region, covered by the MIPAS band D (2040–2170 cm^{-1}). The V5r_CO_m21 retrieval strategy is an update and extension of the retrieval of carbon monoxide from the MIPAS NOM measurements (6-68 km) (Funke et al., 2009) with consideration of non-LTE emission. Retrievals are performed from MIPAS limb emission measured in the MA (20-102 km), NLC (40-102 km) and UA (40-170 km) modes. Calibrated spectra are as supplied by ESA in version 5.02/5.06 (Raspollini et al. (2010) and references therein). The retrieval is performed after a spectral shift retrieval and the non-LTE retrievals of temperature and abundances of ozone, water vapour, nitrous oxide and methane. The IMK/IAA processor simultaneously retrieves microwindow-dependent continuum radiation and zero level calibration corrections (the latter, assumed constant with altitude). Horizontal CO gradients in the latitudinal

Frequency mode	Molecular transition	Altitude coverage	Temporal coverage	O_3		Temperature	
				σ_a	l_c	σ_a	l_c
2	544.86 GHz	?-? km	daily (15 days/month)	?%/?ppm	? km	?-? K	? km
14	576.51 GHz	?-? km	4 days/month (irregular)	?%/?ppm	? km	?-? K	? km
21	551.44 GHz	?-? km	4(1) days/month	?%/?ppm	? km	?-? K	? km
22	576.51 GHz	?-? km	2(1) days/month	?%/?ppm	? km	?-? K	? km
24	576.51 GHz	?-? km	seldom and irregular	?%/?ppm	? km	?-? K	? km

Table 4: Overview of SMR measurements and retrievals of mesospheric ozone. The first four columns specify frequency mode number, frequency of the ozone transition targeted, approximate vertical coverage of retrievals and typical value of number of measurements day per month (the value indicated in brackets was relevant before 2007), respectively. The remaining four columns specify a priori uncertainties, see the text for details.

and longitudinal directions are fitted jointly with the CO vmr. Forward model calculations along the line of sight are done considering gradients (along the LOS) in the non-LTE populations of the emitting levels caused by varying solar illumination conditions (variable solar zenith angle, see Funke et al., 2009).

3.2.2 Discretization and setup

The retrievals are performed from the surface to 200 km over a discrete altitude grid of 1 km up to 50 km, 2 km at 50-100 km, 5 km at 100-110 km, 10 km at 110-150 km, and 25 km from 150-200 km. The selected grid provides balanced accuracy and efficiency. The forward calculations are performed using that same grid. The over-sampled retrieval grid, finer and more extended than MIPAS vertical sampling (approximately 3 km), makes the use of a regularization mandatory in order to obtain stable solutions. A Tikhonov-type smoothing constraint is used for CO. Horizontal CO gradients are regularized by a strong diagonal constraint towards a zero a priori.

The numerical integration of the signal over the 3 km field of view is done using five pencil beams. The selected width of the integration window (apodized instrument line shape function) has been chosen to comply with an apodization accuracy of 0.1%.

3.2.3 Microwindows

The retrievals are performed from selected spectral regions (microwindows) which vary with tangent altitudes in order to optimize computation time and minimize systematic errors (von Clarmann and Echle, 1998). The microwindows used in the carbon monoxide retrieval are listed in Table 5. These height dependent combinations of micro-windows were selected with a trade-off between computation time and total retrieval error. They are a vertical extension of the initial set of microwindows used for the MIPAS carbon monoxide NOM retrieval (z$<$70 km) (Funke et al., 2009), covering CO(1$\rightarrow$0) emissions in the 2040–2120 cm^{-1} range. This microwindow set has been further improved by extension into the 2120–2170 cm^{-1} range, resulting in a better precision and vertical resolution in the lower and middle stratosphere.

3.2.4 A priori and atmospheric inputs

MIPAS V5r_CO_m21 carbon monoxide retrieval setup uses the following inputs:

- a priori is taken from the Whole Atmosphere Community Climate Model with specified dynamics (SD-WACCM) simulations (Garcia et al., 2007) monthly resolved zonal mean climatology (multi-year composite).
- Pressure, line-of-sight information, temperature and temperature horizontal gradients from MIPAS retrieval version V5r_T_m21 (and V5r_NOT_621 above 100 km in the case of UA retrieval) , as well as ozone from MIPAS V5r_O3_m22, water vapor from MIPAS V5r_H2O_m22, and nitrous oxide from MIPAS V5r_N2O_m21 are used.
- Spectroscopic data from HITRAN 2012 (Rothman et al., 2013).

Several inputs are needed for the calculation of the non-LTE populations of the vibrationally excited emitting molecules by GRANADA (Funke et al., 2012). These are the levels of the isotopes ^{12}C ^{16}O(0,1,2), ^{13}C ^{16}O(0,1), and ^{12}C ^{18}O(0,1). Due to the strong V-V coupling of CO and $CO_2(v_3)$ states, the latter molecule is also included using the same GRANADA setup as used in the MIPAS V5r_CO2_m22 retrievals. Further, O_3 non-LTE modelling (as performed in MIPAS V5r_O3_m22 retrievals) is also required in order to properly describe interfering O_3 hot band contributions around 2040-2100 cm^{-1}. In total, the non-LTE model inputs used in V5r_CO_m22 retrievals are:

Table 5: Microwindows and number of internal sub-microwindows at each tangent altitude used in MIPAS V5r_CO_m21 carbon monoxide retrieval. Altitude levels should be read vertically.

Microwindow cm^{-1}	Altitude km																												
																													>1
	1	2	2	2	3	3	3	3	4	4	4	5	5	5	6	6	6	6	7	7	7	8	8	8	9	9	9	9	0
	8	1	4	7	0	3	6	9	2	5	8	1	4	7	0	3	6	9	2	5	8	1	4	7	0	3	6	9	2
(2041.5625, 2046.3750)	0	0	3	3	3	3	3	3	3	3	3	3	3	3	3	3	2	2	2	2	2	2	2	2	2	2	2	2	2
(2059.8125, 2062.1250)	0	0	2	2	2	2	3	2	2	2	2	2	2	2	2	2	2	2	2	2	2	2	2	2	2	2	2	2	2
(2068.5000, 2070.1250)	0	0	1	1	1	1	1	2	1	1	1	1	1	1	1	1	1	1	1	1	1	1	1	1	1	1	1	1	1
(2073.1250, 2073.6250)	0	0	2	0	0	2	2	2	2	2	2	2	2	2	2	2	2	2	2	2	2	2	2	2	2	2	2	2	2
(2081.0000, 2082.4375)	2	1	4	1	1	2	2	2	4	2	2	2	2	2	2	2	2	2	2	2	2	2	2	2	2	2	2	2	2
(2084.6875, 2087.0000)	2	2	2	3	3	1	1	3	2	1	1	1	1	1	1	1	1	1	1	1	1	1	1	1	1	1	1	1	1
(2090.0000, 2090.6875)	0	3	1	1	1	1	1	1	1	1	1	1	1	1	1	1	1	1	1	1	1	1	1	1	1	1	1	1	1
(2094.2500, 2095.8750)	2	3	1	3	1	1	1	1	1	2	2	1	1	1	1	1	2	2	2	2	2	2	2	2	2	2	2	2	2
(2099.0000, 2103.7500)	0	1	3	1	2	3	3	3	3	2	2	3	3	3	3	3	3	3	3	3	3	3	3	3	3	3	3	3	3
(2107.1250, 2111.6875)	2	4	2	2	2	2	2	2	2	2	2	2	2	2	2	2	2	2	2	2	2	2	2	2	2	2	2	2	2
(2114.8750, 2115.8750)	3	5	2	2	2	2	2	2	2	2	2	2	2	2	2	2	1	1	1	1	1	1	1	1	1	1	1	1	1
(2119.3125, 2120.2500)	2	1	1	1	1	1	1	1	1	1	1	1	1	2	2	2	1	1	1	1	1	1	1	1	1	1	1	1	1
(2134.7500, 2137.7500)	3	3	3	4	3	2	2	2	2	2	2	2	2	2	2	2	2	2	2	2	2	2	2	2	2	2	2	2	2
(2139.1875, 2141.0625)	4	3	3	3	3	4	3	4	3	3	3	3	3	3	3	3	3	3	3	3	3	3	3	3	3	3	3	3	3
(2143.8750, 2147.3125)	3	4	4	3	3	2	3	2	3	4	4	3	3	3	3	3	2	2	2	2	2	2	2	2	2	2	2	2	2
(2149.8750, 2151.2500)	4	3	3	2	4	3	2	5	2	3	3	3	3	2	2	2	3	3	3	3	3	3	3	3	3	3	3	3	3
(2154.1875, 2158.6875)	4	3	2	2	2	2	2	2	2	2	2	2	2	2	2	2	2	2	2	2	2	2	2	2	2	2	2	2	2
(2161.8750, 2162.3750)	1	1	1	1	1	1	1	1	1	1	1	1	1	1	1	1	1	1	1	1	1	1	1	1	1	1	1	1	1
(2169.0625, 2169.7500)	1	1	1	1	1	1	1	1	1	2	2	2	2	1	1	1	0	0	0	0	0	0	0	0	0	0	0	0	0

Table 6: Summary of main errors in MIPAS carbon monoxide vmr. 'NLTE' includes errors due to uncertainties in the collisional rates used in the non-LTE model. 'IS' includes errors due to interfering emissions of O_3, N_2O, and H_2O. 'Total' is the root sum square of all errors. Numbers in brackets refer to nighttime conditions (if different from daytime).

Height km	Noise %	IS %	Pointing %	Gain %	T %	ILS %	Spectroscopy %	NLTE %	Total %
20	35	1	1	2	2	1	2	0	35
30	40	3	3	2	3	2	3	5	41
40	30	10	3	1	5	3	5	15	36
50	30	3	2	1	5	1	3	10	32
60	30 (45)	1	2	1	5	1	3	7	32 (46)
70	25 (30)	1	2	1	7	1	3	7	27 (31)
>80	15 (35)	1	2	1	15	1	3	7	22 (39)

- Ozone from the previously retrieved ozone in its version V5r_O3_m22.
- Atomic oxygen concentration derived from the retrieved ozone (V5r_O3_522) below 95 km and from WACCM in its specified dynamics (SD) configuration (Garcia et al., 2007) above.
- Non-LTE collisional scheme and rate constants for CO as in Funke et al. (2012), for CO_2 as described in Sec. 11, and for O_3 as described in Sec. 2.3.
- Solar fluxes required in the non-LTE model are calculated considering the temporal variations of the Sun-Earth distance. Attenuation by solar Fraunhofer lines is taken into account (Hase et al., 2006). The solar background radiance is expressed as a blackbody with effective temperature T_e (in K) depending on wavenumber ν (in cm^{-1}) through T_e=5450+0.25(ν-2000). This parameterization is similar to that developed by Platnick and Fontenla (2008) for 3.7 μm, and they agree within 0.5–-1% at that wavelength.

3.2.5 Error budget

The error budget described here considers the propagation of the measurement noise and of the uncertainties of model parameters onto the retrieved carbon monoxide abundances. Noise-induced retrieval errors and vertical resolutions are estimated routinely for each individual profile by the retrieval algorithm. Systematic errors related to the mapping of uncertain model parameters are estimated for representative profiles only.

The uncertainties assumed for the estimation of the errors have been: 1% for gain calibration, 3% for the instrument line shape, 150 m for elevation pointing, 2K for temperature, and 5% for spectroscopic data.

The modeling of the non-LTE populations of the CO and O_3 vibrational levels is an important source of the MIPAS carbon monoxide systematic error. Non-LTE errors are dominated by the uncertainties in the collisional rates used in the non-LTE model. The estimations provided here are based on Funke et al. (2007). The CO noise error is calculated on the basis of L1b noise-equivalent-spectral-radiances reported for channel D ($\sim$2 nW/($cm^2 cm^{-1}$sr)). Typical values are 15–45%.

The overall estimated error is dominated by propagation of instrumental noise. Dominating systematic errors are the effect of spectroscopic data uncertainty and temperature below 50 km and by the non-LTE above 50 km.

Table 6 summarizes the estimated errors in MIPAS retrieved carbon monoxide vmr.

The vertical resolution of MIPAS retrieved carbon monoxide abundance is the full width at half maximum of the averaging kernels rows. Average vertical resolution is 4-6 km below 55 km. Above, the vertical resolution is 5–10 km during daytime and 10–20 km during nighttime.

Two additional criteria are further used to filter out the retrieved IMK/IAA data in order to guarantee the quality of the profile. The following results are discarded: 1) results where the diagonal value (for individual profiles) or the mean diagonal value (for averages) of the averaging kernel is less (in absolute value) than 0.03, 2) those corresponding to altitudes not sounded by MIPAS (below the lowermost tangent altitude).

3.2.6 Improvements with respect to previous versions

V5r_CO_m21 carbon monoxide baseline is an improvement of the previous V4O_CO_m01 version. The changes from the previous version are:

- Updated L1b database to V5.
- Updated version HITRAN database from the 2004 to the 2012 version.
- Updated versions of temperature (V5r_T_m21), ozone (V5r_O3_m22), water vapour (V5r_H2O_m22), CH_4 (V5r_CH4_m21), and N_2O (V5r_N2O_m21)
- Revised regularization scheme for offset and continuum.
- Optimized retrieval grid.

The average impact on the carbon monoxide retrieval after those changes are shown in Figs. 8 and 9. The values for the new version are around 10–20% larger below 30 km, and 10–20% lower at 35- 50 km. In the mesosphere, particularly above 75 km larger (mostly positive) differences up to 100% occur. These differences can be primarily attributed to the updated L1b database.

3.3 SMR (Chalmers)

This species is retrieved in the same basic manner as previously described for ozone (Sec. 2.6). The measurements and retrievals of CO are summarised in Table 7. Carbon monoxide is covered by several frequency modes, but they have all equal performance and are inverted using the same settings. Only the temporal sampling differs (see Table 7).

SMR covers a single CO transition and the phase-lock loop of the mixer of the front-end covering this transition failed from start of the mission. This has the consequency that the exact frequencies of the spectra are not known, and a special algorithm has been designed to make a rough frequency calibration of CO spectra. This algorithm is described in Rydberg et al. (2016).

N.B.: *The reprocessing of the data set is in progress as part of an ESA project dedicated to it. Specific retrieval settings (in the table), figures showing typical averaging kernels and errors, as well as discussion about the improvements with respect to the previous L2 version (v2.3) will be added when the new products will be available.*

4. Nitric oxide

4.1 ACE-FTS (UoT)

Nitric oxide profiles are retrieved using the same approach as described in Sect. 2.1 for ozone. The retrievals are performed between altitudes of 6 and 107 km using 36 microwindows between 1842 and 1930 cm^{-1}. In

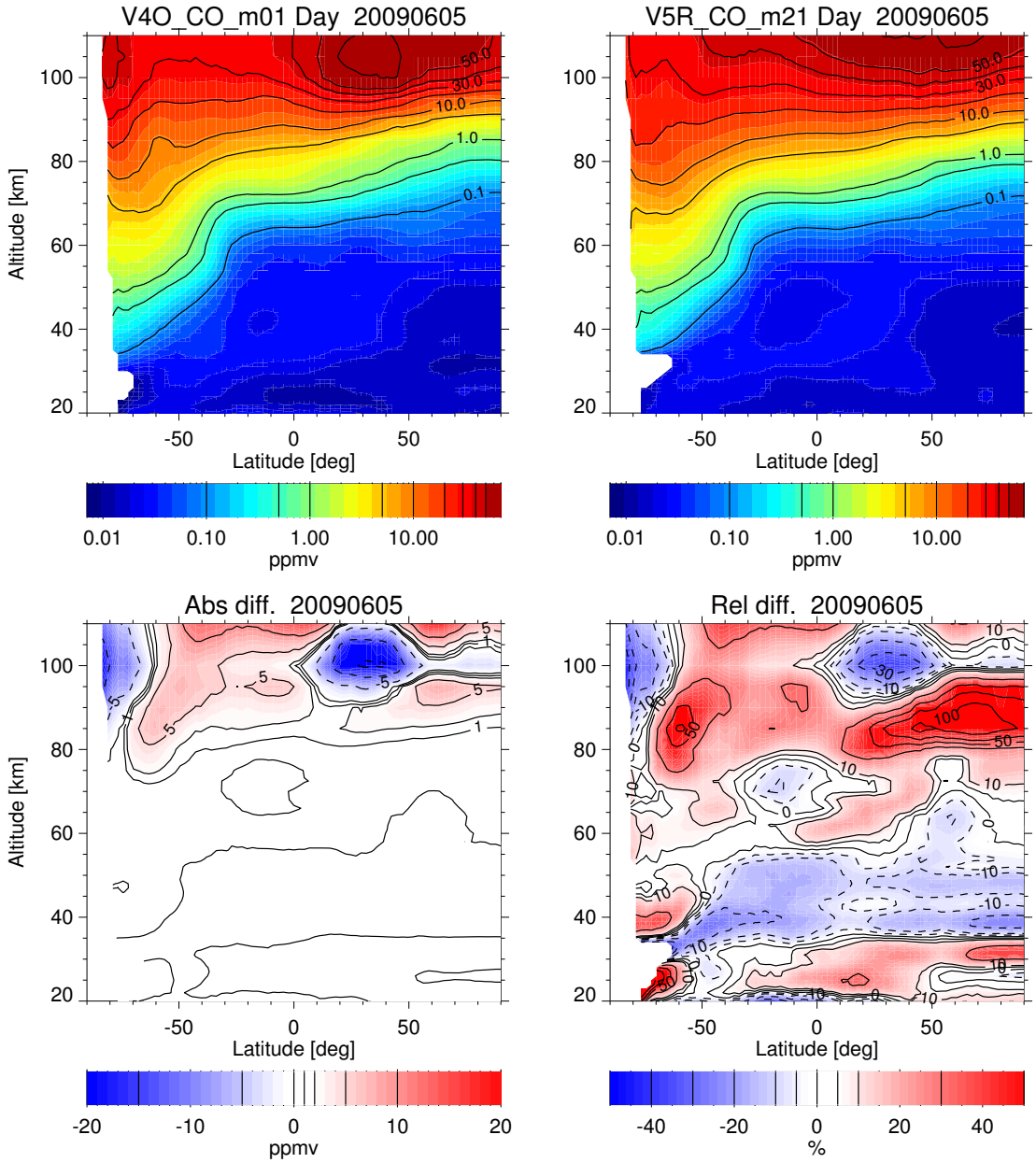

Figure 8: Comparison of CO abundance for daytime conditions (10 am) retrieved in the current V5r_CO_m21 and the previous V4O_CO_m01 versions for 5 June 2009. Lower panels show the V5r_CO_m21–V4O_CO_m01 differences. White areas indicate unavailability of meaningful data.

Frequency mode	Molecular transition	Altitude coverage	Temporal coverage	CO		Temperature	
				σ_a	l_c	σ_a	l_c
14	576.27 GHz	?-? km	4 days/month (irregular)	?%/?ppm	? km	?-? K	? km
22	576.27 GHz	?-? km	2(1) days/month	?%/?ppm	? km	?-? K	? km
24	576.27 GHz	?-? km	seldom and irregular	?%/?ppm	? km	?-? K	? km

Table 7: Overview of SMR measurements and retrievals of mesospheric carbon monoxide. See Table 4 for comments on content.

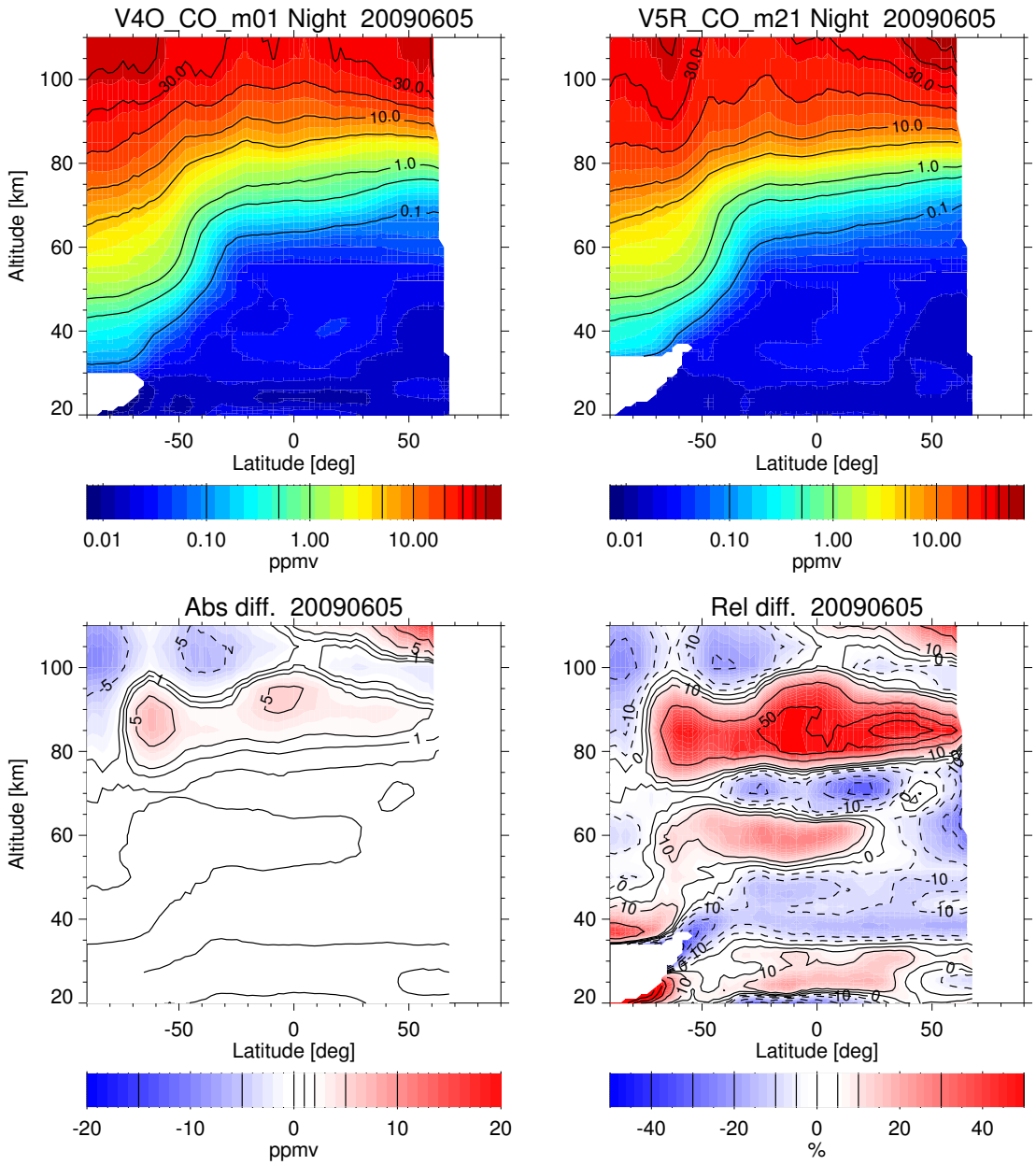

Figure 9: Comparison of CO abundance for nighttime conditions (10 pm) retrieved in the current V5r_CO_m21 and the previous V4O_CO_m01 versions for 5 June 2009. Lower panels show the V5r_CO_m21–V4O_CO_m01 differences. White areas indicate unavailability of meaningful data.

the mesosphere, retrievals account for CO_2 and H_2O as interfering species. Microwindows at 1650, 1950 and 1978 cm^{-1} have been added to improve the results for the water vapour interferences at altitudes below 30 km.

4.2 MIPAS (KIT/IAA)

MIPAS V5r_NO_m21 nitric oxide retrieval is based on constrained inverse modeling of non-LTE limb radiances. That is performed using the IMK/IAA Scientific Processor (von Clarmann et al., 2003, 2009) extended with the non-LTE GRANADA algorithm (Funke et al., 2012), which is able to cope with non-LTE emissions. The basic retrieval equations, the methods for characterization of results through error estimates and vertical and hor-

izontal averaging kernels, the iteration and convergence criteria and the regularization method are described in the Ozone Climate Change Initiative Algorithm Theoretical Basis Document (Ref.: Ozone_cci_ATBD_Phase2_V1_00_01, pp. 60-64, 2014). The MIPAS nitric oxide product described here is reliably retrieved from 20 km from MIPAS measurements in the MA mode and 40 km in the UA and NLC mode up to ∼105 km in polar winter (∼65 km elsewhere). Note that thermospheric nitric oxide retrievals from UA observations of scans with tangent heights >102 km (V5r_NOT_621) are performed with a different retrieval setup (joint retrieval of NO and kinetic temperature) and are described in Sec.5. A description of the specifics of the nitric oxide retrieval V5r_NO_m21 follows.

4.2.1 Strategy

Nitric oxide is retrieved in the log(vmr) domain from spectral lines covering ro-vibrational emissions of the NO main isotope. These have been selected from a broad spectral region, covered by the MIPAS band D (1830–1940 cm^{-1}). The V5r_NO_m21 retrieval strategy is an update and extension of the retrieval of nitric oxide from the MIPAS NOM measurements (6-68 km) (Funke et al., 2005) with consideration of non-LTE emission. Retrievals are performed from MIPAS limb emission measured in the MA (20-102 km), NLC (40-102 km) and UA (40-170 km) modes, in the latter case restricting the scans to tangent heights to altitudes <102 km. Calibrated spectra are as supplied by ESA in version 5.02/5.06 (Raspollini et al. (2010) and references therein). The retrieval is performed after a spectral shift retrieval and the non-LTE retrievals of temperature and abundances of ozone, water vapour, nitrous oxide and methane, and nitric dioxide. The IMK/IAA processor simultaneously retrieves microwindow-dependent continuum radiation and zero level calibration corrections (the latter, assumed constant with altitude).

Photo-chemically induced horizontal inhomogenities along the instrument's line of sight are taken into account for scans close to the terminator (solar zenith angles of 80–100°) by means of a photochemical model (Funke et al., 2012) which constrains the NO_x partitioning, $Q(s)$ =[$NO_2(s)$]/[$NO(s)$], along the optical path, s, of the instrument depending on the solar zenith angle at s. Assuming a homogeneous horizontal distribution of NO_x, the NO and NO_2 abundances at the optical path segment s passing a given altitude level are scaled with respect to the actual abundance at the center of the scan s_0 and the same altitude level as

$$\frac{[\mathrm{NO}(s)]}{[\mathrm{NO}(s_0)]} = \frac{1+Q(s_0)}{1+Q(s)} \tag{27}$$

within the forward calculations of the retrieval.

Horizontal NO_x gradients in the latitudinal and longitudinal directions (acting in a multiplicative sense to the constrained NO_x partitioning along the line of sight) are fitted jointly with the NO vmr.

Horizontal inhomogenities along the instrument's line-of-sight occur also in thermospheric path segments at polar/sub-polar latitudes due to the complex structure of aurorally produced NO. If not considered, such inhomogenities can impact the NO retrieval even at mesospheric and stratospheric altitudes. In the current retrieval version, this is accounted for by applying 3D radiative transfer and introducing an a priori horizontal shape of the auroral oval (obtained from the NOEM model (Marsh et al., 2004)) which is then implicitly scaled by the joint-fitted horizontal NO_x gradients in the latitudinal and longitudinal directions.

4.2.2 Discretization and setup

The retrievals are performed from the surface to 200 km over a discrete altitude grid of 1 km up to 56 km, 2 km at 56-70 km, 2.5 km at 70-105 km 5 km at 105-150 km, and 10 km above. The selected grid provides balanced accuracy and efficiency. The forward calculations are performed using that same grid. The over-sampled retrieval grid, finer than MIPAS vertical sampling (approximately 3 km), makes the use of a regularization mandatory in order to obtain stable solutions. An altitude-dependent Tikhonov-type smoothing constraint is

used for NO. Horizontal NO_x gradients are regularized by a strong and vertically variable diagonal constraint towards a zero a priori.

The numerical integration of the signal over the 3 km field of view is done using five pencil beams. The selected width of the integration window (apodized instrument line shape function) has been chosen to comply with an apodization accuracy of 0.1%.

4.2.3 Microwindows

The retrievals are performed from selected spectral regions (micro-windows) which vary with tangent altitudes in order to optimize computation time and minimize systematic errors (von Clarmann and Echle, 1998). The microwindows used in the nitric oxide retrieval are listed in Table 8. These height dependent combinations of micro-windows were selected with a trade-off between computation time and total retrieval error. They are a vertical extension of the initial set of microwindows used for the MIPAS nitric oxide NOM retrieval (z$<$70 km) (Funke et al., 2005), covering NO(1$\rightarrow$0) emissions in the 1830–1940 cm^{-1} range.

Table 8: Microwindows and number of internal sub-microwindows at each tangent altitude used in MIPAS V5r_NO_m21 nitric oxide retrieval. Altitude levels should be read vertically.

Microwindow cm^{-1}	Altitude km																												
																													1
	1	2	2	2	3	3	3	3	4	4	4	5	5	5	6	6	6	6	7	7	7	8	8	8	9	9	9	9	0
	8	1	4	7	0	3	6	9	2	5	8	1	4	7	0	3	6	9	2	5	8	1	4	7	0	3	6	9	2
(1831.6875,1832.0625)	1	1	1	1	0	1	1	1	1	1	1	1	1	1	1	1	0	0	0	0	0	0	0	0	0	0	0	0	0
(1837.8125,1838.2500)	1	0	1	1	1	0	1	1	1	1	1	1	1	1	1	1	1	1	1	1	1	1	1	1	1	1	1	1	1
(1842.8125,1843.1875)	1	1	1	1	0	0	1	1	1	1	1	1	1	1	1	1	1	1	1	1	1	1	1	1	1	1	1	1	1
(1849.0625,1853.9375)	2	2	2	2	2	2	2	2	2	2	2	2	2	2	2	2	2	2	2	2	2	2	2	2	2	2	2	2	2
(1857.0000,1861.1250)	2	2	2	2	2	2	2	2	2	2	2	2	2	2	2	2	2	2	2	2	2	2	2	2	2	2	2	2	2
(1863.5000,1863.8750)	1	1	1	1	1	1	0	1	1	1	1	1	1	1	1	1	1	1	1	1	1	1	1	1	1	1	1	1	1
(1880.7500,1881.2500)	1	1	1	1	1	1	1	1	1	1	1	1	1	1	1	1	1	1	1	1	1	1	1	1	1	1	1	1	1
(1887.2500,1891.1250)	2	2	2	2	2	2	1	2	2	2	2	2	2	1	1	1	2	2	2	2	2	2	2	2	2	2	2	2	2
(1896.7500,1900.8750)	3	3	3	3	3	3	3	3	3	3	3	3	3	3	3	3	3	3	3	3	3	3	3	3	3	3	3	3	3
(1902.9375,1906.8750)	3	2	2	2	2	2	3	3	3	3	3	3	3	3	3	3	3	3	3	3	3	3	3	3	3	3	3	3	3
(1909.0000,1912.9375)	3	3	2	3	3	2	3	3	3	3	3	3	3	3	3	3	3	3	3	3	3	3	3	3	3	3	3	3	3
(1914.8125,1915.1250)	1	1	1	1	1	0	1	1	1	1	1	1	1	1	1	1	1	1	1	1	1	1	1	1	1	1	1	1	1
(1923.3750,1927.4375)	2	2	2	2	1	2	2	2	1	0	0	2	2	2	2	2	1	1	1	1	1	1	1	1	1	1	1	1	1
(1928.8750,1931.8750)	1	1	1	3	3	3	3	2	0	0	0	3	3	3	3	3	2	2	2	2	2	2	2	2	2	2	2	2	2
(1935.3125,1935.6875)	0	0	1	1	1	1	1	0	0	0	0	0	0	1	1	1	1	1	1	1	1	1	1	1	1	1	1	1	1

4.2.4 A priori and atmospheric inputs

MIPAS V5r_NO_m21 nitric oxide retrieval setup uses the following inputs:

- A priori is computed by means of a photochemical model (Funke et al., 2012) under consideration of NO_2 and O_3 retrieved in a previous step. Above 100 km, the a priori is taken from the NOEM model (Marsh et al., 2004). Since the latter is an empirical model for thermospheric NO daytime concentrations, a SZA-dependent scaling factor obtained from the MIPAS UA day/night climatology is applied for nighttime conditions.

- Pressure, line of sight information, temperature and temperature horizontal gradients from MIPAS retrieval version V5r_TLOS_m21, as well as nitric dioxide from MIPAS V5r_NO2_m21, ozone from MIPAS V5r_O3_m22, and water vapor from MIPAS V5r_H2O_m22 are used.
- Spectroscopic data from HITRAN 2008 (Rothman et al., 2009).

Several inputs are needed for the calculation of the ro-vibrational non-LTE populations of the excited emitting molecules by GRANADA. Funke and López-Puertas (2000) provide information on the effect of each input on the NO levels. The non-LTE model inputs used in V5r_NO_m21 retrievals are:

- Ozone from the previously retrieved ozone in its version V5r_O3_m22.
- Previously retrieved nitric dioxide in its version V5r_NO2_m21.
- Atomic oxygen concentration derived from the retrieved ozone (V5r_O3_m22) below 95 km, from WACCM in its specified dynamics (SD) configuration (Garcia et al., 2007) at 95–135 km, and from MSIS above.
- Atomic nitrogen (N(^4S)) concentrations above 85 km from MSIS, below from photochemical model.
- (N(^2D))abundances have been calculated as described in Vitt et al. (2000), considering an auroral production based on ionization rates from the Atmospheric Ionization Module Osnabrück (AIMOS version 1.6) model (Wissing and Kallenrode, 2009).
- Non-LTE collisional scheme and rate constants as in Funke et al. (2012).
- Solar fluxes required in the non-LTE model are calculated considering the temporal variations of the Sun-Earth distance. Attenuation by solar Fraunhofer lines is taken into account (Hase et al., 2006). The solar background radiance is expressed as a blackbody with effective temperature T_e (in K) depending on wavenumber ν (in cm^{-1}) through T_e=5450+0.25(ν-2000). This parameterization is similar to that developed by Platnick and Fontenla (2008) for 3.7 μm, and they agree within 0.5–-1% at that wavelength.

4.2.5 Error budget

The error budget described here considers the propagation of the measurement noise and of the uncertainties of model parameters onto the retrieved nitric oxide abundances. Noise-induced retrieval errors and vertical resolutions are estimated routinely for each individual profile by the retrieval algorithm. Systematic errors related to the mapping of uncertain model parameters are estimated for representative profiles only. Table 9 summarizes the estimated errors in MIPAS retrieved nitric oxide vmr.

The uncertainties assumed for the estimation of the errors have been: 1% for gain calibration, 3% for the instrument line shape, 150 m for elevation pointing, 2K for temperature, and 10% for spectroscopic data (line intensities and broadening coefficients; based on estimates by J.-M. Flaud, personal communication, 2008). The NO noise error is calculated assuming a 2 nW/(cm^{2}cm^{-1}sr) noise-equivalent-spectral-radiance for channel D. Typical values are 15–22% in the non-polar stratosphere and 20–50% elsewhere.

The overall estimated error is dominated by propagation of instrumental noise. Dominating systematic errors are the effect of spectroscopic data uncertainty and temperature. The modeling of the non-LTE populations of the NO vibrational and rotational levels is a major source of the MIPAS nitric oxide systematic error only above the mesopause (due to uncertainties in the atomic oxygen profile). At lower altitudes, these errors are generally below 3% (Funke et al., 2005). Systematic errors due to uncertainties of interfering species are negligible.

Table 9: Summary of main errors in MIPAS nitric oxide vmr. 'NLTE' includes errors due to uncertainties in the collisional rates used in the non-LTE model. 'Total' is the root sum square of all errors. Numbers in brackets refer to polar winter conditions.

Height km	Noise %	Pointing %	Gain %	T %	ILS %	Spectroscopy %	NLTE %	Total %
20	20 (30)	1	1	2	1	2	0	21 (31)
30	20 (30)	4	2	3	2	5	2	22 (32)
40	15 (40)	5	2	5	3	6	2	18 (41)
50	20 (40)	2	1	3	1	5	2	21 (41)
60	50 (50)	1	1	3	1	3	2	50 (50)
70	(40)	2	1	3	1	2	3	(40)
> 80	(30)	2	1	3	1	1	7	(31)

The vertical resolution of MIPAS retrieved nitric oxide abundance is the full width at half maximum of the averaging kernels rows. Average vertical resolution is 4-6 km below 55 km, 6-10 km at 55–65 km, 10–20 km at 65–95 km, and 15–40 km above.

Two additional criteria are further used to filter out the retrieved IMK/IAA data in order to guarantee the quality of the profile. The following results are discarded: 1) results where the diagonal value (for individual profiles) or the mean diagonal value (for averages) of the averaging kernel is less (in absolute value) than 0.03, 2) those corresponding to altitudes not sounded by MIPAS (below the lowermost tangent altitude).

4.2.6 Improvements with respect to previous versions

V5r_NO_m21 nitric oxide baseline is an improvement of the previous V4O_NO_m01 version. The changes from the previous version are:

- Updated L1b database to V5.
- Updated version HITRAN database from the 2004 to the 2008 version.
- Updated versions of temperature (V5r_TLOS_m21), nitric dioxide (V5r_NO2_m21), and ozone (V5r_O3_m22).
- Revised atomic oxygen (SD-WACCM instead of MSIS at 85–135 km).
- Revised regularization scheme for NO and continuum.
- Inclusion of thermospheric horizontal inhomogenities related to the aurora (2D radiative transport).
- Improved NLTE modelling of chemical excitiation by N(^2D) due to improved photochemical modelling (consideration of particle-produced N(^2D) via AIMOS model)

The average impact on the nitric oxide retrieval after those changes are shown in Figs. 10 and 11. The daytime values of the new version are around 5% smaller around the stratospheric peak altitude ($\sim$40 km) and slightly larger below. Up to 15% lower NO abundances occur in the lower mesosphere, particularly at midlatidudes during winter. In the polar winter mesosphere and lower thermosphere, however, the new version has slightly higher NO abundances (up to 10%). On the other hand, lower thermospheric NO at extra-polar latitudes is smaller (10%) than in the previous version. Note that meaningful NO abundances cannot be retrieved in the extra-polar mesosphere (65–90 km) due to the very low sensitivity of the retrievals.

In nighttime conditions, meaningful NO abundances can only be retrieved in the polar winter mesosphere, in the lower thermosphere, and in the polar summer stratosphere close to the terminator. This is caused by

the very low nighttime NO abundances. In general, larger nighttime NO abundances are obtained with the new version (10–40%).

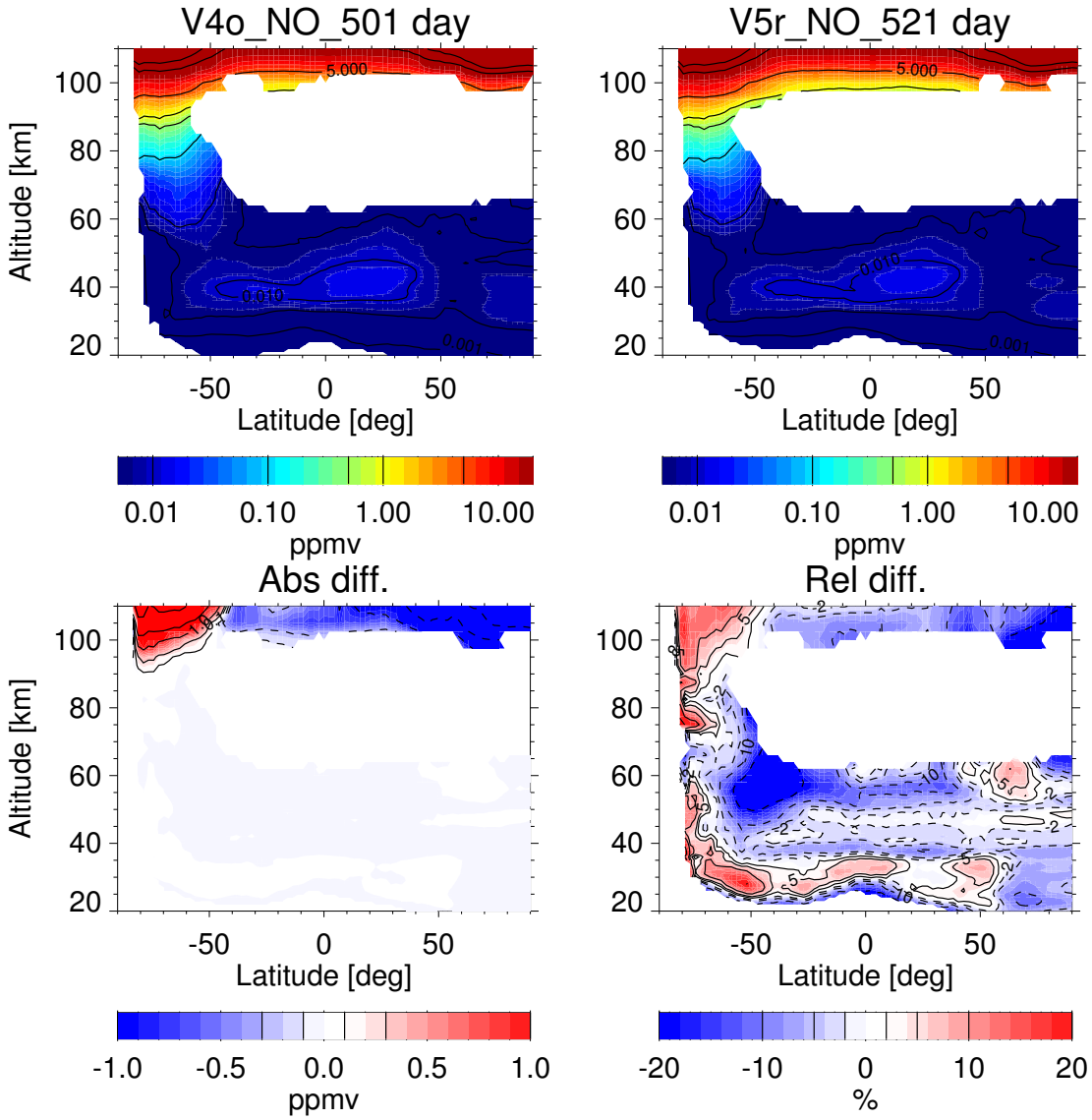

Figure 10: Comparison of NO abundance for daytime conditions (10 am) retrieved in the current V5r_NO_m21 and the previous V4O_NO_m01 versions for 5 June 2009. Lower panels show the V5r_NO_m21–V4O_NO_m01 differences. White areas indicate unavailability of meaningful data.

4.3 OSIRIS (USask)

The OSIRIS optical spectrograph observes scattered sunlight and airglow emission in the near-ultraviolet to near-infrared, from 275-810 nm, with an approximately 1-nm spectral resolution. The optical spectrograph has an approximate 1-km vertical resolution, and measurements are typically vertically separated by 1.5 km. The OSIRIS [NO] retrieval technique, discussed in more detail by Gattinger et al. (2009b, 2010); Sheese et al. (2011a), fits a model spectrum (Becker et al., 1972) to the OSIRIS observations of the NO_2 afterglow continuum over the wavelength range 430-810 nm in order to determine the limb radiance profiles. The definitive measurement of the NO_2 afterglow spectral profile made by Becker et al. (1972) remains unchallenged, as the reaction vessel they used was unique, being 7.5 meters in diameter. They clearly observed a shift of the

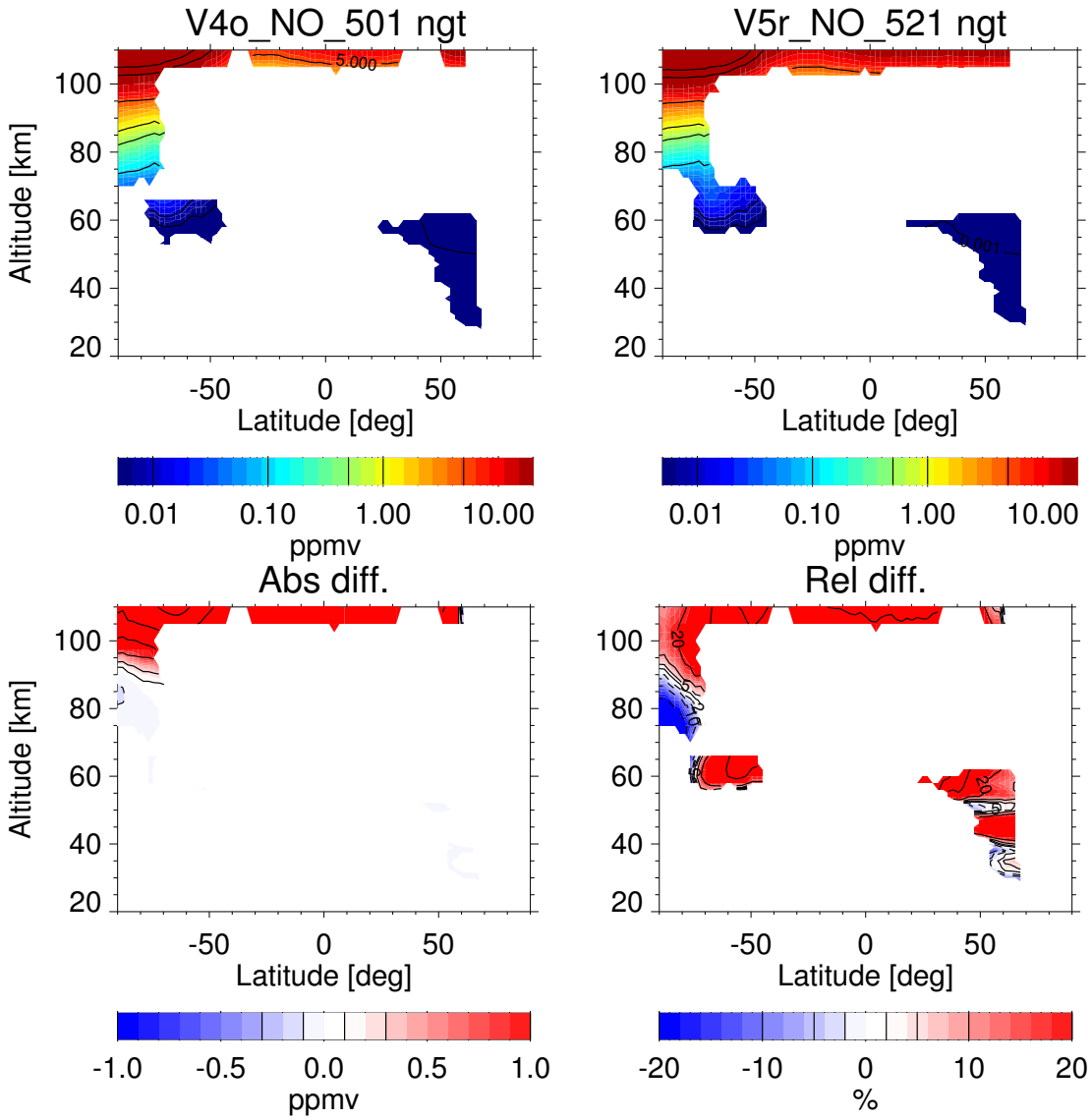

Figure 11: Comparison of NO abundance for nighttime conditions (10 pm) retrieved in the current V5r_NO_m21 and the previous V4O_NO_m01 versions for 5 June 2009. Lower panels show the V5r_NO_m21–V4O_NO_m01 differences. White areas indicate unavailability of meaningful data.

NO_2 continuum spectral peak with vessel pressure, an effect included in the spectral fitting.

Model OH Meinel band and atomic oxygen green line spectra are removed from the OSIRIS observations of the NO_2 continuum. The remaining spectrum is fit to the reference model spectrum to determine the limb brightness at 580 nm, the spectral peak. The limb brightness profile at 580 nm is multiplied by the 450 nm equivalent spectral width of the continuum (Becker et al., 1972) and inverted to determine the total continuum (370-1400 nm) VER profile. Derivations of [NO] from the continuum VER require the reaction coefficient of the bimolecular reaction NO + O $\rightarrow$ NO_2 + $h\nu$ ($k_1 = 4.2 \times 10^{-18}$ cm^3 molecule^{-1} s^{-1}, (Becker et al., 1972)), the reaction coefficient of the termolecular reaction NO + O + M $\rightarrow$ NO_2 + M + $h\nu$ ($k_2 = 15.5 \times 10^{-33} \exp(1160/1.987T)$ cm^6 molecule^{-2} s^{-1}, (Whytock et al., 1976)), and background densities, [M], obtained from a locally run MSIS-E-00 model (Picone et al., 2002a). Retrievals also require accurate atomic oxygen density, [O], and temperature profiles, which are derived from simultaneous common volume OSIRIS measurements of the O_2 A-band at 762 nm (Sheese et al., 2010, 2011b).

An observation (limb radiance) profile **O** is inverted using a form of the tomographic-like algorithm (Sheese

et al., 2011a) to yield an emission intensity profile **V**. In this technique the atmosphere is assumed to be optically thin and is divided into concentric 1-km shells. The iterative tomographic procedure, Eq: 28, is implemented to construct an emission intensity profile **V**,

$$V_j^n = V_j^{n-1} \sum_i \left[\frac{O_i}{\sum_j L_{ij} V_j^{n-1}} \frac{L_{ij}}{\sum_i L_{ij}} \right], \tag{28}$$

where V_j is the calculated emission intensity within the jth atmospheric shell (assumed to be homogeneous), n is the iteration step, L_{ij} is the path-length of the ith observation line-of-sight through the jth atmospheric shell, and the observed signal $O_i = 2\sum_j L_{ij} V_j$.

4.4 SCIAMACHY (KIT)

The retrieval of nitric oxide (NO) number densities from the SCIAMACHY MLT UV spectra is described in detail in Bender et al. (2013). The detailed construction of the forward model air mass matrix for the inversion can be found in Scharringhausen et al. (2008); Langowski et al. (2014). Here we briefly summarise the essential parts of the method.

First we determine the slant column densities of NO (along the line of sight of the instrument) by fitting the calculated NO emissivities to the calibrated measured spectra. From these slant column densities we retrieve the vertical profiles of number densities using a constrained iterative least squares algorithm based on the work by Rodgers (1976). This inversion method is similar to the one used in the retrieval of the MIPAS data products von Clarmann et al. (2003); Funke et al. (2005). For calculating the emissivities we use a high-resolution solar spectrum Chance and Kurucz (2010) and the temperature from the NRLMSISE-00 model Picone et al. (2002c).

4.4.1 NO emissivity

We use the NO gamma bands for the retrieval, similar to previous rocket experiments Cleary (1986); Eparvier and Barth (1992) and space-borne measurements Barth et al. (2003). The NO gamma bands arise when the electronically excited NO molecules relax from the first excited state, $A^2\Sigma^+$, back to the ground state $X^2\Pi$. Both excitation and emission happen in the UV spectral range. Since the molecules are excited by solar UV light, we have to restrict our retrieval to daytime measurements.

The gamma band transitions to the vibrational ground state of the electronic ground state, e.g. the (1, 0), (2, 0) transitions, have high emission rates but the disadvantage of high self-absorption Eparvier and Barth (1992); Stevens (1995). In particular at low altitudes, this self-absorption increases the atmosphere's optical thickness with respect to these bands. As a result the emissivity depends on the total slant column density along the line of sight Eparvier and Barth (1992) leading to non-linearities in the retrieval. However, although the emissivities of the transitions to a different vibrational state, e.g. (0, 1), (0, 2), or (1, 4), are smaller, the self-absorption of these non-resonant bands can be neglected. Therefore, we base our retrieval on the non-resonant vibrational transitions to avoid non-linearities because of self-absorption.

We calculate the emissivities of the NO gamma bands following Stevens and others Eparvier and Barth (1992); Stevens (1995). The vibrational emission rate factors are denoted $g_{v'v''}$ for the transition from the vibrational state v' of the electronically excited state to the vibrational state v'' of the electronic ground state. These vibrational emission rates $g_{v'v''}$ are given by summing over all rotational emission factors $g_{j'j''}$ Eparvier and Barth (1992); Stevens (1995). The individual rotational emission factors are given by:

$$g_{j'j''} = \frac{S(j'j'')}{2j'+1} \omega_{v'v''} \sum_{j=|\Lambda+\Sigma|}^{\infty} \frac{\pi e^2}{mc^2} \lambda_{j'j}^2 \pi F_{j'j} f_{v'0} \frac{S(j'j)}{2j+1} \frac{N_j}{N_0} . \tag{29}$$

Table 10: NO emissivity parameters for the three NO gamma bands used for the retrieval.

	(0, 2)	(1, 4)	(1, 5)
$\lambda_{v'0}$ [nm]	226.5	215.1	215.1
$\lambda_{v'v''}$ [nm]	247.4	255.4	267.4
$f_{v'0}$ [10^{-4}]	3.559	7.010	7.010
$\omega_{v'v''}$	0.2341	0.1115	0.0971

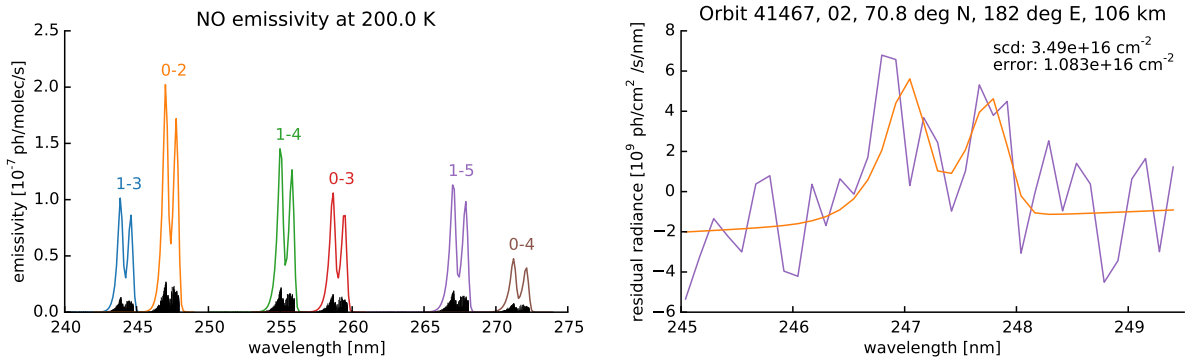

Figure 12: Left panel: Calculated nitric oxide (NO) emission spectrum between 240 nm and 275 nm for an atmospheric temperature of 200 K. The black lines indicate the emissivity of the individual rotational transitions. The coloured lines show the overall emissivity of the vibrational transitions degraded to the SCIAMACHY spectral resolution. Right panel: Spectral fit (orange) of the NO (0, 2) vibrational transition to the SCIAMACHY measured spectrum (purple) at one example tangent point. The example is from 3 February 2010, orbit number 41467 with tangent point coordinates of 71°N, 182°E, 106 km. The numbers indicate the fit result: a slant column density of about 3.5×10^{16} cm^{-2} with an error of about $\pm 1.1 \times 10^{16}$ cm^{-2}.

Here, S are the Hönl–London factors for the rotational transitions Earls (1935); Schadee (1964); Tatum (1967), ω is the branching fraction, λ the transition wavelength, πF is the solar irradiance at that wavelength taken from Chance and Kurucz (2010), and f is the oscillator strength. N_j is the NO population number of the rotational level j and N_0 the population of the vibrational ground state of the electronic ground state Eparvier and Barth (1992). The most important parameters for the emissivity calculation are summarised in Table 10, listing the selected values from Luque and Crosley (1999). The molecular constants can be found in Table 2 of Eparvier and Barth (1992).

The left panel of Fig. 12 shows the calculated emissivities for a selected number of gamma bands in the UV spectral range. We use the three largest ones to retrieve the NO number densities, the (0, 2), the (1, 4), and the (1, 5) transition. The right panel shows the fit of the calculated spectrum of the (0, 2) gamma band to the measured spectrum at one example tangent point. This tangent point is from orbit no. 41467 on 3 February 2010 and lies in the northern polar region at around 106 km. We chose this particular region because it contains measurable amounts of NO such that the emitted intensity is distinctly larger than the background noise.

4.4.2 Forward model

We use a simple description of the measured irradiance I_ν at the frequency ν as the integral over the line of sight:

$$I_\nu = \int_{\text{LOS}} (x(s)\gamma_\nu(s)F_{\nu'}(s) + \sigma_{\text{R}}\varrho_{\text{air}})\,\mathrm{e}^{-\tau_\nu}\mathrm{d}s \tag{30}$$

$$\approx \gamma F \mathrm{e}^{-\tau} \int_{\text{LOS}} x(s)\mathrm{d}s = \gamma F \mathrm{e}^{-\tau} \cdot \varrho_{\text{sc}}\ . \tag{31}$$

In (30), x denotes the number density of the species, γ the emissivity, and $F_{\nu'}$ the solar irradiance at the excitation frequency ν'. We fit the Rayleigh part of the spectrum, $\sigma_{\text{R}}\varrho_{\text{air}}$, as a background signal. We assume that in the spectral range at hand, the signal is attenuated mainly by absorption by air and ozone molecules. Therefore, $\mathrm{e}^{-\tau}$ does not depend on the number density of the species in question and can be integrated separately. The optical depth τ is given by

$$\tau = \sum_i \left[\int_{\text{LOS}} \sigma_i^{\text{abs}}(\nu)\varrho_i^{\text{abs}}(s)\mathrm{d}s + \int_{\text{LFS}} \sigma_i^{\text{abs}}(\nu')\varrho_i^{\text{abs}}(s)\mathrm{d}s \right]\ , \tag{32}$$

where the sum includes all absorbing species. We combine all number-density-independent quantities as indicated on the left side of (31). The final integral over the number density along the line of sight is equal to the slant column density.

4.4.3 Inversion

We invert the forward model by minimising

$$\|\mathbf{K}\vec{x} - \vec{y}\|^2_{S_y^{-1}} + \|\vec{x} - \vec{x}_{\text{a}}\|^2_{S_{\text{a}}^{-1}}\ , \tag{33}$$

where **K** is the Jacobian of the forward model and **S** are the covariance matrices. The subscript "a" denotes the a priori quantities. The construction of the forward model and its Jacobian is described in more detail in Scharringhausen et al. (2008); Langowski et al. (2014) and in Sect. 15.1 of this document.

Doing a 2-D-retrieval, we additionally regularise the solutions with respect to altitude and latitude by introducing regularisation matrices $\mathbf{R}_{\text{alt}}$ and $\mathbf{R}_{\text{lat}}$ Scharringhausen et al. (2008); Bender et al. (2013); Langowski et al. (2014). We then have to minimise

$$\|\mathbf{K}\vec{x} - \vec{y}\|^2_{S_y^{-1}} + \|\vec{x} - \vec{x}_{\text{a}}\|^2_{S_{\text{a}}^{-1}} + \lambda_{\text{alt}}\|\mathbf{R}_{\text{alt}}(\vec{x} - \vec{x}_{\text{a}})\|^2 + \lambda_{\text{lat}}\|\mathbf{R}_{\text{lat}}(\vec{x} - \vec{x}_{\text{a}})\|^2\ . \tag{34}$$

The a priori covariance matrix $\mathbf{S}_{\text{a}}$ is chosen as $\lambda_{\text{a}}\mathbf{I}$ with an empirically tuned parameter λ_{a}. The regularisation matrices $\mathbf{R}_{\text{alt}}$ and $\mathbf{R}_{\text{lat}}$ are finite forward difference matrices with respect to altitude and latitude Steck and von Clarmann (2001); Scharringhausen et al. (2008); Langowski et al. (2014). Carefully tuning λ_{alt} and λ_{lat} prevents large oscillations of the solution in these directions. In particular, we use the following empirical regularisation parameters:

$$\begin{aligned} \lambda_{\text{a}} &= 3 \times 10^{-18}\ , \\ \lambda_{\text{alt}} &= 1 \times 10^{-17}\ , \\ \lambda_{\text{lat}} &= 3 \times 10^{-17}\ . \end{aligned} \tag{35}$$

We minimise (34) with an iterative algorithm Rodgers (1976); von Clarmann et al. (2003); Funke et al. (2005) and the intermediate solutions are

$$\vec{x}_{i+1} = \vec{x}_i + \left(\mathbf{K}^T\mathbf{S}_y^{-1}\mathbf{K} + \mathbf{R}\right)^{-1}\left[\mathbf{K}^T\mathbf{S}_y^{-1}(\vec{y} - \vec{y}_i(\vec{x}_i)) + \mathbf{R}(\vec{x}_{\text{a}} - \vec{x}_i)\right]\ . \tag{36}$$

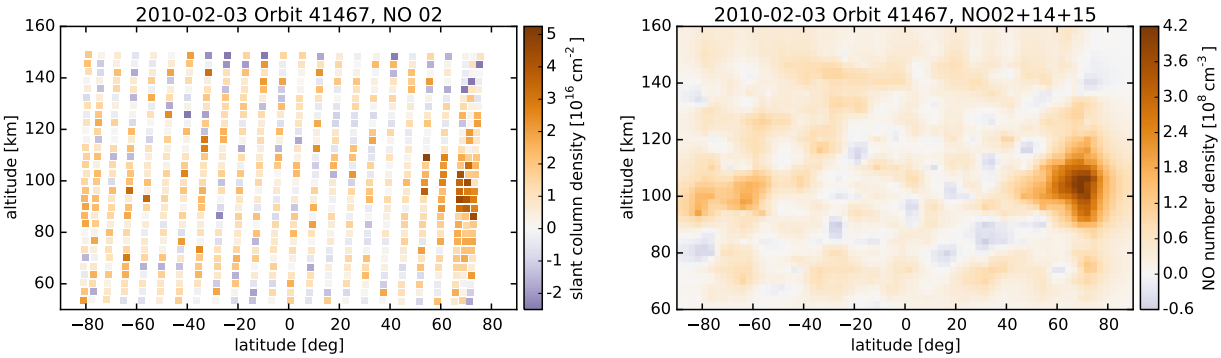

Figure 13: Left panel: Slant column densities from fitting the NO (0, 2) gamma band to the SCIAMACHY spectra from 3 February 2010, orbit no. 41467. Right panel: NO number densities from inverting the slant column densities. Clearly visible are the maxima in the polar regions (60°–80°) between 100 km and 110 km.

We defined the combined regularisation matrix **R** as:

$$\mathbf{R} := \mathbf{S}_a^{-1} + \lambda_{\text{alt}}\mathbf{R}_{\text{alt}}^T\mathbf{R}_{\text{alt}} + \lambda_{\text{lat}}\mathbf{R}_{\text{lat}}^T\mathbf{R}_{\text{lat}} \ . \tag{37}$$

We invert the slant column densities on a 2-D latitude–altitude grid from 90°S to 90°N and from 60 km to 160 km with a grid box size of $2.5^\circ \times 2$ km. Figure 13 demonstrates the method on an example orbit from 3 February 2010 (orbit no. 41467). The left panel shows the slant column densities from fitting the calculated spectra (here only of the NO (0, 2) transition) to the measured spectra from SCIAMACHY. The right panel shows the result from the inversion on the $2.5^\circ \times 2$ km retrieval grid, this time using the three gamma bands (0, 2), (1, 4), and (1, 5) simultaneously.

We assess the vertical resolution with the help of the calculated averaging kernel matrices. The left panel of Fig. 14 shows the (line sums of the) averaging kernel matrix elements for the example orbit (41467 from 3 February 2010 as before). As expected, the largest values occur between 100 km and 120 km. The choice of our retrieval grid, 2 km in altitude compared to about 3 km limb tangent point grid, results in interleaved large and small maxima of the averaging kernels. The right panel of Fig. 14 shows the full widths at half maximum of the averaging kernels where we also marked 10 km altitude resolution. We achieve an altitude resolution of 10 km or better between 70 km and 140 km.

4.4.4 Nominal mode retrieval

We started working on the retrieval of NO from the SCIAMACHY nominal limb scans (-3…93 km). The omission of dedicated tangent points sampling the maximum NO density region between 100 km and 110 km enhances the the retrieved number density values below 90 km. To remedy these enhanced values, we propose to use a non-zero a priori instead of the zero a priori as in the case of the MLT retrieval.

In first tests we compared the MLT results to retrieval results using only tangent points from 50 km to 93 km from the same MLT scans. Our results suggest that using the NOEM model Marsh et al. (2004) as prior input works well, however, it should be scaled by 1/2. We suspect that this factor is necessary because the NOEM model was constructed from SNOE data Barth et al. (2003). Those measurements were carried out at a time of elevated solar activity (1999–2003) compared to the quieter solar times during the SCIAMACHY period (2002–2012).

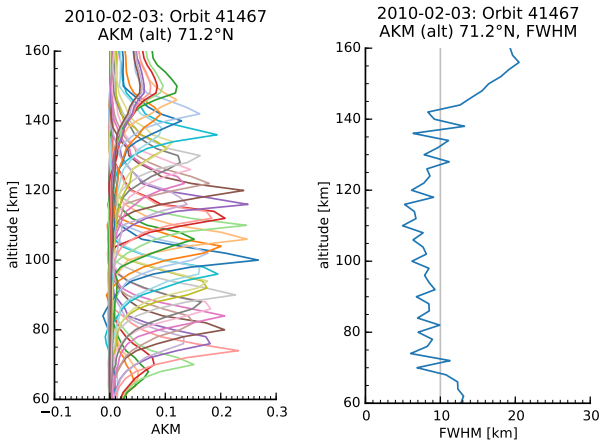

Figure 14: Left panel: Line sums of the averaging kernel matrix for the different altitudes at 71°N. Right panel: Full width at half maximum (FWHM) of the averaging kernel line sums as a measure of the vertical resolution.

4.5 SMR (Chalmers)

Nitric oxide profiles are retrieved using the same approach as previously described for ozone (Sec. 2.6), from the measurement of the thermal emission line centred at 551.7 GHz, which is covered by the frequency mode 21. These measurements are performed on an irregular basis of two observation days in a 14-day cycle (approximately 4 days/month) since 2007. The measurements and retrievals of NO are summarised in Table 11.

N.B.: *The reprocessing of the data set is in progress as part of an ESA project dedicated to it. Specific retrieval settings (in the table), figures showing typical averaging kernels and errors, as well as discussion about the improvements with respect to the previous L2 version (v2.3) will be added when the new product will be available.*

Frequency mode	Molecular transition	Altitude coverage	Temporal coverage	CO		Temperature	
				σ_a	l_c	σ_a	l_c
21	551.7 GHz	?-? km	4(1) days/month	?%/?ppm	? km	?-? K	? km

Table 11: Overview of SMR measurements and retrievals of mesospheric carbon monoxide. See Table 4 for comments on content.

5. Thermospheric Nitric Oxide from MIPAS

MIPAS V5r_NOT_621 thermospheric nitric oxide retrieval is based on constrained inverse modeling of non-LTE limb radiances. That is performed using the IMK/IAA Scientific Processor (von Clarmann et al., 2003, 2009) extended with the non-LTE GRANADA algorithm (Funke et al., 2012), which is able to cope with non-LTE emissions. Funke et al. (2001) describe the particularities of the retrievals under consideration of non-LTE. The basic retrieval equations, the methods for characterization of results through error estimates and vertical and horizontal averaging kernels, the iteration and convergence criteria and the regularization method are described in the Ozone Climate Change Initiative Algorithm Theoretical Basis Document (Ref.: Ozone_cci_ATBD_Phase2_V1_00_01, pp. 60-64, 2014). Thermospheric nitric oxide is reliably retrieved from 100 km to 170 km from MIPAS measurements in the the UA mode. Below 100 km, the profiles are constrained to v5r_NO_621

Table 12: Summary of main errors in MIPAS thermospheric nitric oxide vmr. 'NLTE' includes errors due to uncertainties in the collisional rates used in the non-LTE model. 'Total' is the root sum square of all errors. Numbers in brackets refer to low solar/geomagnetic activity conditions.

Height km	Noise %	Pointing %	Gain %	ILS %	Spectroscopy %	NLTE %	Total %
100	10 (20)	1	1	2	3	5	10 (21)
110	10 (20)	3	1	2	3	5	10 (21)
120	20 (40)	3	1	2	3	20	29 (41)
130	15 (35)	2	1	2	3	30	34 (46)
140	15 (32)	2	1	2	3	50	50 (59)
150	12 (30)	1	1	2	3	50	50 (58)
> 160	12 (25)	1	1	2	3	50	50 (56)

data such that the valid range of this data product spans from 40–170 km. A description of the specifics of the thermospheric nitric oxide retrieval V5r_NOT_621 follows.

5.1 Strategy

Thermospheric nitric oxide is retrieved in the log(vmr) domain from spectral lines covering ro-vibrational emissions of the NO main isotope, covered by the MIPAS band D (1830–1940 cm^{-1}). Retrievals are performed from MIPAS limb emission measured in the UA (40-170 km) mode. Non-LTE is considered as described in Funke et al. (2012) and in Section 4.2 of this document. The retrieval is performed simultaneously to that of V5r_TT_621 thermospheric temperature. The retrieval strategy, the discretization and setup, the microwindows set, the a priori and atmospheric inputs are described in Sec. 14.5 of this document.

5.2 Error budget

The error budget described here considers the propagation of the measurement noise and of the uncertainties of model parameters onto the retrieved nitric oxide abundances. Noise-induced retrieval errors and vertical resolutions are estimated routinely for each individual profile by the retrieval algorithm. Systematic errors related to the mapping of uncertain model parameters are estimated for representative profiles only.

The uncertainties assumed for the estimation of the errors have been: 1% for gain calibration, 3% for the instrument line shape, 150 m for elevation pointing, and 10% for spectroscopic data (line intensities and broadening coefficients; based on estimates by J.-M. Flaud, personal communication, 2008). The thermospheric NO noise error is calculated assuming a 2 nW/($cm^2 cm^{-1} sr$) noise-equivalent-spectral-radiance for channel D. Typical values are 10–30% for high solar/geomagentic activity conditions and 20–50% for low activity conditions.

The overall estimated error is dominated by propagation of instrumental noise. The modeling of the non-LTE populations of the NO vibrational and rotational levels is a major systematic errror source due to uncertainties in the atomic oxygen profile.

The vertical resolution of MIPAS retrieved thermospheric nitric oxide abundance is the full width at half maximum of the averaging kernels rows. Average vertical resolution is 5–15 km for high solar/geomagnetic activity conditions and 10–30 km for low activity.

Results where the diagonal value (for individual profiles) or the mean diagonal value (for averages) of the averaging kernel is less (in absolute value) than 0.03 should be discarded in order to guarantee the quality of the profile.

5.3 Improvements with respect to previous versions

V5r_NOT_621 thermospheric nitric oxide baseline is an improvement of the previous V4O_NOT_601 version. The changes from the previous version are:

- Updated L1b database to V5.
- Updated version HITRAN database from the 2004 to the 2008 version.
- Updated versions of temperature (V5r_T_m21), nitric dioxide (V5r_NO2_m21), and ozone (V5r_O3_m22).
- Revised atomic oxygen (SD-WACCM instead of MSIS below 135 km).
- Revised regularization scheme for NO and kinetic temperature.
- Inclusion of thermospheric horizontal inhomogenities related to the aurora (2D radiative transport).
- Improved NLTE modelling of chemical excitiation by N(^2D) due to improved photochemical modelling (consideration of particle-produced N(^2D) via AIMOS model)

The average impact on the thermospheric nitric oxide retrieval after those changes are shown in Figs. 15 and 16. The volume mixing ratios of the new version are generally larger by 10-50%. Expressed in number densities, however, smaller values are found in the new version around 120 km (not shown).

6. Nitrous oxide

6.1 ACE-FTS (UoT)

Nitrous oxide profiles are retrieved using the same approach as described in Sect. 2.1 for ozone. The retrievals are performed between altitudes of 5 and 95 km using 52 microwindows between 1134 and 1278 cm^{-1} and between 2201 and 2242 cm^{-1}. In the mesosphere, retrievals account for CO and CO_2 isotopologues as interfering species. Ten additional microwindows are included in the retrieval to improve the results for interfering species and isotopologues below 35 km (829, 1228, 1354, 1950, 1978, 2140, 2195, 2525, 2566, and 2623 cm^{-1}).

6.2 MIPAS (KIT/IAA)

The MIPAS V5r_N2O_m21 nitrous oxide retrieval baseline is based on the IMK/IAA algorithm (von Clarmann et al. (2003, 2009)) in its extended version, considering non-Local Thermodynamic Equilibrium (non-LTE) emissions through the calculation of non-LTE vibrational levels populations with the GRANADA model (Funke et al., 2012). The retrieval is based on constrained inverse modeling of limb radiances. The basic retrieval equations, the methods for characterization of results through error estimates and vertical and horizontal averaging kernels, the iteration and convergence criteria and the regularization method are described in the Ozone Climate Change Initiative Algorithm Theoretical Basis Document (Ref.: Ozone_cci_ATBD_Phase2_V1_00_01, pp. 60-64, 2014). We give here important details specific of the N_2O retrieval. N_2O can be reliably retrieved up to 55 km under quiescent conditions and up to 70 km under perturbed conditions (like solar proton events).

6.2.1 Strategy

Nitrous oxide is retrieved from the 7.8 μm spectral region, covered by the MIPAS band B (1215 cm^{-1}–1500 cm^{-1}), using ro-vibrational emissions in the v_1 band of the N_2O main isotope. Non-LTE is considered as described in Funke et al. (2012). The retrieval is performed simultaneously to that of V5r_CH4_m21 methane. The retrieval strategy, the discretization and setup, the microwindows set, the a priori and atmospheric inputs are described in Sec. 10.2 of this document.

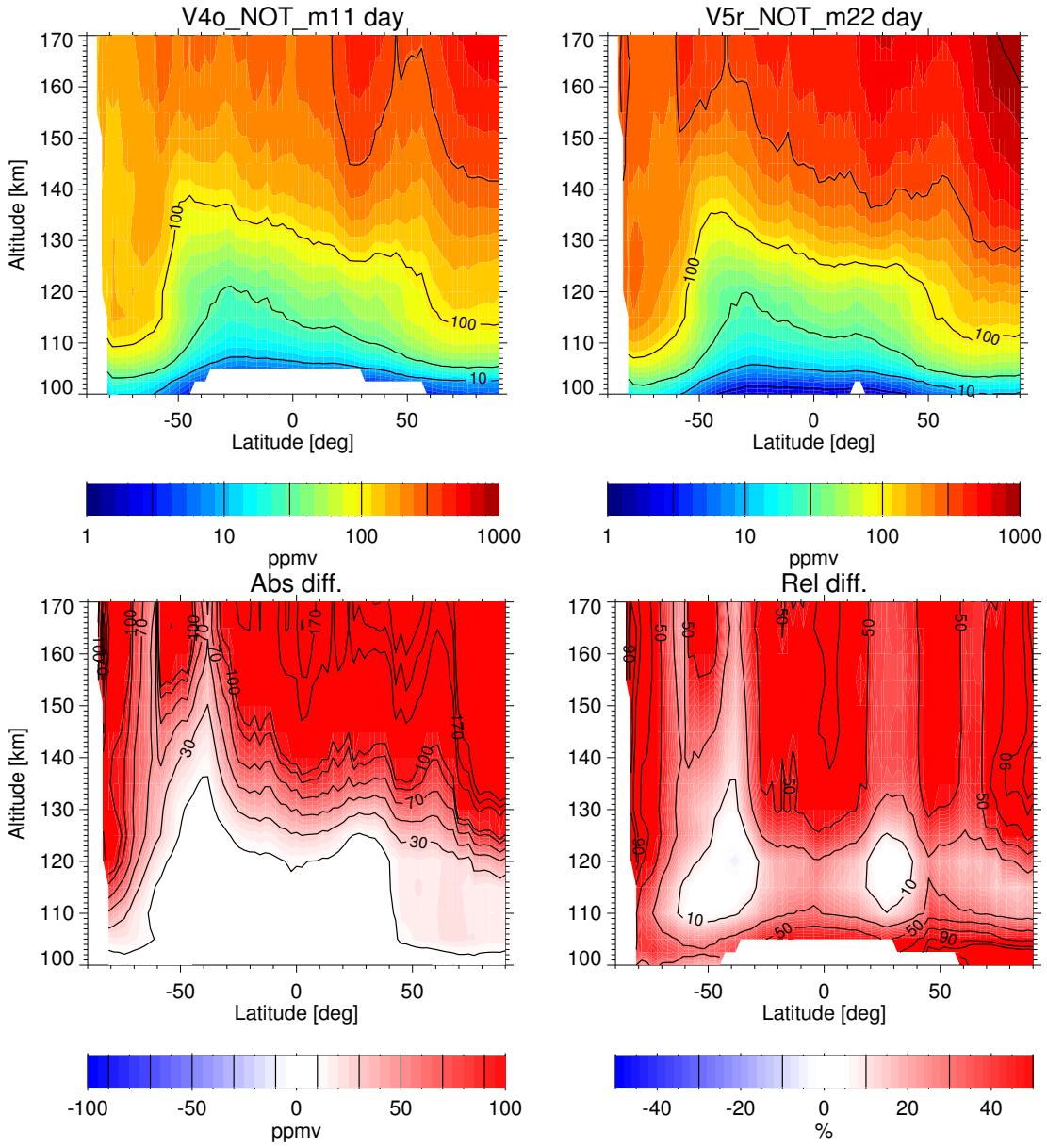

Figure 15: Comparison of thermospheric NO abundance for daytime conditions (10 am) retrieved in the current V5r_NOT_621 and the previous V4O_NOT_601 versions for 5 June 2009. Lower panels show the V5r_NOT_621–V4O_NOT_601 differences. White areas indicate unavailability of meaningful data.

6.2.2 Error budget

The error budget includes the mapping of the measurement noise and the propagation of parameter errors on the retrieved methane abundances. Table 13 summarizes the estimated systematic and random errors in MIPAS retrieved nitrous oxide abundance for unperturbed conditions (partially based on von Clarmann et al. (2009)).

The errors related to the mapping of uncertain model parameters are estimated for representative profiles only. As described in the MIPAS methane retrieval section, the following errors were assumed for their estimation: 1% for gain calibration uncertainty, 3% uncertainty of the instrument line shape in terms of linear loss of modulation efficiency toward the maximum optical path difference, 150 m elevation pointing uncer-

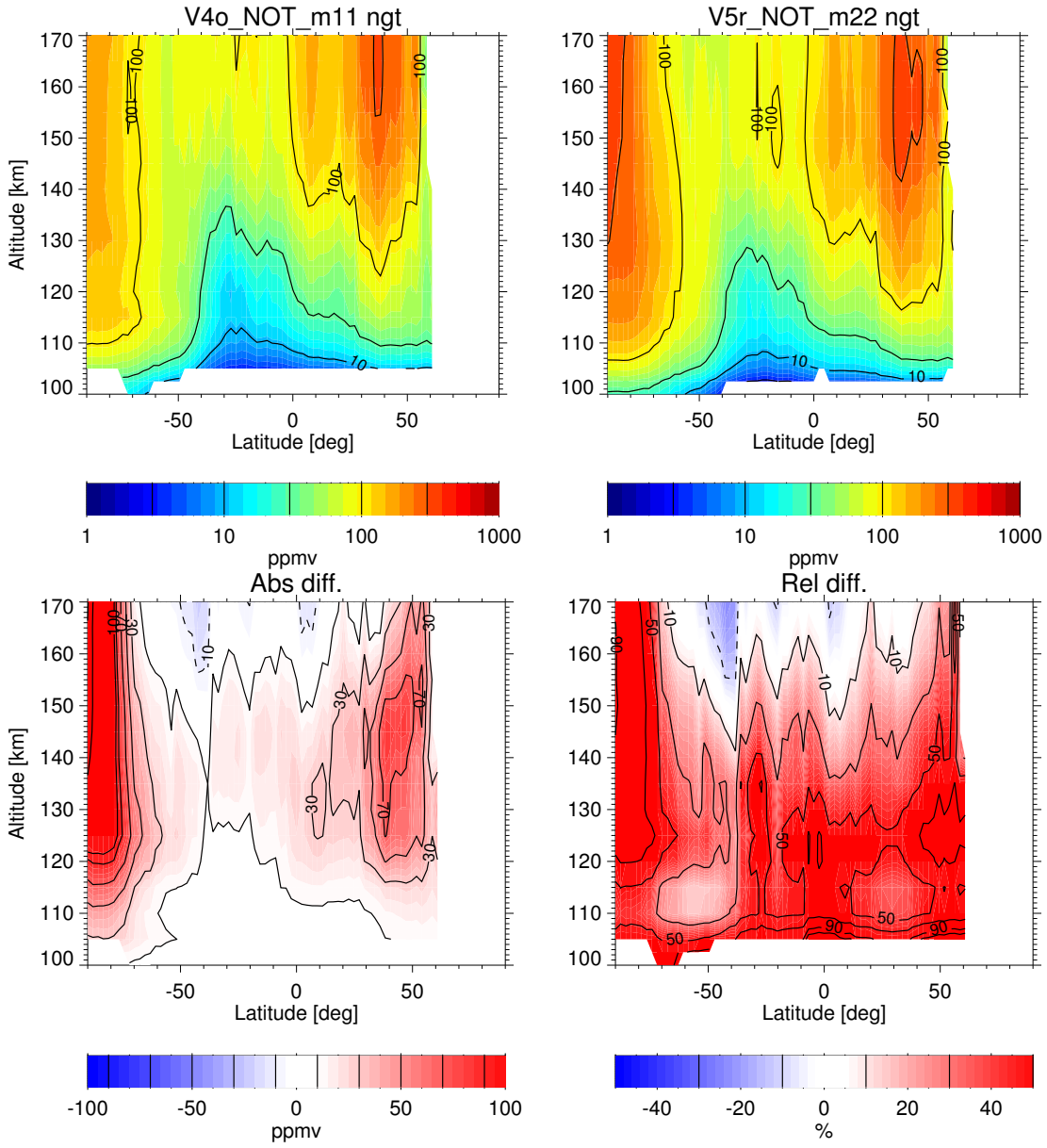

Figure 16: Comparison of thermospheric NO abundance for nighttime conditions (10 pm) retrieved in the current V5r_NOT_621 and the previous V4O_NOT_601 versions for 5 June 2009. Lower panels show the V5r_NOT_621–V4O_NOT_601 differences. White areas indicate unavailability of meaningful data.

tainty and 2K temperature uncertainty. The uncertainties in spectroscopic N_2O data was assumed based on estimates by J.-M. Flaud (personal communication, 2008) and taken as 4–7% uncertainty of the line intensities and broadening coefficients. Overall they infer up to 5% N_2O abundance errors below 40 km, mainly due to uncertainties in the spectroscopic data, and less than 5% above 40 km. Errors due to uncertainties in the non-LTE parameters are negligible below 55 km, altitude to which N_2O can be retrieved from MIPAS measurements.

The noise errors are calculated assuming an wavelength-dependent average of 8 nW/(cm^{2}cm^{-1}sr) noise-equivalent-spectral-radiance (corresponding to MIPAS channel B). Noise-induced retrieval errors and vertical resolutions are estimated routinely for each individual profile by the retrieval algorithm. Typical values are

Table 13: Summary of main systematic and random errors in MIPAS nitrous oxide under quiescent conditions. 'Total' is the root sum square of all errors.

Height	Noise	Pointing	Gain	T	ILS	Spectroscopy	Total error
km	%	%	%	%	%	%	%
20	2	4	0.3	0.6	0.0	11	12
30	5	4	0.1	1.3	3	10	13
40	10	4	2	2	3	6	13
50	30	2	0.3	1	0.9	4.0	30
70	100(20*)	2	0.3	1	0.9	4.0	100(20*)

(*) Noise error during the perturbed conditions of the October 2003 solar proton event (Funke et al., 2011)).

less than 10% below 50 km at low latitudes, below 45 km in the polar summer and 25 km in the polar winter. Noise error rapidly increase above those altitudes, accompanied with the very low nitrous oxide amounts.

The vertical resolution of the N_2O retrieval is the full width at half maximum of the averaging kernels rows. Typical values of average vertical resolution are 3-4 km below 45 km and 6 km at 50-70 km.

Two criteria are further usually applied to the retrieved IMK/IAA data in order to guarantee the quality of the profile. Results which are considered non-trustful are: 1) those where the diagonal value (for individual profiles) or the mean diagonal value (for averages) of the averaging kernel is less (in absolute value) than 0.03. 2) those related to parts of the atmosphere non-sensed by MIPAS (i.e. below the lowermost used tangent altitude) are considered non-trustful.

6.2.3 Updates

The updates with respect to the previous version V4O_N2O_m01 are:

- Updated L1b database to V5.
- Updated version of the HITRAN database.
- Updated regularization (equal to NOM retrieval).
- Updated versions of temperature (V5r_T_m21) as inputs.

These updates resulted in changes generally smaller than 5% in the regions where the N_2O abundance is larger than 10 ppbv (see Fig.17). The noise errors and the vertical resolution barely varied.

7. Nitrogen dioxide

7.1 GOMOS (FMI)

The mesospheric amounts of NO_2 are retrieved from GOMOS stellar occultation measurements using the same approach as for ozone (see Sect. 2.2). The unphysical oscillations discussed in Sect. 2.2 are especially disturbing for NO_2 profiles. Oscillations are attenuated by the modelling covariance and the Tikhonov regularisation discussed above, but for NO_2 it was also decided to exploit a so-called Global DOAS Iterative (GDI) retrieval in the spectral inversion. In the GDI a species is artificially separated into two virtual species X_S and X_D with their respective cross-sections:

$$\sigma_S(\lambda) + \sigma_D(\lambda) = \sigma(\lambda). \tag{38}$$

The spectral inversion is performed in two phases. The first Levenberg-Marquardt fit is applied with X_S=X_0 and X_D as a free parameter together with all other species that we want to retrieve. The fit gives the first value $X_D^{(1)}$. The second fit is applied with X_S=$X_D^{(1)}$. The second value $X_D^{(2)}$ is obtained. The process is iterated until the maximum number of iterations is performed or until a given convergence criterion is reached.

The NO_2 cross section is merged from several laboratory measurements. In the wavelength region 235-500 nm data are from Merienne et al., 1995 and Coquart et al., 1995, in 500-667 nm from Vandaele et al., 1998, and in $\lambda > 667$ from Burrows et al., 1998. Detailed references and data can be found in Keller-Rudek et al. (2013) and additional GOMOS specific details in ATBD.

GOMOS NO_2 retrievals produce acceptable results in the altitude range 20–50 km. During strong particle precipitation events in the polar regions the maximum altitude can reach 70 km. The target resolution for NO_2 is 4 km.

7.2 MIPAS (KIT/IAA)

MIPAS V5r_NO2_m21 nitric dioxide retrieval is based on constrained inverse modeling of non-LTE limb radiances. That is performed using the IMK/IAA Scientific Processor (von Clarmann et al., 2003, 2009) extended with the non-LTE GRANADA algorithm (Funke et al., 2012), which is able to cope with non-LTE emissions. The basic retrieval equations, the methods for characterization of results through error estimates and vertical and horizontal averaging kernels, the iteration and convergence criteria and the regularization method are described in the Ozone Climate Change Initiative Algorithm Theoretical Basis Document (Ref.: Ozone_cci_ATBD_Phase2_V1 _00_01, pp. 60-64, 2014). MIPAS nitric dioxide is reliably retrieved from 20 to 65 km (80 km in polar winter conditions). A description of the specifics of the nitric dioxide retrieval V5r_NO2_m21 follows.

7.2.1 Strategy

Nitric dioxide is retrieved in the log(vmr) domain from spectral lines covering ro-vibrational emissions of the NO_2 main isotope. These have been selected from a broad spectral region, covered by the MIPAS band C (1590–1640 cm^{-1}). The V5r_NO2_m21 retrieval strategy is an update and extension of the retrieval of nitric dioxide from the MIPAS NOM measurements (6-68 km) (Funke et al., 2005) with consideration of non-LTE emission. Retrievals are performed from MIPAS limb emission measured in the MA (20-102 km), NLC (40-102 km) and UA (40-170 km) modes. Calibrated spectra are as supplied by ESA in version 5.02/5.06 (Raspollini et al. (2010) and references therein). The retrieval is performed after a spectral shift retrieval and the non-LTE retrievals of temperature and abundances of ozone, water vapour, nitrous oxide and methane. The IMK/IAA processor simultaneously retrieves microwindow-dependent continuum radiation and zero level calibration corrections (the latter, assumed constant with altitude).

Photo-chemically induced horizontal inhomogenities along the instrument's line of sight are taken into account for scans close to the terminator (solar zenith angles of 80–100°) by means of a photochemical model (Funke et al., 2012) which constrains the NO_x partitioning, $Q(s)$ =[NO(s)]/[$NO_2(s)$], along the optical path, s, of the instrument depending on the solar zenith angle at s. Assuming a homogeneous horizontal distribution of NO_x, the NO and NO_2 abundances at the optical path segment s passing a given altitude level are scaled with respect to the actual abundance at the center of the scan s_0 and the same altitude level as

$$\frac{[NO_2(s)]}{[NO_2(s_0)]} = \frac{1+Q(s_0)}{1+Q(s)} \tag{39}$$

within the forward calculations of the retrieval.

Horizontal NO_x gradients in the latitudinal and longitudinal directions (acting in a multiplicative sense to the constrained NO_x partitioning along the line of sight) are fitted jointly with the NO_2 vmr.

7.2.2 Discretization and setup

The retrievals are performed from the surface to 120 km over a discrete altitude grid of 1 km up to 50 km, 2 km at 50-70 km, 2.5 km at 70-80 km and 5 km at 80-120 km. The selected grid provides balanced accuracy and efficiency. The forward calculations are performed using that same grid. The over-sampled retrieval grid, finer than MIPAS vertical sampling (approximately 3 km), makes the use of a regularization mandatory in order to obtain stable solutions. A Tikhonov-type smoothing constraint is used for NO_2. Horizontal NO_x gradients are regularized by a strong diagonal constraint towards a zero a priori.

The numerical integration of the signal over the 3 km field of view is done using seven pencil beams. The selected width of the integration window (apodized instrument line shape function) has been chosen to comply with an apodization accuracy of 0.1%.

7.2.3 Microwindows

The retrievals are performed from selected spectral regions (micro-windows) which vary with tangent altitudes in order to optimize computation time and minimize systematic errors (von Clarmann and Echle, 1998). The microwindows used in the nitric dioxide retrieval are listed in Table 14. These height dependent combinations of micro-windows were selected with a trade-off between computation time and total retrieval error. They are a vertical extension of the initial set of microwindows used for the MIPAS nitric dioxide NOM retrieval (z$<$70 km) (Funke et al., 2005), covering $NO_2(001\rightarrow000)$ emissions in the 1590–1640 cm^{-1} range.

Table 14: Microwindows and number of internal sub-microwindows at each tangent altitude used in MIPAS V5r_NO2_m21 nitric dioxide retrieval. Altitude levels should be read vertically.

Microwindow cm^{-1}	Altitude km																												
	18	21	24	27	30	33	36	39	42	45	48	51	54	57	60	63	66	69	72	75	78	81	84	87	90	93	96	99	102
(1590.1250, 1590.2500)	0	0	0	0	0	0	0	0	0	0	0	1	1	1	1	1	1	1	1	1	1	1	1	1	1	1	1	1	1
(1590.5000, 1590.7500)	0	0	0	0	0	0	0	0	0	1	1	0	0	1	1	1	1	1	1	1	1	1	1	1	1	1	1	1	1
(1597.5000, 1600.4375)	0	0	0	0	0	0	0	0	0	1	1	1	1	1	1	1	1	1	1	1	1	1	1	1	1	1	1	1	1
(1600.5000, 1601.3750)	1	1	1	0	0	0	2	1	1	1	1	1	1	1	1	1	1	1	1	1	1	1	1	1	1	1	1	1	1
(1601.5000, 1602.6875)	0	0	0	0	0	0	0	0	0	1	1	2	2	2	2	2	2	2	2	2	2	2	2	2	2	2	2	2	2
(1602.7500, 1605.7500)	2	2	2	2	2	0	0	0	2	1	1	1	1	1	1	1	1	1	1	1	1	1	1	1	1	1	1	1	1
(1608.6875, 1609.1250)	0	0	0	0	0	2	0	1	1	1	1	1	1	1	1	1	1	1	1	1	1	1	1	1	1	1	1	1	1
(1615.7500, 1616.3750)	1	1	1	1	1	1	1	1	1	1	1	0	0	1	1	1	1	1	1	1	1	1	1	1	1	1	1	1	1
(1616.5000, 1616.6875)	0	1	1	0	1	1	0	0	0	0	0	0	0	1	1	1	1	1	1	1	1	1	1	1	1	1	1	1	1
(1624.2500, 1627.2500)	2	0	0	0	0	0	0	0	0	2	2	1	1	2	2	2	2	2	2	2	2	2	2	2	2	2	2	2	2
(1627.2500, 1627.8125)	1	0	0	0	0	0	1	1	1	1	1	1	1	1	1	1	1	1	1	1	1	1	1	1	1	1	1	1	1
(1630.9375, 1631.0625)	0	0	0	0	0	0	0	0	0	1	1	1	1	1	1	1	1	1	1	1	1	1	1	1	1	1	1	1	1
(1634.6250, 1634.8750)	1	0	0	0	0	0	0	0	0	1	1	1	1	1	1	1	1	1	1	1	1	1	1	1	1	1	1	1	1
(1635.4375, 1635.6250)	1	1	1	1	1	1	1	1	1	1	1	1	1	1	1	1	1	1	1	1	1	1	1	1	1	1	1	1	1

7.2.4 A priori and atmospheric inputs

MIPAS V5r_NO2_m21 nitric dioxide retrieval setup uses the following inputs:

- A priori is computed by means of a photochemical model (Funke et al., 2012) under consideration of NO_x from a MIPAS dedicated climatology (Funke et al., 2012).
- Pressure, line of sight information, temperature and temperature horizontal gradients from MIPAS retrieval version V5r_T_m21, as well as water vapor from MIPAS V5r_H2O_m22 are used.
- Spectroscopic data from HITRAN 2008 (Rothman et al., 2009).

Several inputs are needed for the calculation of the non-LTE populations of the vibrationally excited emitting molecules by GRANADA. Funke et al. (2012) provide information on the effect of each input on the NO_2 levels. The non-LTE model inputs used in V5r_NO2_m22 retrievals are:

- Ozone from the previously retrieved ozone in its version V5r_O3_m22.
- Atomic oxygen concentration derived from the retrieved ozone (V5r_O3_m22) below 95 km and from WACCM in its specified dynamics (SD) configuration (Garcia et al., 2007) above.
- Non-LTE collisional scheme and rate constants as in Funke et al. (2012).

Forward model calculations along the line of sight are done considering non-LTE horizontal gradient corrections. These account for changes in the populations of the emitting levels along the line of sight due to kinetic temperature variations.

7.2.5 Error budget

The error budget described here considers the propagation of the measurement noise and of the uncertainties of model parameters onto the retrieved nitric dioxide abundances. Noise-induced retrieval errors and vertical resolutions are estimated routinely for each individual profile by the retrieval algorithm. Systematic errors related to the mapping of uncertain model parameters are estimated for representative profiles only. Table 15 summarizes the estimated errors in MIPAS retrieved nitric dioxide vmr.

The uncertainties assumed for the estimation of the errors have been: 1% for gain calibration, 3% for the instrument line shape, 150 m for elevation pointing, 2K for temperature, and 10% for spectroscopic data (line intensities and broadening coefficients; based on estimates by J.-M. Flaud, personal communication, 2008).

The modeling of the non-LTE populations of the 6.2 μm NO_2 vibrational levels is an important source of the MIPAS nitric dioxide systematic error above the stratopause. Non-LTE errors are dominated by the uncertainties in the collisional rates used in the non-LTE model. The estimations provided here assume the following uncertainties: 100% in the NO_2-M quenching rate and 15% in the efficiency of NO_2 photochemical excitation due to NO+O_3.

The NO_2 noise error is calculated assuming a 3.2 nW/(cm^{2}cm^{-1}sr) noise-equivalent-spectral-radiance for channel C. Typical values are 10% in the stratosphere and polar winter mesosphere, and 20–30% elsewhere.

The overall estimated error is dominated by propagation of instrumental noise. Dominating systematic errors are the effect of spectroscopic data uncertainty and temperature below 50 km and by the non-LTE above 50 km.

The vertical resolution of MIPAS retrieved nitric dioxide abundance is the full width at half maximum of the averaging kernels rows. Average vertical resolution (except polar winter) is 3-4 km below 50 km, 4-6 km at 50–60 km and 6–8 km above. For polar winter conditions, vertical resolution is 5-8 km below 30 km and 3-5 km at 30-80 km.

Two additional criteria are further used to filter out the retrieved IMK/IAA data in order to guarantee the quality of the profile. The following results are discarded: 1) results where the diagonal value (for individual profiles) or the mean diagonal value (for averages) of the averaging kernel is less (in absolute value) than 0.03, 2) those corresponding to altitudes not sounded by MIPAS (below the lowermost tangent altitude).

Table 15: Summary of main errors in MIPAS nitric dioxide vmr. 'NLTE' includes errors due to uncertainties in the collisional rates used in the non-LTE model. 'IS' includes errors due to interfering emissions of other molecules (not retrieved by MIPAS). 'Total' is the root sum square of all errors. Numbers in brackets refer to polar winter conditions.

Height km	Noise %	IS %	Pointing %	Gain %	T %	ILS %	Spectroscopy %	NLTE %	Total %
20	20 (50)	1	1	2	2	1	2	0	20 (50)
30	5 (10)	2	3	2	3	2	3	0	8 (12)
40	5 (7)	1	3	1	5	3	8	0	11 (12)
50	15 (5)	1	2	1	3	1	2	5	16 (8)
60	20 (10)	1	2	1	3	1	1	5	21 (12)
70	(10)	1	2	1	3	1	1	5	(12)
80	(30)	1	2	1	3	1	1	5	(31)

7.2.6 Improvements with respect to previous versions

V5r_NO2_m21 nitric dioxide baseline is an improvement of the previous V4O_NO2_m01 version. The changes from the previous version are:

- Updated L1b database to V5.
- Updated version HITRAN database from the 2004 to the 2008 version.
- Updated versions of temperature (V5r_T_m21) and ozone (V5r_O3_m22).
- Revised regularization scheme.
- Inclusion of non-LTE horizontal gradient corrections.

The average impact on the nitric dioxide retrieval after those changes are shown in Figs. 18 and 19. The values for the new version are around 5-15% larger below 30 km, and slightly smaller in about 2-5% at 35-50 km. In the polar night, at 50-70 km, the new version is about 5-10% smaller.

8. Hydroxyl from GOMOS (LATMOS)

GOMOS observes O_2 and H_2O in two dedicated spectrometers SPB1 and SPB2 centred around 765 and 940 nm. These spectral bands contain airglow emission from OH Meinel bands that are visible in dark limb GOMOS spectra. Airglow observations can be useful to better understand atmospheric phenomena that remain in question, such as: the solar forcing on the middle atmosphere through the NOx chemistry. The signal is relatively low and it requires very careful dark charge and stray-light corrections and a filtering of spectra affected by aurorae at high latitude. A preliminary analysis has been made by Bellisario et al. (2014). The authors demonstrated the method and provided a first climatology. A full climatology of OH limb emission will be built covering the period 2002-2012 corresponding almost to a full solar cycle. The signal is too low to obtain OH profiles at single occultation level. Only monthly mean profiles averaged ij specified latitude bands will be created (Level 3 data).

For this task the following steps are done:

1. Extraction of all spectra in the upper and lower background bands of SPB2 for tangent altitudes between 80 and 100 km using GOMOS IPF 6.01 Level1b data. All occultations except bright occultations

are extracted. Check if presence of stray-light variable with altitude flag + aurorae flag. A reference spectrum without OH emission is created by averaging spectra at high altitude (>110km).

2. Independently for each background band (lower and upper) a summation of spectra is made in predefined latitude, longitude, time and altitude ranges:
   - Latitude bands: 10° wide from 90°S to 90°N
   - Time: monthly mean average
   - Altitude layers: 2 km wide from 80 to 100 km

   Before the spectra are summed, each spectrum is corrected by substraction of the high altitude spectrum.

   Filtering: stray-light flagged and aurorae flagged data are discarded.
3. Determination of the baseline in summed spectra using pixels outside of OH emission bands.
4. For each summed spectrum the integration of the OH signal is made over all pixels containing OH emission (after removal of the baseline).

The results will be stored in NetCDF format and compared to published observations and results of chemistry-transport models.

GOMOS spectra extracted from IPFv6 GOMOS products are provided with associated error bars for each spectral pixel. These error bars do not take into account the error that is made during the estimation of the dark current. Therefore these error bars can be very under-estimated compared to the true error on the signal, especially in cases when the SNR is low, which is the case for the faint OH emission signal recorded in the GOMOS background bands. We thus have decided NOT to use the GOMOS product error bars in the frame of the OH/Mesospheo work. Instead, we build a new error bar for each spectrum. This new error bar is computed as the standard deviation of the signal on about 150 spectral pixels in which we are sure there is no emission line. This error bar is the same for all spectral pixels of one spectra. Then when building an averaged spectrum in a latitude/longitude/time bin, we perform a mean of all spectra in this bin, weighted by the new error bar of each spectra. This binned averaged spectrum is computed as well as its associated error bar (still the same for each spectral pixel). At last, when the binned averaged spectrum is spectrally integrated in order to compute the OH emission photon flux (Rayleigh), the error bars are propagated in order to compute an associated error bar to the OH emission photon flux.

9. Water vapour

9.1 ACE-FTS (UoT)

Water vapour profiles are retrieved using the same approach as described in Sect. 2.1 for ozone. The retrievals are performed between altitudes of 5 and 101 km using 48 microwindows between 937 to 2993 cm^{-1}, with no interfering species in the mesosphere and above. An additional six microwindows are included within this range to improve the results for interfering species and isotopologues at low altitudes.

9.2 MIPAS (KIT/IAA)

MIPAS V5r_H2O_m22 water vapor retrieval is based on constrained inverse modeling of non-LTE limb radiances. That is performed using the IMK/IAA Scientific Processor (von Clarmann et al., 2003, 2009) extended with the non-LTE GRANADA algorithm (Funke et al., 2012), which is able to cope with non-LTE emissions. Funke et al. (2001) describe the particularities of the retrievals under consideration of non-LTE. The basic

retrieval equations, the methods for characterization of results through error estimates and vertical and horizontal averaging kernels, the iteration and convergence criteria and the regularization method are described in the Ozone Climate Change Initiative Algorithm Theoretical Basis Document (Ref.: Ozone_cci_ATBD_Phase2_V1_00_01, pp. 60-64, 2014). Water vapor is reliably retrieved from 20 km from MIPAS measurements in the MA mode and 40 km in the UA and NLC mode up to 90 km. A description of the specifics of the water vapor retrieval V5r_H2O_m22 follows.

9.2.1 Strategy

Water vapor is retrieved in the log(vmr) domain from spectral lines covering ro-vibrational emissions of the H_2O main isotope. These have been selected from a broad spectral region, covered by the MIPAS band A (685–970 cm^{-1}), band B (1215–1500 cm^{-1}) and band C (1570–1750 cm^{-1}). The V5r_H2O_m22 retrieval strategy is an extension of the retrieval of water vapor from the MIPAS NOM measurements (6-68 km) (Milz et al., 2009; von Clarmann et al., 2009) with consideration of non-LTE emission and extension of the microwindow set. Retrievals are performed from MIPAS limb emission measured in the MA (20-102 km), NLC (40-102 km) and UA (40-170 km) modes. Calibrated spectra are as supplied by ESA in version 5.02/5.06 (Raspollini et al. (2010) and references therein). The retrieval is performed after a spectral shift retrieval and the non-LTE retrievals of temperature and ozone abundance. The IMK/IAA processor simultaneously retrieves microwindow- and altitude-dependent continuum radiation and zero level calibration corrections (the latter, assumed constant with altitude). Nitrogen dioxide vmr is also jointly fitted in the log domain but not used.

9.2.2 Discretization and setup

The retrievals are performed from the surface to 120 km over a discrete altitude grid of 1 km up to 70 km, 2 km at 70-90 km, 2.5 km at 90-95 km and 5 km at 95-120 km. The selected grid provides balanced accuracy and efficiency. The forward calculations are performed using that same grid. The over-sampled retrieval grid, finer than MIPAS vertical sampling (approximately 3 km), makes the use of a regularization mandatory in order to obtain stable solutions.

The numerical integration of the signal over the 3 km field of view is done using seven pencil beams. The selected width of the integration window (apodized instrument line shape function) avoids channel border effects.

9.2.3 Microwindows

The retrievals are performed from selected spectral regions (micro-windows) which vary with tangent altitudes in order to optimize computation time and minimize systematic errors (von Clarmann and Echle, 1998). The microwindows used in the water vapor retrieval are listed in Table 16. These height dependent combinations of micro-windows were selected with a trade-off between computation time and total retrieval error. They are an extension of the initial set of microwindows used for the MIPAS water vapor NOM retrieval ($z<70$ km) (Milz et al., 2009; von Clarmann et al., 2009). The new microwindows are used in the mesosphere and lower thermosphere and cover non-LTE emission of H_2O. They are centered on first hot band emission lines, very strong, with enhanced non-LTE emission around 70-75 km and affected by non-LTE processes in a different way to the fundamental band lines. Strong fundamental band lines, also deviated from LTE conditions and more sensitive to the rarefied upper atmosphere, are also included. Additionally, one microwindow covering a strong emission line of NO_2 is used in order to avoid instabilities of the UA and NLC retrievals (starting at 40 km).

9.2.4 A priori and atmospheric inputs

MIPAS V5r_H2O_m22 water vapor retrieval setup uses the following inputs:

Table 16: Microwindows used in MIPAS V5r_H2O_m22 water vapor retrieval. Altitude levels should be read vertically.

Microwindow cm^{-1}	Altitude km																													
																														1	1
	1	1	2	2	2	3	3	3	3	4	4	4	5	5	5	6	6	6	6	7	7	7	8	8	8	9	9	9	9	0	0
	5	8	1	4	7	0	3	6	9	2	5	8	1	4	7	0	3	6	9	2	5	8	1	4	7	0	3	6	9	2	5
(795.7500, 796.0000)	1	1	1	1	1	1	1	1	1	1	1	1	1	1	1	1	1	1	1	1	1	1	1	1	1	1	1	1	1	1	1
(808.1875, 808.7500)	1	1	1	1	1	1	1	1	1	1	1	1	1	1	1	1	1	1	1	1	1	1	1	1	1	1	1	1	1	1	1
(825.1250, 825.4375)	1	1	1	1	1	1	1	1	1	1	1	1	1	1	1	1	1	1	1	1	1	1	1	1	1	1	1	1	1	1	1
(827.3750, 827.8125)	1	1	1	1	1	1	1	1	1	1	1	1	1	1	1	1	1	1	1	1	1	1	1	1	1	1	1	1	1	1	1
(1224.7500,1225.2500)	1	1	1	1	1	1	1	1	1	1	1	1	1	1	1	1	1	1	1	1	1	1	1	1	1	1	1	1	1	1	1
(1239.1250,1239.4375)	1	1	1	1	1	1	1	1	1	1	1	1	1	1	1	1	1	1	1	1	1	1	1	1	1	1	1	1	1	1	1
(1244.0000,1244.4375)	1	1	1	1	1	1	1	1	1	1	1	1	1	1	1	1	1	1	1	1	1	1	1	1	1	1	1	1	1	1	1
(1354.6250,1355.0000)	1	1	1	1	1	1	1	1	1	1	1	1	1	1	1	1	1	1	1	1	1	1	1	1	1	1	1	1	1	1	1
(1362.3125,1362.8125)	1	1	1	1	1	1	1	1	1	1	1	1	1	1	1	1	1	1	1	1	1	1	1	1	1	1	1	1	1	1	1
(1372.0625,1372.5000)	1	1	1	1	1	1	1	1	1	1	1	1	1	1	1	1	1	1	1	1	1	1	1	1	1	1	1	1	1	1	1
(1374.7500,1375.3125)	1	1	1	1	1	1	1	1	1	1	1	1	1	1	1	1	1	1	1	1	1	1	1	1	1	1	1	1	1	1	1
(1387.2500,1387.7500)	0	0	0	0	0	0	0	0	0	0	0	0	0	0	1	1	1	1	1	1	1	1	1	1	1	1	1	1	1	1	1
(1394.0000,1395.0000)	0	0	0	0	0	0	0	0	0	0	0	0	0	0	1	1	1	1	1	1	1	1	1	1	1	1	1	1	1	1	1
(1423.5000,1424.5000)	0	0	0	0	0	0	0	0	0	0	0	0	0	0	1	1	1	1	1	1	1	1	1	1	1	1	1	1	1	1	1
(1577.0000,1578.0000)	1	1	1	1	1	1	1	1	1	1	1	1	1	1	1	1	1	1	1	1	1	1	1	1	1	1	1	1	1	1	1
(1582.7500,1583.7500)	0	0	0	0	0	0	0	0	0	0	0	0	0	0	0	0	0	0	1	1	1	1	1	1	1	1	1	1	1	1	1
(1594.0000,1595.0000)	0	0	0	0	0	0	0	0	0	0	0	0	0	0	1	1	1	1	1	1	1	1	1	1	1	1	1	1	1	1	1
(1595.7500,1596.7500)	0	0	0	0	0	0	0	0	0	0	0	0	0	0	1	1	1	1	1	1	1	1	1	1	1	1	1	1	1	1	1
(1618.8750,1619.8750)	0	0	0	0	0	0	0	0	0	0	0	0	0	0	0	0	0	0	1	1	1	1	1	1	1	1	1	1	1	1	1
(1623.3125,1623.8125)	0	0	0	0	0	0	0	0	0	0	0	0	0	0	0	0	0	0	0	0	0	1	1	1	1	1	1	1	1	1	1
(1634.8125,1635.2500)	0	0	0	0	0	0	0	0	0	0	0	0	0	0	0	0	0	0	0	1	1	1	1	1	1	1	1	1	1	1	1
(1671.0000,1672.0000)	0	0	0	0	0	0	0	0	0	0	0	0	0	0	0	0	0	1	1	1	1	1	1	1	1	1	1	1	1	1	1

- H_2O a priori is taken from a MIPAS dedicated climatology (as the one used and described in Funke et al. (2012)).
- Pressure, line of sight information, temperature and temperature horizontal gradients from MIPAS retrieval version V5r_T_m21 are used.
- Spectroscopic data from HITRAN 2008 (Rothman et al., 2009).

GRANADA calculates the non-LTE populations of the vibrational levels of H_2O coupled with those of the electronic-vibrational states of O_2. Several inputs are needed and Funke et al. (2012) provide information on their effect on the H_2O level populations. The non-LTE model inputs used in V5r_H2O_m22 retrievals are:

- H_2O-O_2 vibrational level set, non-LTE collisional scheme and rate constants as in Funke et al. (2012), except that the O_2 electronic-vibrational levels considered here are reduced from the 45 levels considered in Funke et al. (2012) to 22, namely $O_2(X^3\Sigma_g^-, v = 0-12)$, $O_2(a^1\Delta_g, v = 0-5)$ and $O_2(b^1\Sigma_g^+, v = 0-2)$. That only suppresses the high energy (E>17155 cm^{-1}) vibrational levels of the electronic ground state, $O_2(X^3\Sigma_g^-, v = 13-35)$ and does not produce a significant impact on the population of the $O_2(1)$ and the H_2O vibrational levels.
- Ozone from the previously retrieved ozone in its version V5r_O3_522.
- Atomic oxygen concentration derived from the retrieved ozone (V5r_O3_522) below 95 km and from WACCM in its specified dynamics (SD) configuration (Garcia et al., 2007) above.
- Solar incoming fluxes at the top of the atmosphere are calculated with GRANADA taking into account attenuation by Fraunhofer lines (Hase et al., 2006) and a solar background radiance as suggested by Platnick and Fontenla (2008) (see Sect. 2.3.4 for details). Modulations due to temporal variations of the Sun-Earth distance are also included.

Forward model calculations along the line of sight are done considering non-LTE horizontal gradient corrections. These account for changes in the populations of the emitting levels along the line of sight.

9.2.5 Error budget

The error budget described here considers the propagation of the measurement noise and of the uncertainties of model parameters onto the retrieved water vapor abundances. Noise-induced retrieval errors and vertical resolutions are estimated routinely for each individual profile by the retrieval algorithm. Systematic errors related to the mapping of uncertain model parameters are estimated for representative profiles only.

The uncertainties assumed for the estimation of the errors have been: 1% for gain calibration, 3% for the instrument line shape, 150 m for elevation pointing, 2K for temperature, and 3–15% for spectroscopic data (line intensities and broadening coefficients; based on estimates by J.-M. Flaud, personal communication, 2008). Error induced by NO_2 uncertainty have not been considered because NO_2 abundances are jointly fitted.

The modeling of the non-LTE populations of the 6.3 μm H_2O vibrational levels is an important source of the MIPAS water vapor systematic error above the stratopause. Non-LTE errors are dominated by the uncertainties in the collisional rates used in the non-LTE model. The estimations provided here assume the following uncertainties: 50% in the H_2O-O_2 vibrational-vibrational exchange, 50% in the O_2 quenching by atomic oxygen and 30% in the efficiency of O_2 excitation due to O_3 photolysis. Water vapor errors induced by the atomic oxygen uncertainty are generally smaller than 3%. The estimated non-LTE errors depend on the atmospheric conditions and mainly apply to daytime measurements. They are typically negligible below 50 km, 10% at 60-70 km and 35% at 80 km.

Table 17 summarizes the estimated errors in MIPAS retrieved water vapor vmr.

The water vapor noise error is calculated assuming a wavelength-dependent average 20, 8 and 2 nW/(cm^{2}cm^{-1}sr) noise-equivalent-spectral-radiance for channels A, B and C, respectively. Typical values are 10% below 60 km, 20% at 80 km, and larger than 45% above 90 km.

The overall estimated H_2O abundance error, dominated by the effect of spectroscopic data uncertainty below 50 km and by the non-LTE and the noise errors above 50 km, is around 15% below 60 km, 20% at 70 km, 40% at 80 km and 60% at 90 km.

Table 17: Summary of main errors in MIPAS water vapor vmr. 'NLTE' includes errors due to uncertainties in the collisional rates used in the non-LTE model. 'Total' is the root sum square of all errors. 'Spect.' refers to 'Spectroscopy'.

Height km	Noise %	Pointing %	Gain %	T %	ILS %	Spect. %	NLTE %	Total %
20	3	3	3	2	2	17	0	18
30	5	2	2	2	3	17	0	18
40	7	3	0.3	2	3	10	0	13
50	7	2	6	1	0.8	6	5	13
60	10	2	1	1	1	6	10	16
70	15	2	1	1	1	6	10	19
80	20	2	1	1	1	6	35	40
90	45	2	1	1	1	6	45	60

The vertical resolution of MIPAS retrieved water vapor abundance is the full width at half maximum of the averaging kernels rows. Average vertical resolution is 3-4 km below 50 km, 4-5 km at 50–70 km and 5–6 km at 70–90 km.

Two additional criteria are further used to filter out the retrieved IMK/IAA data in order to guarantee the quality of the profile. The following results are discarded: 1) those where the diagonal value (for individual profiles) or the mean diagonal value (for averages) of the averaging kernel is less (in absolute value) than 0.03 are considered non-trustful, and 2) those corresponding to altitudes not sounded by MIPAS (below the lowermost tangent altitude).

9.2.6 Improvements with respect to previous versions

V5r_H2O_m22 water vapor baseline is an improvement of the previous V4O_H2O_m06 version. The changes from the previous version are:

- Updated L1b database to V5.
- Updated version HITRAN database from the 2004 to the 2008 version.
- Updated versions of temperature (V5r_T_m21).
- Inclusion of simultaneously retrieved ozone (V5r_O3_m22) instead of results from models.
- Inclusion of atomic oxygen derived from ozone retrievals (V5r_O3_m22) below 97 km.
- Use of CO_2 abundance from WACCM-SD.
- Improved width of the integration window of the apodized instrument line shape function.

- Extension of top altitude of the continuum retrieval from 30 to 50 km.
- Revised regularization scheme, with a weaker constraint in the mesosphere and above.
- Revised set of microwindows, extended to cover strong non-LTE emission and an additional microwindow sensitive to the jointly retrieved NO_2 abundance (needed particularly for NLC and UA retrievals, starting at 40 km).
- Correction of the aphelion/perihelion Sun-Earth distance in the solar flux calculation.
- Inclusion of a more detailed O_2 scheme in the non-LTE model of V5r_H2O_m21, in which the $O_2(1)$ production from O_3 photolysis is not parameterized anymore and is now calculated after consideration of the detailed set of electronic-vibrational O_2 levels and processes involved.

The average impact on water vapor retrieval after those changes (see Fig.20) is an 6% increase in the middle stratosphere, a reduction of oscillations around the stratopause, a decrease of 10% around 70 km and an 5-15% increase above 75 km (larger in the polar summer). The differences in H_2O abundance between the two versions is slightly smaller for nighttime.

9.3 SMR (Chalmers)

Water vapour profiles are retrieved using the same approach as previously described for ozone (Sec. 2.6). Mesospheric H_2O is retrieved from the measurement of the strong thermal emission line centered at 556.9 GHz, which is covered by the frequency modes 13 and 19. The measurements and retrievals are summarised in Table 18.

N.B.: *The reprocessing of the data set is in progress as part of an ESA project dedicated to it. Specific retrieval settings (in the table), figures showing typical averaging kernels and errors, as well as discussion about the improvements with respect to the previous L2 version (v2.3) will be added when the new products will be available.*

Frequency mode	Molecular transition	Altitude coverage	Temporal coverage	CO		Temperature	
				σ_a	l_c	σ_a	l_c
13	556.9 GHz	?-? km	4 days/month (irregular)	?%/?ppm	? km	?-? K	? km
19	556.9 GHz	?-? km	4(2) days/month	?%/?ppm	? km	?-? K	? km

Table 18: Overview of SMR measurements and retrievals of mesospheric carbon monoxide. See Table 4 for comments on content.

10. Methane

10.1 ACE-FTS (UoT)

Methane profiles are retrieved using the same approach as described in Sect. 2.1 for ozone. The retrievals are performed between altitudes of 5 and 75 km using 55 microwindows between 1245 and 1440 cm^{-1} and 2610 and 3086 cm^{-1}. In the lower mesosphere, retrievals account for H_2O as an interfering species. Four additional microwindows at 1672, 1877, 2620 and 2861 cm^{-1} have been included to improve the handling of interfering species and isotopologues below 45 km.

10.2 MIPAS (KIT/IAA)

MIPAS V5r_CH4_m21 methane is retrieved from MIPAS data from 20 km in the MA mode and 40 km in the UA and NLC modes up to 70 km with the IMK/IAA algorithm in its extended non-LTE version. That allows for consideration of non-Local Thermodynamic Equilibrium (non-LTE) emissions, for which the non-LTE vibrational level populations are calculated with the GRANADA algorithm (Funke et al., 2012). The Scientific Processor is described in more than 50 peer-reviewed publications (i.e., von Clarmann et al., 2003, 2009). Its extended version including non-LTE effects is described in Funke et al. (2001). The retrieval is based on constrained inverse modeling of limb radiances. The basic retrieval equations, the methods for characterization of results through error estimates and vertical and horizontal averaging kernels, the iteration and convergence criteria and the regularization method are described in the Ozone Climate Change Initiative Algorithm Theoretical Basis Document (Ref.: Ozone_cci_ATBD_Phase2_V1_00_01, pp. 60-64, 2014). This version is an improvement of the previous V4Ox_CH4_m01 version. We give now the details specific of the current methane retrieval.

10.2.1 Strategy

V5r_CH4_m21 methane volume mixing ratio is retrieved in the log domain in the 7.6 μm spectral region, within MIPAS band B (1215 cm^{-1}–1500 cm^{-1}), from ro-vibrational emissions of the CH_4 main isotopes. The retrieval of N_2O is performed simultaneously in order to minimize mutual error propagation. Microwindow-dependent zero level calibration corrections, assumed constant with altitude, and microwindow-dependent continuum radiation, dependent on altitude, are also retrieved. The retrieval is performed after the shift, temperature, LOS, temperature horizontal gradients, ozone and water vapor retrievals. We note that the consideration of the temperature horizontal gradients in the methane retrieval avoids convergence problems in the boundary region of the polar vortex. The retrieval setup is based on that described by von Clarmann et al. (2009) for MIPAS NOM methane retrievals (6-68 km). The CH_4 non-LTE model is described in Funke et al. (2012), which in turn is an update of the model described in López-Puertas and Taylor (2001) based on the analysis of MIPAS spectra (López-Puertas et al., 2005). The inversion is applied to MA, NLC and UA mode MIPAS limb emission. The calibrated spectra used are ESA's version 5.02/5.06 (Raspollini et al. (2010)).

10.2.2 Discretization and setup

Retrievals are performed from the surface to 120 km over a discrete altitude grid of 1 km up to 70 km, 2 km at 70-90 km, 2.5 km at 90-95 km and 5 km at 95-120 km. The forward calculations are performed using the same grid. Due to this over-sampled retrieval grid, finer than MIPAS tangent height grid (generally, 3 km), stable solutions need from the use of a regularization.

Regarding the FOV discretization in the forward model calculations, seven pencil beams are used for the numerical integration of the signal over the 3 km field of view for the whole altitude range. A reduced width (by a factor of 2 compared to MIPAS V4O_CH4_m01) of the integration window (apodized instrument line shape function) is also used, which lead to smaller channel border effects.

10.2.3 Microwindows

The set of microwindows used coincides with that generated for the MIPAS CH4+N2O NOM retrieval (von Clarmann et al., 2009). The microwindows optimal boundaries were selected after minimization of estimated errors (von Clarmann and Echle, 1998). Table 19 lists the altitude-dependent microwindows used in the methane and nitrous oxide simultaneous retrieval.

10.2.4 A priori and atmospheric inputs

MIPAS V5r_CH4+N2O_m21 retrieval setup uses the following inputs:

Table 19: Microwindows used in MIPAS V5r_CH4+N2O_m21 methane and nitrous oxide retrieval. Altitude levels should be read vertically.

Microwindow cm^{-1}	Altitude km																													
																													1	1
	1	1	2	2	2	3	3	3	3	4	4	4	5	5	5	6	6	6	6	7	7	7	8	8	8	9	9	9	9	0	0
	5	8	1	4	7	0	3	6	9	2	5	8	1	4	7	0	3	6	9	2	5	8	1	4	7	0	3	6	9	2	5
(1227.8125,1228.5000)	1	1	1	1	1	1	1	1	1	1	1	1	1	1	1	1	1	1	1	1	1	1	1	1	1	1	1	1	1	1	1
(1231.1250,1232.5000)	1	1	1	1	1	1	1	1	1	1	1	1	1	1	1	1	1	1	1	1	1	1	1	1	1	1	1	1	1	1	1
(1234.0000,1235.2500)	1	1	1	1	1	1	1	1	1	1	1	1	1	1	1	1	1	1	1	1	1	1	1	1	1	1	1	1	1	1	1
(1272.0000,1274.8125)	1	1	1	1	1	1	1	1	1	1	1	1	1	1	1	1	1	1	1	1	1	1	1	1	1	1	1	1	1	1	1
(1275.4375,1276.7500)	1	1	1	1	1	1	1	1	1	1	1	1	1	1	1	1	1	1	1	1	1	1	1	1	1	1	1	1	1	1	1
(1290.8125,1292.2500)	1	1	1	1	1	1	1	1	1	1	1	1	1	1	1	1	1	1	1	1	1	1	1	1	1	1	1	1	1	1	1
(1297.4375,1300.2500)	1	1	1	1	1	1	1	1	1	1	1	1	1	1	1	1	1	1	1	1	1	1	1	1	1	1	1	1	1	1	1
(1301.6250,1303.1250)	1	1	1	1	1	1	1	1	1	1	1	1	1	1	1	1	1	1	1	1	1	1	1	1	1	1	1	1	1	1	1
(1305.2500,1306.7500)	1	1	1	1	1	1	1	1	1	1	1	1	1	1	1	1	1	1	1	1	1	1	1	1	1	1	1	1	1	1	1
(1326.8125,1327.6250)	1	1	1	1	1	1	1	1	1	1	1	1	1	1	1	1	1	1	1	1	1	1	1	1	1	1	1	1	1	1	1

- CH_4 and N_2O a priori are taken from a MIPAS dedicated climatology (as the one used and described in Funke et al. (2012)).
- Pressure, line of sight information, temperature and temperature horizontal gradients from MIPAS retrieval version V5r_T_m21 are used.
- Spectroscopic data from HITRAN 2008 (Rothman et al., 2009).

Additionally, several inputs affect the non-LTE populations of the vibrationally excited emitting molecules calculated with GRANADA. More information on the effect of each input on the CH_4 and $N2O$ vibrational levels can be found in Funke et al. (2012) . The non-LTE model inputs used in V5r_CH4+N2O_m21 retrievals are:

- Populations of the $O_2(1)$ vibrational level using water vapor abundances from V5r_H2O_m22 and the water vapor-oxygen non-LTE model as described in Funke et al. (2012) but using the reduced set of O_2 electronic-vibrational levels described in Sec. 9.2. Indeed, these are outputs from the V5r_H2O_m22 retrievals.
- CH_4 and N_2O vibrational levels, non-LTE collisional rates and constants set as in Funke et al. (2012).
- Solar fluxes calculated with GRANADA take into account attenuation by Fraunhofer lines (Hase et al., 2006). The solar background radiance is approximated with the expression suggested by Platnick and Fontenla (2008) (see Sect. 2.3.4 for details). The temporal variations of the solar flux included account for the change of the Sun-Earth distance.
- Atomic oxygen concentration derived from the retrieved ozone (V5r_O3_522).

The forward model also considers horizontal gradient corrections of the non-LTE populations, accounting for changes along the line of sight in kinetic temperature (no SZA dependence is included), particularly when the poles are intercepted during the solstices.

10.2.5 Error budget

The error budget includes the mapping of the measurement noise and the propagation of parameter errors on the retrieved methane abundances. Table 20 summarizes the estimated systematic and random errors in MIPAS retrieved methane abundance (partially based on von Clarmann et al. (2009)).

The errors related to the mapping of uncertain model parameters are estimated for representative profiles only. The following errors were assumed for their estimation: 1% for gain calibration uncertainty, 3% uncertainty of the instrument line shape in terms of linear loss of modulation efficiency toward the maximum optical path difference, 150 m elevation pointing uncertainty and 2K temperature uncertainty. The uncertainties in spectroscopic data was assumed based on estimates by J.-M. Flaud (personal communication, 2008) and taken as an overall 2–8% uncertainty of the line intensities and broadening coefficients. Overall they add 10–20% CH_4 error below 40 km, mainly due to uncertainties in the spectroscopic data, and less than 5% above. Non-LTE errors mainly arise from uncertainties in the O_2(1) vibrational level population. These have been estimated assuming uncertainties in the H_2O-O_2 non-LTE model limited by the setup used by Koukouli et al. (2006) (used in the V4O_CH4_m01 retrieval version) and the one used in this new version (V5r_CH4_m21). The estimated non-LTE errors are negligible below 50 km and smaller than 5% below 70 km, altitude up to which CH_4 can be reliably retrieved from MIPAS measurements.

The noise errors are calculated assuming a wavelength-dependent average of 8 nW/ (cm^2 cm^{-1} sr) noise-equivalent-spectral-radiance (corresponding to MIPAS channel B). Noise-induced retrieval errors and vertical resolutions are estimated routinely for each individual profile by the retrieval algorithm. Typical values are less than 10% below 50 km, 10–20% at 60 km and 50–100% at 70 km.

Table 20: Summary of main errors in MIPAS methane vmr. 'NLTE' includes errors due to uncertainties in the non-LTE model. 'Total' is the root sum square of all errors.

Height km	Noise %	Pointing %	Gain %	T %	ILS %	Spectroscopy %	NLTE %	Total %
20	4	4	0.2	1	0.5	21	0	22
30	5	2	0.6	2	6	14	0	17
40	7	4	3	3	4	11	0	15
50	10	5	2	4	3	2	1	15
60	15	5	2	4	3	2	3	17
70	75	5	2	4	3	2	5	75

Typical values of vertical resolution of the retrieved methane volume mixing ratio (full width at half maximum of the averaging kernel rows) are 3–4 km below 50 km, 5–6 km at 60 km and 6–10 km at 70 km.

Two criteria are further usually applied to the retrieved IMK/IAA data in order to guarantee the quality of the profile: 1) results related to parts of the atmosphere non-sensed by MIPAS (i.e. below the lowermost used tangent altitude) are considered non-trustful. 2) results where the diagonal value (for individual profiles) or the mean diagonal value (for averages) of the averaging kernel is less (in absolute value) than 0.03 are considered non-trustful.

10.2.6 Updates

The differences between the current V5r_CH4_m21 and the previous V4O_CH4_m01 versions are:

- Updated L1b database to V5.
- Updated version of the HITRAN database.

- Updated a priori profiles.
- Updated versions of temperature (V5r_T_m21) and water vapor (V5r_H2O_m22) profiles as inputs.
- Improved width of the integration window of the apodized instrument line shape function, which reduced channel border effects.
- Revised regularization scheme to reconcile with NOM stronger constrains.
- Extension of top altitude of the continuum retrieval from 30 to 60 km.
- Use of a finer retrieval grid in the 74-84 km region.
- Atomic oxygen climatology changed from NRLMSISE-00 to WACCM-SD.

These changes lead to an overall $<$5% variation of the retrieved methane abundance below 65 km (except 10% at polar summer around 60 km) and 10% below 70 km (see Fig.21). The variations are mainly produced by the update of the temperature version and the stronger regularization. Both significantly reduce oscillations which appeared above 40 km in the previous version. The noise error is also reduced from 10-30% to less than 10% at 50 km, from 30-50% to 10-20% at 60 km and from more than 100% to 50-100% at 70 km. Additionally, there is now a smaller latitudinal dependence on the error. The general decrease in the noise error is accompanied by an increase of the vertical resolution from 3-4 km to 5-6 km at 60 km and from 5-6 km to 6-10 km at 70 km.

11. Carbon dioxide

11.1 ACE-FTS (UoT)

Carbon dioxide profiles are retrieved using the same approach as described in Sect. 2.1 for ozone. The retrievals are performed between altitudes of 15 and 125 km using 110 microwindows between 927 and 2444 cm^{-1}, with no interfering species. As the CO_2 VMR is held fixed in the middle atmosphere, these retrieved results serve only as a sanity check below 60 km.

11.2 MIPAS (KIT/IAA)

MIPAS v5r_CO2_622 carbon dioxide retrieval is based on constrained inverse modeling of non-LTE limb radiances. That is performed using the IMK/IAA Scientific Processor (von Clarmann et al., 2003, 2009) extended with the non-LTE GRANADA algorithm (Funke et al., 2012), which is able to cope with non-LTE emissions. Funke et al. (2001) describe the particularities of the retrievals under consideration of non-LTE. The basic retrieval equations, the methods for characterization of results through error estimates and vertical and horizontal averaging kernels, the iteration and convergence criteria and the regularization method are described in the Ozone Climate Change Initiative Algorithm Theoretical Basis Document (Ref.: Ozone_cci_ATBD_Phase2_V1_00_01, pp. 60-64, 2014). Carbon dioxide is reliably retrieved from 70 km up to $\sim$142 km from MIPAS measurements taken in the UA mode. A description of the specifics of the carbon dioxide retrieval v5r_CO2_622 follows, which is based on Jurado-Navarro et al. (2016).

11.2.1 Strategy

Carbon dioxide is retrieved in the long domain from spectral lines covering ro-vibrational emissions of the CO_2 main isotope. These have been selected from a broad spectral region (2300–2380 cm^{-1}) covered by the MIPAS band D.

Retrievals are performed from MIPAS limb emission measured in the UA (40-172 km) mode. Calibrated spectra are supplied by ESA in version 5.02/5.06 (Raspollini et al. (2010) and references therein). The retrieval is performed after a spectral shift retrieval and the non-LTE retrievals of temperature and ozone abundance below 100 km, and the thermospheric temperature and NO retrievals from 100 km up to 172 km (see Secs. 14.5 and 5).

The IMK/IAA processor simultaneously retrieves zero level calibration corrections (the latter, assumed constant with altitude). The line of sight (LOS) is retrieved jointly with the CO_2-vmr, although it is not used in any other retrieval.

The CO_2 profile is regularized by means of a Tikhonov-type (Tikhonov, 1963) smoothing constraint. A strong diagonal constrain is added below 60 km in order to force the retrieved CO_2 to be close to the well-known mixing ratio in the lower mesosphere. Above 60 km, the constrain is optimized to obtain stable calculations with a precision high enough to allow for meaningful physical interpretation of the retrieved CO_2 abundance.

A Tikhonov smoothing constraint is also used for the LOS retrieval, allowing for vertically coarse variations of $\sim$10–20 km of the tangent height spacing with respect to the *a priori*. The LOS of the lowermost tangent height is strongly constrained to the a priori by means of a diagonal regularization. Typically, the obtained degrees of freedom for the LOS retrievals are about 2.

11.2.2 Discretization and setup

The retrievals are performed from the ground to 152 km, although using MIPAS measurements only from 60 km up to 142 km, over a discrete altitude grid of 1 km up to 50 km, 2 km from 50 to 70 km, 1 km from 70 to 80 km, 2 km from 80 to 90 km, 1 km from 90 to 110 km, 2.5 km from 110 to 120 km and 5 km from 120 to 150 km. The selected grid provides balanced accuracy and efficiency. The forward calculations are performed using that same grid. The over-sampled retrieval grid, finer than MIPAS vertical sampling (varying from 3 km below 100 km to 5 km above 100 km), makes the use of a regularization mandatory in order to obtain stable solutions.

The numerical integration of the signal over the 3 km (or 5 km) field of view is done using seven pencil beams. The selected width of the integration window (apodized instrument line shape function) avoids channel border effects.

11.2.3 Microwindows

The retrievals are performed from selected spectral regions (micro-windows) which vary with tangent altitudes in order to optimize computation time and minimize systematic errors (von Clarmann and Echle, 1998).

The selection of the spectral regions sensitive to the CO_2 abundance is performed by calculating the 4.3 μm Jacobians and selecting those regions with a good local response. In this way, and thanks to the excellent MIPAS spectral resolution, we are able to select the spectral points sensitive to the CO_2 vmr, yet with a good signal-to-noise ratio, while excluding lines with non-local responses due to spectral saturation. In addition to the exclusion of spectral points with non-local response, we restricted the microwindows to the strongest lines (mainly fundamental and second hot bands lines that have the larger signal/noise ratio) at each altitude for reasons of computational efficiency. Additionally, spectral regions with interferences from the 636, 628, 627, 638 and 637 CO_2 isotopologues have been suppressed in order to avoid systematic errors caused by the less accurate non-LTE modeling of these minor species. This resulted in a selection of 18 principal spectral regions within the 2300–2380 cm^{-1} range, containing height-dependent microwindows at 23 tangent heights from 60 km up to 142 km (see Fig. 22). The selected spectral points belong mainly to the lines of the fundamental band in the 60–72 km and 102–142 km regions, and of the second hot bands in the 75–102 km region. More detailed information on the microwindows used in the retrieval is given in Appendix A.

11.2.4 A priori and atmospheric inputs

MIPAS V5r_CO2_622 carbon dioxide retrieval setup uses the following inputs:

- CO_2 *a priori* profiles are taken from the Whole Atmosphere Community Climate Model with specified dynamics (SD-WACCM) simulations (Garcia et al., 2014). SD-WACCM is constrained with output from NASA's Modern-Era Retrospective Analysis (MERRA) (Rienecker et al., 2011) below approximately 1 hPa. Garcia et al. (2014) showed SD-WACCM simulations for Prandtl numbers (P_r) of 4 (standard) and 2, corresponding to lower and higher eddy diffusion coefficients, respectively. Here we used the simulations for P_r=2, which gives an overall better agreement with ACE CO and CO_2 and MIPAS CO (Garcia et al., 2014).

- Pressure, line of sight a priori information, temperature (up to 100 km), and temperature horizontal gradients are taken from MIPAS retrieval version V5r_T_m21. O_3 is taken from version V5r_O3_522. The temperature above 100 km is taken from the retrieval of MIPAS data in the NO 5.3 μm region (Bermejo-Pantaleón et al., 2011) from version V5r_TT_621.

- Spectroscopic data from HITRAN 2012 (Rothman et al., 2013).

GRANADA calculates the non-LTE populations of the vibrational levels of CO_2 coupled with that of N_2. Several inputs are needed and Funke et al. (2012) provide information on their effect on the CO_2 level populations. Taken as a basis the inputs for GRANADA as described in Funke et al. (2012), the following updates have been included in the CO_2V5r_CO2_622 retrievals:

- Very important collisional coefficients of many vibrational-vibrational and vibrational-translational processes were significantly updated with the values retrieved from MIPAS spectra as described in Jurado-Navarro et al. (2015). In addition to those, other updates were included:

- Solar incoming fluxes at the top of the atmosphere are calculated with GRANADA taking into account attenuation by Fraunhofer lines (Hase et al., 2006) and a solar background radiance as suggested by Platnick and Fontenla (2008) (see Sect. 2.3.4 for details). Modulations due to temporal variations of the Sun-Earth distance are also included.

- The collisional rates of $CO_2(v_d, v_3)$ + M $\leftrightharpoons$ $CO_2(v'_d, v_3 - 1)$ + M with Δv_d=2–4 and M=N_2, O_2 (processes 8a and 8b in Table 1 of Jurado-Navarro et al., 2015) where the f factor has been changed from 0.82 to 0.7.

- The rate of $N_2(1)$ + O $\rightarrow$ N_2 + O (process 10 in that table) has been updated with a rate coefficient of 4.5×10^{-15} (T/300)$^{1.5}$ cm^{3}s^{-1} and f = 1. This rate has been adapted from Whitson and McNeal (1977) taking the upper limit (within the error bars) at 300 K and re-adjusting the temperature dependence taking into account the measurements at higher temperatures. The values of this new rate at temperatures near 300 K are, however, similar to those used in Jurado-Navarro et al. (2015).

  The non-LTE model for CO_2 also requires the concentrations of O_3, O(^3P) and O(^1D).

- The atomic oxygen and O(^1D) profiles below 100 km were generated from the O_3 retrieved from MIPAS and the photochemical model described in (Funke et al., 2012). Above 100 km, we take the atomic oxygen concentration from WACCM-SD. The O_2 concentrations are taken from the NRLMSIS-00 model (Picone et al., 2002b). The ozone was taken from that retrieved from MIPAS spectra near 10 μm (Gil-López et al., 2005), version V5r_O3_522.

- The O(^1D) profile above 100 km has been updated from the photochemical model of Funke et al. (2012) by using the O_2 photo-absorption cross sections of Ogawa and Ogawa (1975) and Lu et al. (2010), and a new efficiency of O(^1D) production from O_2 photo-absorption that consider that at wavelengths shorter than ∼100 nm the O_2 ionization is the dominant channel. Also, we included an overhead column above the top layer of the model proportional to the scale height of O_2. This O(^1D) photo-production has been compared with that calculated for similar conditions by an independent 1D model UV radiative transfer model (González-Galindo et al., 2005; Garcia et al., 2014) finding differences smaller than 2% at all altitudes.

- A variable solar spectral irradiance (SSI) (Lean et al., 2005) was included in all the photochemical calculations in order to account for solar UV variations along the MIPAS observation period.

Forward model calculations along the line of sight are done considering gradients (along the LOS) in the non-LTE populations of the emitting levels caused by kinetic temperature gradients as well as by different solar illumination conditions (variable solar zenith angle).

11.2.5 Error budget

The error budget described here considers the propagation of the measurement noise and of the uncertainties of model parameters onto the retrieved carbon dioxide abundances. Noise-induced retrieval errors and vertical resolutions are estimated routinely for each individual profile by the retrieval algorithm. Systematic errors related to the mapping of uncertain model parameters are estimated for representative conditions only, namely, mid-latitudes and polar summer conditions.

The uncertainties assumed for the estimation of the errors have been: 1.25% for gain calibration and 3% for the instrument line shape. For temperature we assumed an error of 5 K up to 100 km, 10 K between 100 and 110 km, and 15 K between 110 and 142 km. The other perturbations, are: 1.25% for the gain calibration; 1% for the solar flux; a 50% uncertainty in the concentration of O(^3P); and an uncertainty of 10% in the concentration of O(^1D) below 80 km and 30% above. Errors due to spectroscopic data (line intensities and broadening coefficients) for CO_2 were considered to be of smaller magnitude.

In addition, systematic CO_2 retrieval errors due to uncertainties in the collisional rates used in the non-LTE modeling need to be taken into account. However, since the collisional parameters used in the CO_2 inversion have been retrieved from MIPAS measurement in the same spectral region (see Jurado-Navarro et al., 2015), the CO_2 errors due to the errors of the retrieved collisional rates are expected to be correlated with those introduced by model parameter uncertainties. Therefore the $\Delta CO_2(y_i)$ error due to a given model parameter, y_i, i.e., pressure/temperature, O(^1D), O(^3P), gain calibration and solar flux, were calculated by means of

$$\Delta CO_2(y_i) = \left(\frac{\delta CO_2}{\delta y_i}\right)_{\forall x_j = cte} \Delta y_i + \sum_j \left(\frac{\delta CO_2}{\delta x_j}\right) \Delta x_j(y_i), \tag{40}$$

where the second term in the righthand side accounts for the propagation of the error of model parameters, y_i, through the errors in the retrieved collisional parameters, $\Delta x_j(y_i)$ given by

$$\Delta x_j(y_i) = \left(\frac{\delta x_j}{\delta y_i}\right) \Delta y_i. \tag{41}$$

The sum over j extends over the retrieved collisional parameters, x_j: k_{vv2}, k_{vv3}, k_{vv4}, k_{F1}, k_{F2}, and f_{vt}, whose errors due to the model parameters y_i, $\Delta x_j(y_i)$, are listed in Table 3 of Jurado-Navarro et al. (2015). The first term in the righthand side, where Δy_i is the error of model parameter y_i, has been discussed above. The total systematic error in CO_2 is then calculated by a quadratic sum over the errors of all model parameters, $\Delta CO_2^{\text{Total}} = \sqrt{\sum_i [\Delta CO_2(y_i)]^2}$.

The resulting CO_2 vmr errors are listed in Table 21 for mid-latitudes and polar summer latitudes.

The carbon dioxide noise error is calculated assuming a noise-equivalent-spectral-radiance of 2 nW/(cm^{2}cm^{-1}sr), resulting in values raging from 1% to 14% from 70 to 140 km (see first column in Table 21).

The retrieved CO_2 has a much better accuracy than previous limb emission measurements, because of the highly accurate rate coefficients recently derived from MIPAS, and the simultaneous MIPAS measurements of other key atmospheric parameters needed for the non-LTE modeling like the kinetic temperature and the O_3 concentration. The major systematic error source is the uncertainty of the pressure/temperature profiles, inducing errors of up to 15% above 100 km, and of $\sim$5% around 80 km at mid-latitude conditions. The errors due to uncertainties in the O(^1D) and O(^3P) profiles are within 3–4% in the 100–120 km region, and those due to uncertainties in the gain calibration and in the near-IR solar flux are within $\sim$2% at all altitudes.

Table 21: Errors of the CO_2 vmr for mid-latitudes and polar summer (in parenthesis) conditions. The column 'Total« is the sum root square of the systematic errors (all except random).

Height (km)	Errors (%)						
	Random	Pressure/Temp.	O(^1D)	O(^3P)	Gain (1.25%)	Solar flux (1%)	Total
70	<1 (<1)	0.33 (0.05)	0.14 (0.17)	0.10 (0.09)	0.08 (0.18)	0.03 (0.12)	0.38 (0.3)
75	1 (1)	3.3 (0.36)	1.2 (1.6)	0.8 (0.7)	0.7 (1.7)	0.24 (1.2)	3.7 (2.7)
80	1 (1)	5.1 (0.38)	1.4 (1.8)	0.44 (0.4)	0.8 (2.0)	0.02 (1.1)	5.4 (3.0)
85	1 (1)	3.2 (0.9)	1.2 (1.3)	0.12 (0.17)	0.67 (1.1)	0.19 (0.18)	3.5 (2.0)
90	2 (2)	1.5 (0.6)	1.4 (1.4)	0.44 (0.16)	0.8 (1.1)	0.16 (0.12)	2.3 (1.8)
95	3 (3)	1.0 (6)	1.0 (0.6)	0.03 (0.9)	0.45 (0.08)	0.6 (1.2)	1.6 (6)
100	3 (3)	4.4 (13)	1.1 (4)	1.4 (3.4)	0.34 (2.0)	1.4 (2.8)	5 (15)
105	4 (4)	9 (14)	2.5 (4)	1.6 (3.5)	0.6 (1.8)	1.4 (2.2)	10 (16)
110	5 (4)	11 (13)	3.1 (3.2)	2.5 (3.4)	0.9 (1.3)	1.4 (1.7)	12 (14)
115	5 (5)	10 (13)	1.1 (1.6)	2.2 (2.7)	0.01 (0.34)	0.7 (0.9)	11 (13)
120	6 (5)	11 (14)	0.6 (0.6)	0.8 (2.0)	0.8 (0.02)	0.02 (0.6)	11 (14)
125	7 (7)	12 (15)	1.2 (0.3)	0.13 (1.0)	0.9 (0.31)	0.25 (0.32)	12 (15)
130	9 (9)	13 (16)	1.5 (1.1)	0.9 (0.06)	1.1 (0.6)	0.4 (0.07)	13 (16)
135	11 (12)	13 (16)	2.1 (1.7)	2.1 (0.9)	1.5 (0.9)	0.7 (0.13)	14 (16)
140	13 (14)	14 (16)	2.8 (2.2)	3.4 (1.5)	1.2 (1.1)	1.1 (0.28)	14 (16)

The vertical resolution of MIPAS retrieved carbon dioxide abundance is the full width at half maximum of the averaging kernels rows. The retrieved CO_2 profiles have a vertical resolution of about 5–7 km below 120 km and between 10 and 20 km at 120–142 km.

The CO_2 V5r_CO2_622 data is available only for daytime conditions, solar zenith angle smaller than 85-90°.

Two criteria are further recommended to filter out the CO_2 IMK/IAA data in order to guarantee the quality of the data: 1) those where the diagonal value (for individual profiles) or the mean diagonal value (for averages) of the averaging kernel is less (in absolute value) than 0.03 are considered non-trustful; and 2) those corresponding to altitudes below 70 km.

11.2.6 Brief description of current version and preliminary comparison with other datasets

V5r_CO2_622 baseline is the first version of the CO_2 data. The retrieved CO_2 shows the major features expected and predicted by general circulation models.

Figures 23-24 show a comparison of MIPAS CO_2 abundances with those measured by the ACE and SABER instruments for equinox conditions (March) and solstice conditions (June).

The major results of the comparison can be summarized in:

- MIPAS measurements are generally larger ($\sim$5%) than ACE ones at 80-100 km and 20-30% smaller at 100-120 km.
- MIPAS and SABER agree very well up to 100 km. At 100-120 km, they also agree very well when averaging over all latitudes, but MIPAS is generally larger than SABER except near the equator where MIPAS

is lower. That is, in the 100-120 km region, globally, ACE is the largest, SABER the smallest and MIPAS is in between.

- SABER CO_2 measurements between 100 and 120 km are globally smaller than MIPAS, ACE and WACCM.

More details can be found in López-Puertas et al. (2017a).

12. Sodium

12.1 GOMOS (BISA)

12.1.1 Virtualization of occultations

Most inversion methods in atmospheric remote sensing contain regularization methods to remove spurious oscillations produced by the amplification of the measurement noise. Therefore, very small absorbers cannot be retrieved easily because averaging many profiles leads to a mean profile contaminated by the regularization. As transmittances are by definition normalized measurements, they are excellent candidates to statistical processing (by accumulation) with the relevant error bars. It is therefore expected that the mean or virtual transmittance will show an improved S/N ratio on which the relevant inverse model can be applied once. It is necessary to build a climatology of GOMOS averaged transmittances (also named 'virtual transmittances') as a time-latitude series covering the entire duration of the mission (121 months from 04/2002 to 04/2012). Previous scientific studies have shown that by averaging transmittance signals it is possible to retrieve some minor but important constituents like Na and OClO from GOMOS data.

12.1.2 Statistical analysis

Detection of mono/bimodal distributions The method of virtualization requires a thorough statistical analysis. The homogeneity of the data set being of primary importance, a detection of multimodal distributions is performed by fitting the distribution with theoretical models (using a curve fitting non-linear algorithm). Each bimodal case will be studied separately by trying to understand why this particular bimodality and trying to properly separate each mode.

Detection of outliers The second step of the statistical analysis is the detection and rejection of outliers in each data set. An algorithm has been developed based on the well known Jack's knife method. This robust technique is quite simple and easy to implement. Consider a dataset with N values. Remove the first value and compute the standard deviation based on the data subset with (N-1) elements and repeat this for the N values. It appears that when you remove an outlier, the standard deviation decrease strongly. In the spectral region around the Na doublet, the virtual transmittances may be contaminated by the presence of polar mesospheric clouds (PMC) as illustrated in Fig. 25

12.1.3 Computation of weighted median transmittances

Finally, for each tangent altitude and each wavelength, the weighted median transmittance is calculated instead of the usual mean because the median is known to be more robust against the presence of residual outliers. Furthermore, as the S/N ratio of different measurements can differ considerably, we combine transmittances weighted with respect to the inverse of their estimated measurements errors. A weighted median calculation starts by sorting the transmittance values in increasing order, and rearranging the associated weights in the same fashion. The cumulative distribution of these weights is subsequently evaluated. The

weighted median is then the transmittance value corresponding to the mean level of this cumulative weight distribution.

In Fig. 26 , we demonstrate how a very tiny absorption feature appears when more and more transmittances are combined: the sodium doublet becomes visible and a DOAS inversion scheme can be applied to derive its slant path optical thickness.

Virtualization is the only way to increase the signal-to-noise ratio for an instrument like GOMOS, at the moderate price of decreasing the spatio-temporal sampling to the bin size. From the averaged transmittances, it is not only possible to detect very tiny absorbers (or emitters) but also to apply the standard retrieval algorithm (with a virtual occultation on a same altitude grid) to obtain much more accurate trace species as ozone or nitrogen dioxide. Furthermore, averaged transmittances can be directly analyzed to detect trends that can be interpreted a reliable proxy of a corresponding slant column density.

12.2 SCIAMACHY MLT limb measurements (UB)

The described retrieval algorithm uses a special limb observation mode of the SCIAMACHY instrument referred to as the Mesosphere-Lower Thermosphere (MLT) limb measurements. In this mode SCIAMACHY scans the horizon at tangent heights from about 53 km to about 148 km with 3.3 km vertical sampling. This kind of measurements was performed since summer 2008 for one day each two weeks. In total there are 84 measurement days. The retrievals were done using Level 1 V7.03/7.04 data with calibration flags 1,2,4,5,7 with M-factor correction applied. All measurements during each measurement day were averaged accounting for a shift in the latitude of the ground pixels for neighboring orbits. All limb measurements from this averaged orbit data are passed to the retrieval algorithm to obtain the number densities of the target species on a 2D latitudinal and vertical grid.

The retrieval algorithm used for sodium retrieval is very similar to that employed for Mg/Mg^+ retrieval (see Sect. 15.1). The retrieval is performed in the spectral window 585 - 592.2 nm and the spectral background is subtracted using the intervals 585 - 588.3 nm and 590.3 - 592.2 nm.

Contrary to the Mg/Mg^+ retrieval, the influence of the lower atmosphere needs to be considered in the sodium retrieval algorithm as the Earth's atmosphere is much more transparent in the visible spectral range. Furthermore, solar Fraunhofer lines in the sodium emission spectral range are much narrower than those in the Mg and Mg^+ retrieval window requiring a need for considering small wavelength shifts. The retrieval program uses the shift and line shape information from McNutt and Mack (1963).

The signal to background ratio for sodium lines is higher than that for the Mg/Mg^+ lines and the influence of the Ring effect is negligibly small and its treatment can be omitted.

A correction for the multiple scattering and surface albedo effects is based on the approach suggested by Hedin and Gumbel (2011), who used the ratio of the limb measurement signal to the simulated Rayleigh scattered measurement signal in the vicinity of the Na lines at 40 km as the albedo factor. However, as the MLT limb measurement sequence starts at about 53 km tangent height this approach cannot be used directly. Here, an assumption that the vertical profile of this ratio has roughly the same shape for the same latitude and longitude on different days is used and the profile from MLT measurements is fitted to the vertical shape profile obtained from the nominal limb measurements performed during the surrounding days. The Rayleigh scattering signal is simulated using the SCIATRAN radiative transfer model (Rozanov et al., 2014).

To account for a possible stray light contamination the fit is done including a multiplicative and an additive components of the signal. At each tangent altitude h and wavelength λ we assume that the the multiplicative part of the radiance is proportional to the simulated single scattering signal, $aI_{ss}(h,\lambda)$, and there is a wavelength independent signal b(h). The total incoming radiation $I_{inc}(h,\lambda)$ is given by the sum of both terms $I_{inc}(h,\lambda) = a(h)I_{ss}(h,\lambda) + b(h)$. The coefficients a and b are obtained by a fit in a wavelength region with a non spectral constant solar spectrum. The latter assures that the problem remains well-posed. The spectral region is selected to avoid any atmospheric features (emission, extinction etc.). The nearby wavelength interval between 650 nm and 660 nm includes the H α Fraunhofer line at 656 nm and is well suited for this

fit. We assume that the minimum of the multiplicative component above 20 km tangent altitude provides the albedo factor.

As mentioned above the albedo factor is obtained from the nominal limb measurements performed during the surrounding days. The median of the multiplicative component in the latitudinally and longitudinally co-located region for about 200 orbits of nominal limb measurements is formed for all altitudes. The albedo factor A for this median profile is determined. Between 50 km and 70 km the logarithms of the nominal and the MLT measurements are fitted as factor B (ln MLT $= B$ ln nominal). Fitting the factor B this way puts more weight on the match at the lower altitudes, where it is assumed that the match should be better, as the spectral stray light error is smaller there. The albedo factor for the MLT measurement finally is the product AB.

12.3 SCIAMACHY nominal limb measurements (UB)

The retrieval on the Sodium vertical distribution from the nominal limb measurements of SCIAMACHY is performed within the altitude range 68 - 90 km. The spectral signature between 587.2 and 591.9 nm is analyzed after the baseline signal has been subtracted. The baseline is obtained by a least square fit of a liner polynomial in the same spectral window excluding the range of Na emission features (588.5 – 590.3 nm).

The most crucial effect on the quality of the results has the solar irradiance spectrum which is used to model Na emission features. In opposite to the method described by Langowski et al. (2016) and used for Na retrievals from SCIAMACHY MLT measurements, see Sect. 12.2, we use the solar spectrum from Kurucz (2005) with calibration from (Thuillier et al., 2004), which can be fitted an the measured SCIAMACHY solar irradiance directly without any additional line shape adjustments. A comparison of the solar irradiance spectra from (Chance and Kurucz, 2010) as used for the MLT retrievals (green) and from Kurucz (2005) used here is shown in the left panel of Fig. 27. It is clearly seen the latter spectrum does not show the problem with a wrong deepness of the Fraunhofer lines discussed by Langowski et al. (2016). The high resolution solar spectrum is fitted to monthly mean solar irradiance measured by SCIAMACHY accountig for the following parameters: additive offset, slope, scaling factor, spectral resolution, and wavelength shift. The fit is done between 588 and 591 nm assuming a Gaussian shape of the instrument slit function. The right panel of Fig. 27 shows the monthly mean solar irradiance measured by SCIAMACHY with applied wavelenght shift (blue), the fitted convolved irradiance spectrum from Kurucz (2005) (red) and the high resolution solar irradiance spectrum from Kurucz (2005) with the first three fit parameters applied. The latter spectrum along with the deternined spectral resolution is used in the retrieval process to model the Na emission lines.

The retrieval is done for monthly zonal means of the measured radiances. Mean solar irradiance, geolocation and illumination is calculateded accordigly. The measurement vector is created from all spectra in the selected tangent height range. A baseline is subtracted from both measured and simulated sun-normalized radiances prior the retrieval. The retrieval is done for absolute deviations from the initial guess value (in units of molec/cm^2/km) employing the first order Tikhonov regularization. The zero-order parameter is set to 5E+7 while the first order parameter is 1E-7. The non-linearity of the problem is acoonted for employing an iterative process. The initial guess value is taken from the SCIAMACHY MLT retrieval results and is replaced by the result of the previous iteration at each iterative step. In addition th the sodium vertical profiles the surface albedo is retrieved from the radiance measured at about 38 km tangent height.

Figure 28 shows spectral fits (upper row) and residuals (lower row) for three selected tangent heights (87 km, 81 km, 74 km from left to right). In the upper row the measured spectra a shown in red while the cyan curves depict the modeled signals. The averaging kernels typical for sodium vertical profile retrieval from SCIAMACHY nominal limb measurements are shown in the left panel of Fig. 29. The colored numbers on the right depict the nominal altitudes of the averaging kernels. The averaging kernels have prononced peaks at nominal altitudes but have a maximum value of 0.1 – 0.15 illustrating a strong influence of the initial guess profiles. This influence can however be mitigated by means of an iterative process replacing the initial guess by the result of the previous iteration at each iterative step. The vertical resolution of the retrieval is

estimated at about 7 km. The right panel of Fig. 29 illustrate the depengence of the resulting profile (shown by the slod lines) on the initial guess (shown by the dashed lines). The yealow area marks the retrieval range. It is seen that deviations are mainly determined by a “wrong” shape of the profile above the retrieval range and general shape of the initial guess profile rahter than by the absolute value of the a priori.

12.4 SCIAMACHY nightglow limb measurements (EMAU)

Na profile retrievals in the MLT region are typically based on daytime satellite limb observations of sunlight resonantly scattered in the Na D lines (e.g. Gumbel et al., 2007; Langowski et al., 2016), on satellite stellar occultation measurements (Fussen et al., 2004) or on ground-based observations using LIDARs (e.g. She et al., 2000). The Na D lines also occur as an emission feature in the terrestrial nightglow spectrum (Slipher, 1929) and a first excitation mechanism for the Na D line nightglow emission was proposed in 1939 by Chapman (1939). The mechanism consisted of the following reactions:

$$\mathrm{Na} + \mathrm{O_3} \longrightarrow \mathrm{NaO} + \mathrm{O_2} \qquad \mathrm{k_1} \tag{42}$$

$$\mathrm{NaO} + \mathrm{O} \longrightarrow \mathrm{Na}(^2\mathrm{P}) + \mathrm{O_2} \qquad \mathrm{f\,k_2} \tag{43}$$

$$\mathrm{NaO} + \mathrm{O} \longrightarrow \mathrm{Na}(^2\mathrm{S}) + \mathrm{O_2} \qquad (1-\mathrm{f})\,\mathrm{k_2} \tag{44}$$

$$\mathrm{Na}(^2\mathrm{P}) \longrightarrow \mathrm{Na}(^2\mathrm{S}) + \mathrm{h}\nu \qquad \mathrm{A} \tag{45}$$

Xu et al. (2005) presented a theoretical approach to retrieve MLT Na profiles from observations of vertical volume emission rate profiles of the Na D line nightglow at 589 nm. A main result of this study was that the complex Na chemistry is dominated by 3 reactions, i.e. reactions 42 and 43 of the Chapman mechanism and an additional Na loss reaction

$$\mathrm{Na} + \mathrm{O_2} + \mathrm{M} \longrightarrow \mathrm{NaO_2} + \mathrm{M} \qquad \mathrm{k_3} \tag{46}$$

As demonstrated by Xu et al. (2005), ignoring all other neutral, ionic or photochemical reactions leads to Na retrieval errors of less than 1 % in the 85 – 110 km altitude range, where almost all of the MLT Na resides. Considering only these three reactions leads to the following relationship between the Na nightglow volume emission rate (VER in photons $\mathrm{s^{-1}\ cm^{-3}}$) and Na concentration:

$$[\mathrm{Na}]_{\mathrm{ret}} = \frac{\mathrm{VER/f}}{\mathrm{k_1[O_3] + k_3[O_2][M]}} \tag{47}$$

and

$$\mathrm{VER} = \mathrm{f[Na]\,(k_1[O_3] + k_3[O_2][M])} \tag{48}$$

This is the model used here to retrieve Na concentration profiles from SCIAMACHY Na D line nightglow observations. The basic idea is to retrieve Na D line VER profiles from SCIAMACHY nighttime limb observations and then use the above equation to infer Na density profiles. One issue of this method is that the value of the branching ratio f is still uncertain. Clemesha et al. (1995) report values ranging between 0.05 and 0.2 with a best guess value of $f = 0.1$, based on ground-based observations of vertically integrated Na D line emission rates. Clemesha et al. (1995) also attempted to find an optimum value for f by minimizing the differences between model results and ground-based observations of the slant Na D line emission rate. They obtained a value of $f = 0.093$. Griffin et al. (2001) report a value of $f = 0.14 \pm 0.04$, based on laboratory measurements. Based on the earlier results by Clemesha et al. (1995) and on comparisons of our retrievals with SCIAMACHY

Reaction	Rate constant
Na + $O_3 \longrightarrow$ NaO + O_2	$1.1 \times 10^{-9}\ \exp(-116/T)$
Na + O_2 + M $\longrightarrow$ NaO_2 + M	$(5.0 \times 10^{-30})(T/200)^{-1.22}$

Table 22: Reaction rates of the reactions relevant to the Na profile retrieval from Na nightglow observations (see, e.g. Plane et al. (2015)).

daytime and GOMOS Na observations, we chose a value of $f = 0.09$ for the initial Na profile retrievals from SCIAMACHY Na nightglow measurements presented here. The uncertainty in f is one of the principal sources of error of the current version of the Na profile retrieval from nightglow observations. Future work will attempt constraining the value of f by comparison to co-located ground-based LIDAR observations.

Retrieving Na density profiles using reaction 47 also requires knowledge of several other parameters and rate constants. The O_3 concentration profiles are taken from a monthly averaged O_3 concentration climatology – as a function of geometric altitude – based on GOMOS stellar occultation observations and provided by Viktoria Sofieva (Finish Meteorological Institute). The O_2, N_2 and temperature profiles were taken from the NRL-MSISE-00 model. The reaction rate constants k_1 and k_3 are given in Table 22.

12.4.1 Retrieval approach and self-absorption correction

Due to the limited signal-to-noise ratios (SNR) of the SCIAMACHY nighttime limb spectra, the retrieval of Na profiles is not possible based on individual limb observations. Even for zonally and daily averaged measurements the SNR is not high enough. For this reason, the Na profile retrieval from SCIAMACHY nighttime observations is currently based on monthly averaged limb spectra. All retrievals are based on SCIAMACHY level 1b data version 7.0x calibrated with the `scial1c` tool with all calibration flags applied and including the `M-factor` correction.

Unfortunately, the self absorption of the Na D line emission by Na in the mesopause region cannot be neglected. A self absorption correction similar to the one applied to Na profile retrievals from SCIAMACHY daytime limb observations of resonantly scattered solar radiation (Langowski et al., 2016) has been implemented. The self absorption correction requires an iterative retrieval. One complication is that the Na profiles are not a direct outcome of the inversion procedure, but the inferred VER profiles have to be converted to Na density profiles using the photochemical model described above. In the first iteration the self absorption is neglected and a first estimate of the VER and subsequently Na density profile is retrieved. The Na D line VER profiles are retrieved from SCIAMACHY nighttime observations of the limb (integrated) emission rate (LER) profile measurements using a constrained linear least squares approach. The LER profiles are obtained by spectrally integrating over both Na D lines and subtracting a background based on limb radiances just above and below the Na nightglow emission. The state vector $\vec{x}$ containing the Na D line VER as a function of altitude is estimated by:

$$\vec{x} = \left(\mathbf{K}^T\mathbf{K} + \gamma \cdot \mathbf{R}^T\mathbf{R}\right)^{-1}\mathbf{K}^T\vec{y} \tag{49}$$

with **K** being a matrix containing the geometrical path lengths of each limb line of sight through the different layers of the model atmosphere. The retrieval altitude grid was chosen to be identical to the tangent height grid of the limb observations. $\vec{y}$ corresponds to the measurement vector and contains the LER values as a function of tangent height. γ is the constraint factor and **R** is the standard $\mathbf{L}_1$ constraint matrix minimizing differences between adjacent VER values.

Neglecting self absorption in the first iteration step implies that this first estimate constitutes a lower limit for both VER and Na density. The first estimate of the Na profile is then used to determine the corresponding self absorption correction, followed by the determination of another Na density profile estimate. The self-absorption correction is based on the pre-calculated dependence of transmission as a function of Na slant column density (see Figure 30). During each forward model calculation – from [Na] to LER profiles – the Na slant column density between an atmospheric layer segment and SCIAMACHY is calculated and the transmission curves shown in Figure 30 are applied. Details on the calculation of the transmission curves are provided in Langowski et al. (2016). Additional iterations are performed until the Na densities do not change by more than 1 % at all altitudes between 80 and 105 km. Due to the non-linearity of the self absorption correction it is conceivable that the retrieval diverges. However, diverging retrievals have not occurred.

Figure 31 shows in the top panel the time and tangent height variation of the observed LER profiles (in Rayleigh) for the year 2007 and averaged over the 30° S – 30 ° N latitude range. The bottom panel of the Figure shows the variation of monthly averaged GOMOS ozone concentration for the same year. Both panels show clear evidence of the well-known semi-annual variations at low latitudes.

12.4.2 Sample retrieval results

Figure 32 shows sample retrieval results for November 2008 and a branching ratio of $f = 0.09$. The top panel displays the inverted VER profiles for the first (black) and the following iterations. The final iteration is shown in red. The dashed lines shown around every VER profile represent the propagated error. The LER errors used for this purpose correspond to the standard errors of the mean of the monthly averaged LER profiles. The LER profile and its errors are shown in black in the bottom panel of Figure 32. The red line in the bottom right panel corresponds to the reconstructed or forward modelled LER profile after the last iteration step. The fact that the observed LER profile is well reproduced by the retrieval provides an important consistency check. The middle panel of Fig. 32 shows the retrieved Na profiles after the first (black) and the following iterations. The peak altitude of about 92 km and the peak density of 2000 – 3000 atoms cm^{-3} are now briefly compared to independent studies. Na profiles in the MLT are also retrieved from SCIAMACHY dayglow observations (Langowski et al., 2016). At low latitudes Langowski et al. (2016) find peak altitudes of about 93 km and peak densities typically between 2000 and 3000 atoms cm^{-3}, in good overall agreement with the SCIAMACHY nighttime retrievals presented here. Langowski et al. (2016) also compared the SCIAMACHY daytime retrievals to satellite observations with OSIRIS and GOMOS, as well as LIDAR observations at northern mid and high latitudes and found very good overall agreement. We can therefore conclude that the SCIAMACHY Na nightglow retrievals are in good agreement with independent observations.

The upper panel of Fig. 33 shows comparisons of the Na vertical column density retrieved from SCIAMACHY nightglow observations (red line and symbols) with SCIAMACHY dayglow retrievals (blue line) and GOMOS stellar occultation retrievals (green line) for the year 2008, $f = 0.09$ and the 30° S – 30° N latitude range. Apparently, the SCIAMACHY nighttime retrievals exhibit more variability – most likely due to lower SNR – but the annually averaged vertical column density values agree to within 10%. The lower panel of the Fig. shows a comparison of annually averaged Na profiles. Again, there are some differences, but the overall agreement can be considered good, providing an important confirmation of the Chapman excitation mechanism and showing that an effective branching ratio of $f = 0.09$ leads to realistic results, in agreement with the study by Clemesha et al. (1995). A more detailed validation study will be performed in the future as part of the MesosphEO project.

12.4.3 Retrieval errors

We now briefly discuss possible error sources for the Na profile retrieval. A comprehensive sensitivity analysis was recently described by von Savigny et al. (2016) and the main results are briefly described here. von Savigny et al. (2016) estimated the effect of uncertainties of all relevant parameters required to retrieve Na density profiles from SCIAMACHY Na D line nightglow observations, including uncertainties in O_3, neutral density, temperature, rate constants and the branching ratio f. In addition, the contribution of random measurement errors was determined. Table 23 provides an overview of the considered error sources and their contribution to the total uncertainty.

Determination of a total uncertainty is essentially impossible in a strict mathematical sense. Simply adding the individual relative uncertainties would lead to an overestimation of the actual retrieval uncertainties. The approach taken is that the variances of the individual uncertainty contributions are added to yield the total variance. The obtained total uncertainty estimate is shown in the last row of Table 23 and amounts to 30 – 40 % for the 90 – 100 km altitude range. One of the largest uncertainty contributions is due to the uncertainty in f – as expected. Below and above the Na density peak random uncertainties dominate. Improvement in the knowledge of the branching ratio f from laboratory studies will reduce the uncertainty on the determination of Na concentration using this method.

Parameter	Perturbation	85 km	90 km	95 km	100 km
Branching ratio f	+0.01	-11.7 %	-15.6 %	-16.4 %	-15.3 %
Temperature	+10 K	-0.7 %	-4.3 %	-5.0 %	-4.5 %
Ozone	+5 %	-4.4 %	-7.4 %	-8.0 %	-7.4 %
Neutral density	+10 %	-5.2 %	-1.4 %	-0.7 %	-0.4 %
Random uncertainty	n.a.	50.5 %	17.0 %	10.5 %	27.7 %
k_1	+10 %	-8.3 %	-13.8 %	-14.7 %	-13.8 %
k_3	+10 %	-2.6 %	-0.7 %	-0.4 %	-0.2 %
Total Uncertainty	n.a.	53.0 %	28.3 %	26.2 %	35.6 %

Table 23: Overview of sensitivity study results for the Na profile retrieval (taken from von Savigny et al. (2016)).

13. Noctilucent Clouds

13.1 GOMOS (LATMOS)

GOMOS limb-scatter observations allow the determination of altitude and brightness of NLCs. The two fast 1 kHz photometers centred at 470 and 650 nm are used for the NLC retrieval (Pérot et al., 2010). The photometer signal includes the star signal that is estimated at high tangent altitude and removed. A careful estimation of the stray-light, coming from a the direct sun and from the earth surface and clouds, has to be made before the analysis. In addition UV-visible spectra of the bright limb can be used for the determination of the mean particle radius. The GOMOS NLC measurements have been used to study the asymmetry between the two hemispheres in terms of altitude, brightness and frequency occurrence of NLCs. In MesosphEO project a new analysis of NLC parameters will be made covering the full life of ENVISAT (2002-2012) starting from the IPF 6.01 version of Level 1b GOMOS data. Level 2 product at single occultation level and Level 3 products averaged over latitude bands and time periods will be created.

Level 2 Single occultation products

1. Extraction signal of fast photometers for daylight occultations in GOMOS IPF6 Level1b data. Seasonal and latitudinal limits
2. Subtraction of the stray light using an algorithm derived from the GOMOS bright limb project.
3. Detection of the presence of a NLC. A 3rd degree polynomial fit is applied to the flux curve of the two photometers between 55 and 100 km. In absence of NLC the fit follows well the exponential decrease of the Rayleigh scattering profile and the chi2 of the fit is near 1. If the chi2 of the fit exceeds a threshold of 1.8 for the two photometers we consider that a NLC is present. A visual inspection is made to eliminates false detections (less than 4
4. Retrieval of useful information Detection flag (presence of NLC or not) Altitude of maximum radiance Intensity of maximum radiance

Level 3 averaged products 5-day mean averaged products in 5°-wide latitude bands
Extracted from Level 2 NLC products:

- Frequency of NLC occurrence (number and percentage of PMC detections)
- Mean altitude of maximum radiance
- Mean intensity of maximum radiance

Level2 and Level 3 products will be stored in NetCDF format

13.2 MIPAS (KIT/IAA)

The V5r_PMC_m20 retrieval of polar mesospheric clouds from MIPAS is described in detail in López-Puertas et al. (2009) and García-Comas et al. (2016) and it is based in the following equations.

Assuming optically thin conditions, the limb thermal emission at tangent altitude z_t from a layer of ice particles is given by

$$L(z_t) = \int \epsilon(x,\nu) B[T(x),\nu] \, \mathrm{d}x \, \mathrm{d}\omega \mathrm{d}\nu, \tag{50}$$

where ν is wavenumber, $B(T,\nu)$ is the Planck function and T is the temperature of the emitting particles. The integral over ω is carried out along the instrument instantaneous field of view (FOV), the integral over x is done along its line of sight (LOS) and that over ν over certain wavenumber range $\Delta\,\nu$ (770–920 cm^{-1} in our case). $\epsilon(x,\nu)$ is the emissivity of ice particles that, if we assume them spherical and small compared to the emitting wavelength, is given by

$$\epsilon(x,\nu) = 6\pi \, N(x) \, V(x) \, \nu \ \mathrm{Im}\left(\frac{1-m^2}{m^2+2}\right), \tag{51}$$

where, N and V are the number density and volume of the ice particles, respectively, m is the complex refractive index of ice, and Im represents the imaginary part of the quantity in parenthesis. Inserting Eq. (51) into Eq. (50) and defining the ice volume density $\mathrm{v} = N\,V$, we get

$$L(z_t) = 6\pi \int \mathrm{v}(x) \, B(x,\nu) \ \mathrm{Im}\left(\frac{1-m^2}{m^2+2}\right) \ \nu \, \mathrm{d}\nu \, \mathrm{d}x \, \mathrm{d}\omega. \tag{52}$$

The ice volume density profiles v(x) are retrieved from limb measurements by pseudo-inversion of the vertically discretized and linearized expression of Eq. 52.

We give below the specifications of the current MIPAS PMC retrieval.

13.2.1 Strategy

V5r_PMC_m20 volume densities are derived from water ice thermal emissions around 12 μm (770–920 cm^{-1}) around the polar summer mesopause. MIPAS MA, NLC and UA mode limb measurements taken in the second half of June, July, and first half of August are used for the NH retrievals and taken in the second half of December, January, and first half of February are used for the SH retrievals (see Tables 1 and 2 in García-Comas et al., 2016). The retrieval is performed from 71.5 to 93.5 km using a linearly constrained least square fitting, where the Jacobians were calculated using the KOPRA radiative transfer algorithm (Stiller et al., 2002). The inversion was constrained by a Tikhonov-type scheme (Tikhonov, 1963) using a squared first-order difference matrix to obtain a reasonably smoothed vertical profile of volume densities. The ice particle volume density inversion is applied to MIPAS limb emission after the inversion of kinetic temperature. This is important because the emission of PMCs in the infrared depends, via the Planck function, on temperature. The calibrated spectra used are ESA's version 5.02/5.06 (Raspollini et al. (2010)).

The volume density and the kinetic temperature are assumed to be homogeneously distributed along the line of sight. Physical considerations suggest that the ice particles are warmer than the surrounding gas because they are heated up by absorption of radiation Rapp and Thomas (2006). Based on findings by these authors, we assumed an ice temperature that varies linearly with respect to the gas temperature from +1K at 80 km to +2K at 90 km.

MIPAS integrated (770–920 cm^{-1}) radiance profiles are corrected for an offset variable in altitude, latitude and time. The offset is composed by a constant-with-altitude component depending on latitude, attributed to the instrument calibration, and a component linearly dependent on altitude, most likely due to stray light. The offset is estimated using all scans measured each day. Its vertical slope is calculated from the average of all PMC-free radiance profiles at altitudes above 75 km. The constant-with-altitude component at each latitudinal band is calculated with the mean of the four uppermost altitudes for each individual scan.

13.2.2 Spectral region

Prior to the retrieval, MIPAS radiances in the $\Delta\,\nu$=770–920 cm^{-1} (MIPAS channel A) are integrated at each tangent altitude.

13.2.3 Discretization and setup

Forward model calculations are discretizided in a vertical grid with $\Delta z = 0.5$ km). Retrievals are performed from 71.5 to 93.5 km using the same grid. Due to the over-sampled retrieval grid, finer than MIPAS tangent height grid (generally, 3 km), stable solutions need from the use of a regularization (Tikhonov-type). FOV discretization is done using seven pencil beams for the numerical integration of the signal over the 3 km field.

13.2.4 a priori and atmospheric inputs

MIPAS V5r_PMC_m20 PMC retrieval setup uses the following inputs:

- Pressure, line of sight information and temperature from MIPAS retrieval version V5r_TLOS_m21 are used.
- Ice refractive indices are taken from Toon et al. (1994).

13.2.5 Error budget

The knowledge of the temperature of the ice particles is crucial for the retrieval of volume ice densities. Indeed, the main source of systematic error is that linked to the uncertainties in the kinetic temperature.

Assuming these uncertainties as the systematic errors provided by García-Comas et al. (2014) and listed in Table 26 in Sec. 14.4 of this document, the T_k induced ice volume density error is about 25-30%. Systematic errors originating from other sources are much smaller.

The noise error of the retrieved ice volume density is induced by both the instrumental noise and the temperature noise error. It is estimated from single profiles assuming: a noise-equivalent-spectral-radiance of 20 nW/(cm^{2}cm^{-1}sr) (MIPAS channel A), leading to a noise in the integrated radiances of 60 nW/(cm^{2}cm^{-1}sr), and a temperature noise error of 5K. These lead to 60% error in the single profile retrieved ice volume density.

The vertical resolution of the ice density vertical profiles, in terms of the half-width of the columns of the averaging kernel matrix depends on the observational mode. For the over-sampled NLC mode, it varies from 2.5-3 km at 81–86 km to 3.5–4 km at 90 km. For the MA and UA modes, it is 3.5–4 km. The error in the absolute pointing is about 200 m.

In order to guarantee the quality of the profile, we suggest to discard volume ice density profiles which contain values larger than 4–σ.

13.2.6 Improvements with respect to previous versions

The improvements of version V5r_PMC_m20 with respect to the previous V4O_PMC_m01 version are:

- Updated L1b database to V5.
- Updated versions of temperature and LOS (V5r_TLOS_m21) as inputs.
- Improved offset correction of the integrated radiance profiles by taking into account its altitude and latitudinal variations.
- Retrievals only performed for the scans with converged pressure-temperature profiles instead of the previously done latitude/longitude interpolation.
- Correction of a mistake in the calculation of the volume densities.

The ice volume densities retrieved with this new version nearly double those retrieved with the previous one (see Fig. 34). This is mainly caused by the correction in the calculation of the volume densities.

13.3 SCIAMACHY (EMAU)

The SCIAMACHY limb-scatter observations in the UV spectral range are used to (a) detect NLCs, and (b) retrieve the NLC particle size, based on certain assumptions on the particle shape and particle size distribution. Both the detection of NLCs and the retrieval of particle size is based on SCIAMACHY Level 1 data version 7.0x and the measurements were calibrated using the `scialc` tool provided by ESA with all calibration flags applied. Instrumental degradation – which is particularly pronounced in SCIAMACHY channel 1 used here – was corrected for by applying the `M-factor` correction during the calibration process.

13.3.1 NLC detection

The detection of NLCs in SCIAMACHY limb scatter observation is based on the limb radiance profiles at two UV wavelengths in SCIAMACHY channel 1 (clusters 3 and 4), i.e. λ_1 = 265 nm and λ_2 = 291 nm. More precisely, the limb radiances in 2 nm spectral intervals centered around these wavelengths are employed. The altitude of NLCs is with about 82 – 84 km remarkably constant, allowing a straightforward detection. NLCs always lead to enhancements in the limb radiance profiles, because (a) they scatter solar radiation, and (b) they are optically thin even in limb viewing geometry (Debrestian et al., 1997). Without NLCs present in the instrument's field of view, the limb radiances at wavelengths below 300 nm and above about 60 km tangent

height decrease monotonously with increasing tangent height. However, measurements with strong NLCs will be associated with a positive limb radiance gradient. The detection algorithm consequently checks for a positive limb radiance gradient between 76 km and 88 km tangent height and at both wavelengths (λ_1 and λ_2). If this condition is fulfilled, then an NLC is detected.

Weaker NLCs may not lead to a reversal of the vertical limb radiance gradient, but only affect the absolute value of the (negative) vertical limb radiance gradient. In order to detect these weaker clouds an additional cloud detection criterion was introduced: If the limb radiance ratio between limb radiances at two adjacent tangent heights

$$\Gamma_{\lambda_{1/2}} = \frac{LR_{\lambda_{1/2}}(TH_i)}{LR_{\lambda_{1/2}}(TH_{i+1})} \tag{53}$$

with $TH_{i+1} > TH_i$ is larger than 3 between 76 and 88 km tangent height and for each of the wavelengths λ_1 and λ_2, then an NLC is detected. The NLC detection is performed for both the northern and the southern hemisphere NLC seasons – in contrast to the NLC particle size determination described in the following subsection.

Additional information on the SCIAMACHY NLC detection method can be found in Robert et al. (2009) and Robert (2010).

13.3.2 NLC particle size retrievals

The basic idea behind the NLC particle size retrieval from SCIAMACHY limb-scatter observations in the UV spectral range is to determine the spectral dependence of the NLC scattered radiation and to relate it to precalculated spectral dependencies based on Mie or T-matrix (e.g. Mishchenko and Travis, 1998) calculations. Using limb radiance measurements at wavelengths smaller than 300 nm offers the great advantage that more than about 99% of the detected photons were only scattered once, i.e. the multiple scattering contribution becomes negligibly small (e.g. Kaiser and Burrows, 2003). This is a direct consequence of the massive absorption of radiation by ozone in the stratosphere. The slant optical depth of NLCs is less than about 5×10^{-3} (Debrestian et al., 1997), i.e. the effect of extinction by scattering or absorption by NLCs on the NLC scattering signal is negligible.

In single scattering approximation the NLC scattered limb radiance contribution $I_{NLC}(\lambda, \Theta)$ – being a function of wavelength λ and scattering angle Θ – can be expressed as:

$$I_{NLC}(\lambda, \Theta) = \chi \times \frac{d\sigma}{d\Omega}(\lambda, \Theta) \times S(\lambda) \tag{54}$$

Here, $\frac{d\sigma}{d\Omega}(\lambda, \Theta)$ corresponds to the differential scattering cross section of the NLC particle population, S is the solar irradiance spectrum, and χ is a spectrally neutral proportionality constant. An essential step is the separation of the NLC scattering contribution $I_{NLC}(\lambda, \Theta)$ from the Rayleigh background. This is done in the following way and described in more detail in Robert (2010): the SCIAMACHY limb measurements carried out during the NLC seasons, but without NLC detections are used to construct a Rayleigh background climatology comprising the tangent height and spectral dependence of the Rayleigh scattering contribution. These climatological profiles are then linearly scaled to the limb radiances above NLC altitude for limb measurements with NLC detections, and the scaled Rayleigh background is then subtracted. This approach turned out to be more robust than the approach initially used in von Savigny et al. (2004), which consisted of a logarithmic extrapolation of the limb radiance profiles at tangent heights below about 88 km, based on the vertical variation of the limb radiance at greater tangent heights. Once the Rayleigh background correction has been

performed, the inferred NLC scattering spectrum $I_{NLC}(\lambda, \Theta)$ can be analyzed further.

Equation 54 can be rearranged to yield the sun-normalized NLC scattering spectrum:

$$\frac{I_{NLC}(\lambda, \Theta)}{S(\lambda)} = \chi \times \frac{d\sigma}{d\Omega}(\lambda, \Theta) \tag{55}$$

The spectral dependence of this sun-normalized spectrum can be highly variable, but is typically – in a limited wavelength range – well approximated by a power law:

$$\frac{d\sigma}{d\Omega}(\lambda, \Theta) \propto \lambda^{\alpha} \tag{56}$$

with the spectral or Ångström exponent α. This spectral exponent is determined for the 264 – 300 nm spectral range from the Rayleigh corrected and sun-normalized NLC scattering spectra observed with SCIAMACHY.

In order to retrieve NLC particle size from the SCIAMACHY measurements model simulations of the spectral dependence of the differential scatter cross section are required. These model simulations depend on several essential assumptions:

- Particle size distribution (PSD):
  Various particle size distributions have been assumed in the past to retrieve NLC particle size, including mono-modal normal (e.g. Baumgarten and Fiedler, 2008) and log-normal PSDs (e.g. von Savigny and Burrows, 2007), exponential PSDs (e.g. Bailey et al., 2015) and even a monodisperse PSD (e.g. J. and Witt, 2001). At a particle size workshop held in fall 2014 at the Meteorological Institute of Stockholm University, most of the existing experimental data sets on NLC particle sizes were compared, and it was found that the best agreement between these observations is achieved with a mono-modal log-normal particle size distribution with a width of σ = 1.52. However, since the actual NLC PSD is not known, the SCIAMACHY retrievals are performed for a suite of different assumptions on PSD parameters.

- Particle shape:
  Initially most studies assumed spherical NLC particles. The exact particle shape is still unknown, but given the solid nature of NLC particles, a spherical shape appears extremely unlikely. Currently, most studies assume spheroidal particles (prolate or oblate) with varying aspect ratios. The currently usually used particle shapes are spheroidal needles or plates with an aspect ratio of 2.

Figure 35 shows as an example the dependence of the Ångström exponent for the 265 – 300 nm spectral range as a function of scattering angle and mean radius for an assumed normal PSD and cylindrical particles. The SCIAMACHY limb-scatter observations in the northern high latitudes are characterized by scattering angles between about 20° and 70°. The white dashed lines in Figure 35 indicate as an example the scattering angles at 69° N for both the ascending (poleward) and descending (equatorward) leg of an orbit. Note that during hemispheric summer a large part of the polar cap is illuminated by the sun, i.e. limb-scatter observations are possible during both ascending and descending legs. Taking into consideration that NLC particle radii are generally smaller than about 100 nm, Figure 35 shows that for SCIAMACHY NLC observations in the northern hemisphere, there exists a unique relationship between Ångström exponent and mean radius. This is, however, not the case for SCIAMACHY limb-scatter observations in the southern hemisphere – with scattering angles of 130 – 160°. There are evidently typically more than one particle radius values associated with a given Ångström exponent within the range of possible particle sizes, i.e. a unique determination of the mean radius is not possible for SCIAMACHY limb observations in the southern hemisphere. For this reason, NLC particle sizes are only retrieved from SCIAMACHY limb-scatter observations in the northern hemisphere.

13.3.3 NLC particle size retrieval errors

In case of the NLC particle size retrieval it is not possible to provide an error estimate which is generally valid. This is due to the fact that the optical thickness of NLCs and hence their backscatter ratio (ratio of NLC-scattered radiance and Rayleigh-scattered radiance) is highly variable. This is a consequence of the strong dependence of the particle scattering cross section on particle size – which is $\sigma(r) \propto r^6$ in the Rayleigh limit and about $\sigma(r) \propto r^4 \ldots r^5$ for typical NLC particle sizes. The error characterization performed so far considers three components: (a) errors in the determination of the Ångström exponent obtained from the spectral fit (eqn. 56); (b) errors introduced by the choice of solar irradiance spectrum used in eqn. 55; and (c) errors caused by neglecting the extinction caused by O_3 along the line of sight.

The errors associated with (a) are currently propagated through the particle size retrieval and are used to provide a particle size estimate for every single particle size retrieval. Note that due to the strong non-linearity between particle size and NLC-scattered radiance, the relative error associated with (a) can be as low as a few % of the retrieved radius, and it may exceed 100%.

In terms of (b) we tested the use of different solar spectra for the determination of the Ångström exponent, i.e. SCIAMACHY solar irradiance spectra measured on arbitrarily selected days in 2003 and 2010, the SCIAMACHY solar irradiance spectrum prepared by Skupin et al. (2003), as well as several standard solar irradiance spectra that are part of the MODTRAN software package (i.e., spectra known as Cebula-Kurucz, Chance-Kurucz, New-Kurucz and Thullier-Kurucz spectra). Whether the SCIAMACHY 2003 or 2010 spectrum was used, had a negligible impact on the determination of the Ångström exponent (< 0.02). Using the Skupin et al. (2003) solar spectrum rather than the 2003 SCIAMACHY spectrum increased the Ångström exponent by about 0.13 – note that an increase in Ångström exponent leads to an increased particle size. The Cebula-Kurucz and Thullier-Kurucz spectra affected the Ångström exponent by less than about 0.18, compared to SCIAMACHY 2003. Larger differences were found, when comparing the Change-Kurucz spectrum (change in Ångström exponent of about -0.5) and the New Kurucz spectrum (change exceeding 2.0) with results based on the SCIAMACHY 2003 spectrum. The analysis showed that the impact of the choice of the solar spectrum on the retrieved NLC particles size is generally on the order of a few nm, except for the New Kurucz spectrum, which yields particle radii that can be 100% larger than the retrievals based on one of the other solar spectra. Concluding, the New Kurucz spectrum does not appear to be adequate for NLC particle size determinations in the 265 – 300 nm spectral range. Note that this may well be different for different spectral regions.

Regarding effect (c), i.e. the effect of the spectrally dependent extinction by upper mesospheric O_3 on the inferred Ångström exponent a first order estimation was carried out. MLS/Aura observations of middle atmospheric O_3 were used to obtain O_3 profiles for polar Arctic summer conditions. We then calculated the spectrally dependent extinction of radiation from the tangent point to the instrument and determined its impact on the spectral slope in the 265 – 300 nm spectral region. It was found that neglecting the extinction by O_3 affects the Ångström exponent by about 0.4 and leads to a systematic low bias in the retrieved NLC particle sizes. For typical NLC particle sizes, this effect leads to a particle size retrieval error of up to 30%.

13.3.4 Sample particle size comparisons

As part of the international NLC particle size initiative mentioned above, particle size retrievals from different satellite platforms and the ALOMAR RMR-LIDAR observations were compared. Fig. 36 shows as an example NLC size comparisons for July 2008 and an assumed log-normal PSD (with $\sigma = 1.52$) and retrieved from CIPS/AIM, SOFIE/AIM, SCIAMACHY, SBUV, OSIRIS/Odin and the ALOMAR LIDAR. Overall, differences between the different data sets occur, but the general agreement can be considered good. The SCIAMACHY retrievals roughly lie in the middle of the other data sets.

14. Temperature

14.1 ACE-FTS (UoT)

Temperature profiles are retrieved using the same approach as described in Sect. 2.1 for ozone. The retrievals are performed between altitudes of 15 and 125 km using 110 microwindows between 927 and 2444 cm^{-1}.

14.2 Dilution temperature from GOMOS (BISA)

14.2.1 How to improve the accuracy of temperature retrieval from refractive dilution?

The quality of temperature profile retrievals from inversion of diffractive dilution is strongly determined at high altitude by the transmittance S/N ratio. Therefore, for GOMOS stellar occultations, the only possibility is to increase S/N by binning transmittances, hence reducing the spatio-temporal resolution. However, there are also much brighter planet occultations available that cannot be considered as pointlike light sources. It is therefore interesting to generalize the retrieval technique to the case of extended light sources. We decided to address an extreme case by considering the refractive dilution effect from Sun occultations.

14.2.2 Refractive dilution of the Sun

In solar occultations from a LEO satellite without any imaging system, the observed transmittance is integrated over the angular size of the Sun, resulting in an apparent loss of vertical resolution for the retrieved vertical refractivity profile. However, this loss is apparent because the sampling rate of measurements is usually large with a strong overlap of the observed solar disks between two successive acquisitions that causes redundance. This redundance does not lead to an ill-conditioned inverse problem because the very large S/N ratio is not limited by the brightness of the source but only by the dynamical scale of the sensor. Still, the inverse problem consists of retrieving a profile of refracted angles from a signal produced by a double integration: one along the optical path and one along the angular range under which the Sun is observed. Assuming the spherical homogeneity of the atmosphere around the geolocation of the measurement, we can make use of the symmetry of the problem (see Fig. 37).

Hereafter we will consider the near-infrared domain where contributions of O_3 absorption and Rayleigh scattering may be neglected.

We consider that the Sun consists of horizontal slices spanning an angular domain described by the angle $\theta \in [\theta_b, \theta_t]$ where $\theta_b = -\arctan\left(\frac{\Delta}{2S}\right)$ and $\theta_t = -\theta_b$ respectively refer to the bottom and top edges of the Sun (Fig. 37) . Each slice is seen with the same refraction geometry: the rays are grazing the same spherical surface at the unrefracted tangent altitude h_θ located at a satellite-limb distance L_θ , whereas L and h refer to the Sun center.

The relation between these quantities is obtained by a rotation matrix as:

$$L_\theta = L\cos\theta + h\sin\theta \quad h_\theta = -L\sin\theta + h\cos\theta \tag{57}$$

We can express the total measured transmittance $T(h)$ as:

$$T(h) = \int_{\theta_b}^{\theta_t} G(\theta)(1 - L_\theta \frac{d\alpha_\theta}{dh_\theta})\, d\theta \tag{58}$$

where $G(\theta)$is a normalized brightness distribution related to the solar limb darkening and

$$\int_{\theta_b}^{\theta_t} G(\theta)\, d\theta = 1 \tag{59}$$

The apparent brightness of Sun is not homogeneous because radiation is emitted at different altitudes (i.e. different temperatures) in the photosphere and is attenuated through different layers. In this article, we will use the limb darkening parameterization of Neckel. The relative intensity of a slice subtended by angle θ (with respect to the intensity of the same slice if it would have a constant brightness of 1) can be obtained by integrating the solar limb darkening curve along the slice of constant θ.

The latitudinal dependence of the limb darkening parameterization $sld(\beta)$ is expressed as a function of the cosine of the emission angle β from the Sun surface by:

$$sld(\beta) = a_0 + a_1 \cos(\beta) + a_2 \cos(\beta)^2 + a_3 \cos(\beta)^3 + a_4 \cos(\beta)^4 + a_5 \cos(\beta)^5 \tag{60}$$

where the a_i and their wavelength dependence are given in Table 24. After integration across the solar disk along the horizontal direction, the brightness distribution is obtained as:

$$G(\theta) = 8\zeta \left(a_0 + \frac{\pi a_1}{2\Delta}\zeta + \frac{8a_2}{3\Delta^2}\zeta^2 + \frac{3\pi a_3}{2\Delta^3}\zeta^3 + \frac{128 a_4}{15\Delta^4}\zeta^4 + \frac{5\pi a_5}{\Delta^5}\zeta^5 \right) / \left(\pi \Delta^2 G_\lambda\right) \tag{61}$$

with

$$\zeta(\theta) = \sqrt{\frac{\Delta^2}{4} - S^2 \tan^2(\theta)} \tag{62}$$

and

$$G_\lambda = a_0 + \frac{2}{3}a_1 + \frac{1}{2}a_2 + \frac{2}{5}a_3 + \frac{1}{3}a_4 + \frac{2}{7}a_5 \tag{63}$$

a_0	$0.75267 - \frac{0.265577}{\lambda}$
a_1	$0.93874 + \frac{0.265577}{\lambda} - \frac{0.004095}{\lambda^5}$
a_2	$-1.89287 + \frac{0.012582}{\lambda^5}$
a_3	$2.4223 - \frac{0.017117}{\lambda^5}$
a_4	$-1.71150 + \frac{0.011977}{\lambda^5}$
a_5	$0.49062 - \frac{0.003347}{\lambda^5}$

Table 24: Table of solar limb darkening parameters valid for $0.422 < \lambda[\mu\text{m}]<1.1$

For the inversion, it is useful to work with the complementary transmittance $T_c(h) := 1 - T(h)$. The retrieval of $f(\theta; h) := \frac{d\alpha_\theta}{dh_\theta}$ is obtained from a set of m complementary transmittance measurements $T_c(h_i)$, recorded at successive nominal tangent altitudes h_i:

$$T_c(h_i) = \int_{\theta_b}^{\theta_t} G(\theta) L(\theta; h_i) f(\theta; h_i)\, d\theta \quad \{i = 1 \ldots m\} \tag{64}$$

It has to be underlined that the method used in solar occultations can produce useful data over 6 orders of magnitude. The quality of the data is strongly related to the possibility of the straylight removal, to the level of pointing stability during the acquisition of the reference radiance and during the occultation (typically 1 minute) and to the possibility of cloud screening at lower altitudes.

As occultation measurements are self-calibrating, it is then possible to process the refractive dilution curve to obtain the vertical profile of refraction angles. This is the basis of the method that can be implemented in a very direct way for punctual sources like stars or planets by integration of a simple differential equation. As the numerical integration proceeds downward from the exo-atmospheric domain, the method is particularly well suited for upper atmospheric measurements to the limit of the radiometric sensitivity and the pointing stability. For extended sources like the Sun, a complementary angular inversion is necessary but it leads to a well-conditioned problem due to the very high signal-to-noise ratio.

14.3 Rayleigh scattering temperature from GOMOS (LATMOS)

14.3.1 Principle

The spectrum of the limb sunlight scattering is observed during each star occultation at the same time than the star spectrum. In absence of scattering by aerosol and clouds particles, the observed signal is only due to Rayleigh scattering by air molecules and is directly proportional to atmospheric density. This is the case in the stratosphere above about 30-35 km and in the mesosphere in absence of NLCs. It is then possible to derive the vertical profile of temperature using the hydrostatic equation and the perfect gas law that relate atmospheric temperature, density and pressure. This method is commonly used in Rayleigh temperature lidars. Preliminary tests using GOMOS bright limb observations around 400 nm have shown the possibility to retrieve the temperature profile in the altitude range 35 to 89 km.

14.3.2 Algorithm

For all daylight observations, the limb scattering is estimated in 10 wavelength bands of 20-nm width each from 340 to 540 nm using the upper and lower background spectra.

In order to estimate the contribution of the straylight, a second order polynomial fit is made on the data with tangent altitude above the higher altitude where some signal from the limb scattering is expected, about 100 km. The fit is extrapolated to fthe ull altitude range 35-100 km and removed from the observed signal in order to extract the Rayleigh scattering contribution.

The Rayleigh scattering signal is proportional to the atmospheric density. The temperature profile is computed from the density profile using the methodology developed for Rayleigh lidars (Hauchecorne and Chanin, 1980; Keckhut et al., 1993). Two relations relate atmospheric temperature, pressure and density profiles:

- the perfect gas law : $PV = nRT$ where P is the pressure, V the volume, n the number of moles, R the gas constant and T the temperature
- the hydrostatic equilibrium $dP = -\rho g dz$ where g is the gravity acceleration and dz the altitude increment.

Using these two equations, it is possible to compute the temperature profiles assuming a seed pressure at the top of the profile (about 90 km) taken from the MSIS00 climatological model (Hedin, 1991), and integrating downwards the hydrostatic equation. An example is shown on Fig. 39.

In MesosphEO this method will be applied to the whole database of bright limb GOMOS observations from 2002 to 2012 in order to provide climatology of upper stratospheric-mesospheric temperature. The results will be validated using ground-based Rayleigh lidars from NDACC (Network for the Detection of Chemistry Composition Changes) and available satellite datasets (MIPAS, MLS-AURA, SABER-TIMED).

14.4 Mesospheric kinetic temperature from MIPAS (KIT/IAA)

The MIPAS V5r_T_m21 temperature retrieval baseline is based on the IMK/IAA algorithm in its extended version, allowing non-Local Thermodynamic Equilibrium (non-LTE) emissions through the calculation of non-LTE vibrational levels populations with the GRANADA model (Funke et al., 2012). The IMK/IAA Scientific Processor is described in more than 50 peer-reviewed publications (i.e., von Clarmann et al. (2003, 2009)). The retrieval is based on constrained inverse modeling of limb radiances. The basic retrieval equations, the methods for characterization of results through error estimates and vertical and horizontal averaging kernels, the iteration and convergence criteria and the regularization method are described in the Ozone Climate Change Initiative Algorithm Theoretical Basis Document (Ref.: Ozone_cci_ATBD_Phase2_V1_00_01, pp. 60-64, 2014). We give here important details specific of the temperature retrieval.

14.4.1 Strategy

Temperature is retrieved from the 15 μm spectral region, covered by the MIPAS band A (685–970 cm^{-1}), using ro-vibrational emissions of the CO_2 main isotope. The V5r_T_m21 retrieval strategy is described in García-Comas et al. (2012); García-Comas et al. (2014), which in turn is an extension of the retrieval of temperature from the MIPAS NOM measurements (6-68 km) (von Clarmann et al., 2003, 2009). Retrievals are performed from MIPAS limb emission measured in the MA (20-102 km), NLC (40-102 km) and UA (40-170 km) modes. Calibrated spectra are as supplied by ESA in version 5.02/5.06 (Raspollini et al. (2010) and references therein). The IMK/IAA processor retrieves temperature simultaneously with line of sight information, temperature horizontal gradients and microwindow-dependent continuum radiation and zero level calibration corrections (the latter, assumed constant with altitude). Water vapor and ozone vmr's are also jointly fitted in the log and linear domain, respectively. The retrieval is performed after a spectral shift retrieval and before the non-LTE retrieval of atmospheric species.

14.4.2 Discretization and setup

Retrievals are performed from the surface to 120 km over a discrete altitude grid of 1 km up to 50 km, 2 km at 50-100 km, 2.5 km at 100-105 km and 5 km at 110-120 km. This grid is a compromise between accuracy and efficiency and has been established during numerous test retrievals. Nevertheless, the forward calculations are performed using the finer grid (1 km) up to 88 km and 2 km above 88 km. The over-sampled retrieval grid, finer than MIPAS tangent height grid (generally, 3 km), makes the use of a regularization mandatory in order to obtain stable solutions.

Regarding the forward model setup, five pencil beams are used for the numerical integration of the signal over the 3, km field of view for the whole altitude range. This provides a larger convergence rate than when using less beams. A reduced width (by a factor of 2 compared to MIPAS V5r_T_m11) of the integration window (apodized instrument line shape function) is also used, which lead to smaller channel border effects. Additionally, modeling in spectral simulations of line-mixing effects using the Rosenkranz (1975) approximation and as described by Funke et al. (1998) is included. The latter is required due to the consideration of CO_2 Q-branches.

14.4.3 Microwindows

Microwindows are narrow spectral intervals suited for retrieval of temperature or species abundances profiles. Their optimal boundaries are selected after minimization of estimated errors (von Clarmann and Echle, 1998). Table 25 lists the altitude-dependent microwindows used here and stored in the so-called occupation matrices. Starting from a set of microwindows generated for the MIPAS temperature NOM retrieval (von Clarmann et al., 2009), the set of microwindows was extended in the mesosphere and lower thermosphere by including stronger emission lines, even if affected by non-LTE, more sensitive to the rarefied upper atmosphere. Particular care has been taken to avoid saturated line center regions at lower mesospheric tangent heights in order to minimize vertical crosstalk. Strong Q-branch emissions are used, resulting in an improved temperature and pointing sensitivity not only in the mesosphere but also in the stratosphere (due to the inclusion of the hot band Q-branch emissions around 740 and 791 cm^{-1}).

14.4.4 A priori and atmospheric inputs

Thorough comparisons with independent measurements have lead to the choices listed below. MIPAS V5r_T_m21 temperature retrieval setup uses the following inputs:

- Realistic temperature-pressure *a priori*, which is a merging of ECMWF high resolution operational data assimilation and forecasting system temperatures for pressures larger than 0.1 hPa and NRLMSISE-00

Table 25: Microwindows used in MIPAS V5r_T_m21 temperature retrieval. Altitude levels should be read vertically.

Micro window cm^{-1}	Altitude km
	1 1 2 2 2 3 3 3 3 4 4 4 5 5 5 6 6 6 6 7 7 8 8 9 12
	5 8 1 4 7 0 3 6 9 2 5 8 1 4 7 0 3 6 9 2 5 0 5 0 0
(686.8125, 689.7500)	0 0 0 0 0 0 0 0 0 1 1 1 1 1 1 1 1 1 1 1 1 1 1 1 1
(689.8750, 692.6250)	0 0 0 0 0 0 0 0 0 1 1 1 1 1 1 1 1 1 1 1 1 1 1 1 1
(699.4375, 702.3750)	0 0 0 0 0 0 0 0 0 1 1 1 1 1 1 1 1 1 1 1 1 1 1 1 1
(719.6250, 722.5000)	0 0 0 0 0 0 1 1 1 1 1 1 1 1 1 1 1 1 1 1 1 1 1 1 1
(731.2500, 731.8125)	0 0 1 1 1 1 1 1 1 1 1 1 1 1 1 1 1 1 1 1 0 0 0 0 0
(740.3750, 742.8750)	0 0 0 0 0 0 1 1 1 1 1 1 1 1 1 1 1 1 1 0 0 0 0 0 0
(744.3125, 745.5000)	0 0 1 1 1 1 1 1 1 1 1 1 1 1 1 1 1 1 1 1 0 0 0 0 0
(748.9375, 749.8125)	1 1 1 1 1 1 1 1 1 1 1 1 1 1 1 1 1 1 1 1 0 0 0 0 0
(765.8750, 766.5625)	0 0 1 1 1 1 1 1 1 1 1 1 1 1 1 1 1 1 1 1 0 0 0 0 0
(780.4375, 780.6250)	1 1 1 1 1 1 1 1 1 1 1 1 1 1 1 1 1 1 1 1 0 0 0 0 0
(791.1875, 792.6875)	0 1 1 1 1 1 1 1 1 1 1 1 1 1 1 1 1 1 1 0 0 0 0 0 0
(798.1250, 798.5000)	0 0 1 1 1 1 1 1 1 1 1 1 1 1 1 1 1 1 1 1 0 0 0 0 0
(810.8125, 811.0625)	1 1 1 1 1 1 1 1 1 1 1 1 1 1 1 1 1 1 1 1 0 0 0 0 0
(812.2500, 812.5625)	1 1 1 1 1 1 1 1 1 1 1 1 1 1 1 1 1 1 1 1 0 0 0 0 0

otherwise (Recall that the *a priori* profiles used in a first order difference Tikhonov regularization do not substantially influence the retrieved variable directly but constrain predominantly its vertical gradient).

- An *a priori* of 3 nW·(cm^{2}cm^{-1}sr)$^{-1}$ is used for the offset regularization. This was decided after noting a systematic radiance offset (López-Puertas et al., 2009) and that unregularized offset temperature retrievals lead to problems during polar summer (crosstalk).

- Spectroscopic and corresponding line mixing data from HITRAN 2008 (Rothman et al., 2009).

Additionally, several inputs affect the non-LTE populations of the vibrationally excited emitting molecules calculated with GRANADA. More information on the effect of each input on the CO_2 15μm levels and on the retrieved temperature can be found in Funke et al. (2012) and García-Comas et al. (2014). The non-LTE model inputs used in V5r_T_m21 retrievals are:

- Atomic oxygen climatology from the WACCM model (Garcia et al., 2007) in its specified dynamics (SD) configuration. SD-WACCM (also called WACCM4) constrains the meteorological fields in the troposphere and stratosphere with observations by nudging to NASAÕs Modern-Era Retrospective Analysis (MERRA) (Rienecker et al., 2011) reanalysis data (temperature and horizontal winds) up to approximately 1 hPa (Lamarque et al., 2012).

- Carbon dioxide climatology from the SD-WACCM model using a Prandtl number value of 4. The SD-WACCM CO_2 trend correction takes into account its observed emission growth.

- Non-LTE collisional rate constants set as in Funke et al. (2012).

- Solar fluxes required in the non-LTE model are calculated considering the temporal variations of the Sun-Earth distance. Attenuation by solar Fraunhofer lines is taken into account (Hase et al., 2006). The solar background radiance is expressed as a blackbody with effective temperature T_e (in K) depending on wavenumber ν (in cm^{-1}) through T_e=5450+0.25(ν-2000). This parameterization is similar to that

Table 26: Summary of main systematic and random errors in MIPAS kinetic temperature (in K). Values in parenthesis are the errors in polar summer. 'Non-LTE' includes errors due to uncertainties in the collisional rates and the atomic oxygen used in the non-LTE model. 'Total Sys.' is the root sum square of all the systematic errors.

Source	Altitude [km]				
	20	55	70	85	100
Systematic					
Non-LTE	0.0(0.0)	0.0(0.0)	0.1(0.1)	1.4(4.7)	11(30)
CO_2	0.03	0.01	0.12	2.3	1.6
N_2O_5	0.02	0.03	0.12	0.08	0.05
O_3	0.19	0.07	0.02	0.18	0.14
Spectroscopy	0.9	1.0	0.7	0.5	0.4
Shift	0.01	0.02	0.1	0.3	0.2
Gain	0.09	0.3	0.2	0.4	0.7
ILS	0.14	0.3	0.4	1.7	0.9
Total Sys.	0.9(0.9)	1.1(1.1)	0.9(0.9)	3.3(5.6)	11(30)
Random					
Noise (single scan)	0.5	1.0	1.5	5.1	6.6

developed by Platnick and Fontenla (2008) for 3.7 μm, and they agree within 0.5–-1% at that wavelength.

The forward model also considers horizontal gradient corrections for non-LTE populations, accounting for changes along the line of sight, particularly when the poles are intercepted during the solstices.

14.4.5 Error budget

The error budget includes the mapping of the measurement noise on the retrieved temperatures, as well as the propagation of uncertainties of model parameters onto the results. Noise-induced retrieval errors and vertical resolutions are estimated routinely for each individual profile by the retrieval algorithm. Systematic errors related to the mapping of uncertain model parameters are estimated for representative profiles only. Table 26 summarizes the estimated systematic and random errors in MIPAS retrieved kinetic temperature.

The temperature random retrieval error arises mainly from the propagation of measurement noise through the retrieval. These are calculated assuming an wavelength-dependent average 17 nW/(cm^{2}cm^{-1}sr) noise-equivalent-spectral-radiance. Typical values are 0.2–0.5 K below 50 km, 0.5–2 K at 50–70 km, and 2–7 K above.

The vertical resolution of the temperature retrieval is the full width at half maximum of the averaging kernels rows. Typical values of average vertical resolution are 4 km below 35 km, 3 km at 35–50 km, 4–6 km at 50–90 km, and 6–10 km above.

There are several sources of systematic errors affecting the non-LTE retrievals of kinetic temperature. The most important above the mid-mesosphere are due to the modeling of the non-LTE populations of CO_2 vibrational levels, in particular, those produced by uncertainties in the collisional rates or in the abundance of other species involved in the non-LTE processes. Additionally, the carbon dioxide abundance uncertainty contribute to the systematic error in this region. Uncertainties in the spectroscopy, the gain calibration, the instrument line shape and the interfering species introduce systematic errors particularly below the mid-mesosphere. The overall estimated systematic error is 1 K below 70 km, 1–3 K from 70 to 85 km and 3–11 K from 85 to 100 km. Due to the larger non-LTE effects in the polar summer, these values increase to 1–6 K from 70 to 85 km and 6–30 K from 85 to 100 km under those conditions.

Two criteria are further usually applied to the retrieved IMK/IAA data in order to guarantee the quality of the profile: 1) results where the diagonal value of averaging kernel is less (in absolute value) than 0.03 are considered non-trustful. 2) results related to parts of the atmosphere non-sensed by MIPAS (i.e. below the lowermost used tangent altitude) are considered non-trustful.

14.5 Thermospheric temperature from MIPAS (KIT/IAA)

MIPAS V5r_TT_621 thermospheric temperature retrieval is based on constrained inverse modeling of non-LTE limb radiances. That is performed using the IMK/IAA Scientific Processor (von Clarmann et al., 2003, 2009) extended with the non-LTE GRANADA algorithm (Funke et al., 2012), which is able to cope with non-LTE emissions. Funke et al. (2001) describe the particularities of the retrievals under consideration of non-LTE. The basic retrieval equations, the methods for characterization of results through error estimates and vertical and horizontal averaging kernels, the iteration and convergence criteria and the regularization method are described in the Ozone Climate Change Initiative Algorithm Theoretical Basis Document (Ref.: Ozone_cci_ATBD_Phase2_V1_00_01, pp. 60-64, 2014). Thermospheric temperature is reliably retrieved from 100 km to 170 km from MIPAS measurements in the the UA mode. Below 100 km, the profiles are constrained to v5r_T_621 data such that the valid range of this data product spans from 40–170 km. A description of the specifics of the thermospheric temperaure retrieval V5r_TT_621 follows.

14.5.1 Strategy

Thermospheric temperature is retrieved from spectral lines covering ro-vibrational emissions of the NO main isotope, covered by the MIPAS band D (1830–1940 cm^{-1}). Retrievals are performed from MIPAS limb emission measured in the UA (40-170 km) mode at tangent heights $>$90 km. Non-LTE is considered as described in Funke et al. (2012) and in Section 4.2 of this document. The retrieval is performed simultaneously to that of V5r_NOT_621 thermospheric nitric oxide (see Sec. 5). In addition, zero level calibration corrections (assumed constant with altitude) are fitted jointly. The retrieval is performed after a spectral shift retrieval and the non-LTE retrievals of temperature and abundances of ozone, water vapour, nitrous oxide and methane, nitric dioxide, and nitric oxide below 100 km.

Linear horizontal NO gradients in the latitudinal and longitudinal directions are fitted jointly with the NO vmr. Additionally, non-linear horizontal inhomogenities along the instrument's line-of-sight occur in thermospheric path segments at polar/sub-polar latitudes due to the complex structure of aurorally produced NO. In the current retrieval version, this is accounted for by applying 3D radiative transfer and introducing an a priori horizontal shape of the auroral oval (obtained from the NOEM model (Marsh et al., 2004)) which is then implicitly scaled by the joint-fitted linear horizontal NO gradients in the latitudinal and longitudinal directions.

14.5.2 Discretization and setup

The retrievals are performed from the surface to 200 km over a discrete altitude grid of 1 km up to 56 km, 2 km at 56-70 km, 2.5 km at 70-105 km, and 5 km at 105-200 km. The selected grid provides balanced accuracy and efficiency. The forward calculations are performed using that same grid. The over-sampled retrieval grid, finer than MIPAS vertical sampling (approximately 3 km), makes the use of a regularization mandatory in order to obtain stable solutions. An altitude-dependent Tikhonov-type smoothing constraint is used for NO and T. Below 95 km, a strong diagonal constraint is added such that the a priori (obtained from the prior retrieval of NO and temperature at these altitudes) is reproduced. Horizontal NO_x gradients are regularized by a strong and vertically variable diagonal constraint towards a zero a priori.

The numerical integration of the signal over the 3 km field of view is done using five pencil beams. The selected width of the integration window (apodized instrument line shape function) has been chosen to comply with an apodization accuracy of 0.1%.

14.5.3 Microwindows

The retrievals are performed from selected spectral regions (micro-windows) which vary with tangent altitudes in order to optimize computation time and minimize systematic errors (von Clarmann and Echle, 1998). The microwindows used in the thermospheric temperature and nitric oxide retrieval are listed in Table 27. These height dependent combinations of micro-windows were selected with a trade-off between computation time and total retrieval error. See Bermejo-Pantaleón et al. (2011) for details.

Table 27: Microwindows and number of internal sub-microwindows at each tangent altitude used in MIPAS V5r_TT_m21 thermospheric temperature and MIPAS V5r_NOT_m21 nitric oxide retrieval. Altitude levels should be read vertically.

Microwindow cm^{-1}	Altitude km
	1 1 1 1 1 1 1 1 1 1 1 1 1 1 1 1 1
	9 9 9 9 0 0 1 1 2 2 3 3 4 4 5 5 6 6 7
	0 3 6 9 2 5 0 5 0 5 0 5 0 5 0 5 0 5 0
(1837.8125,1838.2500)	1 1 1 1 1 1 1 1 1 1 1 1 1 1 1 1 1
(1842.8125,1843.1875)	1 1 1 1 1 1 1 1 1 1 1 1 1 1 1 1 1
(1849.0625,1853.9375)	2 2 2 2 2 2 2 2 2 2 2 2 2 2 2 2 2
(1857.0000,1861.1250)	2 2 2 2 2 2 2 2 2 2 2 2 2 2 2 2 2
(1863.5000,1863.8750)	1 1 1 1 1 1 1 1 1 1 1 1 1 1 1 1 1
(1880.7500,1881.2500)	1 1 1 1 1 1 1 1 1 1 1 1 1 1 1 1 1
(1887.2500,1891.1250)	2 2 2 2 2 2 2 2 2 2 2 2 2 2 2 2 2
(1896.7500,1900.8750)	3 3 3 3 3 3 3 3 3 3 3 3 3 3 3 3 3
(1902.9375,1906.8750)	3 3 3 3 3 3 3 3 3 3 3 3 3 3 3 3 3
(1909.0000,1912.9375)	3 3 3 3 3 3 3 3 3 3 3 3 3 3 3 3 3
(1914.8125,1915.1250)	1 1 1 1 1 1 1 1 1 1 1 1 1 1 1 1 1
(1927.1250,1931.8750)	3 3 3 3 3 3 3 3 3 3 3 3 3 3 3 3 3
(1935.3125,1935.6875)	1 1 1 1 1 1 1 1 1 1 1 1 1 1 1 1 1

14.5.4 A priori and atmospheric inputs

MIPAS V5r_TT_621 thermospheric temperature and MIPAS V5r_NOT_621 nitric oxide retrieval setup uses the folllowing inputs:

- A priori is taken from NO (V5r_NO_621) retrieved in a previous step below 100 km. Above, the a priori is taken from the NOEM model (Marsh et al., 2004). Since the latter is an empirical model for thermospheric NO daytime concentrations, a SZA-dependent scaling factor obtained from the MIPAS UA day/night climatology is applied for nighttime conditions.
- Pressure, line of sight information, temperature and temperature horizontal gradients from MIPAS retrieval version V5r_T_m21 is used below 100 km as a priori. Above, pressure and temperature are taken from MSIS. Line of sight is taken from the ESA engineering information, considering the pointing correction retrieved from the uppermost tangent height of the V5r_T_m21 retrieval.
- Spectroscopic data from HITRAN 2008 (Rothman et al., 2009).

Several inputs are needed for the calculation of the ro-vibrational non-LTE populations of the excited emitting molecules by GRANADA. Funke and López-Puertas (2000) provide information on the effect of each input on the NO levels. The non-LTE model inputs used in V5r_TT_621 (and V5r_NOT_621) retrievals are:

- Ozone from the previously retrieved ozone in its version V5r_O3_m22.
- Previously retrieved nitric dioxide in its version V5r_NO2_m21.
- Atomic oxygen concentration derived from the retrieved ozone (V5r_O3_m22) below 95 km, from WACCM in its specified dynamics (SD) configuration (Garcia et al., 2007) at 95–135 km, and from MSIS above.
- Atomic nitrogen (N(^4S)) concentrations above 85 km from MSIS, below from photochemical model.
- (N(^2D))abundances have been calculated as described in Vitt et al. (2000), considering an auroral production based on ionization rates from the Atmospheric Ionization Module Osnabrück (AIMOS version 1.6) model (Wissing and Kallenrode, 2009).
- Non-LTE collisional scheme and rate constants as in Funke et al. (2012).
- Solar fluxes required in the non-LTE model are calculated considering the temporal variations of the Sun-Earth distance. Attenuation by solar Fraunhofer lines is taken into account (Hase et al., 2006). The solar background radiance is expressed as a blackbody with effective temperature T_e (in K) depending on wavenumber ν (in cm^{-1}) through T_e=5450+0.25(ν-2000). This parameterization is similar to that developed by Platnick and Fontenla (2008) for 3.7 μm, and they agree within 0.5–-1% at that wavelength.

14.5.5 Error budget

The error budget described here considers the propagation of the measurement noise and of the uncertainties of model parameters onto the retrieved nitric oxide abundances. Noise-induced retrieval errors and vertical resolutions are estimated routinely for each individual profile by the retrieval algorithm. Systematic errors related to the mapping of uncertain model parameters are estimated for representative profiles only.

The uncertainties assumed for the estimation of the errors have been: 1% for gain calibration, 3% for the instrument line shape, 150 m for elevation pointing, and 10% for spectroscopic data (line intensities and broadening coefficients; based on estimates by J.-M. Flaud, personal communication, 2008). The thermospheric NO noise error is calculated assuming a 2 nW/(cm^{2}cm^{-1}sr) noise-equivalent-spectral-radiance for channel D. Typical values are 10–30% for high solar/geomagentic activity conditions and 20–50% for low activity conditions.

The overall estimated error is dominated by propagation of instrumental noise. The modeling of the non-LTE populations of the NO vibrational and rotational levels is a major systematic errror source due to uncertainties in the atomic oxygen and nitrogen profiles. Another relevant systematic error source is the uncertainty of the absolute pointing correction, retrieved within V5r_T_m21.

The vertical resolution of MIPAS retrieved thermospheric temperature is the full width at half maximum of the averaging kernels rows. Average vertical resolution is 5–10 km for high solar/geomagnetic activity conditions and 10–20 km for low activity.

Results where the diagonal value (for individual profiles) or the mean diagonal value (for averages) of the averaging kernel is less (in absolute value) than 0.03 should be discarded in order to guarantee the quality of the profile.

Table 28: Summary of main errors in MIPAS thermospheric temperature vmr. 'NLTE' includes errors due to uncertainties in the collisional rates used in the non-LTE model. 'Total' is the root sum square of all errors. Numbers in brackets refer to low solar/geomagnetic activity conditions.

Height km	Noise K	Pointing K	Gain K	ILS K	Spectroscopy K	NLTE K	Total K
100	5 (5)	1	1	2	2	3	7 (7)
110	7 (10)	2	1	2	2	8	11 (13)
120	20 (50)	5	1	2	2	10	23 (51)
130	30 (60)	7	1	2	3	15	35 (62)
140	30 (60)	10	2	2	4	15	35 (63)
150	30 (60)	7	2	2	4	20	37 (64)
> 160	30 (50)	5	2	2	5	20	37 (54)

14.5.6 Improvements with respect to previous versions

V5r_TT_621 thermospheric nitric oxide baseline is an improvement of the previous V4O_TT_601 version. The changes from the previous version are:

- Updated L1b database to V5.
- Updated version HITRAN database from the 2004 to the 2008 version.
- Updated versions of temperature (V5r_T_m21), nitric dioxide (V5r_NO2_m21), and ozone (V5r_O3_m22).
- Revised atomic oxygen (SD-WACCM instead of MSIS below 135 km).
- Revised regularization scheme for NO and kinetic temperature.
- Inclusion of thermospheric horizontal inhomogenities related to the aurora (2D radiative transport).
- Improved NLTE modelling of chemical excitiation by N(^2D) due to improved photochemical modelling (consideration of particle-produced N(^2D) via AIMOS model)

The average impact on the thermospheric temperature retrieval after those changes are shown in Figs. 40 and 41. The daytime temperatures for the new version are generally warmer by 10–50 K, except for the polar summer below 140 km (up to 10 K colder). The nighttime temperatures for the new version are 30–50 K warmer above 125 km and upt to 10 K colder below.

14.6 OSIRIS (USask)

In the MLT region, there are 3 predominant mechanisms that produce $O_2(b^1\Sigma_g^+)$, leading to A-band emission (Bucholtz et al., 1986), as illustrated in Fig. 42. First, ground state O_2 can be excited into the $b^1\Sigma_g^+$ state through a collision with an O(^{1}D) atom that was produced via photolysis of O_2 or O_3. The second mechanism is resonant absorption in the Atmospheric Bands, mainly in the A-band and B-band. The third mechanism is a 2-step Barth-type chemical reaction, initiated by a 3-body collision between two atomic oxygen atoms and either a N_2 or O_2 molecule (O + O + M).

The OSIRIS spectral range is from 275 nm to 810 nm with approximately 1 nm spectral resolution and with a vertical field of view corresponding to 1 km at the tangent point, and the absolute limb pointing knowledge is better than 0.5 km at the tangent point. The instrument scans the limb at a rate of approximately 0.75 km/s

and at mesospheric altitudes the exposure time is nominally 2 s. The entire spectrum, from 275 to 810 nm, is obtained with each exposure.

The spectral region of interest within the O_2 A-band, approximately 759 - 767 nm, is dispersed on to 19 rows of pixels of the OSIRIS CCD array, each row has a spectral width of approximately 0.4 nm. For a given OSIRIS scan, 19 emission profiles are determined, one from each of the 19 pixel observation profiles. Each profile is inverted separately, yielding the O_2 A-band emission spectrum at each height within the profile. Each of the inverted spectra is then normalized such that the sum of intensities over the spectrum is equal to 1000 photons/s/cm^3 for comparison with the similarly normalized modelled spectra. This approach only requires an accurate relative intensity calibration rather than an accurate absolute calibration (Gattinger et al., 2009a).

OSIRIS limb radiance profiles are measured at different tangent heights, with a typical vertical difference of 1.5 km. Each of the 19 pixel profiles, with the dark current removed, are separately cubic spline interpolated on to a 1-km grid to give an observation profile **O**; it is assumed that both the latitude and longitude do not vary significantly between the first and last observations within the profile. The observed profile, **O**, is inverted using a form of the tomographic-like algorithm (Degenstein et al., 2003) to yield an emission intensity profile **V**. In this technique the atmosphere is assumed to be optically thin and is divided into concentric 1-km shells. The iterative tomographic procedure (Degenstein et al., 2003), Eq. (65), is implemented to construct an emission intensity profile **V**,

$$V_j^n = V_j^{n-1} \sum_i \left[\frac{O_i}{\sum_j L_{ij} V_j^{n-1}} \frac{L_{ij}}{\sum_i L_{ij}} \right], \tag{65}$$

where V_j is the calculated emission intensity within the jth atmospheric shell (assumed to be homogeneous), n is the iteration step, L_{ij} is the path-length of the ith observation line-of-sight through the jth atmospheric shell, and the observed signal $O_i = 2\sum_j L_{ij} V_j$.

The emission intensities and center wavelengths of 77 spectral lines within the A-band (759-767 nm) are calculated for emission temperatures between 50 - 500 K at 1 K intervals, using the A-band upper and lower state vibrational and rotational constants determined by Babcock and Herzberg (1948) and updated with values from the 2004 HITRAN spectroscopic database Rothman et al. (2005). For each temperature, the modelled emission line spectrum is convolved with the OSIRIS slit function and binned into wavelength intervals that correspond to the OSIRIS CCD pixelated spectrum in the A-band region. The modelled spectra are each normalized such that the sum of intensities over the spectrum is equal to 1000 photons/s/cm^3.

At each height, z, the inverted spectrum, **I**(z), is compared to the modelled emission spectra, **E**(T), which are pre-calculated at 1 K intervals for temperatures between 50 and 500 K. Both the inverted and modelled spectra have been normalized such that the sum of intensities over the spectrum is equal to 1000 photons/s/cm^3. The sum of the square difference between the inverted and modelled A-band spectra is calculated according to Eq. (66),

$$S(z,T) = \sum_p^N \left[I_p(z) - E_p(T) \right]^2, \tag{66}$$

where p is the pixel index and N is the number of pixels in the A-band spectra. The retrieved temperature at height z_i is taken as the temperature that minimizes $S(z_i, T)$. As the radiative lifetime for the A-band is 12 seconds, the $O_2(b^1\Sigma_g^+)$ relative distribution of rotational states is in LTE so that the retrieved temperature is the local atmospheric temperature.

14.7 SMR (Chalmers)

Temperature and water vapour profiles are retrieved simultaneously from the measurement of the same emission line (556.9 GHz), covered by the frequency modes 13 and 19. See Sec. 9.3 for more details on the retrieval parameters.

N.B.: *The reprocessing of the data set is in progress as part of an ESA project dedicated to it. Specific retrieval settings (in the table), figures showing typical averaging kernels and errors, as well as discussion about the improvements with respect to the previous L2 version (v2.3) will be added when the new products will be available.*

15. Metalic species from SCIAMACHY

15.1 SCIAMACHY MLT limb measurements (UB)

The described retrieval algorithm uses a special limb observation mode of the SCIAMACHY instrument referred to as the Mesosphere-Lower Thermosphere (MLT) limb measurements. In this mode SCIAMACHY scans the horizon at tangent heights from about 53 km to about 148 km with 3.3 km vertical sampling. This kind of measurements was performed since summer 2008 for one day each two weeks. In total there are 84 measurement days. The retrievals were done using Level 1 V7.03/7.04 data with calibration flags 1,2,4,5,7 with M-factor correction applied. All measurements during each measurement day were averaged accounting for a shift in the latitude of the ground pixels for neighboring orbits. All limb measurements from this averaged orbit data are passed to the retrieval algorithm to obtain the number densities of the target species on a 2D latitudinal and vertical grid. The Mg retrieval uses spectral range 283.5 - 287 nm while 278 - 281.9 nm range is employed for Mg^+.

The retrieval approach consist of two steps. First, the slant column emission signal is determined from the spectra of each measurement by separating the emission spectrum from the background signal. Then, a forward model and appropriate Jacobians are used to retrieve the number density of the target species from the slant column emissions obtained at the first step.

The background signal is mainly formed by Rayleigh and Raman scattering of solar electromagnetic radiation by air molecules. The latter is accounted for only in Mg retrieval. If needed, a correction for the Raman scattering (so-called Ring effect) is performed before forming the ratio of limb radiance and solar irradiance. The Rayleigh background is fitted as a straight line of this ratio for a small window around the emission lines, but excluding the emission lines. These ranges are 283.5 - 284.5 nm and 286 - 287 nm for Mg and 278 - 279 nm and 281.0 - 281.9 nm for Mg^+. After subtraction of the Rayleigh background, the ratio is multiplied with the solar irradiance again to obtain the pure emission spectrum. The result is fitted with the slit function of the instrument to obtain the slant column emission (SCE) signal. These steps are illustrated in Fig. 43.

The applied Ring effect correction is based on the assumption, that the Raman scattering part of the total scattered light is much smaller than the Rayleigh scattered part, and the Ring-effect can be linearized. This means that a second application of the Ring effect to the spectrum leads to the same changes as the first application. Under this assumption the Ring effect is artificially applied to the measured spectrum $I_1(\lambda)$, which already contains a contribution due to Raman scattering, to yield $I_2(\lambda)$ and the difference $I_1(\lambda) - I_2(\lambda)$ needed for a correction of the Ring effect and to retrieve the non Ring effect affected spectrum I_0:

$$I_2(\lambda) = I_1(\lambda) + \underbrace{\Delta I_{\mathrm{R}2}(\lambda)}_{I_2(\lambda)-I_1(\lambda)} \tag{67}$$

$$I_1(\lambda) = I_0(\lambda) + \underbrace{\Delta I_{\mathrm{R}1}(\lambda)}_{I_1(\lambda)-I_0(\lambda)} . \tag{68}$$

Under the assumption $\Delta I_{\mathrm{R}}(\lambda) = \Delta I_{\mathrm{R}2}(\lambda) = \Delta I_{\mathrm{R}1}(\lambda)$ it follows that

$$I_0(\lambda) = I_1(\lambda) - \Delta I_{\mathrm{R}} = 2I_1(\lambda) - I_2(\lambda). \tag{69}$$

To obtain the slant column densities of the target species, the slant column emissions obtained at the first

retrieval step are multiplied by 4π and divided by emissivity, γ. The latter is defined as

$$\underbrace{\gamma}_{\text{photons s}^{-1}} = \underbrace{P(\theta)}_{\text{Phase function}} \times \underbrace{\pi F_{\lambda_0}}_{\text{photons s}^{-1}\,\text{cm}^{-2}\,\text{nm}^{-1}} \times \underbrace{\frac{1}{4\pi\epsilon_0}\frac{\pi \text{e}^2}{mc^2} f_{ij}\lambda_{ij}^2}_{\text{integrated abs. cross sect. in nm cm}^2} \times \underbrace{\frac{A_{ji}}{\sum_k A_{jk}}}_{\text{rel. Einstein coeff.}} . \quad (70)$$

Here, πF_{λ_0} is the solar irradiance, ϵ_0 is the electric constant, e and m are the electron mass and charge, respectively, and c is the light speed in free space. The wavelength-integrated cross section depends only on the transition wavelength λ_{ij} and the absorption oscillator strength f_{ij} of the transition. Both values are taken from the NIST atomic spectra database (Kramida et al., 2012). The integrated cross section is spectrally distributed over the shape of the line for mesospheric conditions, i.e., a Doppler-broadened Gaussian line shape for each individual line with a FWHM of $\sqrt{\frac{8\,RT\,\ln(2)}{Mc^2}}\lambda_0$ – with the gas constant R, absolute temperature T and molar mass of the atom M. The relative Einstein coefficient in the right hand side of the Eq. (70) accounts for other non resonant emission processes which depopulate the excited state. Not considered are population increases of the excited state through other transitions, which are however considered to be negligibly small.

A directional distribution of re-emitted photons is described by the phase function which is given by

$$P(\theta) = \frac{3}{4}E_1(\cos^2(\theta) + 1) + E_2. \quad (71)$$

The factors E_1 and E_2 depend on the total angular momentum, j, of the lower state and change in total angular momentum, Δj, and are taken from Chandrasekhar (1960) (see Table 29). The first part of the phase function is similar to the Phase function of Rayleigh scattering, while the second part is isotropic. Depending on E_1 and E_2, the phase function is a linear combination of both individual phase functions. The factors E_1

Table 29: E_1 and E_2 depend on the on the total angular momentum, j, of the lower state and change of angular momentum, Δj, (from Chandrasekhar, 1960, table II, page 52).

Δj	E_1	E_2
$+1$	$\frac{(2j+5)(j+2)}{10(j+1)(2j+1)}$	$\frac{3j(6j+7)}{10(j+1)(2j+1)}$
0	$\frac{(2j-1)(2j+3)}{10j(j+1)}$	$\frac{3(2j^2+2j+1)}{10j(j+1)}$
-1	$\frac{(2j-3)(j-1)}{10j(2j+1)}$	$\frac{3(6j^2+5j-1)}{10j(2j+1)}$

and E_2 for the different metal emission lines are shown in Table 30.

Table 30: E_1 and E_2 for different metal lines.

species	wavelength in nm	E_1	E_2
Mg	285.2	1	0
Mg^+	279.6	0.5	0.5
Mg^+	280.4	0	1
Na	589.2 (D2)	0.5	0.5
Na	589.8 (D1)	0	1

For the determination of number density distributions from SCDs, a forward model for calculating SCDs

from number density distributions is used. For a single measurement it is formulated as

$$4\pi I = \int_{\text{LOS}} \gamma n(s_\text{e}) f \left(\int n(s_\text{a}) \text{d}s_\text{a} \right) \text{d}s_\text{e} \tag{72}$$

where n is the target species number density and f represents the absorption term both along the line of sight (LOS) and along the direct solar beam (or line from the Sun (LFS)). The total absorption path is denoted by s_a and s_e stands for the emission pathlength along the line of sight. Thus, the resonance fluorescence signal is integrated along the LOS while absorption occurs on both the LOS and the LFS. Self-absorption by the emitting species introduces a non-linearity into the forward model, however, it is supposed to be weak. Multiple scattering effect is found to be negligible for both Mg/Mg^+ but needs to be considered for Na. Furthermore, absorption by other species, e.g., ozone is assumed to be negligible.

A latitude/altitude grid and the pathways used by the forward model are illustrated in Fig. 44. For each grid cell i the full pathway along the LOS intersecting this grid cell is denoted by Δs_{LOS_i}, $\Delta s_{\text{LOS}_{\text{gc}_{i,j}}}$ denotes the pathway within a grid cell j along the LOS starting from the grid cell i pointing to the satellite, and the pathway within a grid cell j along the LFS is given by $\Delta s_{\text{LFS}_{\text{gc}_{i,j}}}$. Discretizing Eq. (72) and denoting all constant factors by c_1 the following equation for the forward model is obtained:

$$I = c_1 \sum_{i=1}^{m} P_i x_i \Delta s_{\text{LOS}_i} f\left(g_i(x)\right), \text{ where } \quad g_i(x) \equiv \sum_{j=1}^{m} x_j \Delta s_{\text{LOS}_{\text{gc}_{i,j}}} + \sum_{j=1}^{m} x_j \Delta s_{\text{LFS}_{\text{gc}_{i,j}}}. \tag{73}$$

Note that the Phase function P is scattering angle dependent and therefore varies along the LOS.

In a matrix form the forward model is expressed by $\mathbf{K}\vec{x} = \vec{y}$ with the state vector $\vec{x}$ containing the number densities of the target species for all latitude/altitude grid cells of the model atmosphere. The measurement vector $\vec{y}$ contains measured radiances for all limb scans of one orbit, i.e., measurements at different tangent altitudes and latitudes. **K** is the matrix representing the forward model. As the absorption term in Eq. (73) is non linear, Jacobians of the forward model need to be obtained to solve the minimization problem. Differentiating both sides of Eq. (73) the following equation for an element of the Jacobian, $J_{n,k}$ matrix is obtained:

$$J_{n,k} \equiv \frac{\partial I_n}{\partial x_k} = c_1 P_k \Delta s_{\text{LOS}_k} f\big(g_k(x)\big) + c_1 \sum_{i=1}^{m} P_i \Delta s_{\text{LOS}_i} x_i \frac{\partial f(g_i(x))}{\partial g_i(x)} (\Delta s_{\text{LOS}_{\text{gc}_{i,k}}} + \Delta s_{\text{LFS}_{\text{gc}_{i,k}}}). \tag{74}$$

Here, both $f(g_i(x))$ and $\frac{\partial f(g_i(x))}{\partial g_i(x)}$ are calculated numerically.

As the forward modeling is done at a relative coarse spectral grid corresponding to the spectral sampling of the SCIAMACHY instrument, while the Lambert-Beer law used to calculate $f(g_i(x))$ is strictly valid only for monochromatic calculations, an additional correction is needed in a case of a high density of the absorber. This correction is given by

$$f = \frac{\int \sigma(\lambda) \pi F(\lambda) \cdot e^{-\sigma(\lambda) g} \text{d}\lambda}{\int \sigma(\lambda) \pi F(\lambda) \text{d}\lambda}. \tag{75}$$

To perform this correction a high resolution solar spectrum is required. As the latter is not available from SCIAMACHY measurements, the solar spectrum obtained from the balloon-borne measurements carried out in 1978 by Anderson and Hall (1989) and Hall and Anderson (1991) is employed. To account for the solar cycle variation the smoothed high resolution spectrum needs to be matched with the measured solar spectrum from SCIAMACHY. The following instrumental effects of SCIAMACHY are applied to the scaled and peak-scaled high resolution spectrum. The high resolution spectrum is smoothed by convolving it with the SCIAMACHY channel 1 slit function, a hyperbolic function with a FWHM of 0.22 nm:

$$h(\lambda) = \frac{\text{FWHM}^3}{4\pi\sqrt{2}} \frac{1}{(0.5\text{FWHM})^4 + (\lambda - \lambda_0)^4}, \tag{76}$$

and then interpolated to the SCIAMACHY wavelength grid. As a first step, degradations effects are corrected for by fitting the SCIAMACHY solar spectrum to the smoothed high resolution spectrum with a scaling factor. As the next step, the effect of the solar variability is simulated by scaling the spectrum only in the center of the emission lines. It is assumed, that the shape of the emission lines, which are not resolved in the smoothed spectrum, is the same as in the high resolution spectrum. Using different scaling factors for the emission line in order to model the solar variability results in different integrated values. This change can be described by a linear function for each individual line. To consider the variations, this linear function is inverted for the integrated values of the daily measured SCIAMACHY spectrum to obtain the scaling factor, that has to be applied to the emission lines. By doing this, the high resolution spectrum is used to obtain the correct line shape of the lines, while the daily SCIAMACHY spectrum is used to correct for daily variability.

To account for the non-linearity, the inverse problem is solved iteratively using the zero number density of the target species as the initial guess. To avoid unphysical oscillations in the retrieved profile, a priori and smoothing constraints for neighboring latitude and altitude grid cells are used (this type of constraints is often referred to as Tikhonov regularization (Tikhonov, 1943)). The final equation to be solved is written as:

$$\left(\mathbf{J}^T\mathbf{S}_y\mathbf{J} + \mathbf{S}_\mathrm{a} + \lambda_h\mathbf{S}_H^T\mathbf{S}_H + \lambda_\phi\mathbf{S}_\phi^T\mathbf{S}_\phi\right)\vec{x} = \mathbf{J}^T\mathbf{S}_y\vec{y} + \underbrace{\mathbf{S}_\mathrm{a}\underbrace{\vec{x}_\mathrm{a}}_{=0}}_{=0}, \tag{77}$$

where **J** is the Jacobian of the forward model **K** and the a priori covariance matrix $\mathbf{S}_\mathrm{a}$ is chosen as a product of a scalar, λ_apriori, and an identity matrix. $\mathbf{S}_H$ and $\mathbf{S}_\phi$ are the matrices for altitudinal and latitudinal constraints (large sparse matrices with only 2 diagonals of non-zero values) and λ_h and λ_ϕ are the scalar weighting factors for both constraints. $\vec{x}$ is the vector of number densities. On the right-hand side there is the covariance matrix for the SCDs ($\mathbf{S}_y$), which is assumed to be diagonal, the SCDs $\vec{y}$ and the a priori solution $\vec{x}_\mathrm{a}$. The latter is set to zero to avoid any bias on the profile shape. The constraint parameters used in Eq. (77) are listed in Tabel 31.

Table 31: Constraint parameters

Species	λ_h	λ_ϕ	λ_apriori
Mg	5E-8	1E-8	5E-9
Mg^+	1E-7	2E-8	1E-8
Na	1E-7	2E-8	1E-8

15.2 SCIAMACHY nominal limb measurements (UB)

The retrieval of Mg vertical distribution from the nominal limb measurements of SCIAMACHY is performed within the altitude range 68 - 90 km. The spectral signature between 283.0 and 287.5 nm is analyzed after the baseline signal has been subtracted. The baseline is obtained by a least square fit of a liner polynomial in the same spectral window excluding the range of Mg emission features (284.9 – 285.7 nm).

Similarly, to the Na retrievals (see Sect. 12.3) a high resolution solar spectrum is fitted to the monthly mean solar irradiance measured by the SCIAMACHY instrument. The fit is done between 283.0 and 287.5 nm in exactly the same manner as described in Sect. 12.3. The fitted high resolution spectrum is used then in the retrieval process to model the emission signal of Mg. For compatibility reason, the same high resolution solar spectrum as for Mg MLT retrievals (see Sect. 15.1) is used.

Before the main retrieval procedure, a contribution due to inelastic Raman scattering is modeled using the SCIATRAN 3.7.1 radiative transfer model and subtracted from the measured radiances. The monthly mean solar irradiance measured by the SCIAMACHY instrument is used to calculate the Raman scattering.

The retrieval is done for monthly zonal means of the measured radiances. Mean solar irradiance, geolocation and illumination is calculated accordingly. The measurement vector is created from all spectra in the selected tangent height range. A baseline is subtracted from both measured and simulated sun-normalized radiances prior the retrieval. The retrieval is done for absolute deviations from the initial guess value (in units of molec/cm^2/km) employing the first order Tikhonov regularization. The zero-order parameter is set to 5E+7 while the first order parameter is 2E-7. The non-linearity of the problem is accounted for employing an iterative process. The initial guess value is taken from the SCIAMACHY MLT retrieval results and is replaced by the result of the previous iteration at each iterative step.

Figure 45 shows spectral fits (upper row) and residuals (lower row) for three selected tangent heights (87 km, 81 km, 74 km from left to right). In the upper row the measured spectra a shown in red while the cyan curves depict the modeled signals. The averaging kernels typical for sodium vertical profile retrieval from SCIAMACHY nominal limb measurements are shown in the left panel of Fig. 46. The colored numbers on the right depict the nominal altitudes of the averaging kernels. The averaging kernels have pronounced peaks at nominal altitudes but have a maximum value of about 0.1 illustrating a strong influence of the initial guess profiles. This influence can however be mitigated by means of an iterative process replacing the initial guess by the result of the previous iteration at each iterative step. The vertical resolution of the retrieval is estimated at about 9 km. The right panel of Fig. 46 illustrate the dependence of the resulting profile (shown by the solid lines) on the initial guess (shown by the dashed lines). The yellow area marks the retrieval range. It is seen that between 80 and 90 km different a priori assumptions result in very similar retrieved profiles indicating that the overall influence of the a priori information in this altitude range is low. Below 80 km discrepancies increase, however, absolute amounts of Mg at these altitudes are quite low.

The retrieval for Mg^+ is done in a similar way as described above for Mg. The spectral range between 278.5 and 281.5 nm is used. The baseline is fitted excluding the range of Mg^+ emission features (279.3 - 280.7 nm). The latter range is used to fit the solar irradiance. As the maximum of Mg^+ abundance is observed about 5 km above that of Mg, the bulk of Mg^+ is located above the retrieval range. For this reason the vertical profile retrieval of Mg^+ is considered to be unreliable and only a scaling factor for the apriori profile can be retrieved (equivalent of the total column retrieval).

16. Appendix A

Microwindows used in the joint retrieval of CO_2 and line of sight (LOS).

Tangent Height (km)	Microwindows (cm^{-1})
60	2311.188-2311.250, 2314.812-2314.938, 2317.062-2317.375, 2319.000-2319.188, 2319.812-2320.000, 2320.562-2320.688, 2321.438-2321.625, 2323.000-2323.250, 2324.750-2324.938, 2326.188-2326.250, 2326.625-2326.812, 2326.938-2327.062, 2328.562-2328.625, 2329.250-2329.312, 2330.000-2330.062, 2332.500-2332.562, 2334.000-2334.062, 2339.438-2339.500, 2340.938-2341.000, 2346.062-2346.125, 2353.000-2353.062, 2354.375-2354.500, 2355.938-2356.125, 2360.188-2360.312
63	2309.625-2309.688, 2310.375-2310.500, 2311.125-2311.438, 2313.625-2313.812, 2314.688-2314.938, 2315.250-2315.312, 2316.188-2316.250, 2317.062-2317.312, 2317.438-2317.500, 2318.875-2319.188, 2319.688-2320.000, 2320.312-2320.688, 2321.188-2321.688, 2322.812-2323.250, 2324.688-2324.938, 2325.375-2325.625, 2326.000-2326.250, 2326.625-2327.062, 2328.562-2328.625, 2329.000-2329.062, 2329.250-2329.312, 2330.562-2330.750, 2332.125-2332.250, 2332.500-2332.562, 2334.000-2334.062, 2337.688-2337.750, 2339.312-2339.562, 2340.875-2341.000, 2342.625-2342.688, 2344.312-2344.500, 2345.875-2346.125, 2354.375-2354.562, 2355.750-2356.062, 2358.562-2358.875, 2361.312-2361.625, 2363.938-2364.250, 2365.250-2365.500

Continued on next page

32 continued

Tangent Height (km)	Microwindows (cm^{-1})
66	2310.438-2310.562, 2311.125-2311.250, 2314.812-2314.938, 2315.250-2315.312, 2318.938-2319.188, 2319.750-2320.000, 2320.312-2320.375, 2320.562-2320.688, 2321.438-2321.688, 2323.000-2323.312, 2324.750-2324.938, 2325.562-2325.625, 2326.188-2326.250, 2326.625-2327.062, 2328.562-2328.625, 2328.750-2328.812, 2330.562-2330.625, 2332.438-2332.562, 2334.000-2334.062, 2335.938-2336.000, 2339.312-2339.500, 2340.938-2341.000, 2342.625-2342.688, 2344.312-2344.375, 2345.938-2346.125, 2354.312-2354.500, 2355.812-2356.062, 2357.188-2357.438, 2358.562-2358.875, 2360.000-2360.250, 2361.312-2361.562, 2362.750-2362.938, 2364.000-2364.250, 2365.250-2365.500
69	2310.438-2310.562, 2314.812-2314.938, 2318.938-2319.188, 2319.750-2319.938, 2320.562-2320.688, 2321.125-2321.188, 2324.750-2324.938, 2326.188-2326.250, 2326.688-2327.062, 2328.562-2328.812, 2332.438-2332.500, 2334.000-2334.062, 2335.938-2336.000, 2339.312-2339.500, 2340.938-2341.000, 2342.625-2342.688, 2344.312-2344.375, 2354.312-2354.500, 2355.875-2356.000, 2357.188-2357.438, 2358.625-2358.750, 2362.750-2362.938
72	2323.250-2323.312, 2323.875-2324.188, 2324.875-2324.938, 2328.625-2328.812, 2334.000-2334.062, 2335.938-2336.062, 2340.938-2341.000, 2342.625-2342.688, 2346.625-2346.688, 2347.562-2347.625, 2349.938-2350.000, 2350.938-2351.125, 2352.125-2352.250
75	2307.188-2307.250, 2308.125-2308.188, 2308.312-2308.375, 2309.000-2309.062, 2309.625-2309.688, 2316.125-2316.188, 2317.500-2317.562, 2320.312-2320.375, 2321.125-2321.188, 2321.625-2321.688, 2321.938-2322.000, 2323.562-2323.625, 2323.875-2324.188, 2328.750-2328.812, 2329.000-2329.062, 2335.875-2336.062, 2336.312-2336.438, 2336.625-2336.688, 2337.688-2337.750, 2340.938-2341.000, 2342.250-2342.312, 2342.625-2342.688, 2344.188-2344.250, 2346.562-2346.688, 2347.562-2347.812, 2349.750-2350.062, 2350.875-2351.125
78	2306.000-2306.312, 2306.938-2307.188, 2307.812-2307.875, 2308.000-2308.125, 2308.750-2309.062, 2309.625-2309.688, 2310.562-2310.625, 2311.438-2311.500, 2311.688-2311.750, 2312.312-2312.375, 2312.562-2312.625, 2313.188-2313.250, 2313.438-2313.625, 2314.312-2314.438, 2316.062-2316.188, 2316.938-2317.000, 2317.500-2317.562, 2317.750-2317.875, 2318.625-2318.688, 2319.188-2319.312, 2320.000-2320.062, 2320.312-2320.375, 2320.875-2320.938, 2321.125-2321.188, 2321.688-2321.750, 2321.938-2322.000, 2322.500-2322.812, 2323.312-2323.562, 2323.938-2324.188, 2329.625-2329.875, 2330.250-2330.312, 2330.500-2330.562, 2331.125-2331.375, 2332.000-2332.062, 2332.812-2332.875, 2334.062-2334.125, 2335.750-2336.062, 2336.875-2336.938, 2337.125-2337.188, 2338.500-2338.625, 2339.625-2339.688, 2339.875-2339.938, 2340.938-2341.250, 2342.312-2342.438, 2342.688-2342.938, 2343.938-2344.188, 2344.875-2345.438, 2346.125-2346.625
81	2306.000-2306.312, 2306.938-2307.188, 2307.875-2308.125, 2308.750-2309.000, 2309.625-2309.938, 2310.562-2310.812, 2311.438-2311.750, 2312.312-2312.625, 2313.188-2313.562, 2314.062-2314.438, 2314.938-2315.250, 2315.875-2316.125, 2316.688-2317.000, 2317.500-2317.875, 2318.375-2318.688, 2319.188-2319.500, 2320.000-2320.375, 2320.875-2321.188, 2321.688-2322.000, 2322.500-2322.812, 2323.312-2323.562, 2330.250-2330.562, 2331.125-2331.375, 2331.750-2332.062, 2332.562-2332.875, 2333.188-2333.500, 2334.062-2334.375, 2334.625-2334.938, 2335.500-2335.812, 2336.000-2336.312, 2336.875-2337.188, 2337.438-2337.688, 2338.312-2338.625, 2338.812-2339.062, 2339.625-2339.938, 2340.062-2340.375, 2341.000-2341.250, 2341.438-2341.688, 2342.312-2342.562, 2342.688-2342.938, 2343.938-2344.188, 2344.875-2345.125

Continued on next page

32 continued

Tangent Height (km)	Microwindows (cm^{-1})
84	2306.062-2306.312, 2306.938-2307.188, 2307.875-2308.062, 2308.750-2309.000, 2309.625-2309.938, 2310.562-2310.812, 2311.500-2311.750, 2312.312-2312.625, 2313.188-2313.562, 2314.062-2314.438, 2314.938-2315.250, 2315.875-2316.125, 2316.688-2317.000, 2317.562-2317.812, 2318.438-2318.688, 2319.188-2319.500, 2320.000-2320.312, 2320.875-2321.188, 2321.688-2321.938, 2322.500-2322.750, 2323.312-2323.562, 2330.250-2330.562, 2331.125-2331.312, 2331.750-2332.000, 2332.562-2332.812, 2333.188-2333.500, 2334.062-2334.250, 2334.688-2334.875, 2335.500-2335.688, 2336.000-2336.312, 2336.938-2337.188, 2337.438-2337.688, 2338.312-2338.625, 2338.812-2339.000, 2339.625-2339.938, 2340.062-2340.375, 2341.000-2341.250, 2341.438-2341.688, 2342.312-2342.562, 2342.688-2342.938, 2343.938-2344.188
87	2306.000-2306.312, 2306.938-2307.188, 2307.875-2308.125, 2308.750-2309.000, 2309.688-2309.938, 2310.562-2310.812, 2311.438-2311.750, 2312.312-2312.625, 2313.188-2313.562, 2314.062-2314.375, 2314.938-2315.250, 2315.875-2316.125, 2316.688-2317.000, 2317.500-2317.812, 2318.375-2318.688, 2319.188-2319.500, 2320.000-2320.312, 2320.875-2321.188, 2321.688-2322.000, 2322.500-2322.812, 2323.312-2323.562, 2330.250-2330.562, 2331.125-2331.375, 2331.750-2332.062, 2332.562-2332.875, 2333.188-2333.500, 2334.062-2334.375, 2334.625-2334.938, 2335.500-2335.812, 2336.000-2336.312, 2336.875-2337.188, 2337.438-2337.688, 2338.312-2338.625, 2338.812-2339.062, 2339.625-2339.938, 2340.062-2340.375, 2341.000-2341.250, 2341.438-2341.688, 2342.312-2342.562, 2342.688-2342.938, 2343.938-2344.188
90	2306.000-2306.312, 2306.938-2307.188, 2307.875-2308.125, 2308.750-2309.000, 2309.688-2309.938, 2310.562-2310.812, 2311.438-2311.750, 2312.312-2312.625, 2313.188-2313.562, 2314.062-2314.375, 2314.938-2315.250, 2315.875-2316.125, 2316.688-2317.000, 2317.500-2317.812, 2318.375-2318.688, 2319.188-2319.500, 2320.000-2320.312, 2320.875-2321.188, 2321.688-2322.000, 2322.500-2322.812, 2323.312-2323.562, 2330.250-2330.562, 2331.125-2331.375, 2331.750-2332.062, 2332.562-2332.875, 2333.188-2333.500, 2334.062-2334.375, 2334.625-2334.938, 2335.500-2335.812, 2336.000-2336.312, 2336.875-2337.188, 2337.438-2337.688, 2338.312-2338.625, 2338.812-2339.062, 2339.625-2339.938, 2340.062-2340.375, 2341.000-2341.250, 2341.438-2341.688, 2342.312-2342.562, 2342.688-2342.938, 2343.938-2344.188
93	2306.000-2306.312, 2306.938-2307.188, 2307.875-2308.125, 2308.750-2309.000, 2309.688-2309.938, 2310.562-2310.812, 2311.438-2311.750, 2312.312-2312.625, 2313.188-2313.562, 2314.125-2314.375, 2314.938-2315.250, 2315.875-2316.125, 2316.688-2317.000, 2317.500-2317.812, 2318.375-2318.688, 2319.250-2319.500, 2320.000-2320.312, 2320.875-2321.125, 2321.688-2322.000, 2322.500-2322.812, 2323.312-2323.562, 2330.250-2330.500, 2331.125-2331.375, 2331.750-2332.062, 2332.562-2332.875, 2333.188-2333.500, 2334.125-2334.375, 2334.625-2334.938, 2335.500-2335.812, 2336.062-2336.312, 2336.875-2337.188, 2337.438-2337.625, 2338.312-2338.562, 2338.812-2339.062, 2339.625-2339.938, 2340.062-2340.375, 2341.062-2341.312, 2341.438-2341.688, 2342.312-2342.562, 2342.688-2342.938, 2343.938-2344.188
96	2306.000-2306.312, 2306.938-2307.188, 2307.875-2308.125, 2308.750-2309.000, 2309.688-2309.938, 2310.562-2310.812, 2311.438-2311.750, 2312.312-2312.625, 2313.188-2313.562, 2314.125-2314.375, 2314.938-2315.312, 2315.875-2316.125, 2316.688-2317.000, 2317.500-2317.812, 2318.375-2318.688, 2319.250-2319.500, 2320.000-2320.312, 2320.875-2321.062, 2321.688-2322.000, 2322.562-2322.812, 2323.312-2323.562, 2330.250-2330.500, 2331.750-2332.062, 2332.562-2332.875, 2333.188-2333.500, 2334.125-2334.375, 2334.625-2334.938, 2335.500-2335.812, 2336.062-2336.312, 2336.875-2337.188, 2337.438-2337.625, 2338.312-2338.562, 2338.812-2339.062, 2339.625-2339.938, 2340.062-2340.375, 2341.062-2341.312, 2341.438-2341.688, 2342.312-2342.562, 2342.688-2342.938, 2343.938-2344.188, 2346.125-2346.375

Continued on next page

32 continued

Tangent Height (km)	Microwindows (cm^{-1})
99	2306.000-2306.312, 2306.938-2307.188, 2307.875-2308.125, 2308.750-2309.000, 2309.688-2309.938, 2310.562-2310.812, 2311.438-2311.750, 2312.312-2312.625, 2313.188-2313.562, 2314.125-2314.375, 2314.938-2315.312, 2315.875-2316.125, 2316.688-2317.000, 2317.500-2317.812, 2318.375-2318.688, 2319.250-2319.500, 2320.000-2320.312, 2320.875-2321.062, 2321.688-2322.000, 2323.250-2323.562, 2324.125-2324.375, 2330.250-2330.438, 2331.750-2332.062, 2332.562-2332.875, 2333.250-2333.500, 2334.125-2334.375, 2334.625-2334.938, 2335.500-2335.812, 2336.062-2336.312, 2336.875-2337.188, 2337.438-2337.625, 2338.312-2338.562, 2338.812-2339.062, 2339.625-2339.938, 2340.062-2340.375, 2341.062-2341.312, 2341.438-2341.688, 2342.312-2342.938, 2343.938-2344.250, 2346.125-2346.375, 2347.500-2347.750
102	2306.000-2306.312, 2307.000-2307.188, 2307.875-2308.125, 2308.875-2309.188, 2309.688-2309.938, 2310.562-2310.812, 2310.938-2311.188, 2311.500-2311.750, 2312.375-2312.625, 2313.062-2313.562, 2314.125-2314.375, 2315.000-2315.375, 2315.875-2316.125, 2316.688-2317.312, 2317.562-2317.812, 2318.375-2318.688, 2319.250-2319.500, 2320.062-2320.312, 2320.875-2321.250, 2321.688-2321.938, 2323.250-2323.562, 2324.125-2324.438, 2325.000-2325.188, 2326.688-2327.000, 2330.312-2330.500, 2331.750-2332.062, 2332.562-2332.875, 2333.250-2333.500, 2334.125-2334.375, 2334.625-2334.938, 2335.500-2335.750, 2336.062-2336.312, 2336.938-2337.188, 2337.438-2337.625, 2338.312-2338.562, 2338.812-2339.062, 2339.625-2339.938, 2340.062-2340.375, 2341.062-2341.312, 2341.438-2341.688, 2342.312-2342.938, 2343.625-2344.250, 2346.125-2346.375, 2347.438-2347.750, 2349.750-2350.062, 2352.812-2353.062
107	2306.812-2307.062, 2308.875-2309.188, 2310.938-2311.250, 2313.062-2313.312, 2315.000-2315.375, 2317.000-2317.312, 2319.000-2319.312, 2321.000-2321.312, 2322.938-2323.188, 2324.812-2325.125, 2326.688-2327.000, 2328.562-2328.875, 2330.438-2330.688, 2332.250-2332.500, 2334.000-2334.312, 2335.812-2336.062, 2337.500-2337.812, 2339.250-2339.500, 2340.938-2341.250, 2342.562-2342.875, 2344.250-2344.500, 2345.875-2346.125, 2347.438-2347.750, 2349.750-2350.062, 2351.312-2351.625, 2352.812-2353.125, 2354.312-2354.562, 2355.750-2356.000, 2357.188-2357.438, 2358.625-2358.875, 2360.000-2360.250, 2362.688-2362.875, 2365.250-2365.500, 2367.750-2368.000, 2370.188-2370.375, 2371.312-2371.562, 2372.438-2372.688, 2373.562-2373.750, 2374.625-2374.875, 2375.688-2375.938, 2376.750-2376.938
112	2306.812-2307.062, 2308.875-2309.188, 2310.938-2311.250, 2313.062-2313.312, 2315.000-2315.375, 2317.000-2317.312, 2319.000-2319.312, 2321.000-2321.312, 2322.938-2323.188, 2324.812-2325.125, 2326.750-2327.000, 2328.562-2328.875, 2330.375-2330.688, 2332.250-2332.500, 2334.062-2334.312, 2335.750-2336.062, 2337.500-2337.812, 2339.250-2339.500, 2340.938-2341.250, 2342.562-2342.875, 2344.188-2344.500, 2345.875-2346.125, 2347.438-2347.750, 2349.750-2350.062, 2351.312-2351.625, 2352.812-2353.125, 2354.250-2354.625, 2355.750-2356.062, 2357.188-2357.438, 2358.625-2358.875, 2359.938-2360.250, 2361.312-2361.625, 2362.688-2362.938, 2364.000-2364.250, 2365.250-2365.500, 2366.562-2366.750, 2367.750-2368.000, 2368.938-2369.188, 2370.125-2370.375, 2371.312-2371.562, 2372.438-2372.688, 2373.562-2373.812, 2374.625-2374.875, 2375.688-2375.938, 2376.688-2376.938, 2377.750-2377.938

Continued on next page

32 continued

Tangent Height (km)	Microwindows (cm^{-1})
117	2311.000-2311.250, 2313.062-2313.312, 2315.062-2315.312, 2317.062-2317.312, 2319.000-2319.312, 2321.000-2321.312, 2322.938-2323.188, 2324.875-2325.125, 2326.750-2327.000, 2328.562-2328.875, 2330.375-2330.688, 2332.250-2332.562, 2334.062-2334.312, 2335.750-2336.062, 2337.500-2337.812, 2339.188-2339.500, 2340.938-2341.250, 2342.562-2342.875, 2344.188-2344.500, 2345.875-2346.125, 2347.438-2347.750, 2351.312-2351.625, 2352.812-2353.125, 2354.250-2354.625, 2355.750-2356.062, 2357.188-2357.438, 2358.625-2358.875, 2360.000-2360.250, 2361.312-2361.562, 2362.688-2362.938, 2363.938-2364.250, 2365.250-2365.500, 2366.500-2366.750, 2367.750-2368.062, 2368.938-2369.188, 2370.125-2370.375, 2371.312-2371.562, 2372.438-2372.688, 2373.562-2373.812, 2374.625-2374.875, 2375.688-2375.938
122	2313.062-2313.312, 2315.062-2315.312, 2317.062-2317.312, 2319.000-2319.312, 2321.000-2321.250, 2322.938-2323.188, 2324.875-2325.125, 2326.750-2327.000, 2328.562-2328.875, 2330.375-2330.688, 2332.250-2332.500, 2334.062-2334.312, 2335.812-2336.062, 2337.500-2337.750, 2339.250-2339.500, 2340.938-2341.250, 2342.562-2342.875, 2344.250-2344.500, 2345.875-2346.125, 2352.812-2353.125, 2354.312-2354.562, 2355.750-2356.062, 2357.188-2357.438, 2358.625-2358.875, 2360.000-2360.250, 2361.312-2361.562, 2362.688-2362.938, 2363.938-2364.250, 2365.250-2365.500, 2366.500-2366.750, 2367.750-2368.062, 2368.938-2369.250, 2370.125-2370.375, 2371.312-2371.562, 2372.438-2372.688, 2373.562-2373.812, 2374.625-2374.875, 2375.688-2375.938
127	2311.000-2311.188, 2313.062-2313.312, 2315.062-2315.312, 2317.062-2317.312, 2319.000-2319.312, 2321.062-2321.250, 2322.938-2323.188, 2324.875-2325.125, 2326.750-2327.000, 2328.562-2328.812, 2330.375-2330.688, 2332.250-2332.500, 2334.062-2334.312, 2335.812-2336.062, 2337.500-2337.750, 2339.250-2339.500, 2340.938-2341.250, 2342.562-2342.875, 2344.250-2344.500, 2352.812-2353.062, 2354.312-2354.562, 2355.750-2356.062, 2357.188-2357.438, 2358.625-2358.875, 2360.000-2360.250, 2361.312-2361.562, 2362.688-2362.938, 2363.938-2364.250, 2365.250-2365.500, 2366.500-2366.750, 2367.750-2368.062, 2368.938-2369.250, 2370.125-2370.375, 2371.312-2371.562, 2372.438-2372.688, 2373.562-2373.812, 2374.625-2374.875, 2375.688-2375.938
132	2311.000-2311.188, 2313.062-2313.312, 2315.062-2315.250, 2317.062-2317.250, 2319.000-2319.250, 2321.062-2321.312, 2322.938-2323.125, 2324.875-2325.062, 2326.688-2327.000, 2328.562-2328.812, 2330.438-2330.625, 2332.250-2332.438, 2334.000-2334.250, 2335.812-2336.062, 2337.500-2337.750, 2339.188-2339.500, 2340.938-2341.188, 2342.562-2342.875, 2344.250-2344.500, 2352.812-2353.062, 2354.312-2354.562, 2355.750-2356.062, 2357.188-2357.438, 2358.625-2358.875, 2360.000-2360.250, 2361.312-2361.562, 2362.688-2362.938, 2363.938-2364.250, 2365.250-2365.500, 2366.500-2366.750, 2367.750-2368.062, 2368.938-2369.250, 2370.125-2370.375, 2371.312-2371.562, 2372.438-2372.688, 2373.562-2373.812, 2374.625-2374.875, 2375.688-2375.938
137	2311.000-2311.125, 2313.000-2313.250, 2315.062-2315.250, 2317.062-2317.250, 2319.000-2319.250, 2321.062-2321.250, 2323.000-2323.125, 2324.875-2325.062, 2326.750-2327.000, 2328.562-2328.812, 2330.438-2330.625, 2332.250-2332.438, 2334.000-2334.250, 2335.812-2336.062, 2337.500-2337.812, 2339.250-2339.500, 2340.938-2341.188, 2342.562-2342.875, 2344.250-2344.500, 2354.312-2354.562, 2355.750-2356.062, 2357.188-2357.438, 2358.625-2358.875, 2360.000-2360.250, 2361.312-2361.562, 2362.688-2362.938, 2363.938-2364.250, 2365.250-2365.500, 2366.500-2366.750, 2367.688-2368.062, 2368.938-2369.250, 2370.125-2370.375, 2371.312-2371.562, 2372.438-2372.688, 2373.562-2373.812, 2374.625-2374.875, 2375.688-2375.938, 2376.688-2376.938

Continued on next page

32 continued

Tangent Height (km)	Microwindows (cm^{-1})
142	2306.938-2307.000, 2308.938-2309.125, 2311.000-2311.125, 2313.000-2313.250, 2315.062-2315.250, 2317.062-2317.250, 2319.000-2319.250, 2321.062-2321.250, 2323.000-2323.125, 2324.875-2325.062, 2326.750-2327.000, 2328.562-2328.812, 2330.438-2330.625, 2332.250-2332.438, 2334.000-2334.250, 2335.812-2336.062, 2337.500-2337.812, 2339.250-2339.500, 2340.938-2341.188, 2342.562-2342.875, 2344.250-2344.500, 2354.312-2354.562, 2355.812-2356.062, 2357.188-2357.438, 2358.625-2358.875, 2360.000-2360.250, 2361.312-2361.562, 2362.688-2362.938, 2363.938-2364.250, 2365.250-2365.500, 2366.500-2366.750, 2367.688-2368.062, 2368.938-2369.250, 2370.125-2370.375, 2371.312-2371.562, 2372.438-2372.688, 2373.562-2373.812, 2374.625-2374.875, 2375.688-2375.938, 2376.688-2376.938, 2377.750-2377.938
147	2306.938-2307.000, 2308.938-2309.125, 2311.000-2311.125, 2313.000-2313.250, 2315.062-2315.250, 2317.062-2317.250, 2319.000-2319.250, 2321.062-2321.250, 2323.000-2323.125, 2324.875-2325.062, 2326.750-2327.000, 2328.562-2328.812, 2330.438-2330.625, 2332.250-2332.438, 2334.000-2334.250, 2335.812-2336.062, 2337.500-2337.812, 2339.250-2339.500, 2340.938-2341.188, 2342.562-2342.875, 2344.250-2344.500, 2354.312-2354.562, 2355.812-2356.062, 2357.188-2357.438, 2358.625-2358.875, 2360.000-2360.250, 2361.312-2361.562, 2362.688-2362.938, 2363.938-2364.250, 2365.250-2365.500, 2366.500-2366.750, 2367.688-2368.062, 2368.938-2369.250, 2370.125-2370.375, 2371.312-2371.562, 2372.438-2372.688, 2373.562-2373.812, 2374.625-2374.875, 2375.688-2375.938, 2376.688-2376.938, 2377.750-2377.938
152	2306.938-2307.000, 2308.938-2309.125, 2311.000-2311.125, 2313.000-2313.250, 2315.062-2315.250, 2317.062-2317.250, 2319.000-2319.250, 2321.062-2321.250, 2323.000-2323.125, 2324.875-2325.062, 2326.750-2327.000, 2328.562-2328.812, 2330.438-2330.625, 2332.250-2332.438, 2334.000-2334.250, 2335.812-2336.062, 2337.500-2337.812, 2339.250-2339.500, 2340.938-2341.188, 2342.562-2342.875, 2344.250-2344.500, 2354.312-2354.562, 2355.812-2356.062, 2357.188-2357.438, 2358.625-2358.875, 2360.000-2360.250, 2361.312-2361.562, 2362.688-2362.938, 2363.938-2364.250, 2365.250-2365.500, 2366.500-2366.750, 2367.688-2368.062, 2368.938-2369.250, 2370.125-2370.375, 2371.312-2371.562, 2372.438-2372.688, 2373.562-2373.812, 2374.625-2374.875, 2375.688-2375.938, 2376.688-2376.938, 2377.750-2377.938
157	2306.938-2307.000, 2308.938-2309.125, 2311.000-2311.125, 2313.000-2313.250, 2315.062-2315.250, 2317.062-2317.250, 2319.000-2319.250, 2321.062-2321.250, 2323.000-2323.125, 2324.875-2325.062, 2326.750-2327.000, 2328.562-2328.812, 2330.438-2330.625, 2332.250-2332.438, 2334.000-2334.250, 2335.812-2336.062, 2337.500-2337.812, 2339.250-2339.500, 2340.938-2341.188, 2342.562-2342.875, 2344.250-2344.500, 2354.312-2354.562, 2355.812-2356.062, 2357.188-2357.438, 2358.625-2358.875, 2360.000-2360.250, 2361.312-2361.562, 2362.688-2362.938, 2363.938-2364.250, 2365.250-2365.500, 2366.500-2366.750, 2367.688-2368.062, 2368.938-2369.250, 2370.125-2370.375, 2371.312-2371.562, 2372.438-2372.688, 2373.562-2373.812, 2374.625-2374.875, 2375.688-2375.938, 2376.688-2376.938, 2377.750-2377.938
162	2306.938-2307.000, 2308.938-2309.125, 2311.000-2311.125, 2313.000-2313.250, 2315.062-2315.250, 2317.062-2317.250, 2319.000-2319.250, 2321.062-2321.250, 2323.000-2323.125, 2324.875-2325.062, 2326.750-2327.000, 2328.562-2328.812, 2330.438-2330.625, 2332.250-2332.438, 2334.000-2334.250, 2335.812-2336.062, 2337.500-2337.812, 2339.250-2339.500, 2340.938-2341.188, 2342.562-2342.875, 2344.250-2344.500, 2354.312-2354.562, 2355.812-2356.062, 2357.188-2357.438, 2358.625-2358.875, 2360.000-2360.250, 2361.312-2361.562, 2362.688-2362.938, 2363.938-2364.250, 2365.250-2365.500, 2366.500-2366.750, 2367.688-2368.062, 2368.938-2369.250, 2370.125-2370.375, 2371.312-2371.562, 2372.438-2372.688, 2373.562-2373.812, 2374.625-2374.875, 2375.688-2375.938, 2376.688-2376.938, 2377.750-2377.938

Continued on next page

32 continued

Tangent Height (km)	Microwindows (cm^{-1})
167	2306.938-2307.000, 2308.938-2309.125, 2311.000-2311.125, 2313.000-2313.250, 2315.062-2315.250, 2317.062-2317.250, 2319.000-2319.250, 2321.062-2321.250, 2323.000-2323.125, 2324.875-2325.062, 2326.750-2327.000, 2328.562-2328.812, 2330.438-2330.625, 2332.250-2332.438, 2334.000-2334.250, 2335.812-2336.062, 2337.500-2337.812, 2339.250-2339.500, 2340.938-2341.188, 2342.562-2342.875, 2344.250-2344.500, 2354.312-2354.562, 2355.812-2356.062, 2357.188-2357.438, 2358.625-2358.875, 2360.000-2360.250, 2361.312-2361.562, 2362.688-2362.938, 2363.938-2364.250, 2365.250-2365.500, 2366.500-2366.750, 2367.688-2368.062, 2368.938-2369.250, 2370.125-2370.375, 2371.312-2371.562, 2372.438-2372.688, 2373.562-2373.812, 2374.625-2374.875, 2375.688-2375.938, 2376.688-2376.938, 2377.750-2377.938
172	2306.938-2307.000, 2308.938-2309.125, 2311.000-2311.125, 2313.000-2313.250, 2315.062-2315.250, 2317.062-2317.250, 2319.000-2319.250, 2321.062-2321.250, 2323.000-2323.125, 2324.875-2325.062, 2326.750-2327.000, 2328.562-2328.812, 2330.438-2330.625, 2332.250-2332.438, 2334.000-2334.250, 2335.812-2336.062, 2337.500-2337.812, 2339.250-2339.500, 2340.938-2341.188, 2342.562-2342.875, 2344.250-2344.500, 2354.312-2354.562, 2355.812-2356.062, 2357.188-2357.438, 2358.625-2358.875, 2360.000-2360.250, 2361.312-2361.562, 2362.688-2362.938, 2363.938-2364.250, 2365.250-2365.500, 2366.500-2366.750, 2367.688-2368.062, 2368.938-2369.250, 2370.125-2370.375, 2371.312-2371.562, 2372.438-2372.688, 2373.562-2373.812, 2374.625-2374.875, 2375.688-2375.938, 2376.688-2376.938, 2377.750-2377.938

References

Anderson, G. P. and Hall, L. A. (1989). Solar irradiance between 2000 and 3100 angstroms with spectral bandpass of 1.0 angstroms. *J. Geophys. Res.*, 94:6435 – 6441.

Arijs, E., Nevejans, D., Fussen, D., Frederick, P., Ransbeek, E. V., Taylor, F. W., Calcutt, S. B., Werrett, S. T., Heppelwhite, C. L., Pritchard, Burchell, I., and Rodgers, C. D. (1995). The ORA occultation radiometer on EURECA. *Adv. Space Res.*, 16.

Babcock, H. and Herzberg, L. (1948). Fine structure of the red system of atmospheric oxygen bands. *Astrophys. J.*, 108:167–190.

Bailey, S. A., Thomas, G. E., Hervig, M. E., Lumpe, J. D., Randall, C. E., N.Carstens, J., Thurairajah, B., Rusch, D. W., III, J. M. R., and Gordley, L. L. (2015). Comparing nadir and limb observations of polar mesospheric clouds: The effect of the assumed particle size distribution. *J. Atmos. Sol.-Terr. Phys.*, 127:51 – 65.

Barth, C. A., Mankoff, K. D., Bailey, S. M., and Solomon, S. C. (2003). Global observations of nitric oxide in the thermosphere. *J. Geophys. Res.*, 108(A1):1027.

Baumgarten, G. and Fiedler, J. (2008). Vertical structure of particle properties and water content in noctilucent clouds. *Geophys. Res. Lett.*, 35:L10811.

Becker, K. H., Groth, W., and Thran, D. (1972). The mechanism of the air afterglow NO + O $\rightarrow$ NO_2 + hν. *Chem. Phys. Lett.*, 15:Chem. Phys. Lett.

Bellisario, C., Keckhut, P., Blanot, L., Hauchecorne, A., and Simoneau, P. (2014). O_2 and OH night airglow emission derived from gomos-envisat instrument. *J. Atmos. Ocean. Tech.*, 31(6):1301–1311.

Bender, S., Sinnhuber, M., Burrows, J. P., Langowski, M., Funke, B., and López-Puertas, M. (2013). Retrieval of nitric oxide in the mesosphere and lower thermosphere from SCIAMACHY limb spectra. *Atmos. Meas. Tech.*, 6(9):2521–2531.

Bermejo-Pantaleón, D., Funke, B., López-Puertas, M., García-Comas, M., Stiller, G. P., von Clarmann, T., Linden, A., Grabowski, U., Höpfner, M., Kiefer, M., Glatthor, N., Kellmann, S., and Lu, G. (2011). Global observations of thermospheric temperature and nitric oxide from mipas spectra at 5.3 µm. *J. Geophys. Res.*, 116(A10):A10313.

Bogumil, K., Orphal, J., Homann, T., Voigt, S., Spietz, P., Fleischmann, O. C., Vogel, A., Hartmann, M., Bovensmann, H., Frerik, J., and Burrows, J. P. (2003). Measurements of molecular absorption spectra with the SCIAMACHY pre-flight model: instrument characterization and reference data for atmospheric remote sensing in the 230-2380 nm region. *J. Photochem. Photobiol. A*, 157:167–184.

Boone, C. D., Nassar, R., Walker, K. A., Rochon, Y., McLeod, S. D., Rinsland, C. P., and Bernath, P. F. (2005). Retrievals for the atmospheric chemistry experiment Fourier-transform spectrometer. *Appl. Opt.*, 44:7218–7231.

Boone, C. D., Walker, K. A., and Bernath, P. F. (2013). Version 3 retrievals for the Atmospheric Chemistry Experiment Fourier Transform Spectrometer (ACE-FTS). In Bernath, P. F., editor, *The Atmospheric Chemistry Experiment ACE at 10: A Solar Occultation Anthology*, pages 103–127. A. Deepak Publishing.

Bucholtz, A., Skinner, W., Abreu, V., and Hays, P. (1986). The dayglow of the O_2 atmospheric band system. *Planet. Space Sci.*, 34(11):1031–1035.

Carlotti, M. (1988). Global-fit approach to the analysis of limb-scanning atmospheric measurements. *Appl. Opt.*, 27:3250–3254.

Chance, K. and Kurucz, R. (2010). An improved high-resolution solar reference spectrum for earth's atmosphere measurements in the ultraviolet, visible, and near infrared. *J. Quant. Spectrosc. Ra.*, 111(9):1289–1295.

Chandrasekhar, S. (1960). *Radiative Transfer*. Dover Publ.

Chapman, S. (1939). Notes on atmospheric sodium. *Astrophys. J.*, 90:309 – 316.

Cleary, D. D. (1986). Daytime high-latitude rocket observations of the no γ, δ, and ε bands. *J. Geophys. Res.*, 91(A10):11337–11344.

Clemesha, B. R., Simonich, D. M., Takahashi, H., Melo, S. M. L., and Plane, J. M. C. (1995). Experimental-evidence for photochemical control of the atmospheric sodium layer. *J. Geophys. Res.*, 100:18909 – 18916.

Davis, S. P., Abrams, M. C., and Brault, J. W. (2001). *Fourier Transform Spectroscopy*. Academic.

Debrestian, D. J., Lumpe, J. D., Shettle, E. P., and et al. (1997). An analysis of poam ii solar occultation observations of polar mesospheric clouds in the southern hemisphere. *J. Geophys. Res.*, 192(D2):1971 – 1981.

Degenstein, D., Llewellyn, E., and Lloyd, N. (2003). Volume emission rate tomography from a satellite platform. *Appl. Opt.*, 42:1441–1450.

Earls, L. T. (1935). Intensities in $^2\Pi - ^2\Sigma$ transitions in diatomic molecules. *Phys. Rev.*, 48:423–424.

Eparvier, F. G. and Barth, C. A. (1992). Self-absorption theory applied to rocket measurements of the nitric oxide (1, 0) γ band in the daytime thermosphere. *J. Geophys. Res.*, 97(A9):13723–13731.

Eriksson, P. (2016). Odin/SMR: Algorithms Theoretical Basis Document - Level 2 processing. Technical report, Department of Earth and Space Sciences, Chalmers University of Technology.

Eriksson, P., Buehler, S. A., Davis, C. P., Emde, C., and Lemke, O. (2011). ARTS, the atmospheric radiative transfer simulator, version 2. *J. Quant. Spectrosc. Radiat. Transfer*, 112:1551–1558.

Eriksson, P., Merino, F., Murtagh, D., Baron, P., Ricaud, P., and de La Noë, J. (2002). Studies for the Odin sub-millimetre radiometer: 1. Radiative transfer and instrument simulation. *Can. J. Phys.*, 80:321–340.

Fischer, J., Gamache, R. R., Goldman, A., Rothman, L. S., and Perrin, A. (2003). Total internal partition sums in the 2000 edition of the HITRAN database. *J. Quant. Spectrosc. Radiat. Transfer*, 82:401– 412.

Froidevaux, L., Jiang, Y. B., Lambert, A., Livesey, N. J., Read, W. G., Waters, J. W., Browell, E. V., Hair, J. W., Avery, M. A., McGee, T. J., Twigg, L. W., Sumnicht, G. K., Jucks, K. W., Margitan, J. J., Sen, B., Stachnik, R. A., Toon, G. C., Bernath, P. F., Boone, C. D., Walker, K. A., Filipiak, M. J., Harwood, R. S., Fuller, R. A., Manney, G. L., Schwartz, M. J., Daffer, W. H., Drouin, B. J., Cofield, R. E., Cuddy, D. T., Jarnot, R. F., Knosp, B. W., Perun, V. S., Snyder, W. V., Stek, P. C., Thurstans, R. P., and Wagner, P. A. (2008). Validation of aura microwave limb sounder stratospheric ozone measurements. *Journal of Geophysical Research: Atmospheres*, 113(D15):n/a–n/a. D15S20.

Funke, B., Baumgaertner, A., Calisto, M., Egorova, T., Jackman, C. H., Kieser, J., Krivolutsky, A., López-Puertas, M., Marsh, D. R., Reddmann, T., Rozanov, E., Salmi, S.-M., Sinnhuber, M., Stiller, G. P., Verronen, P. T., Versick, S., von Clarmann, T., Vyushkova, T. Y., Wieters, N., and Wissing, J. M. (2011). Composition changes after the "Halloween" solar proton event: the High-Energy Particle Precipitation in the Atmosphere (HEPPA) model versus MIPAS data intercomparison study. *Atmos. Chem. Phys. Discuss.*, 11(3):9407–9514.

Funke, B., López-Puertas, M., , Bermejo-Pantaleón, D., von Clarmann, T., Stiller, G. P., Höpfner, M., Grabowski, U., and Kaufmann, M. (2007). Analysis of nonlocal thermodynamic equilibrium CO 4.7 μm fundamental, isotopic and hot band emissions measured by the Michelson Interferometer for Passive Atmospheric Sounding on Envisat. *J. Geophys. Res.*, 112(D11).

Funke, B. and López-Puertas, M. (2000). Nonlocal thermodynamic equilibrium vibrational, rotational, and spin state distribution of NO(ν= 0,1,2) under quiescent atmospheric conditions. *J. Geophys. Res.*, 105(D4):4409–4426.

Funke, B., López-Puertas, M., García-Comas, M., Kaufmann, M., Höpfner, M., and Stiller, G. (2012). GRANADA: A Generic RAdiative traNsfer AnD non-LTE population algorithm. *J. Quant. Spectrosc. Radiat. Transfer*, 113(14):1771–1817.

Funke, B., López-Puertas, M., García-Comas, M., Stiller, G. P., von Clarmann, T., Höpfner, M., Glatthor, N., Grabowski, U., Kellmann, S., and Linden, A. (2009). Carbon monoxide distributions from the upper troposphere to the mesosphere inferred from 4.7 μm non-local thermal equilibrium emissions measured by MIPAS on Envisat. *Atmos. Chem. Phys.*, 9(7):2387–2411.

Funke, B., López-Puertas, M., Stiller, G., v. Clarmann, T., and Höpfner, M. (2001). A new non-LTE retrieval method for atmospheric parameters from mipas-envisat emission spectra. *Adv. Space Res.*, 27(6-7):1099–1104.

Funke, B., López-Puertas, M., von Clarmann, T., Stiller, G. P., Fischer, H., Glatthor, N., Grabowski, U., Höpfner, M., Kellmann, S., Kiefer, M., Linden, A., Mengistu Tsidu, G., Milz, M., Steck, T., and Wang, D. Y. (2005). Retrieval of stratospheric nox from 5.3 and 6.2 µm nonlocal thermodynamic equilibrium emissions measured by michelson interferometer for passive atmospheric sounding (mipas) on envisat. *J. Geophys. Res.*, 110(D9):D09302.

Funke, B., Stiller, G. P., von Clarmann, T., Echle, G., and Fischer, H. (1998). CO_2 line mixing in MIPAS limb emission spectra and its influence on retrieval of atmospheric parameters. *J. Quant. Spectrosc. Radiat. Transfer*, 59(3–5):215–230.

Fussen, D., Vanhellemont, F., Bingen, C., Kyrola, E., Tamminen, J., Sofieva, V., Hassinen, S., Seppala, A., Verronen, P., Bertaux, J.-L., Hauchecorne, A., Dalaudier, F., Renard, J.-B., Fraisse, R., Fanton dAndon, O., Barrot, G., Mangin, A., Theodore, B., Guirlet, M., Koopman, R., Snoeij, P., , and Saavedra, L. (2004). Global measurement of the mesospheric sodium layer by the star occultation instrument gomos. *Geophys. Res. Lett.*, 31:L24110.

Garcia, R. R., López-Puertas, M., Funke, B., Marsh, D. R., Kinnison, D. E., Smith, A. K., and González-Galindo, F. (2014). On the distribution of CO_2 and CO in the mesosphere and lower thermosphere. *Journal of Geophysical Research: Atmospheres*, 119(9):5700–5718.

Garcia, R. R., Marsh, D. R., Kinnison, D. E., Boville, B. A., and Sassi, F. (2007). Simulation of secular trends in the middle atmosphere. *J. Geophys. Res.*, 112.

García-Comas, M., Funke, B., Gardini, A., López-Puertas, M., Jurado-Navarro, A., von Clarmann, T., Stiller, G., Kiefer, M., Boone, C. D., Leblanc, T., Marshall, B. T., Schwartz, M. J., and Sheese, P. E. (2014). Mipas temperature from the stratosphere to the lower thermosphere: Comparison of vm21 with ace-fts, mls, osiris, saber, sofie and lidar measurements. *Atmos. Meas. Tech.*, 7(11):3633–3651.

García-Comas, M., Funke, B., López-Puertas, M., Bermejo-Pantaleón, D., Glatthor, N., Clarmann, T. v., Stiller, G. P., Grabowski, U., Boone, C. D., French, W. J., Leblanc, T., López-González, M. J., and Schwartz, M. (2012). On the Quality of MIPAS Kinetic Temperature in the Middle Atmosphere. *Atmos. Chem. Phys.*, 12:6009–6039.

García-Comas, M., González-Galindo, F., Funke, B., Gardini, A., Jurado-Navarro, A., López-Puertas, M., and Ward, W. E. (2016). MIPAS observations of longitudinal oscillations in the mesosphere and the lower thermosphere: Part 1. Climatology of odd-parity daily frequency modes. *Atmospheric Chemistry and Physics Discussions*, pages 1–35.

Gattinger, R., Lloyd, N., Bourassa, A., Degenstein, D., McDade, I., and Llewellyn, E. (2009a). Observation of the 557.7 nm to 297.2 nm brightness ratio in the auroral spectrum withOSIRIS on Odin. *Can. J. Phys.*, 87:1133–1137.

Gattinger, R. L., Evans, W. F. J., McDade, I. C., Degenstein, D. A., and Llewellyn, E. J. (2009b). Observation of the chemiluminescent NO + O $\rightarrow$ NO_2 + $h\nu$ reaction in the upper mesospheric dark polar regions by OSIRIS on odin. *Can. J. Phys.*, 87:925–932.

Gattinger, R. L., McDade, I. C., Suzan, A. L. A., Boone, C. D., Walker, K. A., Bernath, P. F., Evans, W. F. J., Degenstein, D. A., Yee, J. H., Sheese, P., and Llewellyn, E. J. (2010). NO_2 air afterglow and O and NO densities from Odin-OSIRIS night and ACE-FTS sunset observations in the Antarctic MLT region. *J. Geophys. Res.*, 115:D12301.

Gil-López, S., López-Puertas, M., Kaufmann, M., Funke, B., García-Comas, M., Koukouli, M. E., Glatthor, N., Grabowski, U., Höpfner, Stiller, G. P., and von Clarmann, T. (2005). Retrieval of stratospheric and mesospheric O_3 from high resolution MIPAS spectra at 15 and 10 μm. *Adv. Space Res.*, 36(5):943–951.

González-Galindo, F., López-Valverde, M. A., Angelats i Coll, M., and Forget, F. (2005). Extension of a Martian general circulation model to thermospheric altitudes: UV heating and photochemical models. *Journal of Geophysical Research*, 110:09008.

Gorshelev, V., Serdyuchenko, A., Weber, M., Chehade, W., and Burrows, J. P. (2014). High spectral resolution ozone absorption cross-sections – part 1: Measurements, data analysis and comparison with previous measurements around 293 k. *Atmospheric Measurement Techniques*, 7(2):609–624.

Griffin, J., Worsnop, D. R., Brown, R. C., Kolb, C. E., and Herschbach, D. R. (2001). Chemical kinetics of the nao(a)+o(3p) reaction. *J. Phys. Chem. A*, 105:1643 – 1648.

Gumbel, J., Fan, Z. Y., Waldemarsson, T., Stegman, J., Witt, G., Llewellyn, E., She, C.-Y., and Plane, J. M. C. (2007). Retrieval of global mesospheric sodium densities from the odin satellite. *Geophys. Res. Lett.*, 34:L04813.

Hall, L. A. and Anderson, G. P. (1991). High resolution solar spectrum between 2000 and 3100 angstroms. *J. Geophys. Res.*, 96:927 – 931.

Hase, F., Demoulin, P., Sauval, A. J., Toon, G. C., Bernath, P. F., Goldman, A., Hannigan, J. W., and Rinsland, C. P. (2006). An empirical line–by–line model for the infrared solar transmittance spectrum from 700 to 5000 cm^{-1}. *J. Quant. Spectrosc. Radiat. Transfer*, 102(3):450–463.

Hauchecorne, A. and Chanin, M. (1980). Density and temperature profiles obtained by lidar between 35 and 70 km. *Geophys. Res. Lett.*, 7:565–568.

Hedin, A. (1991). Extension of the MSIS Thermosphere Model into the Middle and Lower Atmosphere. *Planet. Space Sci.*, 96(A2):1159–1172.

Hedin, J. and Gumbel, J. (2011). The global mesospheric sodium layer observed by odin/osiris in 2004–2009. *J. Atmos. Sol. Terr. Phys.*, 73:2221–2227.

J., G. and Witt, G. (2001). Rocket-borne photometry of nlc particle populations. *Adv. Space Res.*, 28(7):1053 – 1058.

Jurado-Navarro, A. A., López-Puertas, M., Funke, B., Garcia-Comas, M., Gardini, A., González-Galindo, F., Stiller, G. P., von Clarmann, T., Grabowski, U., and Linden, A. (2016). Global distributions of CO2 volume mixing ratio in the middle and upper atmosphere from MIPAS high resolution spectra. *Atmospheric Measurement Techniques Discussions*, 2016:1–25.

Jurado-Navarro, A. A., López-Puertas, M., Funke, B., García-Comas, M., Gardini, A., Stiller, G. P., and von Clarmann, T. (2015). Vibration-vibration and vibration-thermal energy transfers of CO_2 with N_2 from MIPAS high resolution limb spectra. *Journal of Geophysical Research*, page 2015JD023429.

Kaiser, J. W. and Burrows, J. P. (2003). Fast weighting functions for retrievals from limb scattering measurements. *J. Quant. Spectrosc. Radiat. Transfer*, 77(3):273 – 283.

Keckhut, P., Hauchecorne, A., and Chanin, M. (1993). A critical review of the data base acquired for the long term surveillance of the middle atmosphere by rayleigh lidar. *J. Atm. Ocean. Tech.*, 10:850–867.

Keller-Rudek, H., Moortgat, G. K., Sander, R., and Sörensen, R. (2013). The MPI-Mainz UV/VIS Spectral Atlas of Gaseous Molecules of Atmospheric Interest. *Earth System Science Data*, 5:365–373.

Koukouli, M., López-Puertas, M., Gil-López, S., Funke, B., Milz, M., and for the IAA/IMK MIPAS/ENVISAT team (2006). Water vapour profiles and non-lte parameters from its mesospheric emissions derived from mipas/envisat. In *Geophys. Res. Abstracts, 8, 03303, SRef-ID: 1607-7962/gra/EGU06-A- 03303*.

Kramida, A., Ralchenko, Y., Reader, J., and NIST ASD Team (2012) (2012). Nist atomic spectra database (version 5.0).

Kuntz, M. (1997). A new implementation of the Humlicek algorithm for the calculation of the voigt profile function. *J. Quant. Spectrosc. Radiat. Transfer*, 57:819–824.

Kurucz, R. (2005). New atlases for solar flux, irradiance, central intensity, and limb intensity. *Mem. S.A.It. Suppl.*, 8:189 – 191.

Kyrölä, E., Tamminen, J., Sofieva, V., Bertaux, J. L., Hauchecorne, A., Dalaudier, F., Fussen, D., Vanhellemont, F., Fanton D'Andon, O., Barrot, G., Guirlet, M., Mangin, A., Blanot, L., Fehr, T., Saavedra de Miguel, L., and Fraisse, R. (2010). Retrieval of atmospheric parameters from GOMOS data. *Atmospheric Chemistry & Physics*, 10:11881–11903.

Lamarque, J.-F., Emmons, L. K., Hess, P. G., Kinnison, D. E., Tilmes, S., Vitt, F., Heald, C. L., Holland, E. A., Lauritzen, P. H., Neu, J., Orlando, J. J., Rasch, P. J., and Tyndall, G. K. (2012). CAM-chem: description and evaluation of interactive atmospheric chemistry in the Community Earth System Model. *Geoscientific Model Development*, 5:369–411.

Langowski, M., Sinnhuber, M., Aikin, A. C., von Savigny, C., and Burrows, J. P. (2014). Retrieval algorithm for densities of mesospheric and lower thermospheric metal atom and ion species from satellite-borne limb emission signals. *Atmos. Meas. Tech.*, 7(1):29–48.

Langowski, M. P., von Savigny, C., Burrows, J. P., Rozanov, V. V., Dunker, T., Hoppe, U.-P., Sinnhuber, M., and Aikin, A. C. (2016). Retrieval of sodium profiles in the mesosphere and lower thermosphere from SCIAMACHY limb emission. *Atmos. Meas. Tech.*, 9:295 – 311.

Lean, J., Rottman, G., Harder, J., and Kopp, G. (2005). SORCE Contributions to New Understanding of Global Change and Solar Variability. *Solar Physics*, 230(1-2):27–53.

López-Puertas, M., Funke, B., Gil-López, S., von Clarmann, T., Stiller, G. P., Höpfner, M., Kellmann, S., Fischer, H., and Jackman, C. H. (2005). Observation of NO_x enhancement and ozone depletion in the northern and southern hemispheres after the October–November 2003 solar proton events. *J. Geophys. Res.*, 110(A9).

López-Puertas, M., Funke, B., Jurado-Navarro, A. A., Garcia-Comas, M., Gardini, A., Boone, C. D., Rezac, L., and Garcia, R. R. (2017a). Validation of the MIPAS CO_2 volume mixing ratio in the mesosphere and lower thermosphere and comparison with WACCM simulations. *Journal of Geophysical Research*, 122:1–22.

López-Puertas, M., García-Comas, M., Funke, B., Bermejo-Pantaleón, D., Höpfner, M., Grabowski, U., Stiller, G. P., von Clarmann, T., and von Savigny, C. (2009). Measurements of polar mesospheric clouds in infrared emission by MIPAS/ENVISAT. *J. Geophys. Res.*, 114.

López-Puertas, M., Garcia-Comas, M., Funke, B., Gardini, A., Clarmann, T. v., Stiller, G. P., Glatthor, N., Laeng, A., Kaufmann, M., Sofieva, V. F., Froidevaux, L., and Walker, K. A. (2017b). MIPAS Observations of Ozone in the Middle Atmosphere. *Atmospheric Measurement Techniques*, submitted.

López-Puertas, M. and Taylor, F. W. (2001). *Non-LTE radiative transfer in the Atmosphere*. World Scientific Pub., Singapore.

Lu, H. C., Chen, H. K., Chen, H. F., Cheng, B. M., and Ogilvie, J. F. (2010). Absorption cross section of molecular oxygen in the transition $E^3\Sigma_u^- v$= 0–$X^3\Sigma_g^-$ v= 0 at 38 K. *Astronomy and Astrophysics*, 520:A19.

Luque, J. and Crosley, D. R. (1999). Transition probabilities and electronic transition moments of the $A^2\Sigma^+$–$X^2\Pi$ and $D^2\Sigma^+$–$X^2\Pi$ systems of nitric oxide. *J. Chem. Phys.*, 111(16):7405–7415.

Marsh, D. R., Solomon, S. C., and Reynolds, A. E. (2004). Empirical model of nitric oxide in the lower thermosphere. *Journal of Geophysical Research (Space Physics)*, 109(A18):7301–+.

Marsh, D. R., Solomon, S. C., and Reynolds, A. E. (2004). Empirical model of nitric oxide in the lower thermosphere. *J. Geophys. Res.*, 109(A7):A07301.

McNutt, D. P. and Mack, J. E. (1963). Telluric absorption, residual intensities, and shifts in the fraunhofer d lines. *JGR*, 68(11):3419 – 3429.

Merino, F., Murtagh, D., Eriksson, P., Baron, P., Ricaud, P., and de La Noë, J. (2002). Studies for the Odin sub-millimetre radiometer: 3. Performance simulations. *Can. J. Phys.*, 80:357–373.

Milz, M., v. Clarmann, T., Boone, C., Chauhan, S., Deuber, B., Feist, D., Funke, B., Glatthor, N., Grabowski, U., Griesfeller, A., Haefele, A., M.Höpfner, Kämpfer, N., Kellmann, S., Linden, A., Müller, S., Oelhaf, H. N. H., Remsberg, E., Schiller, C., Stiller, G., Tanaka, T., Vómela, H., Walker, K., Wetzel, G., Yokota, T., and Zhang, G. (2009). Validation of water vapour profiles (version 13) retrieved by the IMK/IAA scientific retrieval processor based on full resolution spectra measured by MIPAS onboard Envisat. *Atmos. Meas. Tech.*, 2:379–399.

Mishchenko, M. I. and Travis, L. D. (1998). Capabilities and limitations of a current fortran implementation of the t-matrix method for randomly oriented, rotationally symmetric scatterers. *J. Quant. Spectrosc. Radiat. Tranfer*, 60:309 – 324.

Murtagh, D., Frisk, U., Merino, F., Ridal, M., Jonsson, A., Stegman, J., Witt, G., Eriksson, P., Jiménez, C., Megie, G., de La Noë, J., Ricaud, P., Baron, P., Pardo, J. R., Hauchcorne, A., Llewellyn, E. J., Degenstein, D. A., Gattinger, R. L., Lloyd, N. D., Evans, W. F. J., McDade, I. C., Haley, C., Sioris, C., von Savigny, C., Solheim, B. H., McConnell, J. C., Strong, K., Richardson, E. H., Leppelmeier, G. W., Kyrölä, E., Auvinen, H., and Oikarinen, L. (2002). An overview of the Odin atmospheric mission. *Can. J. Phys.*, 80:309–319.

Ogawa, S. and Ogawa, M. (1975). Absorption Cross Sections of $O_2(a^1\Delta_g)$ and $O_2(X^3\Sigma_g^-)$ in the Region from 1087 to 1700 Å. *Canadian Journal of Physics*, 53(19):1845–1852.

Pérot, K., Hauchecorne, A., Montmessin, F., Bertaux, J.-L., Blanot, L., Dalaudier, F., Fussen, D., , and Kyrölä, E. (2010). First climatology of polar mesospheric clouds from gomos/envisat stellar occultation instrument. *Atm. Chem. Phys.*, pages 2723–2735.

Picone, J., Hedin, A., Drob, D., and Aikin, A. (2002a). NRL-MSISE-00 empirical model of the atmosphere: Statistical comparisons and scientific issues. *J. Geophys. Res.*, 107:1468–1483.

Picone, J., Hedin, A., Drob, D., and Aikin, A. (2002b). NRLMSISE-00 empirical model of the atmosphere: Statistical comparisons and scientific issues. *J. Geophys. Res.*, 107(A12):1468, doi:10.1029/2002JA009430.

Picone, J. M., Hedin, A. E., Drob, D. P., and Aikin, A. C. (2002c). Nrlmsise-00 empirical model of the atmosphere: Statistical comparisons and scientific issues. *J. Geophys. Res.*, 107(A12):1468.

Plane, J. M. C., Feng, W., and Dawkins, E. C. M. (2015). The mesosphere and metals: chemistry and changes. *Chem. Rev.*, 115:4497 – 4541.

Platnick, S. and Fontenla, J. (2008). Model Calculations of Solar Spectral Irradiance in the 3.7-αm Band for Earth Remote Sensing Applications. *J. Appl. Meteor. Climatol.*, 47:124–134.

Press, W. H., Flannery, B. P., Teukolsky, S. A., and Vetterling, W. T. (1992). *Numerical Recipes in Fortran, 2nd Edition*. Cambridge University Press, New York, New York, USA.

Rapp, M. and Thomas, G. E. (2006). Modeling the microphysics of mesospheric ice particles: Assessment of current capabilities and basic sensitivities. *Journal of Atmospheric and Solar-Terrestrial Physics*, 68:715 – 744.

Raspollini, P., Carli, B., Ceccherini, S., Forzieri, G., Sgheri, L., Ridolfi, M., Carlotti, M., Papandrea, E., Arnone, E., Dinelli, B. M., Castelli, E., Remedios, J., Sembhi, H., Dudhia, A., Lopez-Puertas, M., Funke, B., Flaud, J.-M., von Clarmann, T., Hoepfner, M., Oelhaf, H., Fischer, H., Kiefer, M., Kleinert, A., Chipperfield, M., .Perron, G., Aubertin, G., Birk, M., Wagner, G., Gessner, R., Mosner, P., Schmitt, M., Fehr, T., D'Alba, L., and Niro, F. (2010). Level 2 near–real–time analysis of MIPAS measurements on ENVISAT. In *Eight years of MIPAS measurements*, volume SP-686, pages 011–d2. ESA Publication Division.

Rienecker, M. M., Suarez, M. J., Gelaro, R., Todling, R., Bacmeister, J., Liu, E., Bosilovich, M. G., Schubert, S. D., Takacs, L., Kim, G.-K., Bloom, S., Chen, J., Collins, D., Conaty, A., da Silva, A., Gu, W., Joiner, J., Koster, R. D., Lucchesi, R., Molod, A., Owens, T., Pawson, S., Pegion, P., Redder, C. R., Reichle, R., Robertson, F. R., Ruddick, A. G., Sienkiewicz, M., and Woollen, J. (2011). MERRA: NASA's Modern-Era Retrospective Analysis for Research and Applications. *J. Climate*, 24(14):3624–3648.

Robert, C. E. (2010). Investigation of noctilucent cloud properties and their connection with solar activity. *Dissertation, University of Bremen*, page 175 pp.

Robert, C. E., von Savigny, C., Burrows, J. P., and Baumgarten, G. (2009). Climatology of noctilucent cloud radii and occurrence frequency using sciamachy. *J. Atmos. Sol.-Terr. Phys.*, 71(3–4):408 – 423.

Rodgers, C. D. (1976). Retrieval of atmospheric temperature and composition from remote measurements of thermal radiation. *Rev. Geophys.*, 14(4):609–624.

Rodgers, C. D. (2000). *Inverse methods for atmospheric sounding: Theory and practice*. World Scientific.

Rosenkranz, P. W. (1975). Shape of the 5 mm oxygen band in the atmosphere. *IEEE Trans. Antennas Propag.*, AP–23(4):498–506.

Rothman, L., Gordon, I., Babikov, Y., Barbe, A., Benner, D. C., Bernath, P., Birk, M., Bizzocchi, L., Boudon, V., Brown, L., Campargue, A., Chance, K., Cohen, E., Coudert, L., Devi, V., Drouin, B., Fayt, A., Flaud, J.-M., Gamache, R., Harrison, J., Hartmann, J.-M., Hill, C., Hodges, J., Jacquemart, D., Jolly, A., Lamouroux, J., Roy, R. L., Li, G., Long, D., Lyulin, O., Mackie, C., Massie, S., Mikhailenko, S., Müller, H., Naumenko, O., Nikitin, A., Orphal, J., Perevalov, V., Perrin, A., Polovtseva, E., Richard, C., Smith, M., Starikova, E., Sung, K., Tashkun, S., Tennyson, J., Toon, G., Tyuterev, V., and Wagner, G. (2013). The HITRAN 2012 molecular spectroscopic database. *Journal of Quantitative Spectroscopy and Radiative Transfer*, 130(0):4–50. {HITRAN2012} special issue.

Rothman, L., Jacquemart, D., Barbe, A., Benner, D. C., Birk, M., Browne, L., Carleer, M., Jr, C. C., Chance, K., Coudert, L., Dana, V., Devi, V., Flaud, J.-M., Gamache, R., Goldman, A., Hartmann, J.-M., Jucks, K., Maki, A., Mandin, J.-Y., Massien, S., Orphal, J., Perrin, A., Rinsland, C., Smith, M., Tennyson, J., Tolchenov, R., Toth, R., Auwera, J. V., Varanasi, P., and Wagner, G. (2005). The HITRAN 2004 molecular spectroscopic database. *J. Quant. Spectrosc. Radiat. Transfer*, 96:139–204.

Rothman, L. S., Gordon, I. E., Barbe, A., Benner, D. C., Bernath, P. F., Birk, M., Boudon, V., Brown, L. R., Campargue, A., Champion, J., Chance, K., Coudert, L. H., Dana, V., Devi, V. M., Fally, S., Flaud, J., Gamache, R. R., Goldman, A., Jacquemart, D., Kleiner, I., Lacome, N., Lafferty, W. J., Mandin, J., Massie, S. T., Mikhailenko, S. N., Miller, C. E., Moazzen-Ahmadi, N., Naumenko, O. V., Nikitin, A. V., Orphal, J., Perevalov, V. I., Perrin, A., Predoi-Cross, A., Rinsland, C. P., Rotger, M., Šimečková, M., Smith, M. A. H., Sung, K., Tashkun, S. A., Tennyson, J., Toth, R. A., Vandaele, A. C., and Vander Auwera, J. (2009). The HITRAN 2008 molecular spectroscopic database. *J. Quant. Spectrosc. Radiat. Transfer*, 110:533–572.

Rozanov, V., Rozanov, A., Kokhanovsky, A., and Burrows, J. (2014). Radiative transfer through terrestrial atmosphere and ocean: Software package {SCIATRAN}. *Journal of Quantitative Spectroscopy and Radiative Transfer*, 133:13 – 71.

Ruyten, W. (2004). Comment on "A new implementation of the Humlicek algorithm for the calculation of the Voigt profile function" by M. Kuntz [JQSRT 57(6) (1997) 819–824]. *J. Quant. Spectrosc. Radiat. Transfer*, 86:231–233.

Rydberg, B., Eriksson, P., Kiviranta, J., Skyman, A., and Murtagh, D. (2016). Odin/SMR algorithm theoretical basis document - Level 1b processing. Technical report, Department of Earth and Space Sciences, Chalmers University of Technology.

Schadee, A. (1964). The formation of molecular lines in the solar spectrum (errata: 17 537). *B. Astron. Inst. Neth.*, 17:311–357.

Scharringhausen, M., Aikin, A. C., Burrows, J. P., and Sinnhuber, M. (2008). Global column density retrievals of mesospheric and thermospheric MgI and MgII from SCIAMACHY limb and nadir radiance data. *J. Geophys. Res.*, 113(D13):D13303. WOS:000257797900001.

Serdyuchenko, A., Gorshelev, V., Weber, M., Chehade, W., and Burrows, J. P. (2014). High spectral resolution ozone absorption cross-sections – part 2: Temperature dependence. *Atmospheric Measurement Techniques*, 7(2):625–636.

She, C. Y., Chen, S., Hu, Z., Sherman, J., Vance, J. D., Vasoli, V., White, M. A., Yu, J., and Krueger, D. A. (2000). Eight-year climatology of nocturnal temperature and sodium density in the mesopause region (80 to 105 km) over fort collins, co (41n,105w). *Geophys. Res. Lett.*, 27:3289 – 3292.

Sheese, P. (2009). *Mesospheric ozone densities retrieved from OSIRIS observations of the O_2 A-band dayglow*. PhD thesis, York University, Toronto.

Sheese, P. E., Gattinger, R. L., Llewellyn, E. J., Boone, C. D., and Strong, K. (2011a). Nighttime nitric oxide densities in the Southern Hemisphere mesosphere-lower thermosphere. *Geophys. Res. Lett.*, 38:L15812.

Sheese, P. E., Llewellyn, E. J., Gattinger, R. L., Bourassa, A. E., Degenstein, D. A., Lloyd, N. D., and McDade, I. C. (2010). Temperatures in the upper mesosphere and lower thermosphere from osiris observations of O_2 A-band emission spectra. *Can. J. Phys.*, 88:919–925.

Sheese, P. E., McDade, I. C., Gattinger, R. L., and Llewellyn, E. J. (2011b). Atomic oxygen densities retrieved from Optical Spectrograph and Infrared Imaging System observations of O_2 A-band airglow emission in the mesosphere and lower thermosphere. *J. Geophys. Res.*, 116:D01303.

Skupin, J., Noel, S., Wuttke, M. W., Bovensmann, H., Burrows, J. P., Hoogeven, R., Kleipool, Q., and Lichtenberg, G. (2003). In-flight calibration of the sciamahcy solar irradiance spectrum. *Adv. Space Res.*, 32:2129 – 2134.

Slipher, V. M. (1929). Emissions in the spectrum of the light of the night sky. *Publ. Astron. Soc. Pacific*, 41:262 – 263.

Sofieva, V. F., Tamminen, J., Haario, H., Kyrölä, E., and Lehtinen, M. (2004). Ozone profile smoothness as a priori information in the inversion of limb measurements. *Annales Geophysicae*, 22(10):3411–3420.

Sofieva, V. F., Vira, J., Kyrölä, E., Tamminen, J., Kan, V., Dalaudier, F., Hauchecorne, A., Bertaux, J., Fussen, D., Vanhellemont, F., Barrot, G., and Fanton D'Andon, O. (2010). Retrievals from GOMOS stellar occultation measurements using characterization of modeling errors. *Atmospheric Measurement Techniques*, 3(4):1019–1027.

Steck, T. and von Clarmann, T. (2001). Constrained profile retrieval applied to the observation mode of the Michelson Interferometer for Passive Atmospheric Sounding. *Appl. Opt.*, 40(21):3559–3571.

Stevens, M. H. (1995). Nitric oxide γ band fluorescent scattering and self-absorption in the mesosphere and lower thermosphere. *J. Geophys. Res.*, 100(A8):14735–14742.

Stiller, G. P., von Clarmann, T., Fischer, H., Funke, B., Glatthor, N., Grabowski, U., Höpfner, M., Kiefer, M., and Milz, M. (2002). *Entwicklung eines Auswerte-Algorithmus und eines Datenverarbeitungssystems für das MIPAS Satellitenexperiment*, volume FZKA 6703 of *Wissenschaftliche Berichte*. Forschungszentrum Karlsruhe.

Tamminen, J., Kyrölä, E., Sofieva, V. F., Laine, M., Bertaux, J., Hauchecorne, A., Dalaudier, F., Fussen, D., Vanhellemont, F., Fanton-D'Andon, O., Barrot, G., Mangin, A., Guirlet, M., Blanot, L., Fehr, T., Saavedra de Miguel, L., and Fraisse, R. (2010). GOMOS data characterisation and error estimation. *Atmospheric Chemistry & Physics*, 10:9505–9519.

Tatum, J. B. (1967). The interpretation of intensities in diatomic molecular spectra. *Astrophys. J. Suppl.*, 14:21–55.

Thuillier, G., Floyd, L., Woods, T., Cebula, R., Hilsenrath, E., Herse, M., and Labs, D. (2004). Solar irradiance reference spectra. In et al., J. P., editor, *Solar Variability and its Effect on the Earth's Atmosphere and Climate System*, page 171. AGU, Washington, DC.

Tikhonov, A. (1963). On the solution of incorrectly stated problems and method of regularization. *Dokl. Akad. Nauk. USSR*, 151(3):501–504.

Tikhonov, A. N. (1943). On the stability of inverse problems. *Proc. of the USSR Acad. of Science*, 39(5):195 – 198.

Toon, O. B., Tolbert, M. A., Koehler, B. G., Middlebrook, A. M., and Jordan, J. (1994). Infrared optical constants of H_2O ice, amorphous nitric acid solutions, and nitric acid trihydrates. *J. Geophys. Res.*, 99(D12):25,631–25,654.

Vitt, F. M., Cravens, T. E., and Jackman, C. H. (2000). A two–dimensional model of thermospheric nitric oxide sources and their contributions to the middle atmospheric chemical balance. *J. Atmos. Solar–Terr. Phys.*, 62(8):653–667.

von Clarmann, T. and Echle, G. (1998). Selection of optimized microwindows for atmospheric spectroscopy. *Appl. Opt.*, 37(33):7661–7669.

von Clarmann, T., Glatthor, N., Grabowski, U., Höpfner, M., Kellmann, S., Kiefer, M., Linden, A., Mengistu Tsidu, G., Milz, M., Steck, T., Stiller, G. P., Wang, D. Y., Fischer, H., Funke, B., Gil-López, S., and López-Puertas, M. (2003). Retrieval of temperature and tangent altitude pointing from limb emission spectra recorded from space by the Michelson Interferometer for Passive Atmospheric Sounding (MIPAS). *J. Geophys. Res.*, 108(D23).

von Clarmann, T., Glatthor, N., Grabowski, U., Höpfner, M., Kellmann, S., Kiefer, M., Linden, A., Tsidu, G. M., Milz, M., Steck, T., Stiller, G. P., Wang, D. Y., Fischer, H., Funke, B., Gil-López, S., and López-Puertas, M. (2003). Retrieval of temperature and tangent altitude pointing from limb emission spectra recorded from space by the michelson interferometer for passive atmospheric sounding (mipas). *J. Geophys. Res.*, 108(D23):4736.

von Clarmann, T., Höpfner, M., Kellmann, S., Linden, A., Chauhan, S., Funke, B., Grabowski, U., Glatthor, N., Kiefer, M., Schieferdecker, T., Stiller, G. P., and Versick, S. (2009). Retrieval of temperature, h_2o, o_3, hno_3, ch_4, n_2o, $clono_2$ and clo from mipas reduced resolution nominal mode limb emission measurements. *Atmos. Meas. Tech.*, 2(1):159–175.

von Savigny, C. and Burrows, J. P. (2007). Latitudinal variation of nlc particle radii derived from northern hemisphere sciamachy/envisat limb measrurements. *Adv. Space Res.*, 40(6):765 – 771.

von Savigny, C., Kokhanovsky, A., Bovensmann, H., Eichmann, K.-U., Kaiser, J. W., Noel, S., Rozanov, A. V., Skupin, J., and Burrows, J. P. (2004). Nlc detection and particle size determination: First results from sciamachy on envisat. *Adv. Space Res.*, 23(4):851 – 856.

von Savigny, C., Langowski, M. P., Zilker, B., Burrows, J. P., Fussen, D., and Sofieva, V. F. (2016). First mesopause na retrievals from satellite na d-line nightglow observations. *Geophys. Res. Lett.*, revised.

von Savigny, C., Robert, C. E., Baumgarten, G., Bovensmann, H., and Burrows, J. P. (2009). Comparison of nlc particle sizes derived from sciamachy/envisat observations with ground-based lidar measurements at alomar (69° n). *Atmos. Meas. Tech.*, 2:523 – 531.

West, G. A., Weston, R. E., and Flynn, G. W. (1978). The influence of reactant vibrational excitation on the $O(^3P)$+O_3 bimolecular reaction rate. *Chem. Phys. Lett.*, 56:429–433.

West, G. A., Weston Jr., R. E., and Flynn, G. W. (1976). Deactivation of vibrationally excited ozone by $O(^3P)$ atoms. *Chem. Phys. Lett.*, 42(3):488–493.

WGS 84 (1998). *Implementation Manual Version 2.4*. European Organization for the Safety of Air Navigation, Brussels, Belgium, the Institute of Geodesy and Navigation, University FAF, Munich, Germany.

Whitson, M. E. and McNeal, R. J. (1977). Temperature dependence of the quenching of vibrationally excited N_2 by NO and H_2O. *The Journal of Chemical Physics*, 66(6):2696–2700.

Whytock, D. A., Michael, J. V., and Payne, W. A. (1976). Absolute rate constants for O + NO + $N_2 \rightarrow NO_2$ + N_2 from 217-500 K. *Chem. Phys. Lett.*, 42:466–471.

Wissing, J. M. and Kallenrode, M.-B. (2009). Atmospheric Ionization Module OSnabrück (AIMOS) 1: A 3D model to determine atmospheric ionization by energetic charged particles from different populations. *J. Geophys. Res.*

Xu, J., Smith, A. K., and Wu, Q. (2005). A retrieval algorithm for satellite remote sensing of the nighttime global distribution of the sodium layer. *J. Atmos. Sol. Terr. Phys.*, 67:739 – 748.

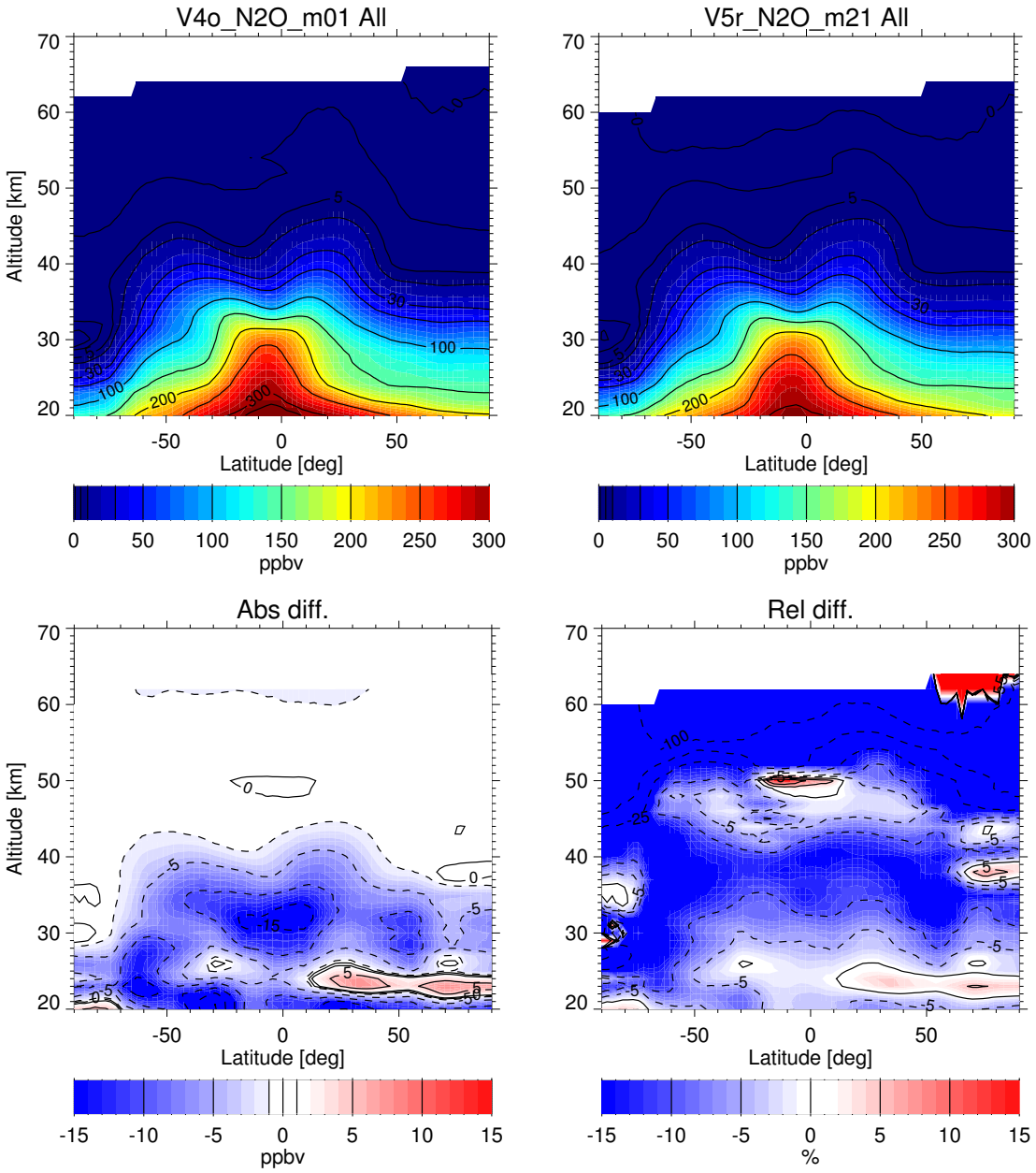

Figure 17: Comparison of N_2O abundance retrieved in the current V5r_N2O_m21 and the previous V4O_N2O_m01 versions for 3 June 2009.

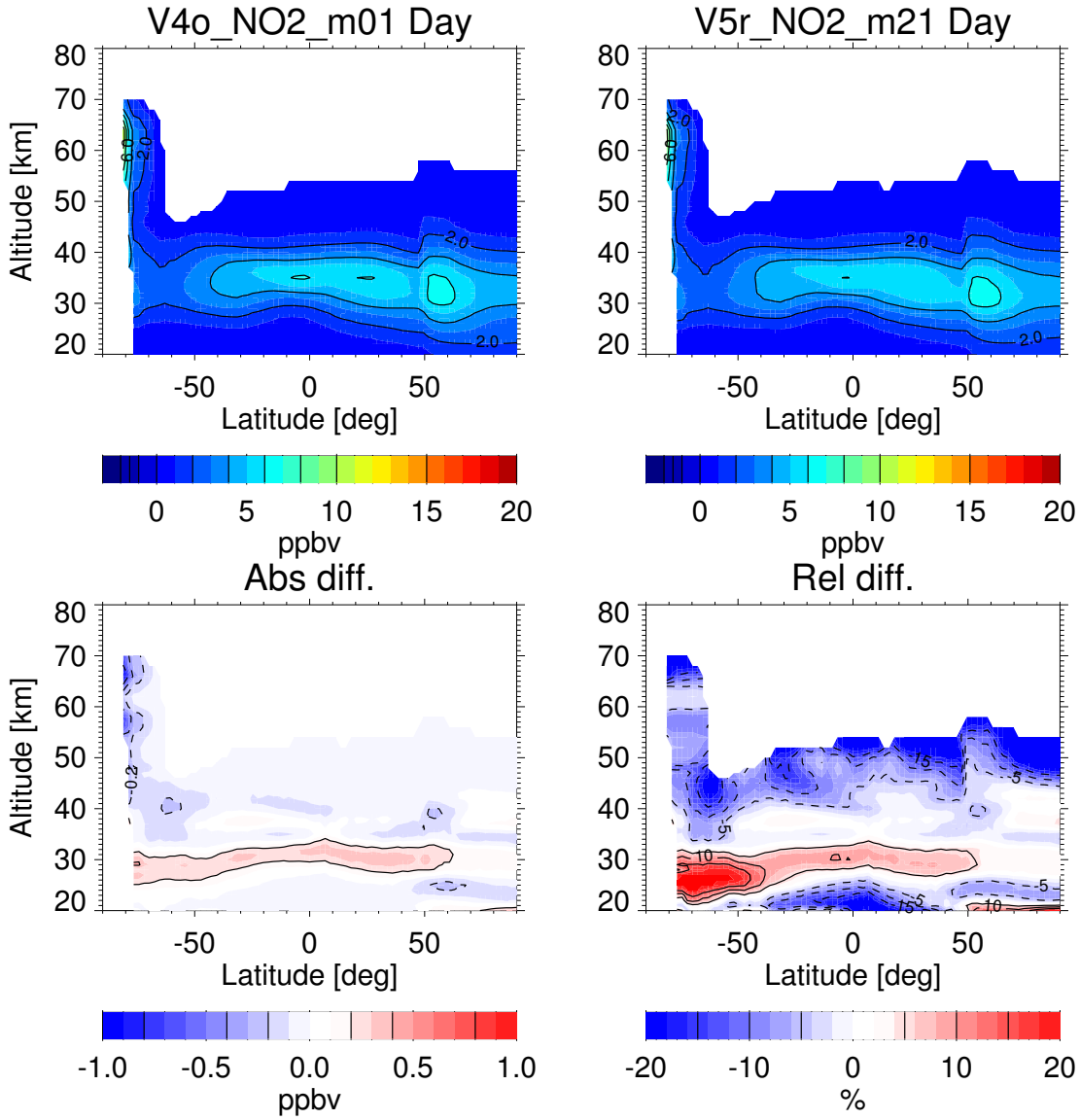

Figure 18: Comparison of NO_2 abundance for daytime conditions (10 am) retrieved in the current V5r_NO2_m21 and the previous V4O_NO2_m01 versions for 5 June 2009. Lower panels show the V5r_NO2_m21–V4O_NO2_m01 differences. White areas indicate unavailability of meaningful data.

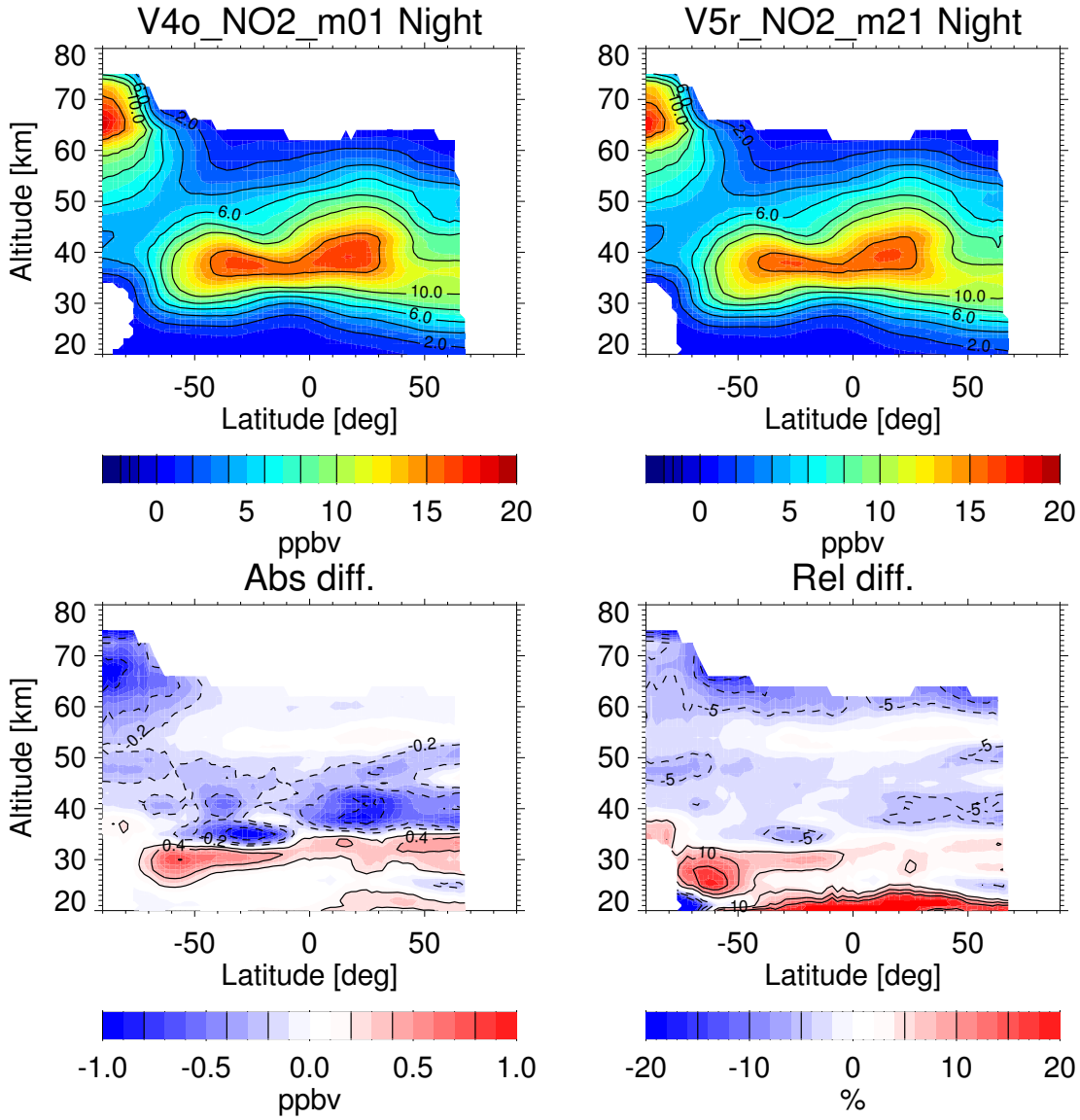

Figure 19: Comparison of NO_2 abundance for nighttime conditions (10 pm) retrieved in the current V5r_NO2_m21 and the previous V4O_NO2_m01 versions for 5 June 2009. Lower panels show the V5r_NO2_m21–V4O_NO2_m01 differences. White areas indicate unavailability of meaningful data.

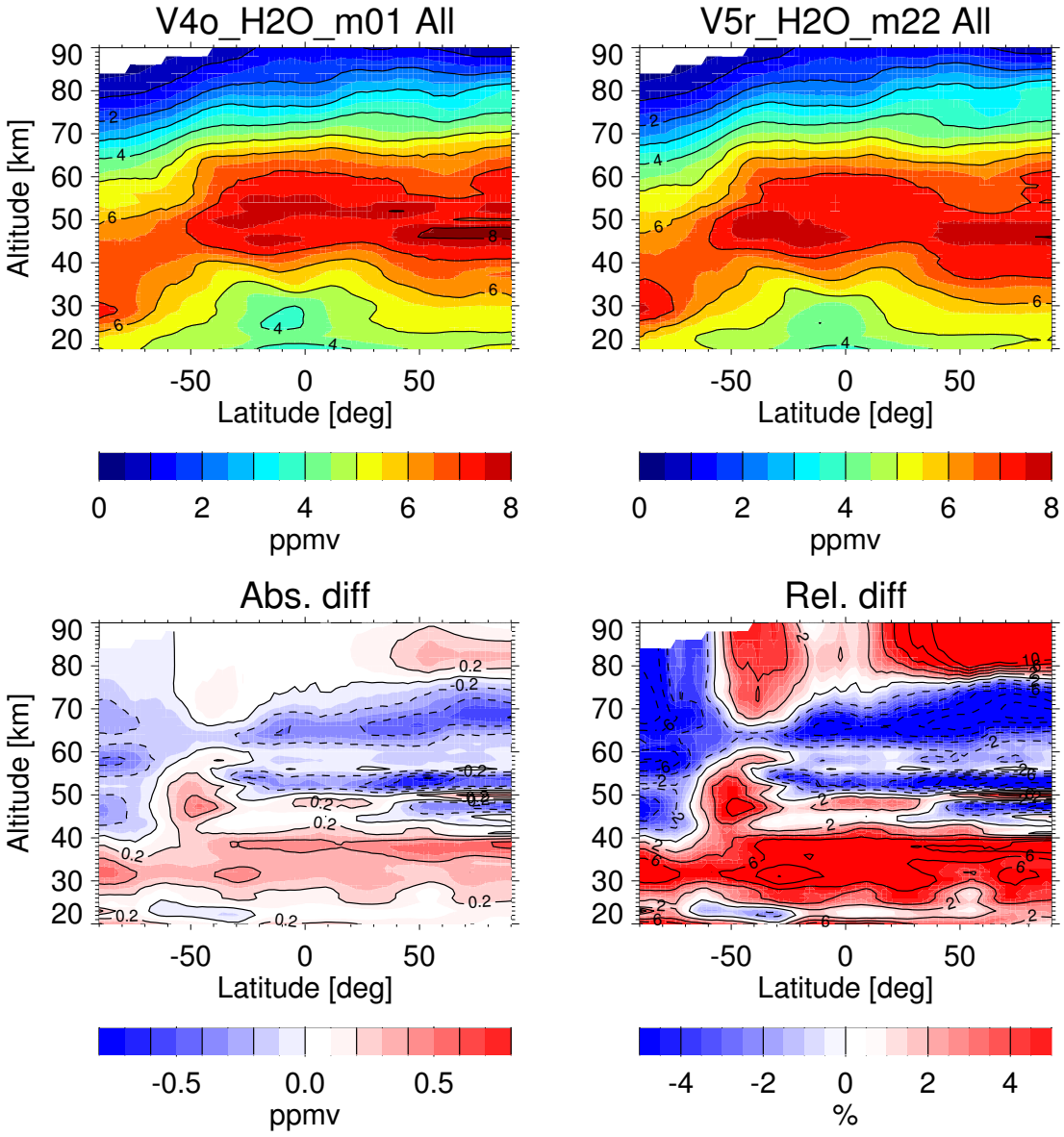

Figure 20: Comparison of H_2O abundance retrieved in the current V5r_H2O_m22 and the previous V4O_H2O_m06 versions for 3 June 2009. White areas indicate unavailability of meaningful data.

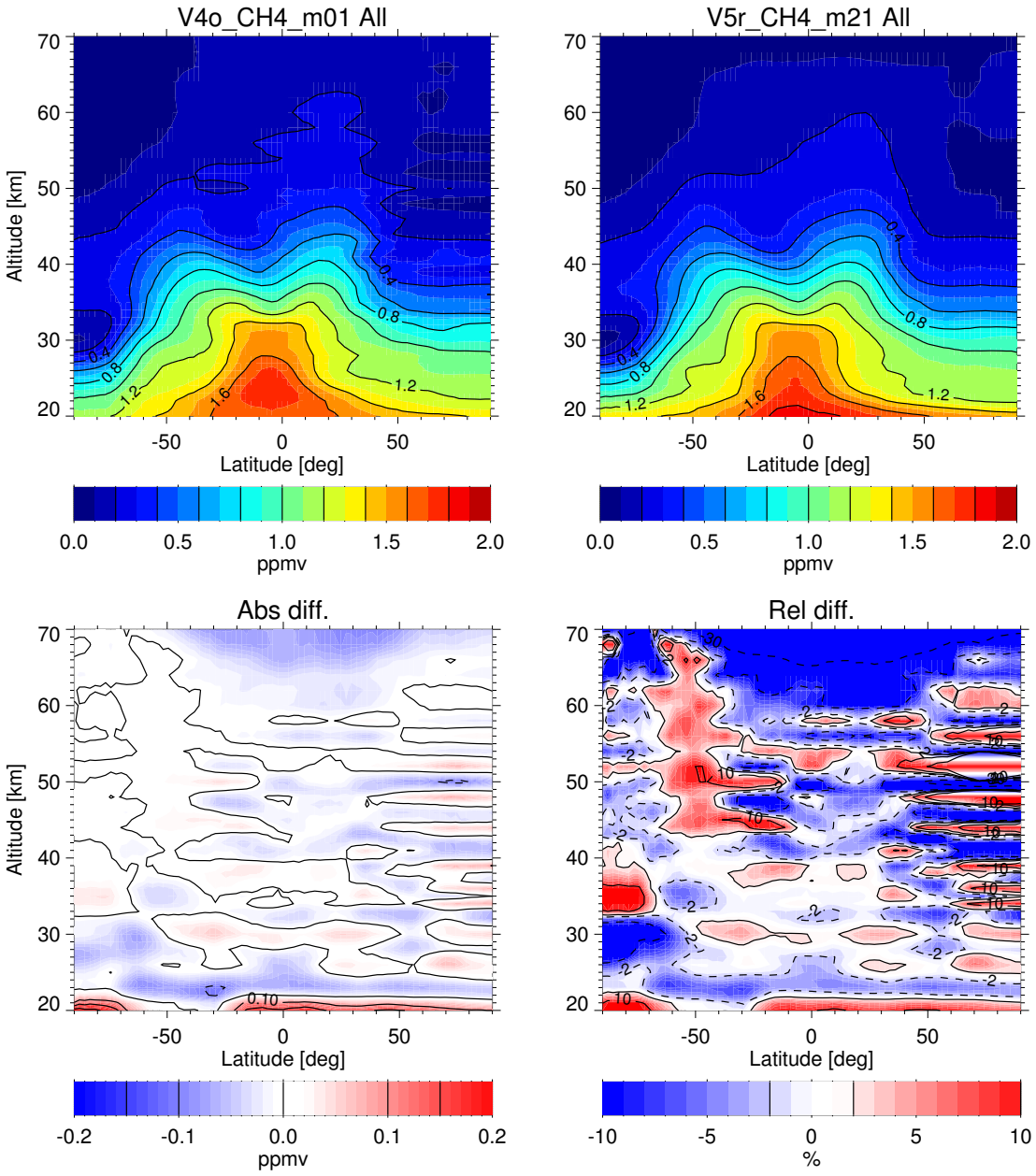

Figure 21: Comparison of CH_4 abundance retrieved in the current V5r_CH4_m21 and the previous V4O_CH4_m01 versions for 3 June 2009.

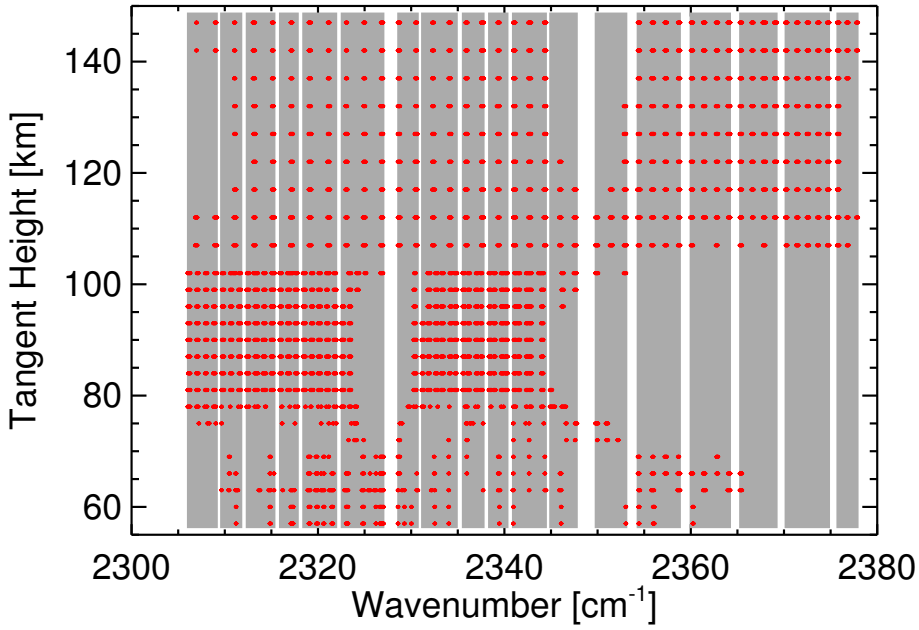

Figure 22: Occupation matrix used in the CO_2 retrieval in the 4.3 μm spectral region. Shaded regions represent the spectral regions selected and red dots the microwindow mask at each tangent height. The specific microwindows used in the retrieval are listed in Appendix A.

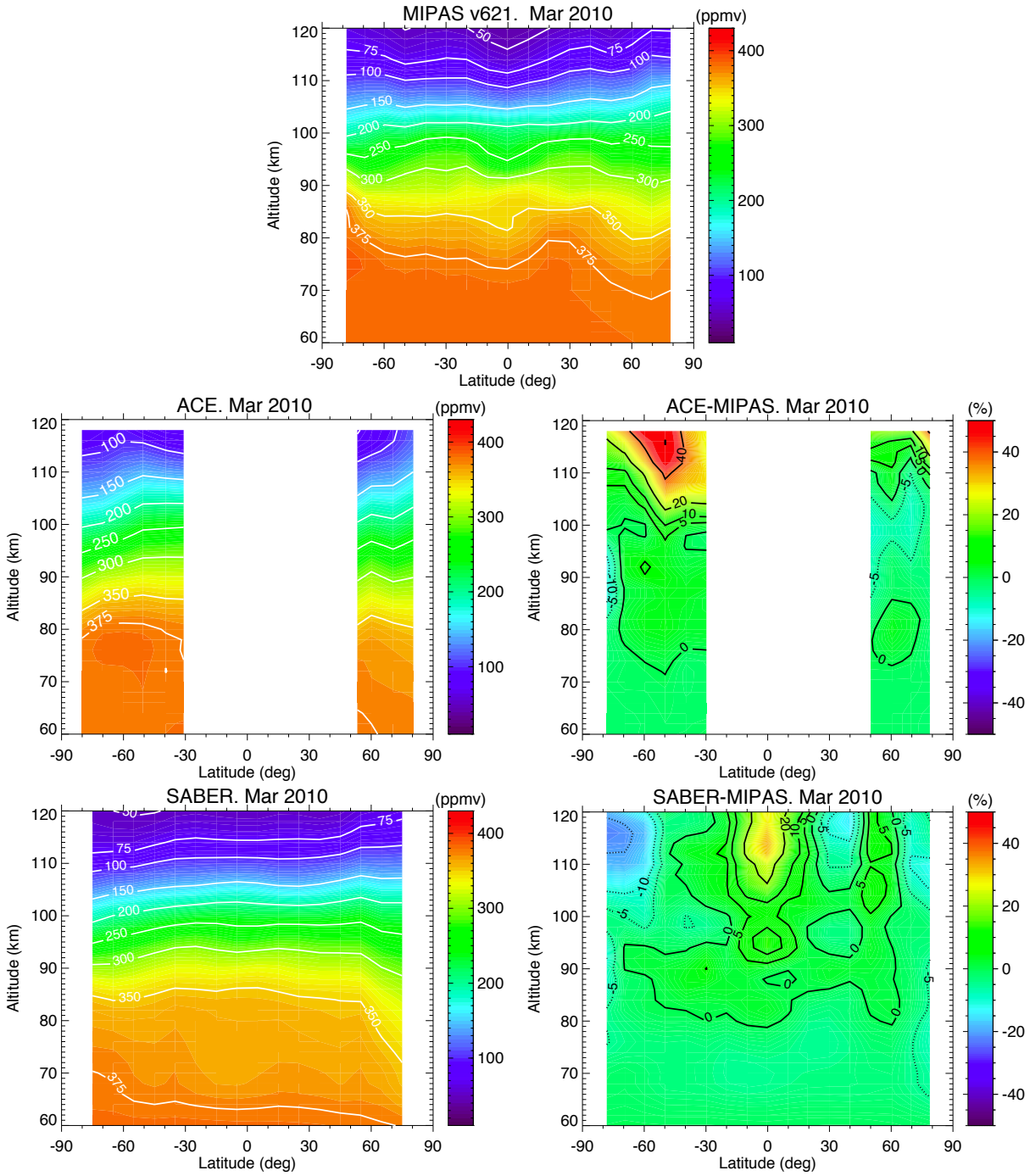

Figure 23: CO_2 vmr abundances for March 2010. Left panels: zonal mean distribution of MIPAS, ACE, and SABER. Right panels: CO_2 relative differences with respect to MIPAS (in %.)

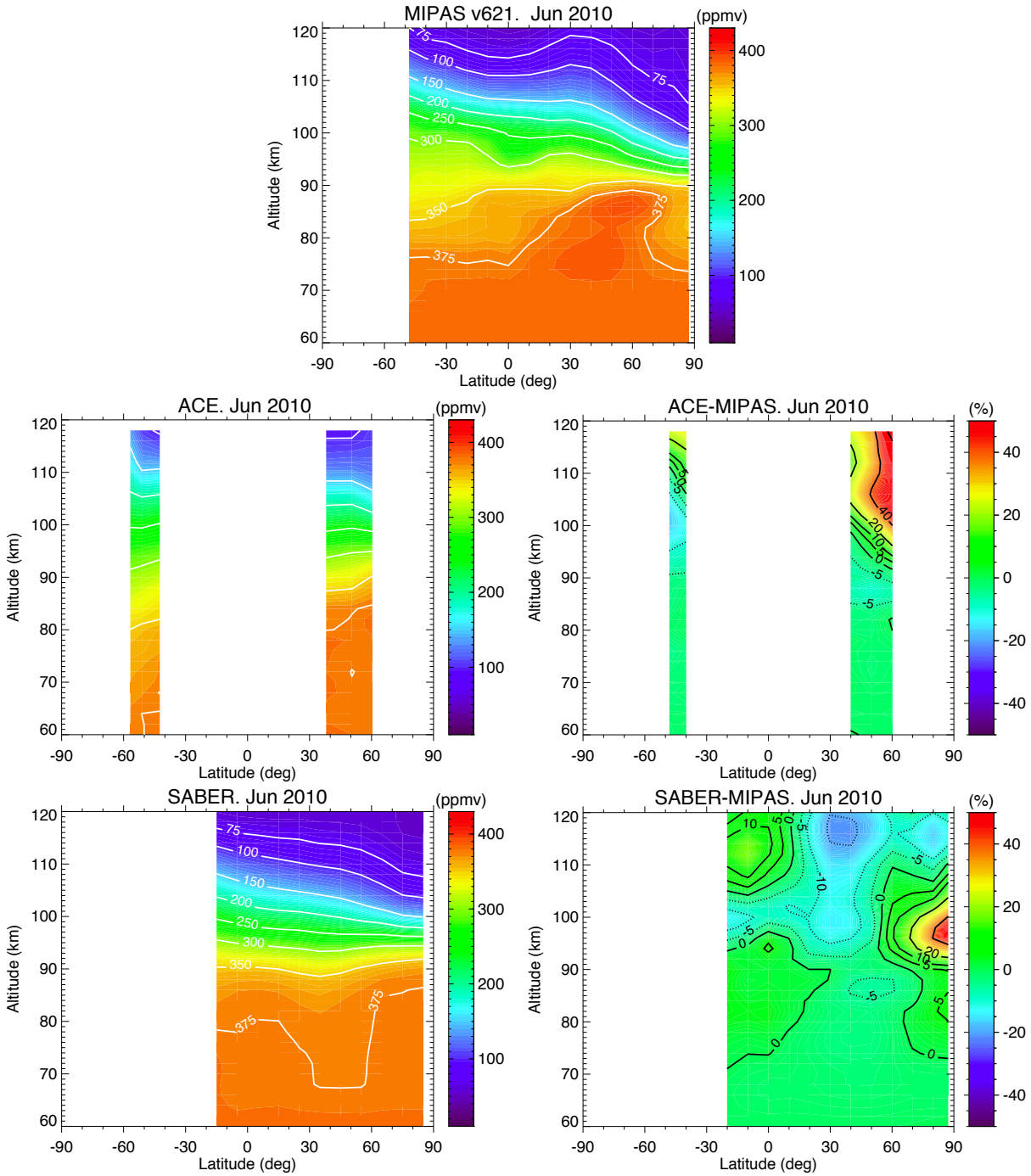

Figure 24: As Fig. 23 but for June 2010.

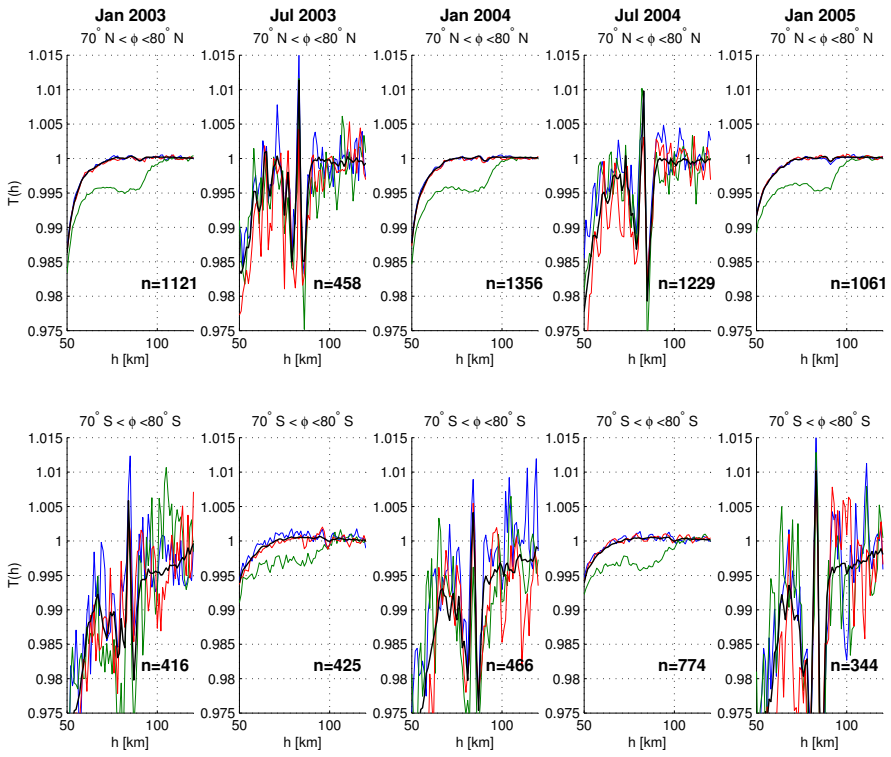

Figure 25: Median transmittances as a function of tangent height for polar bins during the months January and July from 2003 till 2005. The number of occultations in the bin is indicated by n. In each subplot, red and blue colors correspond to control pixels (with only a smooth ozone absorption) whereas the green color represents a pixel associated with the D_2 sodium absorption that exhibits a depression due to the Na mesospheric layer. The black curve is the mean transmittance in a 20 nm window around the the Na absorption region. Close to summer solstices in each hemisphere, PMC dips and "flashes" are clearly seen around 83 km, for all wavelengths.

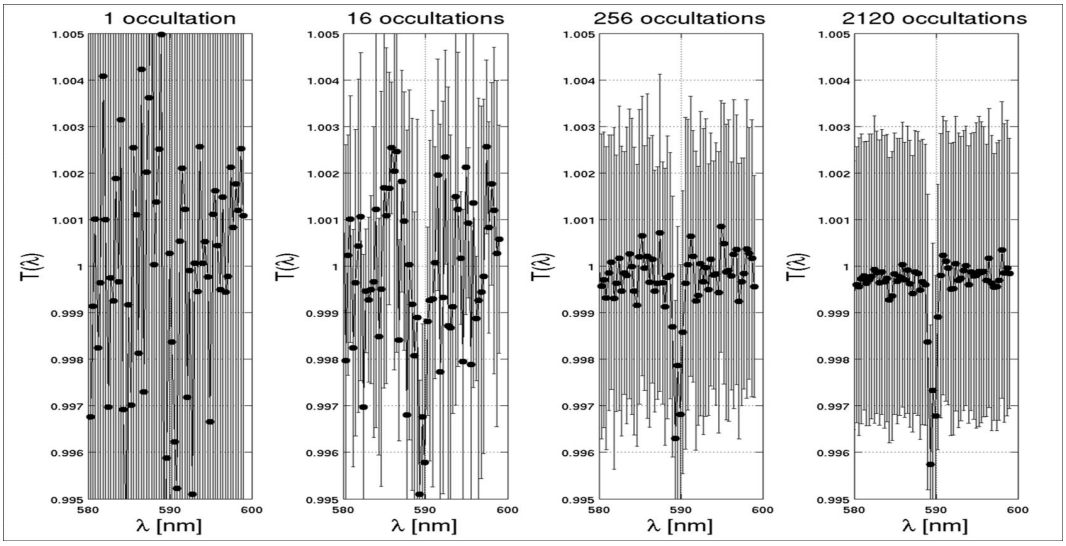

Figure 26: GOMOS weighted median transmittances as a function of the number of occultations used in the bin 70 deg.N - 80 deg.N in January 2005. Notice how the sodium doublet emerges from the noise of the averaged transmittances wheras it is hardly visible for an individual occultation.

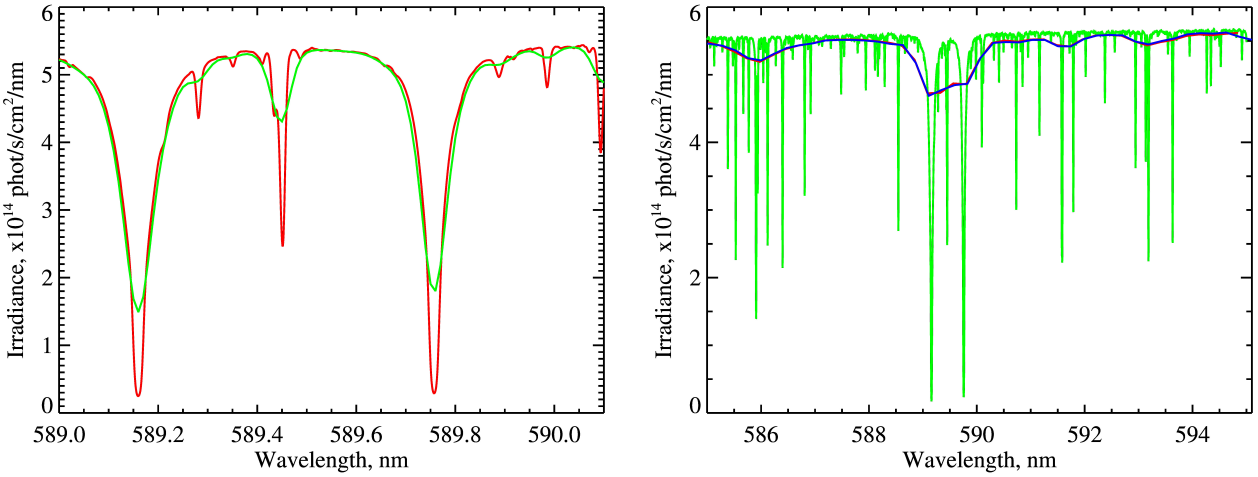

Figure 27: Left panel: Solar irradiance spectra from (Chance and Kurucz, 2010) as used for the MLT retrievals (green) and from Kurucz (2005) used in nominal limb measurements retrievals. Right panel: monthly mean solar irradiance spectrum for September 2007 obtained from SCIAMACHY measurements (blue), solar irradiance spectrum from Kurucz (2005) convolved and fitted to SCIAMACHY measurements (red) and high resolution solar irradiance spectrum from Kurucz (2005) with fitting parameters applied (red).

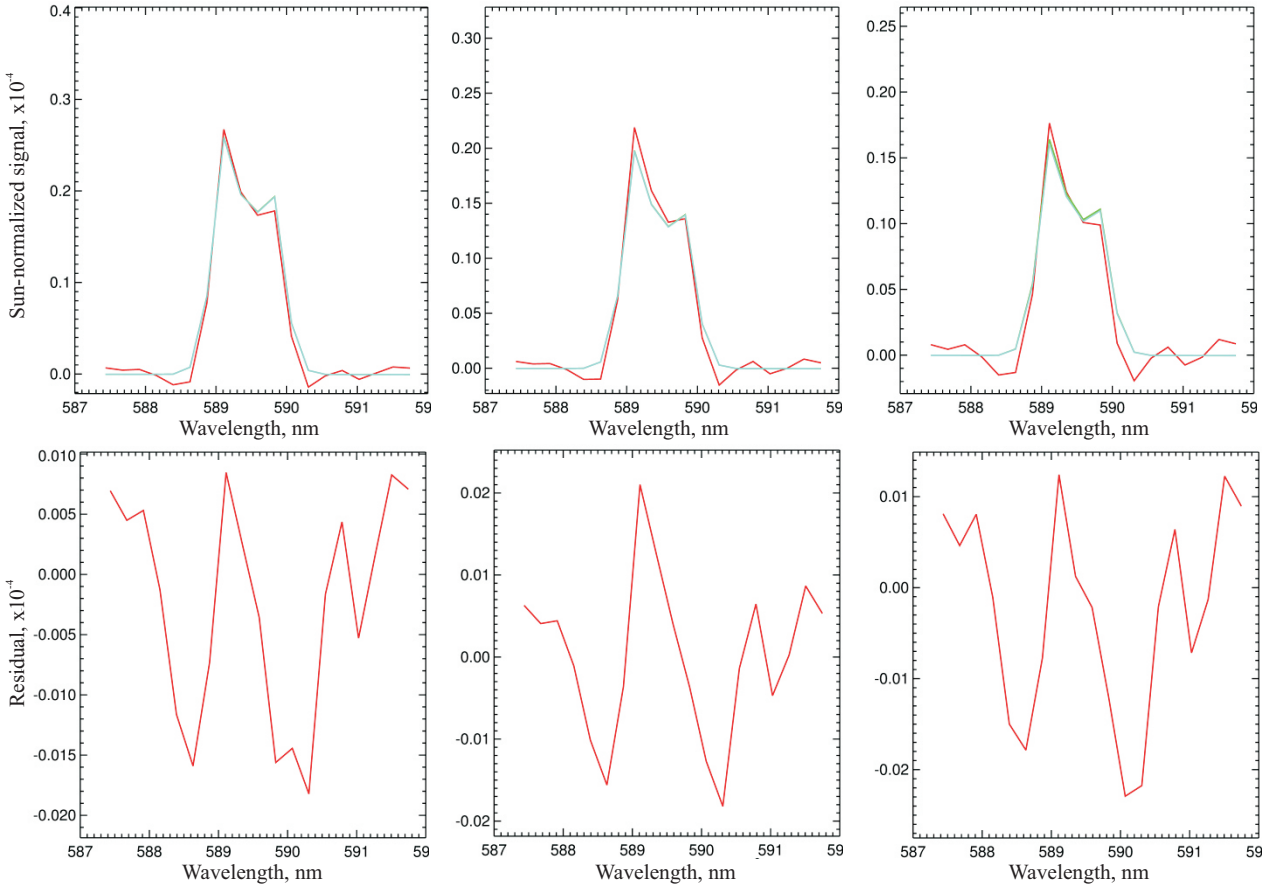

Figure 28: Spectral fits and fit residuals for sodium retrieval from nominal limb measurements of SCIAMACHY. The upper row shows the measured (red) and simulated (cyan) radiance with removed baseline. The lower row show the spectral residuals. Columns show the results for different tangen heights: 87 km, 81 km, 74 km (left to right).

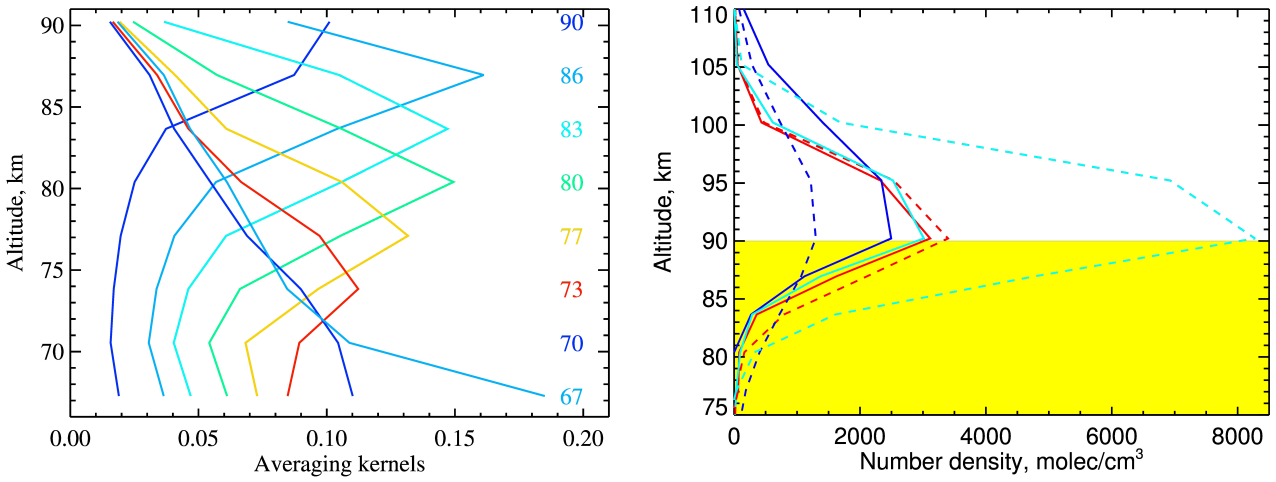

Figure 29: Left panel: typical averaging kernels for Na retrieval. Right panel: retrieval results (solid lines) for different initial guess profiles assumed (dashed lines). Yelow area depicts the retrieval range.

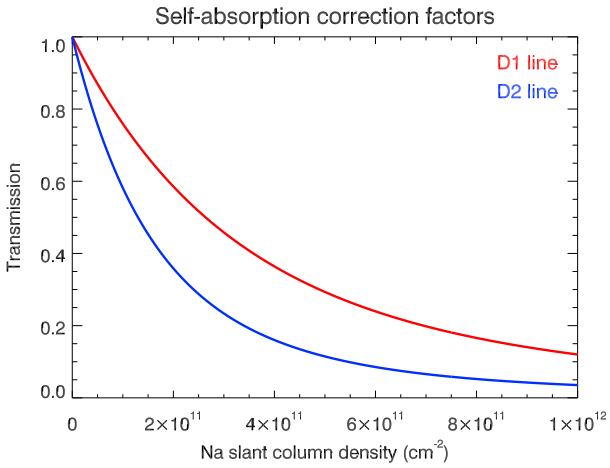

Figure 30: Dependence of transmission on Na slant column density calculated separately for the D1 and D2 lines of Na. The transmission correction factors are used for the self absorption correction.

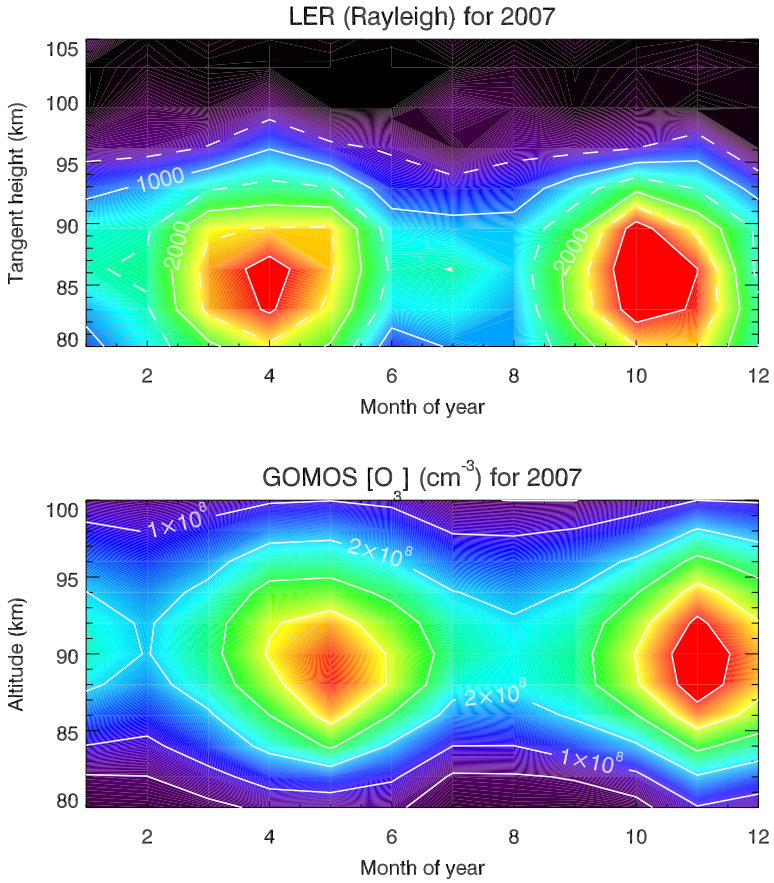

Figure 31: Top panel: Na D line limb emission rate (LER) in Rayleigh (1 R $= 10^6$ photons s^{-1} cm^{-2}) as a function month of the year 2007 and tangent height. Bottom panel: Time and altitude dependence of monthly averaged O_3 densities retrieved from GOMOS stellar occultation observations. The data in both panels were averaged over the 30° S to 30° N latitude range.

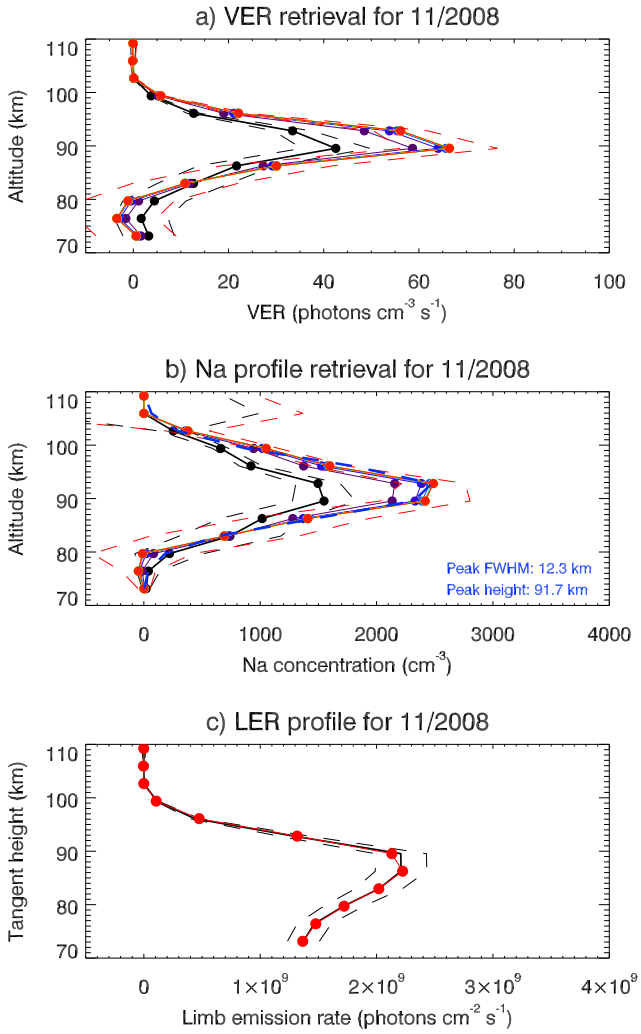

Figure 32: Sample iterative retrieval of Na D line VER (top panel) and Na profiles (middle panel) for November 2008 and a branching ratio of $f = 0.09$ (black line: first iteration; red line: last iteration). The dashed lines correspond to the propagated errors of the mean of the integrated limb emission rates (LER). Bottom panel: The black solid line shows the observed limb emission rate (LER) profile – spectrally integrated over both the D1 and D2 line. The dashed black lines show the standard error of the mean of the monthly averaged LER profiles. The red line shows the forward modelled LER profile based on the last iteration of the Na profile retrieval. Figure taken from von Savigny et al. (2016).

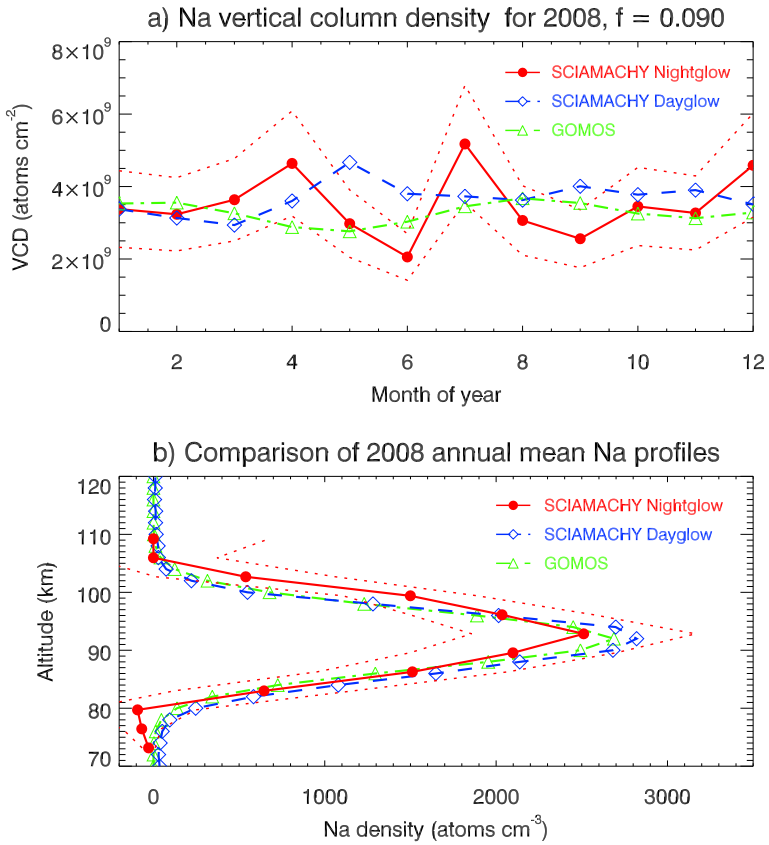

Figure 33: Top panel: Comparison of monthly averaged Na vertical column density (VCD) for 2008 retrieved from SCIAMACHY nightglow observations ($f = 0.09$; red solid line) with retrievals based on SCIAMACHY dayglow observations (blue dashed line) and GOMOS stellar occultations (green dash-dotted line). Bottom panel: Comparison of annually averaged Na density profiles retrieved from SCIAMACHY nightglow and dayglow measurements as well as GOMOS observations (same line/colour convention as in top panel). The red dotted lines in the two panels correspond to the total retrieval uncertainties presented in Table 23. Figure taken from von Savigny et al. (2016).

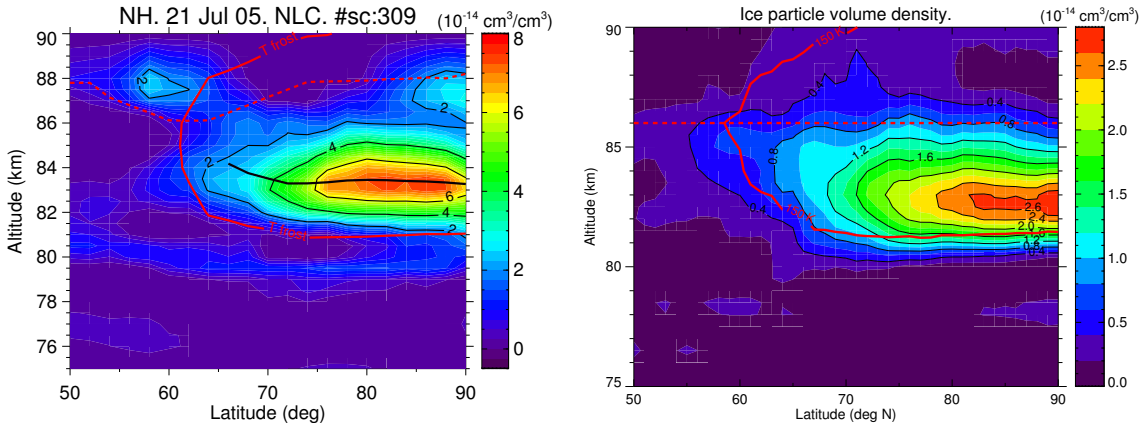

Figure 34: Comparison of NH ice volume density retrieved in the current V5r_PMC_m20 (left) and the previous V4O_PMC_m01 (right) versions for 19-21 June 2009. The solid red line indicates the 150 K temperature contour, and the red dashed line is the mesopause as measured by MIPAS. **Figure to be revised!!**

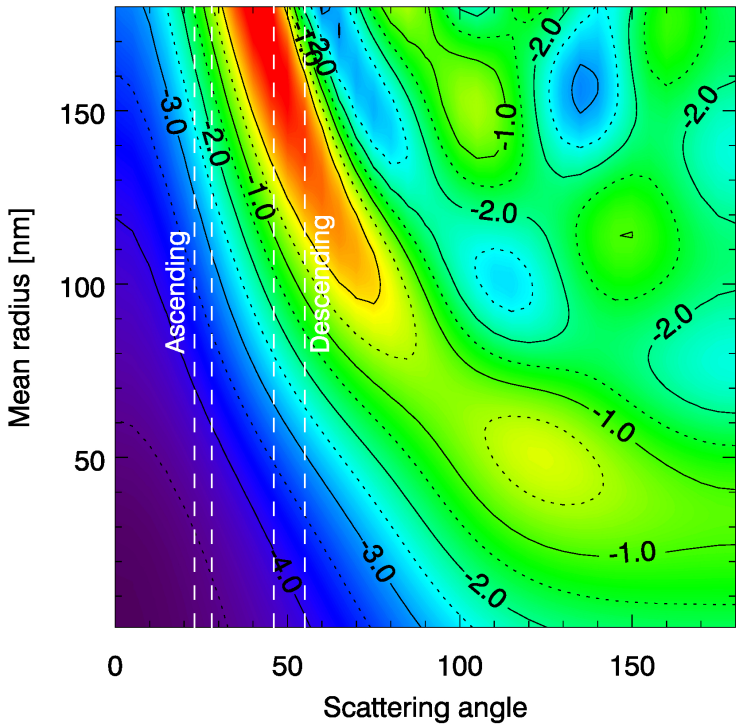

Figure 35: Ångström exponent in the 265 nm to 300 nm spectral window for a Gaussian particle size distribution with $\sigma = 24$ nm, cylindrical particles with an aspect ratio of $\epsilon = 1.0$ as a function of scattering angle and mean radius. The white dashed lines indicate the scattering angles of SCIAMACHY limb observations above ALOMAR (69° N) for the ascending and descending parts of the orbit. The scattering angles for Southern Hemisphere observations at polar latitudes are about 130° – 160° (Figure taken from von Savigny et al. (2009)).

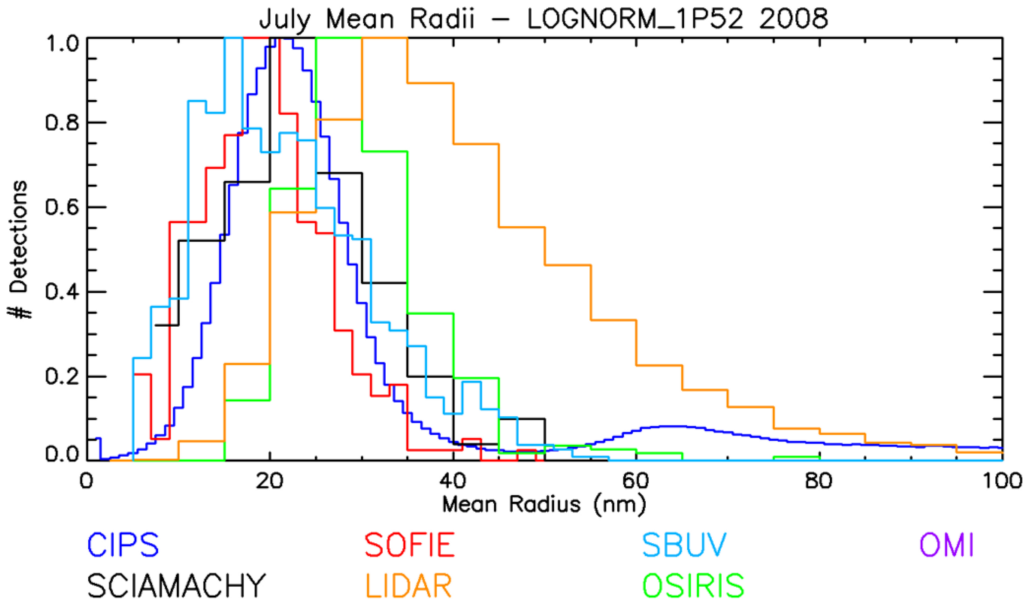

Figure 36: Comparison of NLC particle size retrievals for July 2008 assuming a log-normal PSD with $\sigma = 1.52$ (Figure created by Scott Bailey, Virginia Technical University, Blacksburg).

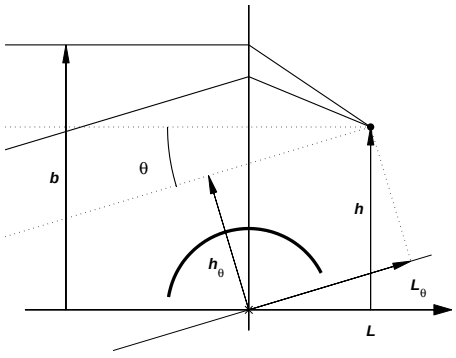

Figure 37: Geometry for angular integration across the solar disk.

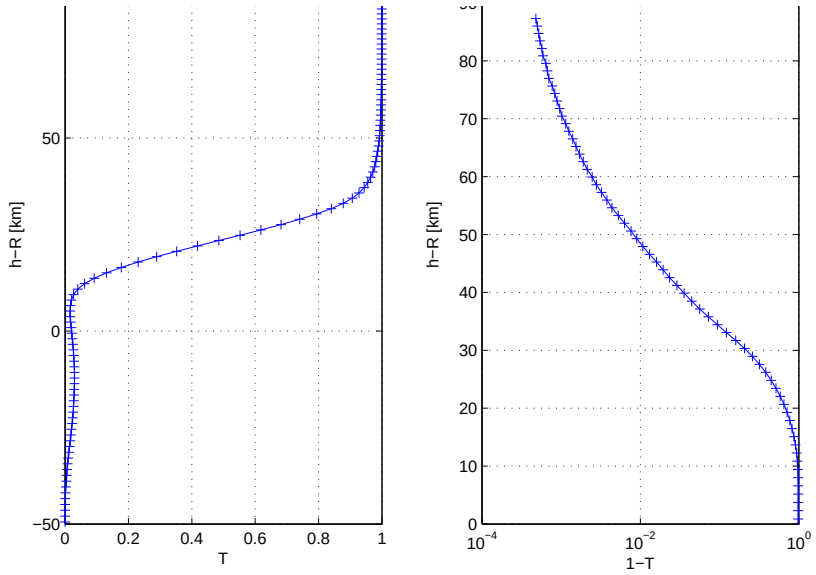

Figure 38: A typical transmittance measurement in a solar occultation observed by ORA Arijs et al. (1995). Notice the strong absorption by the Pinatubo stratospheric aerosol around $h - R \simeq 10$ km. The signal is produced by a current measurement and is virtually free of shotnoise.

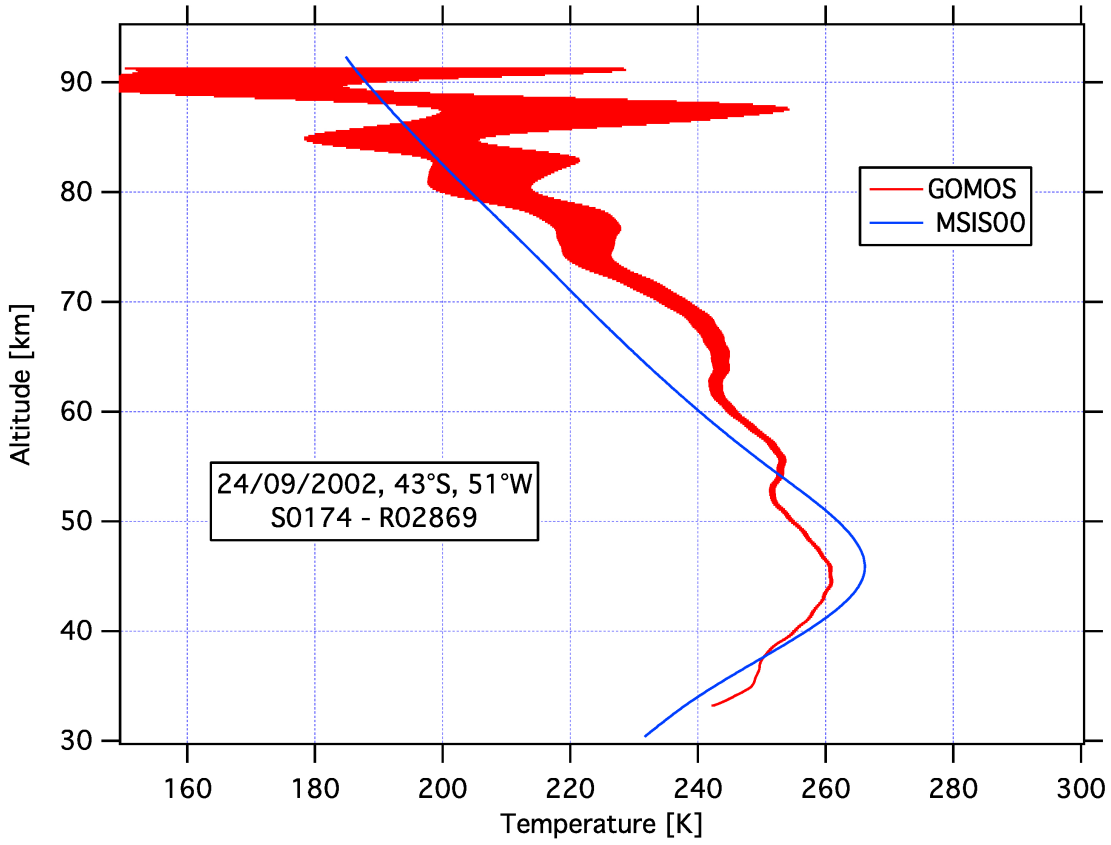

Figure 39: Example of temperature profile inverted from limb scattering in the 360-380 nm spectral interval on 24 September 2002. The corresponding MSIS00 climatological profile is shown.

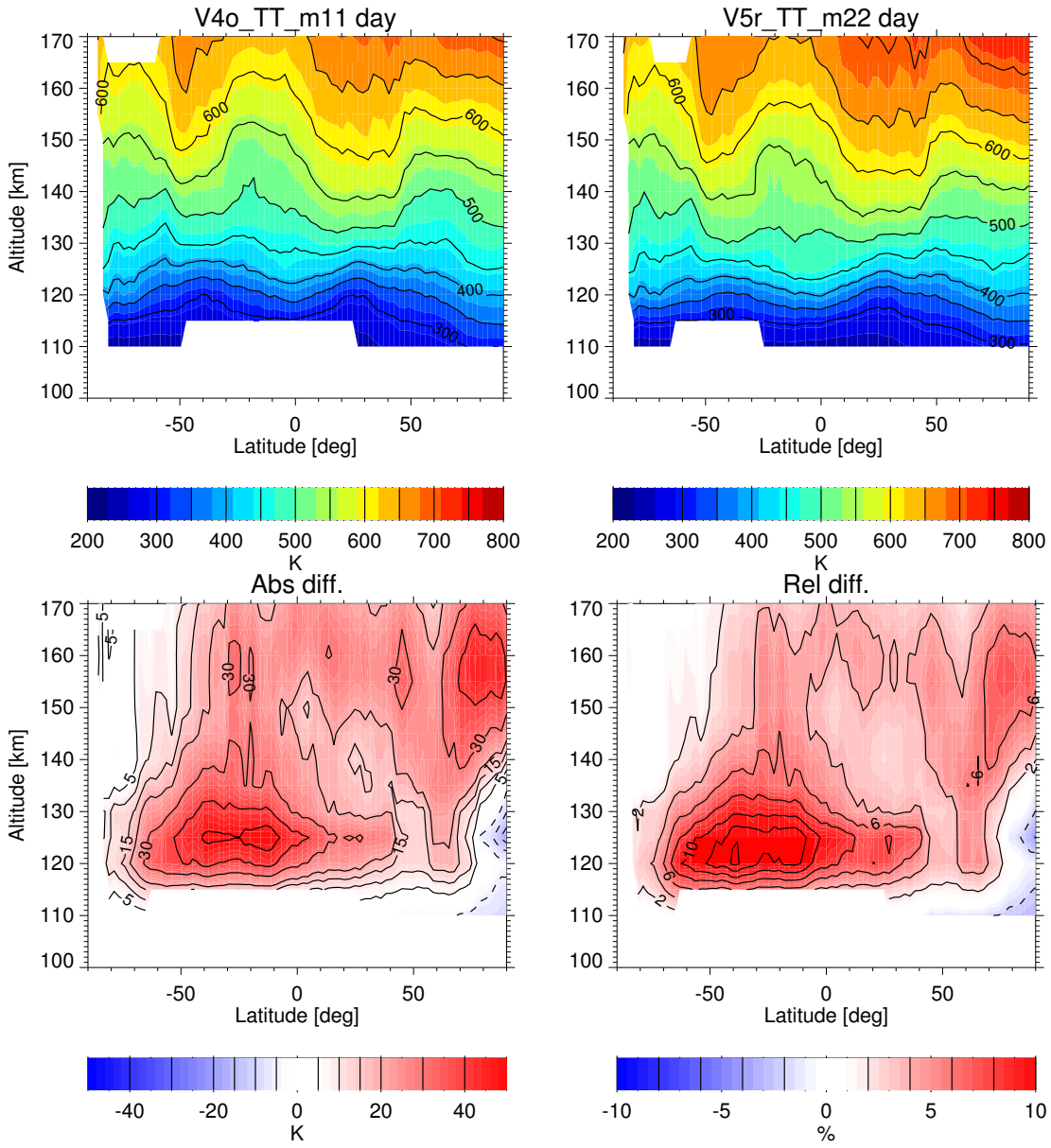

Figure 40: Comparison of thermospheric temperatures for daytime conditions (10 am) retrieved in the current V5r_TT_621 and the previous V4O_TT_601 versions for 5 June 2009 (low solar activity). Lower panels show the V5r_TT_621–V4O_TT_601 differences. White areas indicate unavailability of meaningful data.

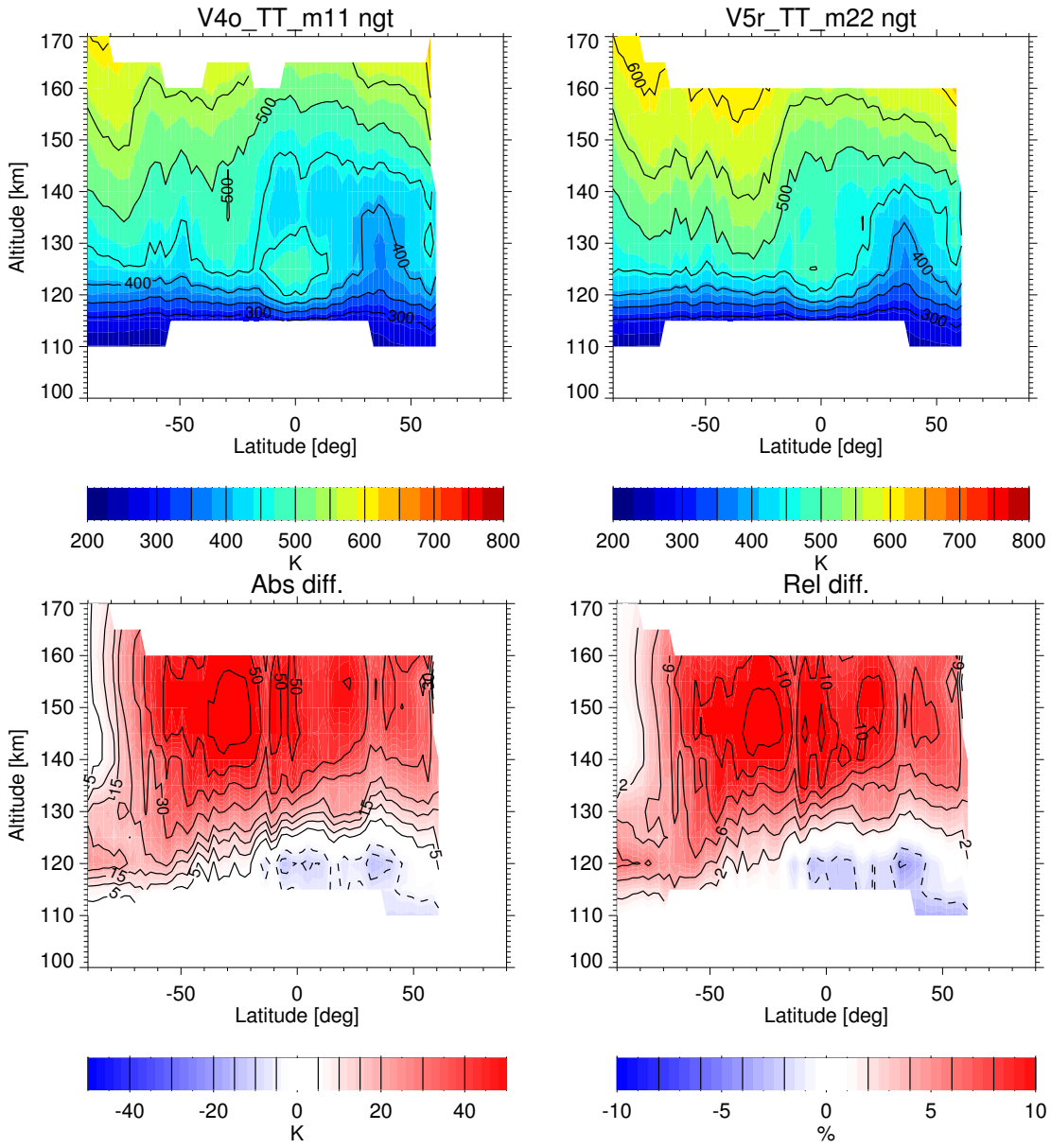

Figure 41: Comparison of thermospheric temperatures for nighttime conditions (10 pm) retrieved in the current V5r_TT_621 and the previous V4O_TT_601 versions for 5 June 2009 (low solar activity). Lower panels show the V5r_TT_621–V4O_TT_601 differences. White areas indicate unavailability of meaningful data.

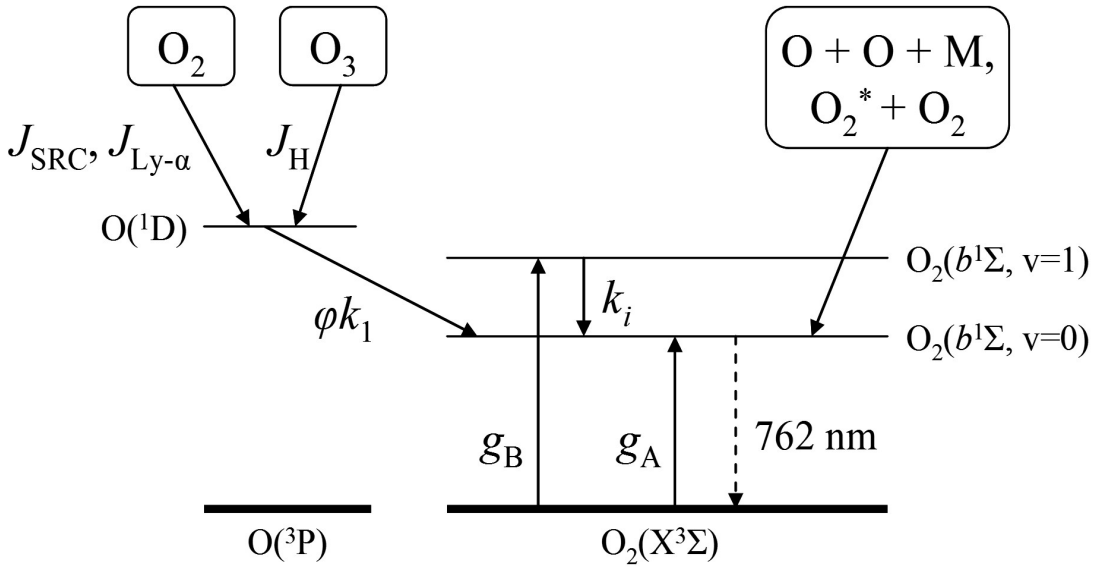

Figure 42: Schematic of significant production mechanisms of A-band dayglow emission. J and g terms are photochemical reaction coefficients, and k terms are collisional quenching rates.

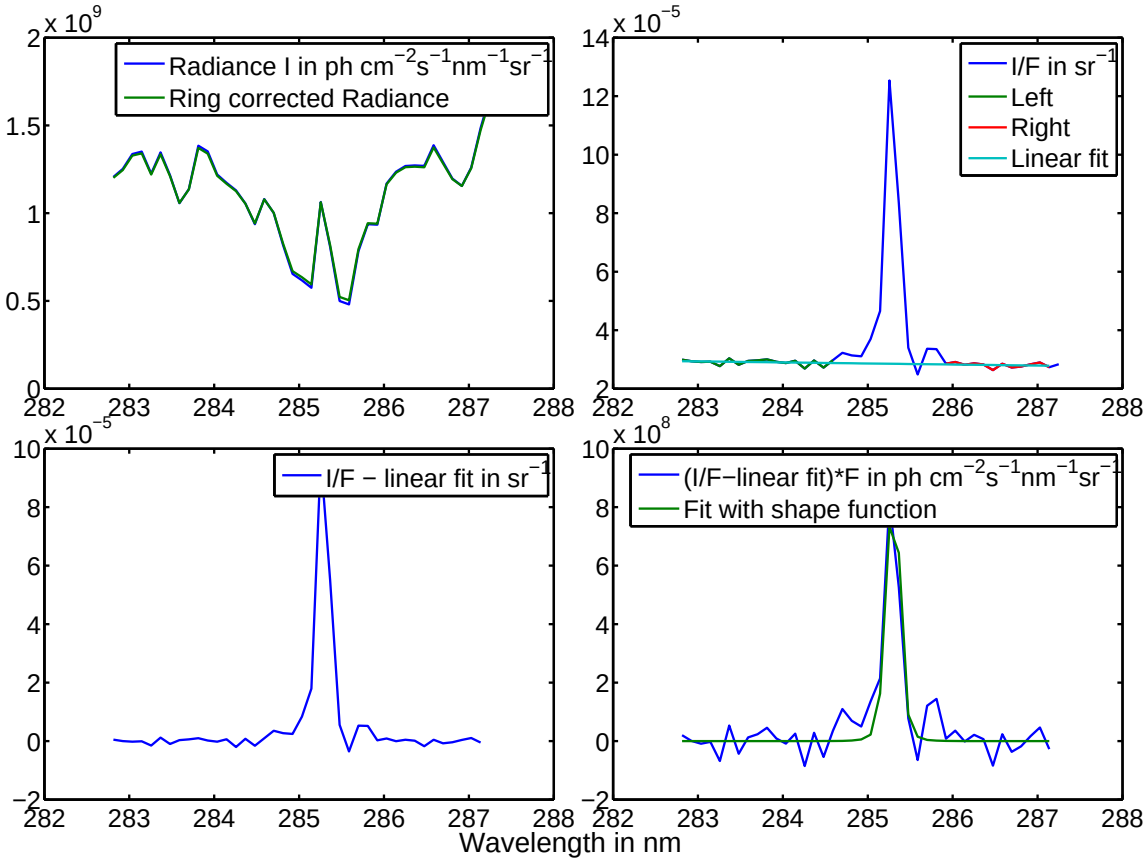

Figure 43: Slant column emission (SCE) determination. First, the Ring effect correction is applied to the limb radiance I (top left panel). The limb radiance is divided by the solar irradiance F and the wavelength region left and right to the line are used for a linear fit of the background radiation (top right panel). The linear fit is subtracted from the ratio I/F (bottom left panel) and the spectrum is again multiplied with the solar irradiance F (bottom right panel). Finally, the area of the emission line is fitted with the slit function of the instrument.

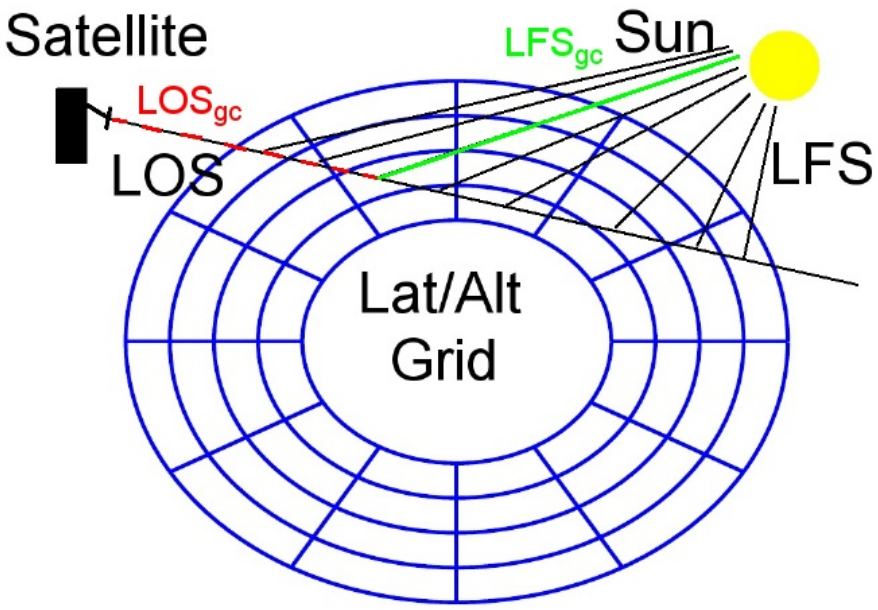

Figure 44: Longitude/altitude grid and pathways used by the forward model.

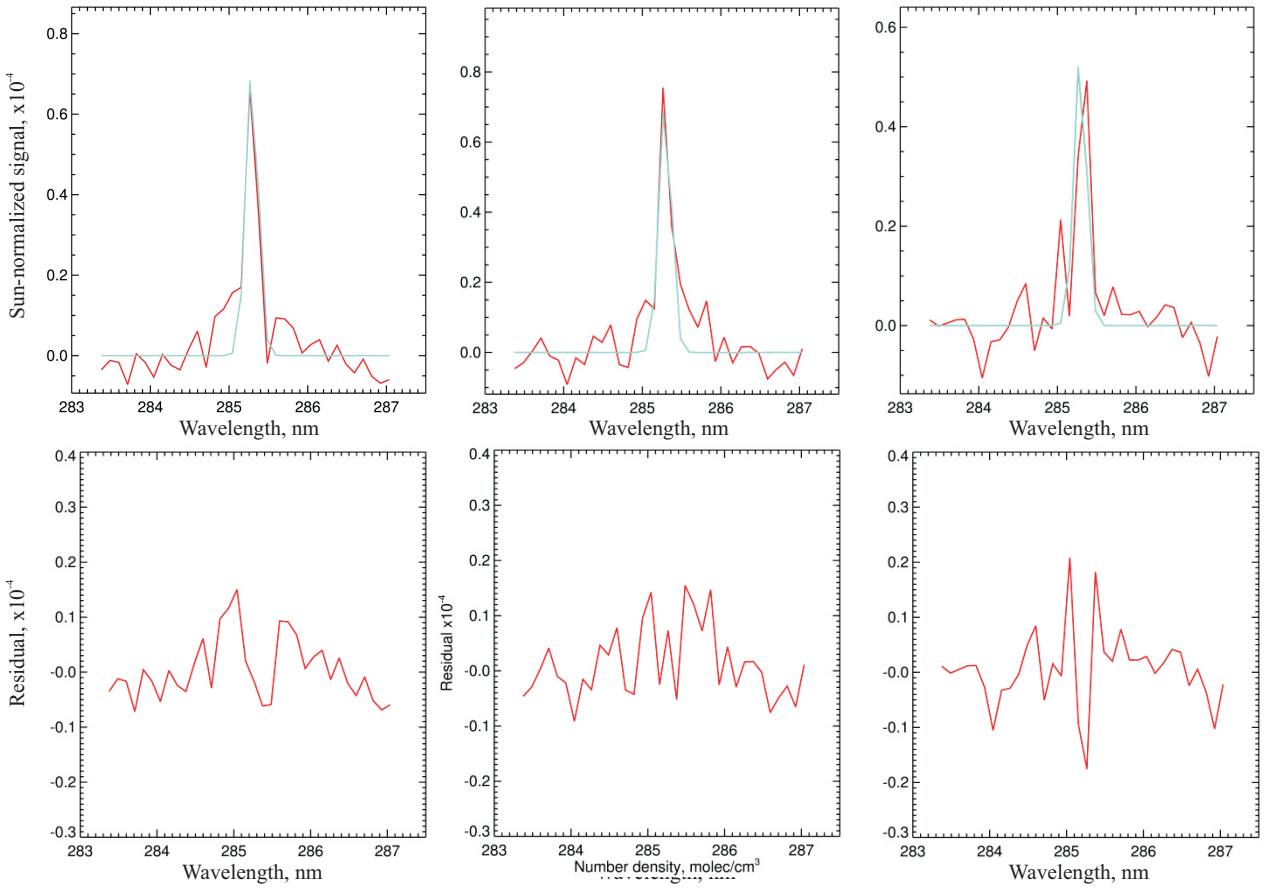

Figure 45: Spectral fits and fit residuals for sodium retrieval from nominal limb measurements of SCIAMACHY. The upper row shows the measured (red) and simulated (cyan) radiance with removed baseline. The lower row show the spectral residuals. Columns show the results for different tangent heights: 87 km, 81 km, 74 km (left to right).

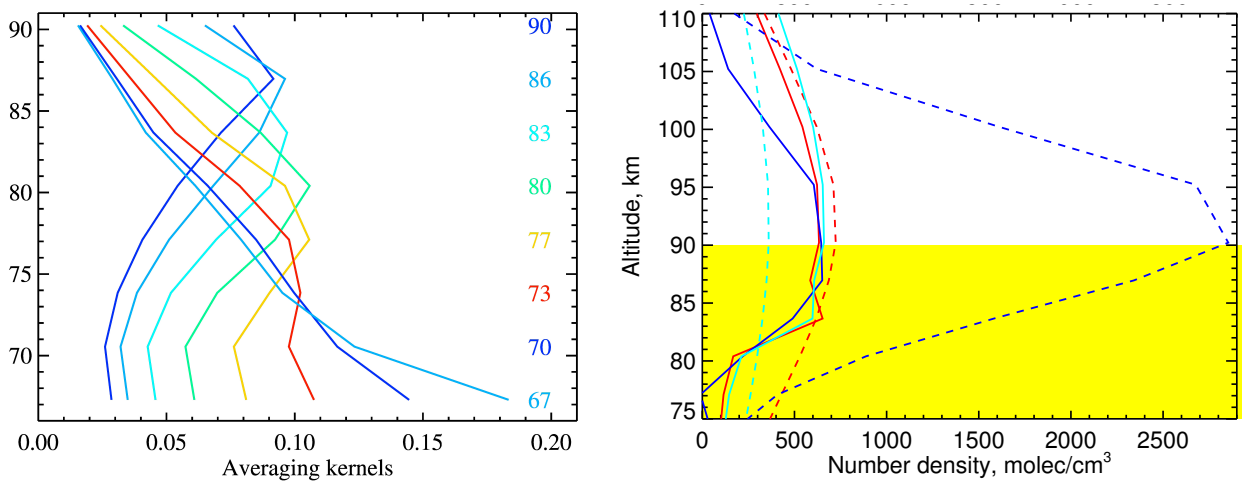

Figure 46: Left panel: typical averaging kernels for Mg retrieval. Right panel: retrieval results (solid lines) for different initial guess profiles assumed (dashed lines). Yellow area depicts the retrieval range.